

CHESTS (C)

LIBRARY Michigan State University

## This is to certify that the dissertation entitled

MECHANICAL MODELING AND SIMULATION OF POROUS POLYMER NETWORKS: LOAD INDUCED LOSS OF SATURATION IN ISOTROPIC ELASTOMERS AND PRESSURE DRIVEN SEEPAGE IN DIRECTIONALLY REINFORCED ELASTOMERS

presented by

**HUA DENG** 

has been accepted towards fulfillment of the requirements for the

Ph.D. degree in Mechanical Engineering

Major Professor's Signature

Date

MSU is an Affirmative Action/Equal Opportunity Employer

PLACE IN RETURN BOX to remove this checkout from your record.

TO AVOID FINES return on or before date due.

MAY BE RECALLED with earlier due date if requested.

DATE DUE	DATE DUE	DATE DUE
	-	

5/08 K:/Proj/Acc&Pres/CIRC/DateDue.indd

# MECHANICAL MODELING AND SIMULATION OF POROUS POLYMER NETWORKS: LOAD INDUCED LOSS OF SATURATION IN ISOTROPIC ELASTOMERS AND PRESSURE DRIVEN SEEPAGE IN DIRECTIONALLY REINFORCED ELASTOMERS

By

#### **HUA DENG**

#### A DISSERTATION

Submitted to
Michigan State University
in partial fulfillment of the requirements
for the degree of

DOCTOR OF PHILOSOPHY

Mechanical Engineering

2009

#### **ABSTRACT**

MECHANICAL MODELING AND SIMULATION OF POROUS POLYMER NETWORKS: LOAD INDUCED LOSS OF SATURATION IN ISOTROPIC ELASTOMERS AND PRESSURE DRIVEN SEEPAGE IN DIRECTIONALLY REINFORCED ELASTOMERS

By

#### **HUA DENG**

Elastomeric gels are high molecular weight crosslinked polymer networks immersed in a low molecular weight liquid medium. In the liquid environment, they could undergo a large deformation associated with swelling or shrinking in response to environmental stimuli, such as change in temperature, chemistry of the liquid bath, and light exposure. This valuable property makes them useful in a wide range of applications in drug delivery, surgical dressings, artificial tissue, and control material in engineering, which motivate the desire to better understand their underlying mechanical response.

In gels the polymer and liquid components mix in definite proportions as determined primarily by entropic and enthalpic effects. Mechanical loading can also alter the mixture proportions by absorbing or driving out the liquid. Gel swelling in the absence of mechanical loading is often described by a generalized Flory-Huggins equation, which accounts for the effects between such a treatment and the broader hyperelstic theory which accounts for the effect of mechanical loading. In this study we consider loadings that can lead to both fluid gain (swelling increase) and fluid loss (swelling reduction). For loadings that give fluid gain, we then consider a situation in which the amount of available fluid is limited. In this case, increased loading may reach a point at which no additional fluid is available for uptake into the gel system. This results in a transition of the gel from a state of liquid saturation to a state in which it is no longer saturated. This transition is first considered in the context of homogeneous deformation where an appropriate hyperelastic analysis shows that

the transition from saturation to nonsaturation gives rise to an abrupt mechanical stiffening. Then two kinds of inhomogeneous deformation problems are investigated, including everting an axially loaded tube and twisting a hollow tube that originally swells freely in the liquid bath. Various boundary displacements and traction conditions are applied so as to study how these alter the original fluid distribution. It is found that certain boundary conditions generate an overall volume increase after free swelling, which results in a stiffer mechanical response after loss of saturation.

These static problems describe equilibrium situations in which both the fluid component and the polymer matrix component of the system are at rest. However, a more complicate phenomenon - which attracts abundant research interests - fluid diffusion through polymer networks requires further study of the relative motion between the fluid and the polymer network. A mixture theory is then invoked to specifically deal with separate mechanical balance principles for each component. Pressure driven fluid seepage problems for both isotropic and anisotropic (fiber reinforced) gels are discussed based on this framework.

To my family

#### **ACKNOWLEDGMENTS**

First I would like to take this chance to thank my major advisor, Dr. Thomas Pence, for his guidance, instruction and support through the course of my doctoral study and research. His expertise in solid mechanics and related areas makes me feel easy to handle any difficulty during my 4 years Ph. D. career. He is always willing to help me out as much as he could not only in my academic research but also in my personal affairs. I would also like to thank my advisor Dr. Neil Wright for his support, in particular valuable suggestions on the details of my dissertation format.

Second, I want to thank Professor Ronald Averill, Professor Xiaobo Tan, and Professor Seungik Baek for serving on advisory committee. Their insightful comments on my research are greatly appreciated. Professor Seungik Baek's experience in the similar research field has helped me a lot in completing the theoretical work of this study.

Third, I want to thank my family for giving me the chance to experience this transient, but wonderful journey of life in this world, even though not much achievement has been made yet.

Finally, I also would like to thank friends at Michigan State who have offered me generous help: Dr. Li Sun, Guokai Zeng, Dr. Yang Fang, Fang Xie, Dr. Tengfei Luo and many others. I want to express my special thank to Ms Manshan Li for her love and support in my life.

### **Table of Contents**

List	of Fi	gures	/iii
1		oduction	1
	1.1 1.2	Background	2 11
2	Mod		15
	2.1 2.2		15 22
3	Hom	ogeneous Deformation	29
	3.1	Equibiaxial Stress	30
	3.2	Uniaxial Stress	34
	3.3	Experimental Validation	39
	3.4		41
	3.5		47
	3.6	Summary	52
4	Ever	sion of a Swollen Cylindrical Tube	55
	4.1	The Inhomogeneous Deformation of an Everted Tube under Axial	
			56
	4.2		61
	4.3	•	68
	4.4		<b>7</b> 9
5	Twis	ting of a Cylindrical Tube	80
	5.1	The state of the s	81
	5.2	•	86
	5.3		89
	5.4		96
	5.5		07
	5.6	The state of the s	15
6	Seep	age Through a Fiber Reinforced Hyperelastic Layer 1	18
	6.1	• • • • • • • • • • • • • • • • • • • •	19
	6.2		26
	6.3	• • • • • • • • • • • • • • • • • • • •	30

	6.4	Steady State Diffusion through a Fiber Reinforced Layer	132
	6.5	General Formulation for Non Steady State Diffusion	150
	6.6	Summary	172
7	Conc	lusion	174
AP	PEND	IX	177
A Nondimensional Form of Governing Equations of Steady State		imensional Form of Governing Equations of Steady State	
		sion Problem	178
В	Funct	tions $F_1(g')$ and $F_2(g')$	179
$\mathbf{C}$	Funct	cion $F_3(f', f'', f''', g', g'', g''')$	180
Bib	liogran	ohv	182

## List of Figures

2.1	The constitutive function $h(J)$ in (2.8) for various $\chi$ . Vaues of $J$ giving $h(J) = 0$ model gel dilation on the basis of mixing entropy and mixing enthalpy, but do not account for the elastic effect of polymer crosslinking.	19
2.2	The constitutive expression $h(J) + \mu J^{-1/3}$ for various $\chi$ when $\mu = 0.01M$ . The new term $\mu J^{-1/3}$ describes the effect of crosslinks. Values of $J$ giving $h(J) + \mu J^{-1/3} = 0$ describe free swelling	20
2.3	The free swelling stretch ratio $\zeta$ as given by (2.14) and (2.15) is a function of $\bar{M}$ , $\chi$ and $\xi$ . The dependence of $\zeta$ on $\xi$ is shown for various $\bar{M}$ and various $\chi$	25
3.1	Stress-stretch behavior and volume-stretch behavior for equibiaxial loading of a saturated gel with $\bar{M}=100$ and $\chi=0.425$ showing the effect of different $\xi$	32
3.2	Stress-stretch behavior for equibiaxial loading with $\bar{M}=100,\chi=0.425,$ and $\xi=0.$ Three nonsaturated response curves are depicted. Each nonsaturated response branches off of the saturated response "backbone curve"	33
3.3	Stress-stretch behavior and volume-stretch behavior for uniaxial loading of a saturated gel with $\bar{M}=100$ and $\chi=0.425$ showing the effect of different $\xi$	36
3.4	Stress-stretch behavior for uniaxial loading with $\bar{M}=100,\chi=0.425,$ and $\xi=0.$ Three nonsaturated response curves are depicted	38
3.5	The dependence of volume and stress on uniaxial stretch for $\bar{M}=100,~\chi=0.425,~{\rm and}~\xi=1.$ Three nonsaturated examples are shown corresponding to loss of saturation at $\lambda_{uni-A}^*=1.5, 1.6$ and $1.7.\ldots$	40
3.6	Stress-stretch behavior and volume-stress behavior for uniaxial testing of a saturated gel as given by R. Monroe in [74]	42

3.7	Stress-stretch behavior for equitriaxial loading of a saturated gel with $\bar{M}=100$ and $\chi=0.425$ showing the effect of different $\xi$ . For $\xi>0.038$ the graphs are monotonic. For $0<\xi<0.038$ the graphs are decreasing on a finite interval in $\xi$	44
3.8	Critical value $\xi_{crit}$ for the existence of a local stress maximum in the equitriaxial stress response. For $\xi > \xi_{crit}$ the response is monotonic.	45
3.9	Stress-stretch behavior for equitriaxial loading with $\bar{M}=100, \chi=0.425$ , and $\xi=0.5$ showing three examples of nonsaturated response. Since the stretch $\lambda=J^{1/3}$ , no additional stretch is possible after loss of saturation.	46
3.10	Comparison of a saturated and a nonsaturated gel under uniaxial load. On the left is a comparison of the hard device energy expression. On the right is the resultant force as a function of stretch. As in Figure 3.5 the constitutive parameters are given by $\bar{M}=100,~\chi=0.425$ and $\xi=1.$ The transitions are taken to occur at $\lambda=1.5,1.6$ and $1.7.$	50
4.1	Radial deformation $(\bar{r}=r/(\zeta R_i))$ and local volume change ratio as a function of radial position. As in previous figures, $\bar{M}=100$ and $\chi=0.425$ . The cylinder geometry is such that $R_0=2R_i$	63
4.3	Resultant axial force as a function of mechanical stretch and total volume as a function of mechanical stretch for both the everted cylinder and the uneverted cylinder using the same material parameters as in Figure 4.1. For the everted cylinder, the reference geometry is again such that $R_0 = 2R_i$	66
4.4	Total volume after eversion as a function of mechanical stretch, and resultant force as a function of mechanical stretch, for various values of $\xi$ , again using $\bar{M}=100, \ \chi=0.425$ and $R_0=2R_i$	69
4.6	Local volume change $J$ versus $\hat{\lambda}_z$ for an everted cylinder with $R_o = 2R_i$ and material parameters $\bar{M} = 100$ , $\chi = 0.425$ and either $\xi = 0$ or $\xi = 1$ . On the left, $\xi = 0$ and the loss of saturation corresponds to that depicted in Figure 4.5. After loss of saturation, increasing stretch redistributes the finite amount of fluid from the outer region to the inner region. On the right, $\xi = 1$ and the loss of saturation corresponds to that depicted in Figure 4.7. For the nonsaturated cylinder, increasing stretch now redistributes the finite amount of fluid from the inner region to the outer region.	74
	0	•

78	Resultant axial force as a function of mechanical stretch for the everted cylinder with $R_o=2R_i$ . Material parameters correspond to those in Figure 4.3(c), namely: $\bar{M}=100,\chi=0.425,{\rm and}\xi=1.$ Three different values of $V_{liq}$ are considered, corresponding to $\hat{\lambda}_z^*=0.8,0.9,{\rm and}1.0.$ The nonsaturated response curve is first above, and then below, the saturated response curve, and so mirrors the case of this material under homogeneous deformation (Figure 3.10(b)).	4.8
82	Free swelling volume change $J_{fs}$ and stretch $\zeta$ for different $\alpha$ on the basis of (2.3) and (5.1) using (5.3)	5.1
90	$J$ normalized by the free swelling value $J_{fs}=\zeta^3$ as a function of $\bar{R}=R/R_i$ (panels (a) and (c)); and the twist $g=\theta-\Theta$ as a function of $\bar{R}$ (panels (b) and (d)), for boundary conditions given by (5.19) and (5.20) with $R_o/R_i=2$ . The problem is equivalent to that presented in [48] and panels (a), (b), (c) correspond respectively to Figures 1, 4, 5 in [48]	5.2
91	Normal stress $\sigma_{rr}$ for the same problem as described in Figure 5.2	5.3
97	Additional graphs for the boundary value problem described in Figure 5.3. The dashed lines in panels (a) and (c) give the baseline associated with a pure polymer (no liquid) by showing the volume ratio $V_{poly}/V_{fs} = J_{fs}^{-1} \dots \dots \dots \dots \dots$	5.6
100	Additional graphs for the boundary value problem described in Figure 5.4	5.8
103	$\sigma_{rr}(r_i)$ versus $\delta$ for $\alpha=0$ . Panel (a) is the magnified portion of panel (b) near $\delta=1$ . Panel (c) provides additional curves near $\delta=1$ with the top curve for $T^*=0.8$ ; bottom curve for $T^*=1.0$ , and with additional curves for $T^*$ increments of 0.01 in between	5.9
105	(a) Torque vs. twist relation with $\alpha=0$ for the boundary conditions (5.24). Here $T^*=0.937$ , $\psi=0.90$ corresponds to the local maximum. Also $T^*=0.377$ , $\psi=1.70$ is the effective limit of our numerical calculation and corresponds to $\delta=0.15$ . (b) Volume ratio $V/V_{fs}$ versus twist angle $\psi$ for the same problem.	5.10
106	The post-maximum solutions for $\alpha = 0$ . These correspond to a continuation of panels (a) - (d) of Figure 5.4. Now $T^*$ decreases with increasing $\psi$ as is evident from panel (d)	5.11

5.12	Mechanical behavior for the nonsaturated solutions when loss of saturation takes place at a standard solution with $T^* = 0.6$ . Here $\alpha = 0$ and $V_{liq} = 40.469LR_i^3$ . The solid curve in each panel corresponds to the instant of transition while the other curves correspond to increasing $T^*$ . The values of $\psi$ associated with $T^* = 0.60$ , 0.80, 1.00, 1.20, 1.40 are $\psi = 0.418$ , 0.562, 0.708, 0.858, 1.011 respectively	110
5.13	Mechanical behavior for nonsaturated solutions when loss of saturation takes place at the post-maximum solution with $T^*=0.6$ . Here $\alpha=0$ and $V_{liq}=53.371LR_i^3$ . The solid curve in each panel corresponds to the instant of transition while the other curves correspond to increasing $T^*$ . The values of $\psi$ associated with $T^*=0.60,0.80,1.00,1.20,1.40$ are $\psi=1.412,2.053,2.800,3.632,4.533$ respectively	112
5.14	Saturated and nonsaturated torque-twist response for $\alpha=0$ . Two examples are shown, each corresponding to $T^*=0.6$ . The square markers on the nonsaturated curves represent computational points and the intervening dots are to guide the eye. The transition on the left occurs at a standard solution (corresponding to the solutions displayed in Figure 5.12). The transition on the right occurs at a post-maximum solution (corresponding to the solutions displayed in Figure 5.13)	113
5.15	Saturated, transition and nonsaturated states associated with loss of saturation taking place from a standard solution when $\psi=0.42$ . Thus $\psi=0.62$ corresponds to a nonsaturated state. For comparison, the response for a hypothetical $\psi=0.62$ saturated state is also shown	114
5.16	Saturated, transition and nonsaturated states associated with loss of saturation taking place from a post-maximum solution when $\psi=1.41$ . Thus $\psi=1.60$ corresponds to a nonsaturated state. For comparison, the response for a hypothetical $\psi=1.60$ saturated state is also shown.	116
6.1	Mapping of fluid and solid particles	120
6.2	Free swelling of a fiber reinforced layer	127
6.4	The variation of the change in orientation angle $\omega-\Omega$ (in radians) with $\xi=0$ and $M/\mu=100,~\chi=0.425.$	135
6.5	Representation of a pressure differential that will cause diffusional fluid seepage through a fiber reinforced layer	136
6.6	Comparison of the numerical results with the experimental data [24] .	142

6.7	The variation of nondimensional displacement in the thickness direction after free swelling at $P_H - P_0 = 200 psi$ with $\gamma = 0$ for $\xi = 0$ and $\xi = 1$	143
6.8	The normal displacement of the free surface vs. pressure difference for the material parameters in Figure 6.7(a) with $\xi=0$ and Figure 6.7(b) with $\xi=1$	144
6.9	Variation of the fluid flux $q/\rho_0^f$ and the required reactive shear stress $\sigma_{xx}^{mix}(H)$ with pressure difference $P_H-P_0$ for various fiber reinforcement coefficients $\bar{\gamma}$ with $\xi=0,\ n=5,\ \alpha=1.556\times 10^{19}\ gm/cc\cdot day$ when the boundary conditions are given by (6.67)	146
6.10	The fibers become curved in the inhomogeneous deformation associated with pressure driven fluid seepage as depicted in panel (c). This is a schematic representation	147
6.11	The fiber geometry at various seepage rates with $\bar{\gamma}=2.0,\xi=0,n=5$ and $\alpha=1.556\times 10^{19}~gm/cc\cdot day$ when the boundary conditions are given by (6.67). ( $x_f$ denotes the projected distance onto $x$ -axis between an arbitrary point on the fiber and the tip (z=0) of the same fiber.) .	148
6.12	Variation of the fluid flux $q/\rho_0^f$ and shear displacement $f(H)-\Gamma(H)$ with pressure difference $P_H-P_0$ for various fiber reinforcement coefficients $\overline{\gamma}$ with $\xi=0,\ n=5,\ \alpha=1.556\times 10^{19}\ gm/cc\cdot day$ when the boundary conditions are given by (6.68)	149
6.13	The shear displacements as a function of the initial fiber orientation under a free surface traction boundary condition at $Z=H.$	151
6.14	The normal displacements as a function of initial fiber orientations with a free surface traction boundary condition at $Z=H$	152
6.15	The fiber geometry at various seepage rates with $\bar{\gamma}=2.0,\xi=0,n=5$ and $\alpha=1.556\times 10^{19}~gm/cc\cdot day$ when the boundary conditions are given by (6.68). The common slope value at $Z=H$ in (b) is a direct consequence of the boundary conditions (6.68) <sub>4</sub> and (6.68) <sub>5</sub>	153
6.16	An explicit forward time-stepping scheme	157
6.17	Change in compaction during transient diffusion in the absence of fibers $(\bar{\gamma}=0)$ for a material with $\xi=0$ , $M/\mu=100$ . In this simulation the steady state seepage with $P_H-P_0=50psi$ is abruptly altered to $P_H-P_0=200psi$ .	159

6.18	The variation of $\rho^f/\rho_0^f$ along the thickness for the simulation considered in Figure 6.17	160
6.19	The variation of normal stresses along the thickness direction for the simulation considered in Figure 6.17	161
6.20	The amount of fluid in the layer changes with time: from its initial steady state value (where $P_H - P_0 = 50psi$ ), and finally approaching the final steady state value (where $P_H - P_0 = 200psi$ )	162
6.21	The change of interstitial fluid amount with time for various pressure difference. Free swelling state $(P_H - P_0 = 0)$ is abruptly altered when $P_H - P_0$ is suddenly changed to 50psi, 100psi, 200psi, 300psi, and 400psi, respectively	163
6.22	The shear and normal contraction associated with fiber reinforced transient diffusion where $\bar{\gamma}=1.0,\Omega=45^{\circ},{\rm and}\xi=0.\ldots$	166
6.23	The shear and normal contraction associated with fiber reinforced transient diffusion where $\bar{\gamma} = 10.0$ , $\Omega = 45^{\circ}$ , and $\xi = 0$	167

## Chapter 1

### Introduction

By a gel we mean a system of crosslinked polymer chains mixed together with a low molecular weight liquid. In the liquid environment, gels could undergo a large deformation associated with swelling or shrinking. Their wide applications in drug delivery [1,2], surgical dressings [3], artificial tissue [4] (skin, articular cartilage, etc.) and control material (micro-control [5], smart materials, etc.) in engineering motivate the desire to better understand their underlying mechanical response. Depending on the nature of the elastomer and fluid, a variety of ambient conditions, such as temperature [6,7], pH of the liquid bath [8,9], and light exposure [10,11], could possibly determine the amount of liquid that is absorbed into or expelled out of the gel. This is typically coupled with the mechanical deformation of the polymer network. Thermodynamical and mechanical balance principles describe these processes, in which case a central issue is the development of a modeling framework that is sufficiently general to accommodate these effects upon specification of appropriate constitutive relations. One possible framework is that of small deformation; such theories describe swelling by allowing for parametric dependence of constitutive parameters (e.g. elastic constants, osmotic pressure) on the underlying electrochemistry (e.g. concentrations, charge density) [12]. Such linear descriptions are useful for describing mechanical behavior in fixed ranges wherein issues of large strain, instability, and transition from saturation to unsaturation do not arise. However, in certain situations such phenomena cannot be avoided, or will even be exploited, in which case it is necessary to consider a finite strain description.

#### 1.1 Background

Gels are high molecular weight crosslinked polymer networks immersed in a low molecular weight liquid. When water is the liquid, then these are typically referred to as hydrogels. The liquid can also be organic in nature as for example discussed in Chapter 7 of Treloar's well known treatise *The Physics of Rubber Elasticity* [13]. Although hydrogels would generally be much softer than a rubbery material infused with an organic liquid, both are regarded as gels for the purpose of this thesis, and we shall use the term gel throughout in this broad sense.

Some of the earliest experiments on the stress-stretch behavior of swollen gels were performed by Gee [14]. Simple uniaxial tension tests were made on a range of vulcanized rubbers at various degrees of swelling. The experimental results depart greatly from those predicted by the standard large strain theories of rubber elasticity. These classical theories are associated with a Gaussian statistical mechanics treatment of the polymer chains. Similar tests can also be found in [15] and [16].

McKenna et al. [17] carried out torsional and uniaxial compression tests on both dry and swollen cylindrical rubbers. They concluded that the dry-state elastic free energy function could also describe the elastic behavior of swollen gels for non-highly cross-linked rubbers. This implies that the presence of liquid molecules does not affect the elastic component of the free energy function. Their experiments are claimed to be consistent with the Frenkel-Flory-Rehner assumption that the total energy of swollen networks is comprised of the free energy of mixing and the elastic free energy.

There are also many models [12, 18] that treat equilibrium mechanical behavior of gels in the setting of the classical small strain tensor  $\varepsilon = \frac{1}{2}(\nabla \mathbf{u} + \nabla \mathbf{u}^T)$  (where  $\mathbf{u}$  is the displacement vector) within the theory of linear elasticity. These include the small strain linear theory of poroelasticity [19]. They are not useful for our purposes and will be omitted from what follows. Instead, it is necessary to use large strain elasticity theory.

A separate, and complicating issue is the internal flow of fluid in gels so as to achieve equilibrium if the system is not initially in equilibrium. The diffusion of fluid through polymer networks has been investigated a great deal [20–23]. One of the most frequently referred to modern set of experiments on this can be found in [24], where Paul and Ebra-Lima measured the non-linear diffusion of twelve organic liquids through a swollen gel membrane. The diffusion was induced by the pressure difference across the membrane. The diffusion coefficients and also the material parameters of both the fluid and the hyperelastic rubber material were determined from their experimental results. These material constants were then widely adopted in later modeling frameworks.

One of the earliest continuum theories that can be used to describe the large strain behavior of incompressible hyperelastic materials was presented by Mooney [25] and Rivlin [26]. This apples to rubber-like materials but does *not*, in its original presentation, account for gel mixtures where the interaction of the elastomer and liquid is present. Their basic theory involves an energy argument that the elastic free energy  $\Phi$  depends only on the three principal stretches  $\lambda_1$ ,  $\lambda_2$  and  $\lambda_3$ . In current notation, their model is equivalent to the expression

$$\Phi = \Phi(\lambda_1, \lambda_2, \lambda_3) = \frac{\mu}{2} \left[ (1 - \xi) \left( \lambda_1^2 + \lambda_2^2 + \lambda_3^2 - 3 \right) + \xi \left( \lambda_1^2 \lambda_2^2 + \lambda_2^2 \lambda_3^2 + \lambda_3^2 \lambda_1^2 - 3 \right) \right],$$
(1.1)

where  $\mu > 0$  is the shear modulus for infinitesimal strains and  $\xi$  (obeying  $0 \le \xi \le 1$ ) is

the Mooney-Rivlin adjustable parameter. Because this model is for an incompressible hyperelastic material, implying volume preservation during mechanical deformation, it leads to a constraint condition  $\lambda_1\lambda_2\lambda_3=1$  on the three stretches. In the case associated with  $\xi=0$ , eq. (1.1) retrieves the neo-Hookean strain energy function

$$\Phi = \Phi(\lambda_1, \lambda_2, \lambda_3) = \frac{\mu}{2} \left( \lambda_1^2 + \lambda_2^2 + \lambda_3^2 - 3 \right), \tag{1.2}$$

which arises from a Gaussian statistical treatment of polymer chain entropy.

One of the basic issues for the mechanical behavior of gels is how much they swell depending on their liquid environment. In the absence of load this is called free swelling. For a given value of free swelling, the question arises as to how an additional applied load on the swollen gel further deforms the gel. Various hyperelastic models have been used for this purpose. In other words, these models seek to predict how stresses applied to a swollen gel cause additional stretch beyond that associated with free swelling. The more chemistry oriented literature often accomplished this by balancing the elastic free energy (as a function of the stretches) with the work done by the principal stresses  $\sigma_1$ ,  $\sigma_2$  and  $\sigma_3$ . This then gives the relation between the principal stresses and the principal stretches. In addition to the Mooney-Rivlin material mentioned above, some of the other energy functions that have been used for this purpose include the constrained chain model [27,28], localization model [29,30], liquid-like model [31,32], and eight-chain model [33]. Han et al. [34] compared these models and concluded that the constrained chain model fits experimental data [35–38] best for both dry and swollen states, whereas the eight-chain model of Arruda and Boyce shows less agreement with the experimental data. However, later Arruda and Boyce [39] questioned the calculation executed by Han et al. [34] and put forward their eight-chain non-Gaussian Model in order to account for the same trends as in the experimental data for large stretches. On this basis, they then proposed a hybrid model that suitably combines the Flory-Erman constrained chain model (so as to capture the main features of stress-strain behavior for small strains) and the Arruda-Boyce eight-chain model (which was developed to describe the large strain behavior well). The strain energy density function of this hybrid model gives rise to the following stress-strain relationship for uniaxial loading:

$$\sigma = \left[\nu_p^{\frac{2}{3}} \frac{Nk\Theta}{6} \frac{\sqrt{n}}{\lambda_c} \mathcal{L}^{-1} \left(\frac{\nu_p^{-\frac{1}{3}} \lambda_c}{\sqrt{n}}\right) \left(\lambda^2 - \frac{1}{\lambda}\right) + \frac{1}{2} N_J k\Theta \nu_p \left(A_1 \lambda^2 - A_2 \frac{1}{\lambda}\right)\right]. \tag{1.3}$$

Here  $\nu_p$  is the volume fraction of the polymer relative to the dry state and represents the degree of swelling, N is the number of chains in the polymer per unit unswellen volume,  $N_J$  is the junction density, k is Boltzmann's constant,  $\Theta$  is absolute temperature, n is the number of links in the chain,  $\lambda_c = [(\lambda^2 + 2/\lambda)/3]^{1/3}$ ,  $\mathcal{L}^{-1}()$  is the inverse Langevin function, and  $A_1, A_2$  are both functions of  $\lambda$  and  $\nu_p$ . These are too complicated to be discussed in detail here and the reader is referred to [39] for more information.

In summary, the treatments described above in [27–34] seek to use the theory of hyperelasticity to model gels after free swelling has occurred. They account for the strain energy function of hyperelastic materials and give a reasonable linear approximation to the neo-Hookean model. The main distinction between different models lies in the modification of the strain energy function for moderate and large deformation.

In order for a model to also determine the amount of swelling, it is necessary to connect the mechanical response to the interaction between the polymer network and the liquid which together make up the gel. The attempt to make this connection was made over half a century ago. The swelling of the gels depends upon the interaction between the solid elastomer and the surrounding liquid. One of the earliest experimental measurements on this interaction goes back to [40], where Gee and Treolar gave a thermodynamic description of the rubber-benzene mixture system by measur-

ing the vapor pressures. A statistical mechanical theory of the equilibrium degree of swelling was presented by Flory [41] and Huggins [42,43] separately. Based on this theory, the free energy of mixing H is

$$H = M[(\nu^{-1} - 1)ln(1 - \nu) + \chi(1 - \nu)], \tag{1.4}$$

where M and  $\chi$  are material parameters, and  $\nu$  is the volume fraction of the elastomer in the mixture. They seek to determine the free swelling ratio  $1/\nu$  by an energy argument that seeks to account for: (1) the mixing entropy of elastomer and liquid; (2) mixing enthalpy of elastomer and liquid; and (3) strain energy of the elastomer. If a system is originally in non-equilibrium, then it is assumed that internal fluid diffusion will occur until equilibrium is achieved. This diffusion process can be described by a mixture theory approach. For now we restrict attention to equilibrium configurations once any fluid redistribution is complete.

On the basis of Flory-Huggins theory, Treloar [44] more formally introduced an extra term that explicitly accounts the work due to tractions when load is applied. By this treatment, the swelling equilibrium associated with homogeneous deformation under simple loading conditions could be determined. Treloar [45] later considered the problem of a cylinder subjected to combined axial extension and torsion about the axis. For large deformation the radial distribution of the stress, strain, and the amount of swelling are obtained by numerical analysis. It is found that the gel volume decreases with the torsion.

Wineman and Rajagopal and co-workers constructed a continuum mechanical treatment incorporating finite strain on the basis of mixture theory, as discussed in a series of papers [46–48]. In [48] they consider a static problem where a relative rotation was applied to the two lateral surfaces of a swollen hollow cylinder. Their main purpose was to find the fluid redistribution with various twist moments. However,

they limited attention to boundary conditions that did not allow for volume change after swelling. In an even earlier paper [49], Wineman, Rajagopal, and co-workers consider a torsion problem that does treat load dependent volume change using a full mixture theory formulation. As in [45], they find that torsion causes volume decrease; this corresponds to the expelling of fluid.

In this work, I have examined similar static boundary value problems with different loading conditions. Both volume decrease and volume increase associated with the applied load can be obtained. The latter case corresponds to fluid absorption. For these static problems it is not necessary to involve mixture theory and so are similar to the classical approach of Treloar [45]. For the case of fluid absorption, it may further be the case that insufficient fluid is present to attain a saturated state. In this case, the associated transition from saturation to unsaturation is considered. In particular, it will be indicated how the overall mechanical response becomes stiffer if this transition takes place will be indicated.

These are not the only continuum models that have been developed to treat the swelling behavior of gels. Instead of introducing the mixing free energy, Marra and Ramesh and collaborators [50,51] introduce an evolution internal variable  $\alpha$ , which is defined as the volume ratio of the interstitial fluid in the current state to that in the reference state. It is assumed that this internal variable acts as the only independent variable of the specified free energy function. To describe the volume change (called actuation in their article) they consider the total free energy function as the sum of elastic energy and an additional energy term due to the effects of free actuation, which means uniform expansion or contraction of the polymer in the fluid. This corresponds to the statement, in current notion

$$W = \Phi(I_1, I_2) + g(I_3, \alpha), \tag{1.5}$$

where W represents the total free energy and  $\Phi$  can be regarded as some elastic energy that is appropriate for an incompressible material. This  $\Phi$  is typically taken to be in the neo-Hookean, Mooney-Rivlin or even the more general Ogden [52] form. The function g in (1.5) is claimed to account for the effects of free actuation. The three invariants and the material parameters in  $\Phi$  and g are all assumed to be functions of  $\alpha$ . Then an evolution law for the internal variable  $\alpha$  is developed. Uniaxial and equibiaxial loading tests were performed. Experimental data are obtained and used in fitting the material parameters in Ogden energy function. These parameters are then substituted into a finite element model. It was then claimed that the numerical results show good agreement with the data.

Certain hydrogels exhibit phase changes of various kinds such as an abrupt volume increase when either the temperature or chemistry of the liquid is changed. These are sometimes called *stimulus-repsonse hydrogels*. Dolbow et al. [53–55] presented a continuum model for volume transitions in hydrogels that exhibit a sudden collapse in volume at a specific temperature. Their model includes a sharp-interface separating swollen and collapsed phases. With obeying the deformational and diffusion potential coherence across the interface, a set of equations of force balance and chemical potential balance were derived in the domain of each phase and on the interface as well.

Another aspect of interests in the swelling behavior of gels is the study of fluid diffusion through hyperelastic material. A variety of theoretical treatments [56, 57] have been developed to model the mechanical and thermodynamical behaviors of such diffusion process. A common-used biphasic theory called the theory of porus media (TPM), involving the mixture theory and volume fractions, is applicable to such non-linear diffusion problems. One of the earliest presentations of this treatment can be found in the work of Bowen [58]. His framework, which involves partial stresses for the solid and fluid phases, makes use of mass balances, momentum balances, an

energy balance law and the Clausius-Duhem inequality.

Many material models generalizations were then subsequently embedded into this binary mixture theory, such as a viscoelastic model [59] and an elasto-viscoplastic model [60,61]. Different numerical methods based on finite element analysis have also been developed and used to study the phenomenon of consolidation in the porous media, including Galerkin finite element method and least-square mixed finite element method [62], [63]. Within this framework, Markert [64] has presented a 3-D finite element analysis on the nonlinear fluid flow through a porous polyurethane form.

Ehlers et al. [65, 66] followed a related energy and entropy balance treatment and used it to simulate the elastic deformation of liquid saturated porous solids. In particular these works introduce the idea of a fully compact material meaning that all the internal pores have been closed, squeezing out all the fluid. Their energy functions are designed to give this full compaction only in the limit as appropriate normal stress components trend to negative infinity.

The compressibility condition on the solid and the fluid phase of the mixture is always an important fact to be considered in TPM. Palomar and Doblare [67] utilized an Augmented Lagrangian formulation to enforce the incompressibility condition on both the solid and fluid phase based on a fibre-reinforced porohyperelastic model. Diebels extended the mixture theory and applied it to both incompressible and compressible binary systems [68].

Specifically, [61,67,69] deal with material anisotropy. The numerical examples in [67] show how the additional stiffness due to the fiber reinforcing causes the fibrous materials to exhibit less deformation under the same amount of extensile load. Among the more interesting results obtained in [67] is the demonstration that the introduction of fiber network leads to a higher relative fluid diffusion velocity as well as a higher pore pressure in an unconfined compression simulation.

Under the TPM framework, Markert et al. [70] derived a set of full contact

boundary conditions at the interface of two saturated porous media with the assumption that there is no dissipative effects at the interface. These conditions include the solid velocity continuity condition, the normal seepage velocity continuity condition, the pore-fluid pressure jump condition and the solid effective normal stress jump condition. The latter two conditions have the property that if two identical porous bodies are put in contact with each other then both the pore pressure and the solid effective normal stress are continuous. However if the two contacting porous bodies have different solid-fluid phase ratio at the interface, then the pore pressure and the solid effective normal stress exhibit a jump and mixture theory arguments are used to obtain detailed expressions for these jump (see equation (47) and (48) of [70]).

However none of the works [56–70] obviously takes into account the interacting behavior between the fluid and the solid skeleton. To also connect the mechanical response to the interaction between the polymer network and the interstitial fluid, Rajagopal, Wineman and collaborators (Rajagopal et al. [46], Gandhi et al. [47] and references therein) introduced a Flory-Huggins type term in the free energy expression so as to account for the interacting continua in the diffusion problems. Pressure-induced diffusion through spherical and cylindrical geometries were studied in [46,47]. Diffusion through a porous swollen layer with lateral stretch and shear deformation was also considered in [47]. In particular these works provide numerical solutions to boundary value problems with one lateral surface held fixed while only the pressure was specified on the other surface.

These treatments also pointed out some controversies with respect to specifying the tractions on the solid and fluid boundaries. In an alternative but related variational treatment, Baek and Srinivasa [71] extremize the Helmholtz potential of the system containing the swollen solid and the fluid over all admissible system configurations. This variational procedure involves the mass conservation equations for both the solid/fluid mixture phase and the surrounding pure fluid phase. This results

in a set of governing equations and boundary conditions. Energy dissipation is also considered in [71] to account for frictional effects as the fluid diffuses through the elastomer.

Other means for arriving at this framework are also possible. This includes that given recently in [72] and [73]. In partcular, the treatment in [72] introduces the the liquid phase concentration as an independent variable prior to the requirement that the liquid component fraction in the gel be given by  $1 - \nu$ . The equivalent of this constraint is enforced by a Lagrange multiplier in [72]. The condition for free swelling is then found to be given by a requirement that the chemical potential for the pure liquid, say  $\mu_{liq}$ , is equal to an appropriate variation of the gel's total free energy with respect to a change in concentration.

#### 1.2 Objectives and Scope

The main purpose of this research is to model the mechanical deformation and also the redistribution of the concentration of fluid throughout the system in response to changes in load or displacement at the system boundary. In so doing, it distinguishes between saturated and nonsaturated gels. Numerical analysis is introduced to obtain the equilibrium deformation of the polymer network, from which the redistribution of the concentration of fluid is derived. This is based on the assumption of volume additivity that the volume of the mixture is the sum of that of the elastomer (solid phase) and that of the interistic fluid (fluid phase).

In particular, even though both the polymer matrix component and the fluid component of the gel system are regarded as individually incompressible when isolated from the other component, the overall gel system, as long as it is saturated, is then described in terms of a hyperelastic framework in which the gel is nominally compressible. This is because a fixed amount of polymer component can be

regarded as defining a gel patch (or gel "element"). The amount of fluid component within such a gel element can change, giving rise to a change in the volume of the gel element. In other words, redistribution of the fluid component with respect to the matrix component generates a local volume change. This is in keeping with the Treloar's treatment. He writes in [13] that if a rubber that is incompressible in the absence of a liquid swelling agent is subsequently swollen, then

"... the swollen rubber in continuous equilibrium with a surrounding liquid may be regarded, from the purely formal standpoint, as having mechanical properties equivalent to those of a compressible material."

In particular, since the rubber that is referred to in the above quote is regarded as being in contact with a liquid bath, the situation refers to a state of liquid saturation. Thus the saturated equilibrium response is described by a single stored energy density function W. The present work has taken the Frenkel-Flory-Rehner assumption that total energy of the gel is comprised of elastic free energy and mixing free energy, which are additive. The choice of the specific form of elastic free energy is not the central problem in this work, therefore the specific Mooney-Rivlin model will be adopted for modeling isotropic gels. The Flory-Huggins equation (1.4) will be used for the mixing free energy. Then the total free energy W for a swollen gel depends only on the deformation gradient F through the principal stretches  $\lambda_1, \lambda_2, \lambda_3$ , or equivalently the three invariants  $I_1, I_2, I_3$  of the left Cauchy-Green deformation tensor B, namely  $FF^T$ . By virtue of (1.1) and (1.4), this becomes

$$W = \Phi(\lambda_1, \lambda_2, \lambda_3) + H(\nu). \tag{1.6}$$

The saturated Cauchy stress tensor then follows from this stored energy density as

in compressible hyperelasticity

$$\boldsymbol{\sigma} = \frac{1}{J} \frac{\partial W}{\partial \mathbf{F}} \mathbf{F}^T. \tag{1.7}$$

The local volume change in the deformation then directly correlates to the local change in fluid content.

If, however, the amount of liquid is limited, and in particular assume that all the liquid is imbibed at some point in the loading process, the system then becomes nonsaturated. A constant reaction stress  $-p\mathbf{I}$  is generated so as to enforce the global constraint that the overall volume of the gel remains fixed at the instant when the transition from a saturated state to a nonsaturated state occurs. This gives the nonsaturated Cauchy stress tensor

$$\sigma = \frac{1}{J} \frac{\partial W}{\partial \mathbf{F}} \mathbf{F}^T - p\mathbf{I}. \tag{1.8}$$

Thus (1.7) and (1.8) give the relation between stress and deformation for homogeneous deformation (**F** independent of location). For nonhomogeneous deformation without any body forces the stress field must satisfy

$$\operatorname{div} \boldsymbol{\sigma} = \mathbf{0}. \tag{1.9}$$

These equations are usually nonlinear and hard to obtain analytical solutions. Therefore it is necessary to invoke numerical routines in order to obtain simulated results.

The above hyperelastic framework could describe equilibrium situations in which both the fluid component and the polymer matrix component of the system are at rest. In particular, each material point in the gel is regarded as a two component mixture of polymer matrix and interpenetrating liquid. For a sort of more complicate problems where there is relative motion between the fluid and matrix components, so it is necessary to invoke the broader continuum mechanical framework that specifically deals with separate mechanical balance principles for each component. This broader framework is known by a number of names, including: large deformation mixture theory, the theory of interacting continua, and the large deformation biphasic theory. To this end, the process of fluid diffusion through hyperelastic media is investigated in this work, where a major focus is on time dependent swelling as liquid diffuses within the elastomeric matrix.

The structure of this work is outlined as follows. The hyperelastic theory for the static mechanical response of swollen gels is developed in Chapter 2. The discussion of the stress-strain swelling response under homogeneous deformation is discussed in Chapter 3. Boundary value problem of an everted tube subject to an axial load is considered in Chapter 4. The inhomogeneous deformation response of the axially loaded tube is compared to the homogeneous deformation response of the axially loaded tube when it is not everted. Chapter 5 deals with a boundary value problem of a hollow tube with a relative twist at its lateral surfaces. Different radial displacement and traction boundary conditions are considered along with the prescribed twist. In Chapter 6, certain flow problems where fluid exhibits both steady-state and non-steady-state seepage through the hyperelastic gel are studied. These seepage problems consider the possibility of pressure driven fluid diffusion through a fiber reinforced gel, such that the isotropic diffusion problem is retrieved as a special case.

For the equilibrium mechanical response discussed in Chapter 2 through Chapter 5, it is a main object to investigate the effects of fluid saturation and loss of saturation in the system on the polymer network deformation as well as fluid redistribution under certain mechanical loadings with different boundary conditions. While as for fluid seepage problems it is assumed that there is always enough fluid flowing through the polymer network so that there is no necessity to consider the loss of saturation at all.

## Chapter 2

## Modeling of the Swelling Behavior of Elastomeric Gels

## 2.1 The Flory-Huggins Equation for the Determination of Free Swelling

The most basic description of large strain effects in elastomeric gels concerns the determination of the amount of fluid that perfuses a polymer matrix when it is placed in a liquid bath. Let  $\nu$  denote the volume fraction of polymer matrix so that  $1-\nu$  is the volume fraction of the fluid component. A standard development proceeds by taking molecular chain arguments for configurational entropy of crosslinked macromolecules within a liquid bath, and coupling these to a phenomenological description of enthalpy of mixing [13, 44]. The requirement of a stationary free energy then leads to the equation

$$\underbrace{M\left[\ln\left(1-\nu_{fs}\right)+\nu_{fs}+\chi\nu_{fs}^{2}\right]}_{\text{dilution}} + \underbrace{\mu\nu_{fs}^{1/3}}_{\text{crosslinking}} = 0$$
(2.1)

for the free-swelling value of  $\nu$  which, as indicated above, will be denoted by  $\nu_{fs}$ . Here M>0,  $\chi$  and  $\mu>0$  are constitutive parameters that may vary with temperature, pH, fluid chemistry, and other environmental factors. As indicated in (2.1), two separate effects can be identified, that associated with dilution and that associated with crosslinking. In the absence of crosslinking, the equation reduces to that for

the effect of dilution alone, and this is the equation that is usually referred to as the Flory-Huggins equation [13]. The dilution term itself models the two effects of mixing entropy and mixing enthalpy. The term containing  $\chi$  models the latter and is positive for the standard case wherein polymer-polymer and liquid-liquid grouping is favored over polymer-liquid grouping. In particular, larger  $\chi$  favors polymer-polymer aggregation so that  $\nu_{fs}$  increases with  $\chi$ . The remaining part of the dilution term models the entropy contribution of polymer-liquid mixing to the free energy. In particular, the parameter M is identified as the product of the ideal gas constant and the absolute temperature divided by the molar volume of the liquid.

The utility of a theory that delivers (2.1) is due in no small part to the fact that (2.1) has a unique solution  $\nu_{fs}$  that takes values on the physically relevant interval  $0 < \nu_{fs} < 1$ . This solution is here referred to as the free swelling polymer volume fraction. It is completely determined by  $\chi$  and the ratio  $\mu/M$ . Thus one may then write  $\nu_{fs} = \hat{\nu}_{fs}(\chi, \mu/M)$ . Increasing either  $\chi$  or  $\mu/M$  favors a more tightly bound gel and so increases  $\hat{\nu}_{fs}(\chi, \mu/M)$ .

The connection between free swelling and hyperelasticity follows by introducing the deformation mapping that takes the polymer component from its original unswellen location X to its stressed, swellen location y. Let  $J = \det F$  where  $F = \partial y/\partial X$  is the deformation gradient of the mapping y(X). Correspondence between J and  $\nu$  is immediate if both the polymer component and the fluid component are individually incompressible since simple mixing then gives the identification  $J = 1/\nu$ . Thus J is the volumetric swelling of the gel as measured with respect to the polymer component before liquid was present. It is therefore required that

$$J \ge 1. \tag{2.2}$$

Historically, the original development leading to (2.1) employed a notion of physical

variations. In particular, rather than using physical arguments to obtain an explicit energy to minimize, the original papers of Flory and Treloar employ an argument which requires that there is no change in the free energy of the system in the event that a single fluid particle is transferred between the gel and the pure liquid which surrounds the gel. Although the free swelling volume fraction appears in (2.1), the original arguments leading to this equation actually depend more on the concept of occupied volume rather than the related concept of volume fraction. The connection between occupied volume and volume fraction then follows from  $J=1/\nu$ . The argument involving fluid particle transfer can thus be viewed as a variation with respect to J. Accordingly, the energy that is formally minimized can be found by substituting  $\nu_{fs} \to 1/J$  in (2.1), integrating the resulting expression with respect to J, and, if desired, returning to the original volume fraction variable via  $J \to 1/\nu_{fs}$ . This gives, to within an integration constant, an energy expression with the following terms

effects of mixing enthalpy 
$$\underbrace{-M\chi\nu_{fs}}_{\text{effects of mixing entropy}} + \underbrace{M\left(\frac{1}{\nu_{fs}} - 1\right)\ln\left(1 - \nu_{fs}\right)}_{\text{effects of mixing entropy}} + \underbrace{\frac{3\mu}{2}\nu_{fs}^{-2/3}}_{\text{effects of network elasticity}}$$

$$\underbrace{(2.3)}$$

Hence (2.1) is equivalent to determining the free-swelling value of J as the root of

$$\frac{d}{dJ}\Big(H(J) + \Psi(J)\Big) = 0, (2.4)$$

with

$$H(J) = M((J-1)\ln(1-J^{-1}) + \chi(1-J^{-1})), \tag{2.5}$$

and

$$\Psi(J) = \frac{3\mu}{2} J^{2/3}.\tag{2.6}$$

Here  $H + \Psi$  is the overall free energy, the former accounting for polymer-fluid inter-

action (mixing entropy and mixing enthalpy), the latter accounting for elastomeric deformation of the crosslinking network. The limiting case  $\mu \to 0$  corresponds to the absence of crosslinking and hence no elastic effect. Equation (2.4) then reduces to h(J) = 0 where we have introduced the notation

$$h(J) \equiv \frac{\partial H}{\partial J}.\tag{2.7}$$

It is to be remarked that (2.2) and (2.4) can be regarded as a general framework, which retrieves the well known equation (2.1) once the specific mathematical forms (2.5) and (2.6) are invoked. Thus statements involving the functions H and  $\Psi$  need not be tied to (2.5) and (2.6) unless specifically indicated. Similarly, (2.7) is a definition for h that is not tied to any constitutive form. For the specific constitutive function (2.5), h is given by

$$h(J) = M \left[ \ln \left( 1 - J^{-1} \right) + J^{-1} + \chi J^{-2} \right]. \tag{2.8}$$

The basic behavior of this framework with the usual forms (2.5) and (2.6) is sensitive to whether  $\chi < 1/2$  or  $\chi > 1/2$  as described next.

If (2.5) and (2.6) hold and  $\chi > 0.5$  then there is a unique value of J > 1 that causes h to vanish. This value of J corresponds to free swelling in the absence of crosslinking and we denote this value by  $J_{ncl}$  where the subscript refers to nocrosslinking. Thus  $h(J_{ncl}) = 0$  and  $J_{ncl} = 1/\hat{\nu}_{fs}(\chi, 0)$ . Moreover h(J) < 0 for  $1 < J < J_{ncl}$  and h(J) > 0 for  $J > J_{ncl}$ . Consequently  $J_{ncl}$  provides a local minima of H. One also finds that  $J_{ncl} < 2\chi/(2\chi - 1)$  and that  $J_{ncl} \to \infty$  as  $\chi \to 0.5$ .

If (2.5) and (2.6) hold and  $\chi < 0.5$  then there are no solutions to h(J) = 0 because h(J) < 0 for all J > 1. Hence for  $\chi < 0.5$  the infimum of H is achieved as  $J \to \infty$ . Since  $h(J) \to 0$  as  $J \to \infty$  it is convenient to formally define  $J_{ncl} \equiv \infty$  for  $\chi < 0.5$ . The derivative h'(J) > 0 for all J > 1. These qualitative features are

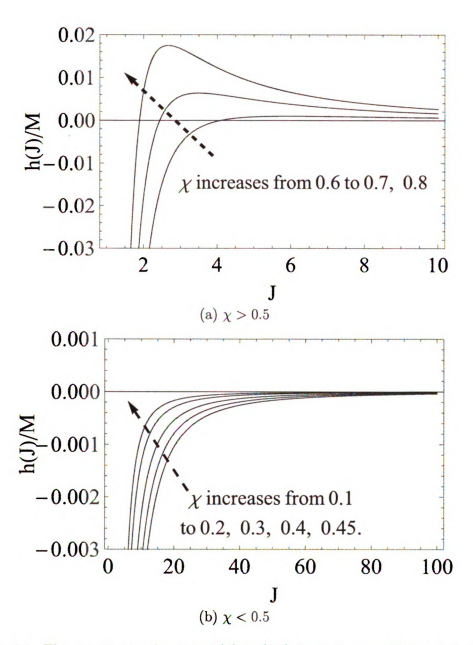


Figure 2.1: The constitutive function h(J) in (2.8) for various  $\chi$ . Vaues of J giving h(J) = 0 model gel dilation on the basis of mixing entropy and mixing enthalpy, but do not account for the elastic effect of polymer crosslinking.

summarized in Figure 2.1.

Accounting for elastic interconnection  $(\mu>0)$ , equations (2.4)-(2.6) become  $h(J)+\mu J^{-1/3}=0$ . In conjunction with (2.8) this recovers (2.1) for the free swelling value  $J_{fs}\equiv 1/\nu_{fs}$ . There is a unique finite  $J_{fs}$  solution to (2.4)-(2.6) for all  $\chi$  whenever  $\mu>0$ , which is formally given by  $J_{fs}=1/\dot{\nu}_{fs}(\chi,\mu/M)$ . This solution obeys the inequality  $J_{fs}< J_{ncl}$  as would be expected since the crosslinking inhibits swelling. Further  $h(J)+\mu J^{-1/3}$  is respectively positive or negative as J is respectively greater than or less than  $J_{fs}$ . Figure 2.2 indicates these relations.

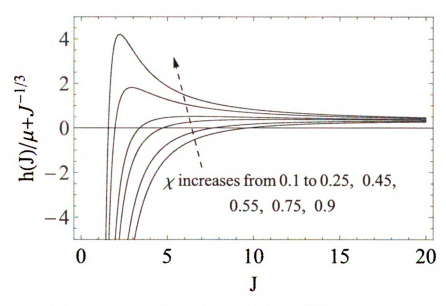


Figure 2.2: The constitutive expression  $h(J) + \mu J^{-1/3}$  for various  $\chi$  when  $\mu = 0.01M$ . The new term  $\mu J^{-1/3}$  describes the effect of crosslinks. Values of J giving  $h(J) + \mu J^{-1/3} = 0$  describe free swelling.

A simple interpretation concerns polymer that has some original volume, say  $V_{poly}$ , when free of liquid. Placing this nominally dry polymer into a liquid bath causes it to swell by uptake of fluid. The resulting gel occupies new volume  $JV_{poly}$  where J minimizes the free energy  $H(J) + \Psi(J)$ . For the energy forms (2.5) and (2.6) this free energy involves the three previously mentioned effects, one of which favors swelling (the configurational entropy), one of which opposes it (crosslinking),

and one of which could go either way (mixing enthalpy) although it opposes swelling in the standard case  $\chi>0$ . In all cases, crosslinking ( $\mu>0$ ) ensures that the swollen volume remains finite. If crosslinks are not present ( $\mu=0$ ) then the mixing enthalpy must sufficiently favor same phase agglomeration ( $\chi>0.5$ ) for the swollen volume to remain finite. However if crosslinking is not present and the mixture enthalpy is not sufficiently conducive to this same phase agglomeration ( $\mu=0$  and  $\mu=0$  and  $\mu=0$ ) then  $\mu=0$ 0 and  $\mu=0$ 1 then  $\mu=0$ 2 and the polymer goes into solution, dispersing itself throughout the fluid bath.

Implicit in the above discussion is a requirement that sufficient liquid is available for saturation of polymer with the liquid. This requires that

$$JV_{poly} \le V_{poly} + V_{liq},\tag{2.9}$$

where  $V_{liq}$  is the original fluid volume prior to introduction of polymer. If (2.9) holds then the gel swells to its energetically favored saturation value. However if J as determined on the basis of (2.4) is larger than that permitted by (2.9) then the swelling is limited by the availability of fluid to the value

$$J_* \equiv 1 + V_{liq}/V_{poly} \tag{2.10}$$

which is less than the free swelling value  $J_{fs}$  determined on the basis of (2.4). The gel is then no longer saturated. In what follows the use of a subscript \* or a superscript \* will denote a value that demarcates a transition between saturation and nonsaturation.

#### 2.2 Hyperelastic Constitutive Theory

In free swelling, the deformation gradient of the mapping  $\mathbf{y}(\mathbf{X})$  is  $\mathbf{F} = J_{fs}^{1/3}\mathbf{I}$  where  $\mathbf{I}$  is the identity tensor. In order to treat more general deformations due to the effect of mechanical loading, we now consider a hyperelastic framework. Let  $\mathbf{B} = \mathbf{F}\mathbf{F}^T$  and  $\mathbf{C} = \mathbf{F}^T\mathbf{F}$  and let  $I_1$ ,  $I_2$  and  $I_3$  be the associated principal scalar invariants

$$I_1 = \text{Trace}\mathbf{B}, \qquad I_2 = \frac{1}{2} \Big( I_1^2 - \text{Trace}(\mathbf{B}^2) \Big), \qquad I_3 = \det \mathbf{B} = J^2.$$

The overall stored energy density will be expressed as the sum of elastic free energy of the polymer network  $\Phi$  and a mixing free energy H

$$W(\mathbf{F}) = \Phi(I_1, I_2, J) + H(J). \tag{2.11}$$

The mixing energy H is the same as that discussed in the previous section and its derivative will continue to be denoted by h (viz. equation (2.7)). The specific Flory-Huggins form (2.5) for H will be used in the examples that follow.

#### 2.2.1 Free Swelling

In the absence of mechanical loading, the associated free swelling is determined by minimizing W in the class of simple volumetric expansions  $\mathbf{F} = J^{1/3}\mathbf{I}$  so that  $I_1 = 3J^{2/3}$  and  $I_2 = 3J^{4/3}$ . Thus J is determined on the basis of

$$\frac{d}{dJ}\left(\Phi(3J^{2/3}, 3J^{4/3}, J) + H(J)\right) = 0. \tag{2.12}$$

Comparison with (2.4) indicates that correspondence with the free swelling frame-

work described in the previous section will follow provided that

$$\Phi(3J^{2/3}, 3J^{4/3}, J) = \Psi(J) + \text{constant.}$$

Correspondence with the particular Flory-Huggins form (2.6) will obtain if

$$\Phi(3J^{2/3}, 3J^{4/3}, J) = \frac{3\mu}{2}J^{2/3} + \text{constant.}$$

In what follows we shall use the Mooney-Rivlin form for the elastic energy  $\Phi$  of the polymer network

$$\Phi = \Phi(I_1, I_2) = \frac{\mu}{2} \Big[ (1 - \xi) \big( I_1 - 3 \big) + \xi \big( I_2 - 3 \big) \Big], \qquad (0 \le \xi \le 1). \tag{2.13}$$

The case  $\xi=0$  gives the neo-Hookean specialization. For any  $\xi$  obeying  $0 \le \xi \le 1$  in (2.13), one finds that

$$\Phi(3J^{2/3}, 3J^{4/3}, J) = \frac{3\mu}{2} \Big( (1 - \xi)J^{2/3} + \xi J^{4/3} - 1 \Big)$$

so that the special neo-Hookean case of  $\xi=0$  retrieves the original equation (2.1) upon taking  $J=J_{fs}=1/\nu_{fs}$ . For the more general Mooney-Rivlin form with  $\xi>0$  equation (2.1) is augmented so as to contain an additional term and so becomes

$$M\left[\ln\left(1-\nu_{fs}\right)+\nu_{fs}+\chi\nu_{fs}^{2}\right]+\mu\left[(1-\xi)\nu_{fs}^{1/3}+2\xi\nu_{fs}^{-1/3}\right]=0. \tag{2.14}$$

Introduce the free swelling stretch ratio

$$\zeta \equiv J_{fs}^{1/3} = \nu_{fs}^{-1/3},\tag{2.15}$$

where  $\nu_{fs}$  is the root of (2.14). This root now depends upon  $\xi$  in addition to  $\chi$  and

 $\mu/M$ . As such, the free swelling behavior under (2.14) is not as simply described as was the case for (2.1). Some indication of the effect of the new constitutive parameter  $\xi$  upon  $\nu_{fs}$  can be obtained by taking representative values for  $\chi$  and  $\mu/M$ . To this end we follow [48] where the equivalent of a neo-Hookean  $\Phi$  is considered for the modeling of a vulcanized rubber in contact with toluene as considered by Paul and Ebra-Lima in [24]. The following values are taken in [48]:  $M=2.379\times 10^8 dyne/cm^2$ ,  $\chi=0.425$  and  $\mu=2.375\times 10^6 dyne/cm^2$ . Note for these values that the dimensionless parameter  $\bar{M}=M/\mu=100.17\approx 100$ . The value of the free swelling stretch ratio  $\zeta$  as a function of  $\xi$  for various  $\bar{M}$  and  $\chi$  are shown in Figure 2.3. The dotted curves in Figure 2.3(a) and Figure 2.3(b) are respectively associated with the above parameters  $\bar{M}=100$  and  $\chi=0.425$ .

#### 2.2.2 Saturated Stress and Nonsaturated Stress

Let **T** and  $\sigma$  give the first Piola-Kirchhoff and Cauchy stress tensors, respectively. They are connected by

$$\sigma = \frac{1}{J} \mathbf{T} \mathbf{F}^T. \tag{2.16}$$

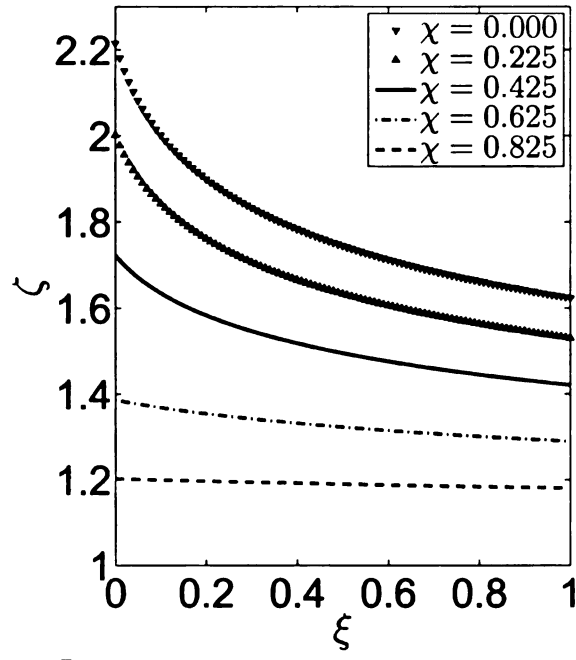
Mechanical equilibrium is governed by the usual equations

Div 
$$\mathbf{T} = \mathbf{0}$$
 on  $\Omega_{\mathbf{X}}$ ,  $\Leftrightarrow$  div  $\boldsymbol{\sigma} = \mathbf{0}$  on  $\Omega_{\mathbf{y}}$ , (2.17)

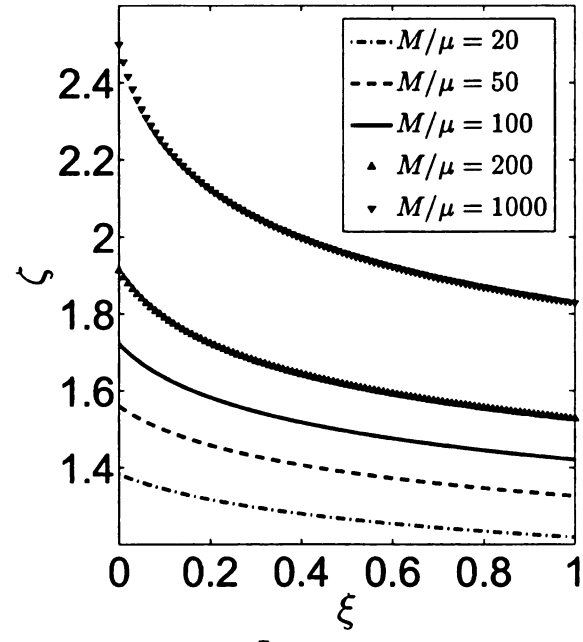
where  $\Omega_{\mathbf{X}}$  and  $\Omega_{\mathbf{y}}$  denote the gel domain in the reference and deformed configuration, respectively. We continue to let  $V_{poly}$  and  $V_{liq}$  be the volume of polymer and fluid respectively. In particular

$$V_{poly} = \int_{\mathbf{\Omega_X}} dV_{\mathbf{X}}.$$
 (2.18)

After mixing the local gel volume is J so that the overall gel volume is



(a)  $\bar{M}=100$  and  $\chi$  varying from 0.000 to 0.825



(b)  $\chi=0.425$  and  $\bar{M}$  varying from 20 to 1000

Figure 2.3: The free swelling stretch ratio  $\zeta$  as given by (2.14) and (2.15) is a function of  $\bar{M}$ ,  $\chi$  and  $\xi$ . The dependence of  $\zeta$  on  $\xi$  is shown for various  $\bar{M}$  and various  $\chi$ 

$$V \equiv \int_{\mathbf{\Omega_X}} J \, dV_{\mathbf{X}}.\tag{2.19}$$

The maximum overall gel volume is  $V_{poly} + V_{liq}$  corresponding to uptake of all fluid into the gel. So long as this does not occur the gel is able to saturate. The system is not saturated only if  $V = V_{poly} + V_{liq}$ . Together this gives the global constraint

$$\int_{\Omega_{\mathbf{X}}} (J-1) \, dV_{\mathbf{X}} \le V_{liq}. \tag{2.20}$$

If the system is saturated then the first Piola-Kirchhoff stress tensor is given by  $\mathbf{T} = \partial W/\partial \mathbf{F}$  and the saturated Cauchy stress tensor is

$$\boldsymbol{\sigma} = \frac{2}{J} \mathbf{F} \frac{\partial \Phi}{\partial \mathbf{C}} \mathbf{F}^T + h(J) \mathbf{I}, \qquad \text{(saturated)},$$

where the first term on the right hand side follows exactly as from conventional hyperelasticity and the second term on the right hand side follows upon recalling that  $\partial J/\partial {\bf F} = J {\bf F}^{-T}$ .

If, however, the material is not saturated, then a constant reaction stress  $-p\mathbf{I}$  is generated so as to enforce the constraint (2.20). This gives the nonsaturated Cauchy stress tensor

$$\boldsymbol{\sigma} = \frac{2}{J} \mathbf{F} \frac{\partial \Phi}{\partial \mathbf{C}} \mathbf{F}^T + h(J) \mathbf{I} - p \mathbf{I}, \qquad \text{(not saturated)}.$$

Thus, as in incompressible hyperelasticity, there is a pressure contribution to the Cauchy stress tensor that is not determined by the deformation.

Here, however, it is important to emphasize that the constraint (2.20) is a global one. This is in contrast to the situation in conventional incompressible hyperelasticity in which the constraint  $\det \mathbf{F} = 1$  is a local one. The pointwise constraint in incompressible hyperelastic gives rise to a reactive pressure that can vary spatially. In

contrast, the pressure p in (2.22) takes the same value at every point in the nonsaturated gel. In particular, since p in (2.22) is constant, a condition of spatially varying J does not generally permit the last two terms in (2.22) to be consolidated into a single term with redefined p.

Evaluating  $\partial \Psi / \partial {f C}$  in terms of the dependence on  $I_1, I_2, J$  gives

$$\boldsymbol{\sigma} = -\frac{2}{J}\frac{\partial\Phi}{\partial I_2}\mathbf{B}^2 + \frac{2}{J}\left(\frac{\partial\Phi}{\partial I_1} + I_1\frac{\partial\Phi}{\partial I_2}\right)\mathbf{B} + \left(\frac{\partial\Phi}{\partial J} + h(J)\right)\mathbf{I}, \quad \text{(saturated)}, \quad (2.23)$$

while the nonsaturated Cauchy stress tensor becomes

$$\boldsymbol{\sigma} = -\frac{2}{J}\frac{\partial\Phi}{\partial I_2}\mathbf{B}^2 + \frac{2}{J}\left(\frac{\partial\Phi}{\partial I_1} + I_1\frac{\partial\Phi}{\partial I_2}\right)\mathbf{B} + \left(\frac{\partial\Phi}{\partial J} + h(J) - p\right)\mathbf{I}, \quad \text{(not saturated)}.$$
(2.24)

For the uniform expansion  $\mathbf{F} = J^{1/3}\mathbf{I}$ , the saturated Cauchy stress (2.23) is a multiple of the identity tensor, say  $\boldsymbol{\sigma} = -\hat{p}(J)\mathbf{I}$ . Here  $\hat{p}(J)$  gives the mechanical pressure associated with a given value of J and hence a given local fluid concentration within the gel. The condition  $\hat{p}(J_{fs}) = 0$  recovers the free swelling condition (2.12).

A simple but fundamental application of (2.23) is to determine the infinitesimal shear modulus G and bulk modulus K for a saturated gel. First consider a simple shearing deformation after free swelling:  $y_1 = \zeta X_1 + \kappa \zeta X_2$ ,  $y_2 = \zeta X_2$ ,  $y_3 = \zeta X_3$ , where  $\kappa$  is the amount of shear. For this deformation, the shear stress  $\sigma_{12}$  for a saturated gel is obtained from (2.23) in the form

$$\sigma_{12} = G(\kappa)\kappa, \qquad G(\kappa) = \frac{2}{\zeta} \frac{\partial \Phi}{\partial I_1} + 2\zeta \frac{\partial \Phi}{\partial I_2}.$$
 (2.25)

The infinitesimal shear modulus for a saturated gel is therefore given by

$$G(0) = 2\left(\frac{1}{\zeta}\frac{\partial\Phi}{\partial I_1} + \zeta\frac{\partial\Phi}{\partial I_2}\right)\Big|_{I_1 = 3\zeta^2, I_2 = 3\zeta^4, J = \zeta^3}.$$
 (2.26)

Another important elastic parameter for saturated gel is the infinitesimal bulk modulus K. Consider a uniform compression:  $\mathbf{y} = \beta \zeta \mathbf{X}$ , where  $\beta$  is the compression stretch after free swelling. The associated uniform compression stress  $\sigma$  derived from (2.23) is

$$\sigma = \frac{2}{\beta \zeta} \frac{\partial \Phi}{\partial I_1} + 4\beta \zeta \frac{\partial \Phi}{\partial I_2} + \frac{\partial \Phi}{\partial J} + h(J). \tag{2.27}$$

By definition bulk modulus is given by

$$K = -V\frac{\partial \sigma}{\partial V} = -\beta^3 \zeta^3 V_0 \frac{\partial \sigma}{\partial (\beta^3 \zeta^3 V_0)} = -\frac{\beta}{3} \frac{\partial \sigma}{\partial \beta}.$$
 (2.28)

Incorporating (2.23) into (2.28), and assuming that  $I_1$ ,  $I_2$ , and J are mutually independent in the expression of  $\Phi$  (which is not unusual), the infinitesimal bulk modulus for the saturated gel is then given by

$$K\Big|_{\beta=1} = \frac{2}{3\zeta} \frac{\partial \Phi}{\partial I_1} - \frac{4\zeta}{3} \frac{\partial \Phi}{I_2} - \zeta^3 \left[ \frac{\partial^2 \Phi}{\partial J^2} + \frac{dh(J)}{dJ} \right] - 4\zeta \frac{\partial^2}{\partial I_1^2} - 16\zeta^5 \frac{\partial^2 \Phi}{\partial I_2^2} \Big|_{I_1 = 3\zeta^2, I_2 = 3\zeta^4, I_3 = \zeta^3}.$$
(2.29)

## Chapter 3

## **Homogeneous Deformation**

In this chapter we consider the homogeneous deformation response using the constitutive forms (2.13) and (2.5) in (2.11). Since J is a constant for homogeneous deformation, condition (2.20) reduces to the same condition as in free swelling, namely (2.9). This in turn is equivalent to the condition  $J \leq J_*$  where  $J_*$  is defined in (2.10). The Cauchy stress tensor then follows from (2.23) and (2.24) as

$$\sigma = \frac{\mu}{J} \left[ (1 - \xi + \xi I_1) \mathbf{B} - \xi \mathbf{B}^2 \right] + h(J) \mathbf{I}, \qquad (1 \le J < J_*), \qquad (3.1)$$

$$\sigma = \frac{\mu}{J} \Big[ (1 - \xi + \xi I_1) \mathbf{B} - \xi \mathbf{B}^2 \Big] + (h(J_*) - p) \mathbf{I}, \qquad (J = J_*).$$
 (3.2)

Since the term  $(h(J_*) - p)$  in (3.2) involves constant  $h(J_*)$  and an arbitrary constant p, it follows that  $h(J_*)$  can be absorbed into p. However in later chapters, when nonhomogeneous deformation is considered, it will be necessary to retain h(J) in the nonsaturated Cauchy stress tensor.

We now consider in turn: equibiaxial loading, uniaxial loading, and equitriaxial loading. Each is referred to a coordinate system with mutually orthogonal unit vectors  $e_1$ ,  $e_2$ ,  $e_3$ .

#### 3.1 Equibiaxial Stress

This is the specialization  $\sigma = \sigma(\mathbf{e}_1 \otimes \mathbf{e}_1 + \mathbf{e}_2 \otimes \mathbf{e}_2)$  and we restrict attention to deformations that preserve the loading symmetry so that  $\mathbf{F} = \lambda(\mathbf{e}_1 \otimes \mathbf{e}_1 + \mathbf{e}_2 \otimes \mathbf{e}_2) + (J/\lambda^2)\mathbf{e}_3 \otimes \mathbf{e}_3$ . For a saturated material it follows from (3.1) that

$$\mu \left[ \frac{\lambda^2}{J} + \xi \left( \frac{\lambda^2}{J} \left( \lambda^2 - 1 \right) + \frac{J}{\lambda^2} \right) \right] + h(J) = \sigma, \quad \text{(saturated)}, \quad (3.3)$$

and

$$\mu \left[ \frac{J}{\lambda^4} + \xi \left( \frac{J}{\lambda^4} \left( 2\lambda^2 - 1 \right) \right) \right] + h(J) = 0, \qquad \text{(saturated)}. \tag{3.4}$$

The second equation provides the relation between J and  $\lambda$  whereupon the first equation provides  $\sigma$  in terms of either  $\lambda$  or J. The graph of stress vs. stretch passes through the point  $(\lambda, \sigma) = (\zeta, 0)$  which corresponds to the state of free swelling. Recalling the requirement that  $J \geq 1$  consider the limit  $J \to 1$  in (3.3) and (3.4). For h in (3.4) given by (2.8) this limit gives

$$\lambda \sim \begin{cases} \left[ -\frac{M}{\mu(1-\xi)} \ln\left(1 - J^{-1}\right) \right]^{-1/4}, & \text{if } 0 \le \xi < 1, \\ \left[ -\frac{M}{2\mu} \ln\left(1 - J^{-1}\right) \right]^{-1/2}, & \text{if } \xi = 1, \end{cases}$$

$$(3.5)$$

so that, in all cases,  $J \to 1$  as  $\lambda \to 0$ . According to (3.3) this requires  $\sigma \to -\infty$  as follows:

$$\sigma \sim h(J) \sim M \ln (1 - J^{-1}) \sim \begin{cases} -\mu (1 - \xi) \lambda^{-4}, & \text{if } 0 \le \xi < 1, \\ \\ -2\mu \lambda^{-2}, & \text{if } \xi = 1. \end{cases}$$
 (3.6)

Thus the limit  $\sigma \to -\infty$  forces all of the liquid out of the gel, and in this limit  $\lambda \to 0$ .

Returning to the overall stress behavior, we find for  $M=100\mu$  and  $\chi=0.425$  that J is monotone in  $\lambda$  for all  $0 \le \xi \le 1$ . The graph of  $\sigma$  vs.  $\lambda$  is also found to be monotone for these parameters (Figure 3.1). Thus increasing stretch corresponds to both increasing stress and increasing fluid content. This situation holds so long as  $J < J_*$ .

A transition from a state of saturation to a state of nonsaturation occurs when  $J=J_*$ . This occurs at a unique value of  $\lambda$ , say  $\lambda_{eqbi}^*$ , and a unique value of stress, say  $\sigma_{eqbi}^*$ . For  $\lambda \geq \lambda_{eqbi}^*$  the value of J remains fixed at  $J_*$  and the relation between stress and stretch is now determined on the basis of (3.2). This gives  $\mathbf{F}=\lambda(\mathbf{e}_1\otimes \hat{\mathbf{e}}_1+\mathbf{e}_2\otimes \mathbf{e}_2)+(J_*/\lambda^2)\mathbf{e}_3\otimes \mathbf{e}_3$  and

$$\sigma = \mu \left[ (1 - \xi) \left( \frac{\lambda^2}{J_*} - \frac{J_*}{\lambda^4} \right) + \xi \left( \frac{\lambda^4}{J_*} - \frac{J_*}{\lambda^2} \right) \right], \qquad \text{(not saturated)}.$$
 (3.7)

It is to be remarked that the nonsaturated response does not depend upon h(J).

The solid curve in Figure 3.2 shows the saturated backbone curve  $\sigma$  vs.  $\lambda$  for  $\xi=0$ . The transition stretch  $\lambda_{eqbi}^*$  can take on any value as determined by  $J_*$ , and three values of  $\lambda_{eqbi}^*$  are taken as examples. At each such  $\lambda_{eqbi}^*$  there is a transition from saturated to nonsaturated response, and the associated nonsaturated response curve that branches off of the backbone curve does so in a continuous but nonsmooth fashion. The nonsaturated response involves an abrupt stiffening as evidenced by the greater slope of the nonsaturated curve at the branch point. To be specific, suppose  $\lambda \geq \lambda_{eqbi}^*$  so that the gel is not saturated because insufficient liquid is available. Consider the difference in the value of stress for the nonsaturated response and the value of stress for a hypothetical saturated response had sufficient liquid been

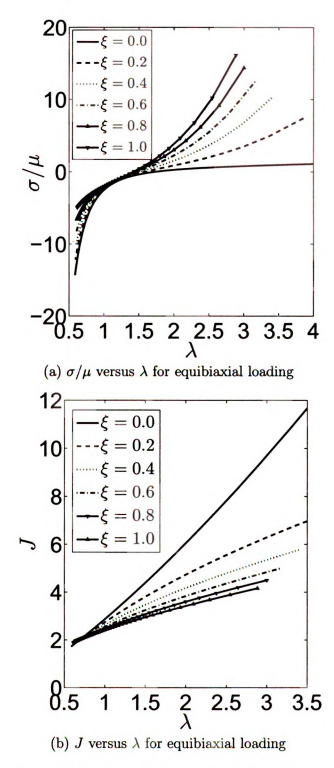


Figure 3.1: Stress-stretch behavior and volume-stretch behavior for equibiaxial loading of a saturated gel with  $\bar{M}=100$  and  $\chi=0.425$  showing the effect of different  $\xi.$ 

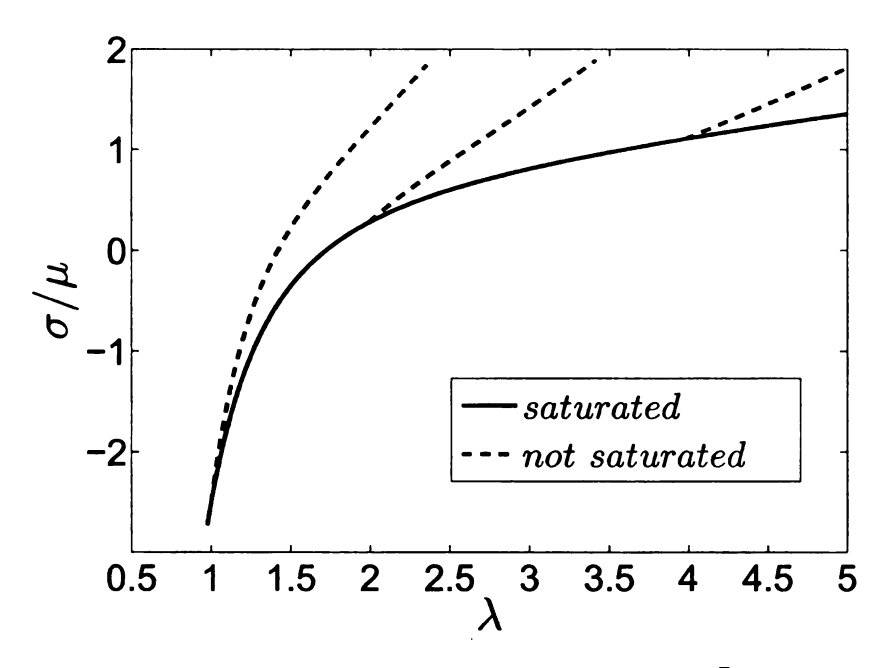


Figure 3.2: Stress-stretch behavior for equibiaxial loading with  $\bar{M}=100,~\chi=0.425,$  and  $\xi=0$ . Three nonsaturated response curves are depicted. Each nonsaturated response branches off of the saturated response "backbone curve".

available. This difference is

$$\sigma_{non} - \sigma_{sat} = \left[ \mu (1 - \xi) \lambda^2 \left( \frac{1}{J_*} - \frac{1}{J} \right) \right] + \left[ \frac{\mu (1 - \xi)}{\lambda^4} (J - J_*) \right] + \left[ \mu \xi \lambda^4 \left( \frac{1}{J_*} - \frac{1}{J} \right) \right] + \left[ \frac{\mu \xi}{\lambda^2} (J - J_*) \right],$$

$$(3.8)$$

where J in the above expression is the saturation value. Since  $J > J_*$  if  $\lambda > \lambda_{eqbi}^*$  it follows that each of the four separate bracketted terms in the above expression is positive after loss of saturation. One therefore formally verifies that  $\sigma_{non} > \sigma_{sat}$  if  $\lambda > \lambda_{eqbi}^*$ . In addition, by differentiating the expression in (3.8) with respect to  $\lambda$  and then evaluating the result at  $\lambda = \lambda_{eqbi}^*$  and  $J = J_*$ , one obtains the slope difference at the location where a nonsaturated response curve branches off of the saturation

response curve. This calculation gives

$$\frac{d}{d\lambda} \left( \sigma_{non} - \sigma_{sat} \right) \Big|_{\lambda = \lambda_{eqbi}^*} = \mu \left[ (1 - \xi) \left( \frac{\lambda^2}{J_*^2} + \frac{1}{\lambda^4} \right) + \xi \left( \frac{\lambda^4}{J_*^2} + \frac{1}{\lambda^2} \right) \right] \Big|_{\lambda = \lambda_{eqbi}^*} \frac{dJ}{d\lambda} \Big|_{\lambda = \lambda_{eqbi}^*}. \tag{3.9}$$

Noting that the bracketted term in the above expression is positive, it follows that the sign of the above expression is determined by the sign of the derivative  $dJ/d\lambda$ . Since, as remarked above, J increases with  $\lambda$  it follows that the slope difference is strictly positive, thus quantifying the abrupt stiffening.

Returning to Figure 3.2 it is observed that two of the three nonsaturated response curves depicted in this figure involve values of  $J_*$  that give  $\sigma_{eqbi}^* > 0$ . For these two  $J_*$  there is sufficient liquid for free swelling and the resulting loss of saturation occurs once  $\sigma$  increases to  $\sigma_{eqbi}^* > 0$ . The third nonsaturated response curve depicted in Figure 3.2 involves a value  $J_*$  that gives  $\sigma_{eqbi}^* < 0$ . In this case there is insufficient liquid for free swelling to proceed to its saturated value. Thus the value  $\sigma = 0$  occurs on a nonsaturated response curve. A biaxial compressive stress will, in this case, give a response that proceeds down the nonsaturated curve until it joins the saturated backbone curve. The resulting transition from nonsaturated to saturated response now involves an abrupt softening in the Cauchy stress response.

#### 3.2 Uniaxial Stress

This is the specialization  $\boldsymbol{\sigma} = \sigma \mathbf{e}_1 \otimes \mathbf{e}_1$  and we again restrict attention to deformations that preserve the loading symmetry so that  $\mathbf{F} = \lambda \mathbf{e}_1 \otimes \mathbf{e}_1 + \sqrt{J/\lambda}(\mathbf{e}_2 \otimes \mathbf{e}_2 + \mathbf{e}_3 \otimes \mathbf{e}_3)$ . For a saturated gel it follows from (3.1) that

$$\mu\left[(1-\xi)\frac{\lambda^2}{J} + 2\xi\lambda\right] + h(J) = \sigma, \qquad \text{(saturated)}, \qquad (3.10)$$

and

$$\mu\left[\left(1-\xi\right)\frac{1}{\lambda} + \xi\left(\lambda + \frac{J}{\lambda^2}\right)\right] + h(J) = 0, \qquad \text{(saturated)}. \tag{3.11}$$

The latter provides the kinematic relation between J and  $\lambda$  (Figure 3.3(b)) while the former then gives the relation between uniaxial stress  $\sigma$  and stretch ratio  $\lambda$  (Figure 3.3(a)). The graph of stress vs. stretch again passes through the free swelling point  $(\lambda, \sigma) = (\zeta, 0)$ . The predicted behavior associated with the possibility of squeezing out all of the liquid in uniaxial stress again requires the consideration of  $J \to 1$ . For h given by (2.8) it is again found that  $\lambda \to 0$  as  $J \to 1$ . In particular, one finds that  $\lambda \sim O([\ln((J-1)^{-1})]^{-1/2})$  if  $0 < \xi \le 1$ , while  $\lambda \sim O([\ln((J-1)^{-1})]^{-1})$  if  $\xi = 0$ . In all cases  $\sigma \to -\infty$  as  $\lambda \to 0$ . As regards the overall stress behavior, we find that  $\sigma$  is monotonically increasing with  $\lambda$  when  $M = 100\mu$  and  $\chi = 0.425$  for all  $0 \le \xi \le 1$ .

For  $\xi = 0$  it is found that the volume increases monotonically with axial stretch (viz. Figure 3.3(b)). Thus, as in the case of equibiaxial stress, there will be a loss of saturation when  $J = J_*$ . The stress vs. stretch response must then be determined using (3.2). This gives

$$\sigma = \mu \left(\frac{\lambda^2}{J_*} - \frac{1}{\lambda}\right) \left(1 - \xi + \xi \frac{J_*}{\lambda}\right), \quad \text{(not saturated)}.$$
 (3.12)

Even though we are currently considering the case  $\xi=0$  we have, for the sake of later discussion, given the more general expression in the above equation. Returning again to the case  $\xi=0$ , the associated nonsaturated response curve can again be regarded as branching off of the backbone saturated response curve. As shown in Figure 3.4, each nonsaturated response curve is well separated from the backbone curve. Indeed as  $\lambda \to \infty$  the  $\xi=0$  specialization of (3.10) and (3.11) give

$$J \sim \left(\bar{M}(\frac{1}{2} - \chi)\right)^{1/2} \lambda^{1/2} + \frac{1}{3 - 6\chi} + O(\lambda^{-1/2}),$$
  $(\xi = 0, \text{ saturated}),$  (3.13)

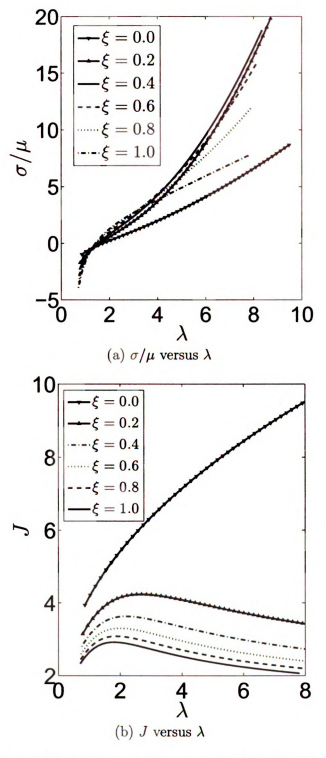


Figure 3.3: Stress-stretch behavior and volume-stretch behavior for uniaxial loading of a saturated gel with  $\bar{M}=100$  and  $\chi=0.425$  showing the effect of different  $\xi$ .

and

$$\sigma \sim \frac{\mu}{\left(\bar{M}(\frac{1}{2} - \chi)\right)^{1/2}} \lambda^{3/2} - \frac{2\mu}{3\bar{M}(1 - 2\chi)^2} \lambda + O(\lambda^{1/2}), \qquad (\xi = 0, \text{ saturated}).$$
(3.14)

Specifically, the Cauchy stress for the saturated gel is  $O(\lambda^{3/2})$  as  $\lambda \to \infty$ . In contrast, (3.12) indicates that the Cauchy stress for the nonsaturated gel is  $O(\lambda^2)$ , which accounts for the increasing separation between the response curves in Figure 3.4.

It is useful to note that the separation between the saturated and nonsaturated stress response for the  $\xi=0$  gel is not present in the corresponding first Piola-Kirchhoff stress. Recalling (2.16) it follows that this stress is  $\mathbf{T}=T\mathbf{e}_1\otimes\mathbf{e}_1$  with  $T=\sigma J/\lambda$ . It then follows from (3.10) and (3.11) that the large stretch Piola-Kirchhoff stress response of the saturated  $\xi=0$  gel is

$$T \sim \mu \lambda - \mu \left( \bar{M}(\frac{1}{2} - \chi) \right)^{1/2} \lambda^{-3/2} + O(\lambda^{-2}), \qquad (\xi = 0, \text{ saturated}).$$
 (3.15)

Turning to the first Piola-Kirchhoff stress response of a  $\xi = 0$  gel that is not saturated, it is immediate from (3.12) that

$$T = \mu \lambda - \mu \frac{J_*}{\lambda^2},$$
  $(\xi = 0, \text{ not saturated}).$  (3.16)

Thus the saturated and nonsaturated Piola-Kirchhoff stress response have the same leading order behavior as  $\lambda \to \infty$ . Moreover, the separation between the saturated and nonsaturated Piola-Kirchhoff stress response curves is  $O(\lambda^{-3/2})$  as the stretch increases, and hence vanishingly small. Since first Piola-Kirchhoff stress directly scales with applied load in a standard testing device, it follows that such a testing device may have difficulty distinguishing between saturated response and nonsaturated response.

The situation is even more complicated for  $0 < \xi \le 1$  since we find for this case that J exhibits a local maximum, say  $J_{max}$ , at a finite value of uniaxial stretch.

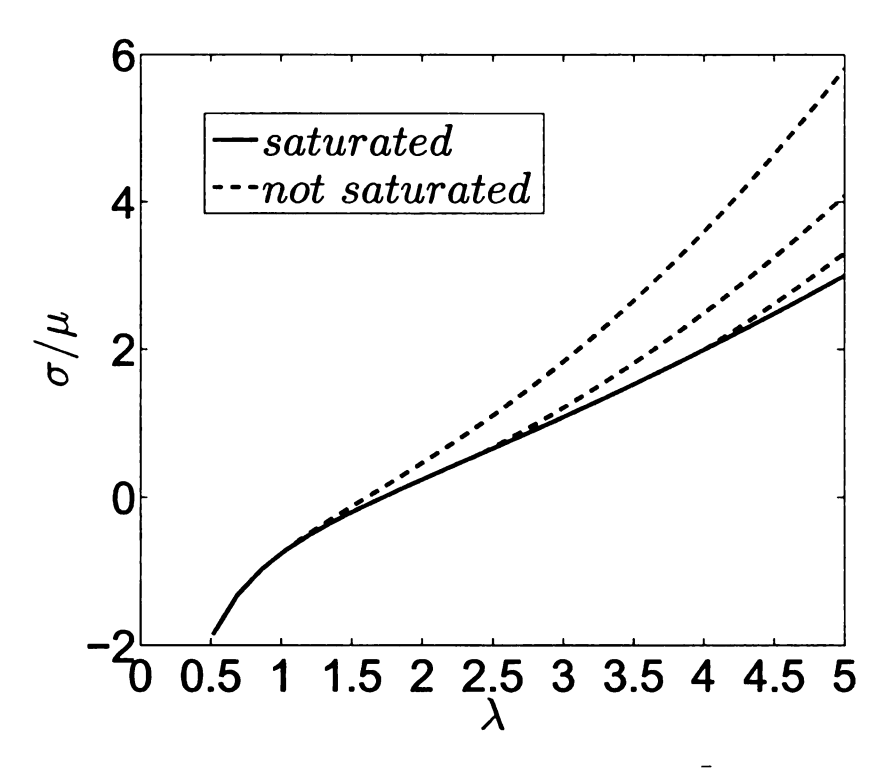


Figure 3.4: Stress-stretch behavior for uniaxial loading with  $\bar{M}=100,~\chi=0.425,$  and  $\xi=0.$  Three nonsaturated response curves are depicted.

If  $J_{max} < J_*$  then there is always sufficient liquid for the gel to remain saturated. However if  $J_{max} > J_*$  then the saturation value of J will be greater than  $J_*$  on a finite interval of stretch, say  $\lambda_{uni-A}^* < \lambda < \lambda_{uni-B}^*$  where the endpoint values  $\lambda_{uni-A}^*$ ,  $\lambda_{uni-B}^*$  correspond to  $J = J_*$  in uniaxial loading. On this interval the nonsaturated response is given by (3.12). The nonsaturated response curve therefore branches off of the backbone curve at  $\lambda_{uni-A}^*$  and rejoins the backbone curve at  $\lambda_{uni-B}^*$ . This is shown in Figure 3.5, where it is to be remarked that the separation between the  $\xi = 1$  saturated and nonsaturated stress response is difficult to distinguish (unlike the  $\xi = 0$  case shown in Figure 3.4).

By a development parallel to that giving (3.8) one may show that any nonsaturated uniaxial response curve is above the backbone saturated uniaxial response curve. The change in slope where a nonsaturated response curve connects to a saturated response curve can also be found by the type of development that led to (3.9) for the equibiaxial case. The corresponding result for uniaxial stress is

$$\frac{d}{d\lambda} \left( \sigma_{non} - \sigma_{sat} \right) \Big|_{\lambda = \lambda_{uni}^*} = \mu \left[ (1 - \xi) \frac{\lambda^2}{J_*} + \frac{\xi}{\lambda^2} \right] \Big|_{\lambda = \lambda_{uni}^*} \frac{dJ}{d\lambda} \Big|_{\lambda = \lambda_{uni}^*}. \tag{3.17}$$

The sign of this expression is again determined by the derivative term  $dJ/d\lambda$ . This derivative is positive at  $\lambda_{uni-A}^*$  and negative at  $\lambda_{uni-B}^*$ . Thus, under increasing stretch, an abrupt stiffening occurs in the Cauchy stress for both the loss of saturation transition at  $\lambda_{uni-A}^*$  and for the regain of saturation transition at  $\lambda_{uni-B}^*$ .

#### 3.3 Experimental Validation

In this section, we refer to R. Monroe's experimental data obtained by uniaxial stretch tests on hydrogels [74] in order to validate hyperelastic constitutive models of the type presented here. Monroe constructed a uniaxial load frame that performs

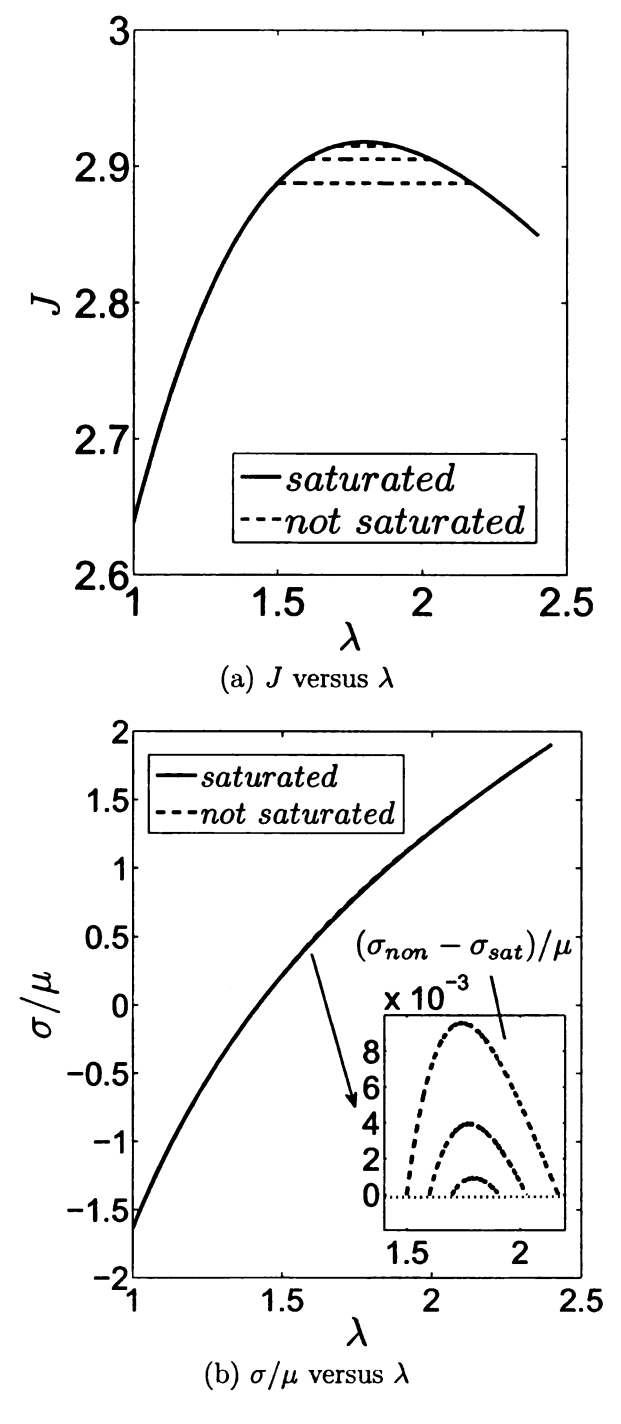


Figure 3.5: The dependence of volume and stress on uniaxial stretch for  $\bar{M}=100$ ,  $\chi=0.425$ , and  $\xi=1$ . Three nonsaturated examples are shown corresponding to loss of saturation at  $\lambda_{uni-A}^*=1.5, 1.6$  and 1.7.

individual or coupled experiments of stretching and swelling. The results shows the monotone stress stretch behavior of hydrogel in the uniaxial loading tests (Figure 3.6(a)). Monroe found that the hydrogel volume increases with the applied load until it achieves maximum swelling (Figure 3.6(b)). After that, further increase loading was found to make the hydrogel shrink. This non-monotone volume change behavior is consistent with the prediction of our hyperelastic constitutive model (c. f. Figure 3.3) with a selected combination of material constants (0 <  $\xi \le 1$ ,  $\bar{M} = 100$ ,  $\chi = 0.425$ ).

One of the main goals in [74] is to determine the material parameters from both saturated and unsaturated testing, and then fit the stress-stretch constitutive equations that are derived from the same free energy function as in (2.11). However, to fit best with the experimental data, instead of using the form of (2.13), Monroe [74] chose an alternative free energy model (Ogden Model) for the elastic free energy  $\Phi$ :

$$\Phi(\lambda_1, \lambda_2, \lambda_3) = \sum_{i=1}^{N} \frac{\mu_i}{\alpha_i} (\lambda_1^{\alpha_i} + \lambda_2^{\alpha_i} + \lambda_3^{\alpha_i} - 3)$$
(3.18)

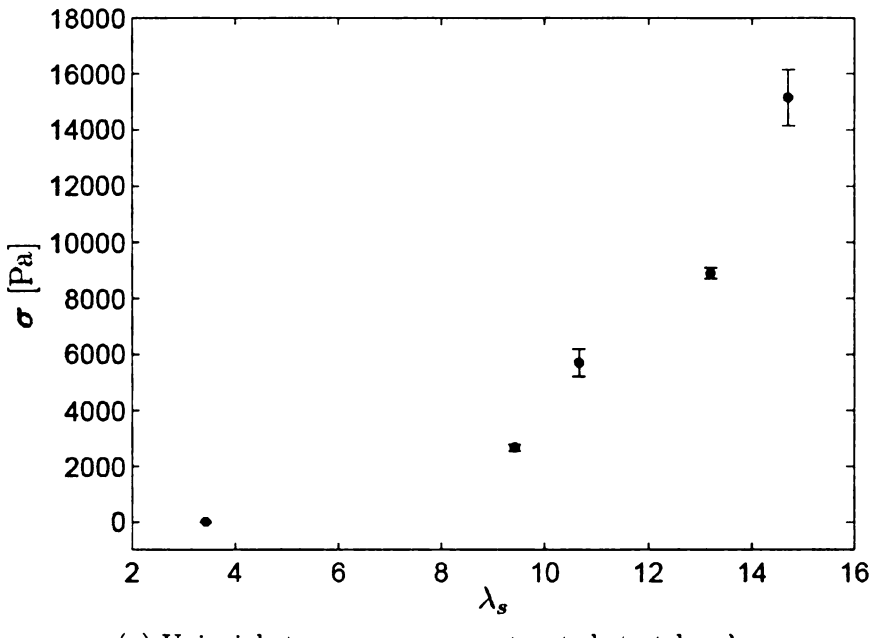
where  $\mu_i$  and  $\alpha_i$  are material parameters obtained from fitting data.

In this work we use the Mooney-Rivlin form for the convenience of numerical calculation, but it is the general approach to introduce different material models as well as material parameters to make the theoretical prediction in consistent with the realistic mechanical behavior of hydrogels that are composed of different polymers and solvents.

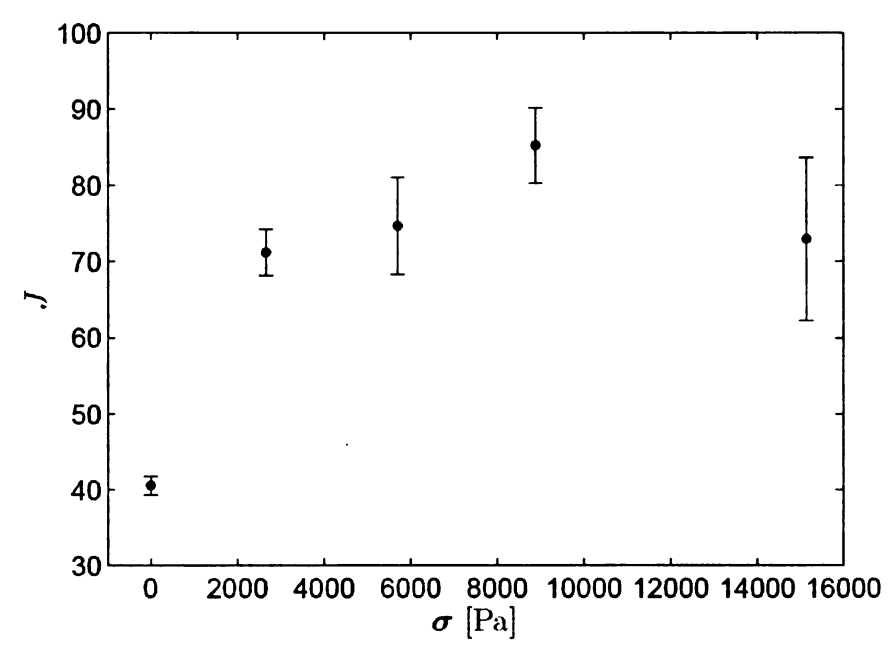
#### 3.4 Equitriaxial Stress

This is the specialization  $\sigma = \sigma \mathbf{I}$  with  $\mathbf{F} = J^{1/3}\mathbf{I}$ . The relation between  $\sigma$  and J then follows from (3.1) and (2.8) as

$$\sigma = \mu [(1 - \xi)J^{-1/3} + 2\xi J^{1/3}] + M[J^{-1} + \chi J^{-2} + \ln(1 - J^{-1})]. \tag{3.19}$$



(a) Uniaxial stresses  $\sigma$  versus saturated stretches  $\lambda s$ 



(b) Volume ratios J versus uniaxial stresses  $\sigma$ 

Figure 3.6: Stress-stretch behavior and volume-stress behavior for uniaxial testing of a saturated gel as given by R. Monroe in [74].

Thus (3.19) with  $\sigma=0$  and  $J=1/\nu_{fs}$  retrieves (2.14). As one would anticipate,  $\sigma>0$  implies  $J>1/\nu_{fs}$  and vice-versa. Consider again  $\bar{M}=100$  and  $\chi=0.425$ . The graph of  $\sigma$  vs.  $\lambda=J^{1/3}$  is then found to be monotonically increasing provided  $\xi>0.038$ . However if  $\xi<0.038$  we find that the graph of  $\sigma$  vs.  $\lambda$  exhibits a stress maximum (Figure 3.7). For  $0<\xi<0.038$  the stress maximum is followed by stress minimum, after which the stress is once again monotonically increasing. For  $\xi=0$  the stress is monotonically decreasing to zero as  $\lambda\to\infty$ .

Similar behavior occurs for values of  $\bar{M}=M/\mu$  and  $\chi$  that are close to  $(\bar{M},\chi)=(100,0.425)$ . Specifically, it is found that the graph of  $\sigma$  vs.  $\lambda=J^{1/3}$  is monotonically increasing for all  $\lambda$  only if  $\xi$  is greater than a critical value  $\xi_{crit}$ . This critical value varies with both  $\bar{M}$  and  $\chi$  (see Figure 3.8). For certain values of  $\bar{M}$  and  $\chi$  it is found that  $\xi_{crit}=1$  meaning that there always exists a local maximum in the stress response for equitriaxial loading. This occurs for example if  $\bar{M}=100$  and  $\chi\geq 0.752$  as can be seen from Figure 3.8(b).

As is well known in hyperelasticity in general, nonmonotone stress response behavior of the type encountered here when  $\bar{M}=100,~\chi=0.425,$  and  $0\leq \xi<0.038$  is implicated in various loss of stability phenomena. Such issues are beyond the scope of this dissertation. In contrast, for  $\bar{M}=100,~\chi=0.425,$  and  $\xi>0.038$  no such issues arise. Then, J increases with  $\sigma$  and loss of saturation occurs at the constraining value  $J=J_*$  when  $\sigma=\sigma_{eqtri}^*\equiv \mu[(1-\xi)J_*^{-1/3}+2\xi J_*^{1/3}]+M\big[J_*^{-1}+\chi J_*^{-2}+\ln(1-J_*^{-1})\big].$  For  $\sigma\geq\sigma_{eqtri}^*$  no additional expansion is possible, and the deformation gradient is therefore stalled at  $\mathbf{F}=J_*^{1/3}\mathbf{I}$ . The reactive pressure -p in (3.2) then renders the equitriaxial stress  $\sigma$  as formally indeterminant for  $J=J_*$  (see dashed curves in Figure 3.9).

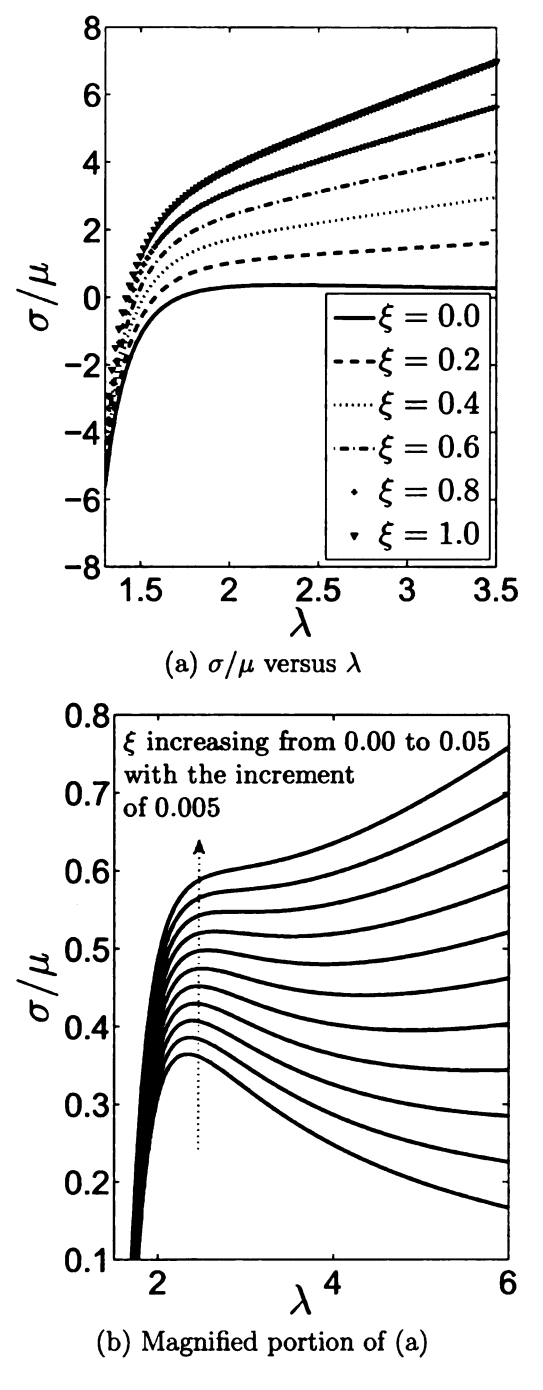


Figure 3.7: Stress-stretch behavior for equitriaxial loading of a saturated gel with  $\bar{M}=100$  and  $\chi=0.425$  showing the effect of different  $\xi$ . For  $\xi>0.038$  the graphs are monotonic. For  $0<\xi<0.038$  the graphs are decreasing on a finite interval in  $\xi$ .

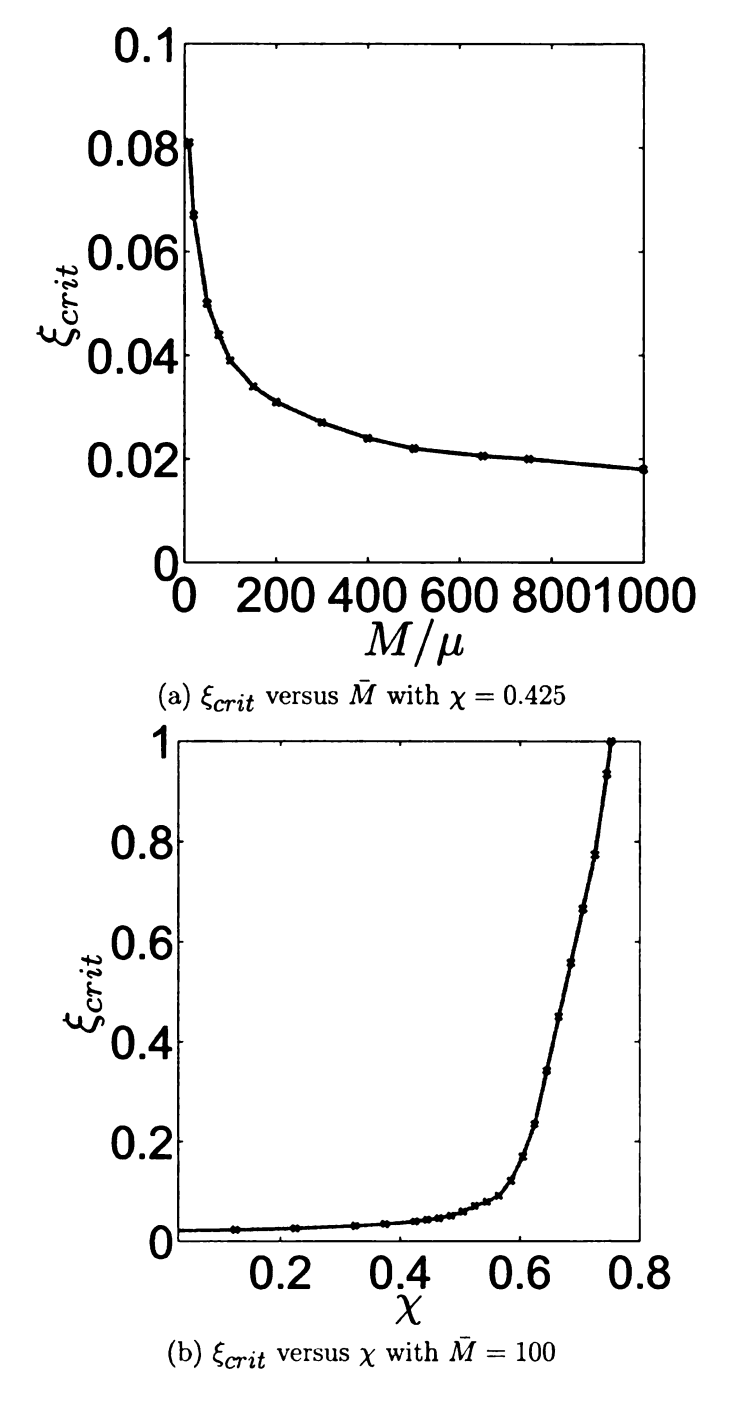


Figure 3.8: Critical value  $\xi_{crit}$  for the existence of a local stress maximum in the equitriaxial stress response. For  $\xi > \xi_{crit}$  the response is monotonic.

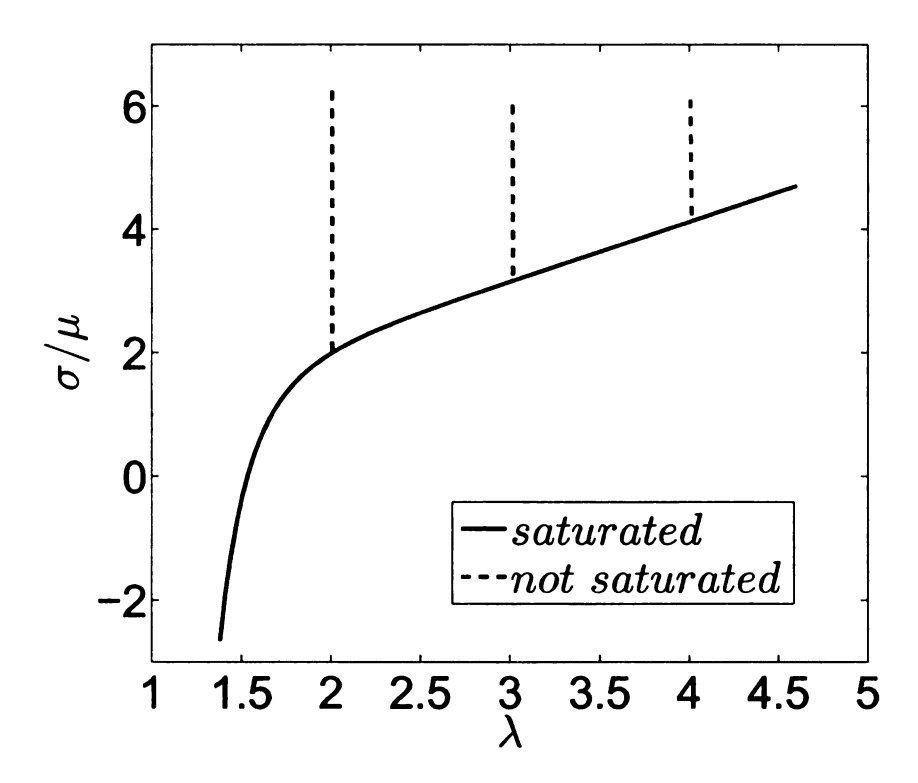


Figure 3.9: Stress-stretch behavior for equitriaxial loading with  $\bar{M}=100,\,\chi=0.425,$  and  $\xi=0.5$  showing three examples of nonsaturated response. Since the stretch  $\lambda=J^{1/3}$ , no additional stretch is possible after loss of saturation.

### 3.5 Some Energy Considerations

We close this section on homogeneous deformation with some remarks upon the energetic aspects of saturated response vs. nonsaturated response. A standard expectation would be that a saturated response would minimize an appropriate energy with respect to all nonsaturated responses, since the former is able to take on any value of J. We consider this issue in the context of uniaxial response, since that case offered the intriguing behavior such that, for certain  $\xi$ , there could be a load induced loss-of-saturation followed later by a load induced regain-of-saturation. Following the previous development in Section 4.2, we again restrict attention to deformations that preserve uniaxial symmetry and we also assume that there is sufficient liquid for a saturated free swelling.

Consider a unit cube that is oriented with respect to  $(\mathbf{e}_1, \mathbf{e}_2, \mathbf{e}_3)$  prior to swelling and prior to the application of load. After free swelling, let the two sides with normal  $\mathbf{e}_1$  be subject to a uniform normal traction with resultant normal force P and let the four remaining sides be traction free. The cube is deformed into a rectangular parallelepiped with stretch ratios  $\lambda_1 = \lambda$  and  $\lambda_2 = \lambda_3 = \sqrt{J/\lambda}$ . One may distinguish between either a hard loading device or a soft loading device. In the hard device,  $\lambda$  is regarded as given. For the soft loading device, P is regarded as given.

The energy to be minimized for the hard device is simply the stored energy density as given by the integral of  $W(\mathbf{F})$  over the reference configuration. Since the reference configuration is the unit cube, it follows from (2.11) that

$$E_{hard} = \bar{E}_{hard}(\lambda, J) \equiv \Phi(\lambda^2 + 2J/\lambda, 2\lambda J + J^2/\lambda^2, J) + H(J). \tag{3.20}$$

For  $\Phi$  given by (2.13) the expression for  $\bar{E}_{hard}$  is

$$\bar{E}_{hard}(\lambda, J) = \frac{\mu}{2} \left[ (1 - \xi_{1})(\lambda^{2} + \frac{2J}{\lambda} - 3) + \xi(2J\lambda + \frac{J^{2}}{\lambda^{2}} - 3) \right] + H(J).$$
 (3.21)

For the hard device, one minimizes  $\bar{E}_{hard}(\lambda, J)$  with respect to J at fixed  $\lambda$ . Formally, the first step in the minimization involves seeking solutions to

$$\frac{\partial}{\partial J}\bar{E}_{hard} = 0, \tag{3.22}$$

which gives an equation for J provided that J obeys  $J \leq J_*$ . Notice that (3.22) with (3.21) retrieves (3.11).

The soft device energy expression differs from the hard device expression by subtracting the work that is done on the gel by the loading device. This represents the change in potential energy of a conservative loading device so that the system under consideration involves both gel and loading device. The work of the load P on the unit cube is  $P(\lambda - 1)$  so that

$$E_{soft} = \bar{E}_{soft}(\lambda, J, P) \equiv \bar{E}_{hard}(\lambda, J) - P(\lambda - 1). \tag{3.23}$$

For the soft device, one minimizes  $\bar{E}_{soft}(\lambda, J, P)$  with respect to both J and  $\lambda$  at fixed P. Formally, the first step in the minimization involves seeking solutions to

$$\frac{\partial}{\partial J}\bar{E}_{soft} = 0,$$
 and  $\frac{\partial}{\partial \lambda}\bar{E}_{soft} = 0.$  (3.24)

Using  $\bar{E}_{soft} = \bar{E}_{hard} - P(\lambda - 1)$  it follows that (3.24) is equivalent to

$$\frac{\partial}{\partial J}\bar{E}_{hard} = 0, \quad \text{and} \quad \frac{\partial}{\partial \lambda}\bar{E}_{hard} - P = 0.$$
 (3.25)

Since  $P = \sigma \lambda_2 \lambda_3 = \sigma J/\lambda$  one verifies for  $\Phi$  given by the Mooney-Rivlin form (2.13) that (3.25) is the same as (3.10) and (3.11).

Thus both the hard and soft device analysis retrieves the saturation relation (3.11) between  $\lambda$  and J for uniaxial stress. This is a standard type of argument

in hyperelasticity, although in the present context of a saturated gel it permits the determination of the fluid fraction (1-1/J). In addition, the soft device analysis gives the load that is necessary to support this deformation. These relations hold so long as  $J \leq J_*$ . If, however, the solution to the above equations require that  $J > J_*$  then the minimization is found to be given by taking  $J = J_*$ . In this case the gel is not saturated. Viewed in this fashion, the nonsaturated minimization occurs on the boundary of the minimization domain. It follows that a nonsaturated solution can never provide a lower minimum than that of the saturated solution, since the saturated minimization is able to explore a larger space of J values. Such considerations arise generally if a hyperlastic material is composed of a mixture of substances where one or more of them (here the liquid) is in limited supply.

For specified  $\lambda$ , let the solution to (3.22) be  $J = \bar{J}_{sat}(\lambda)$ . Figure 3.10(a) displays  $\bar{E}_{hard}(\lambda, \bar{J}_{sat}(\lambda))$  vs.  $\lambda$  for the standard constitutive forms (2.5) and (2.13) with  $\xi = 1$ . This is the hard device energy associated with liquid saturation in uniaxial stress. This panel also displays the nonsaturated hard device energies  $\bar{E}_{hard}(\lambda, J_*)$  that are associated with the transitions previously displayed in Figure 3.5. The nonsaturated gels involve more energy than the saturated gel, although it is a small effect in the figures. The saturated hard device energy  $\bar{E}_{hard}(\lambda, \bar{J}_{sat}(\lambda))$  takes on its smallest value at  $\lambda = \zeta$  which corresponds to free swelling.

In this context it is instructive to consider the graph of uniaxial load P as a function of  $\lambda$  for both saturated and nonsaturated response, again using the constitutive forms (2.5) and (2.13). The relation between P and  $\lambda$  for saturated response follows from (3.10) and (3.11) using  $P = \sigma J/\lambda$ . The graph of this relation now supplies a backbone curve. The corresponding relation between P and  $\lambda$  for nonsaturated response follows from (3.12) using  $P = \sigma J_*/\lambda$ . Since the reference area of the unit cube is unity, it follows that the load P is simply the first Piola-Kirchhoff stress T, which we recall appeared previously in (3.15) and (3.16) for the case of the  $\xi = 0$  gel.

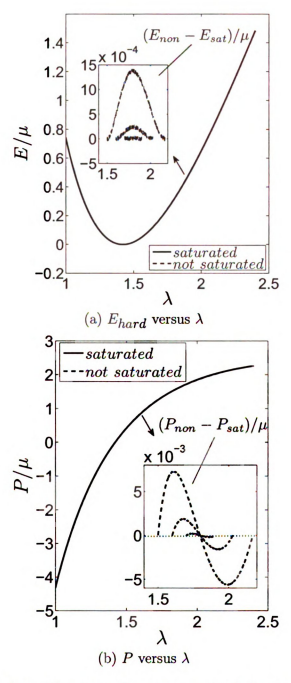


Figure 3.10: Comparison of a saturated and a nonsaturated gel under uniaxial load. On the left is a comparison of the hard device energy expression. On the right is the resultant force as a function of stretch. As in Figure 3.5 the constitutive parameters are given by  $\tilde{M}=100,~\chi=0.425$  and  $\xi=1$ . The transitions are taken to occur at  $\lambda=1.5,1.6$  and 1.7.

For general  $\xi$  it follows on the basis of the above considerations that

$$P_{non} - P_{sat} = \mu(J - J_*) \left[ (1 - \xi) \frac{1}{\lambda^2} + \xi \left( \frac{J_* + J}{\lambda^3} - 1 \right) \right]. \tag{3.26}$$

Here  $J = J(\lambda)$  follows from (3.11), and so is given by the function  $J = \bar{J}_{sat}(\lambda)$  as defined above.

Consider again the case that is associated with Figure 3.10 in which the nonsaturated response is confined to the interval  $\lambda_{uni-A}^* \leq \lambda \leq \lambda_{uni-B}^*$  where  $\lambda_{uni-A}^*$  and  $\lambda_{uni-B}^*$  depend upon  $J_*$ . The graph of the P vs.  $\lambda$  saturated backbone curve is depicted in Figure 3.10(b) along with the nonsaturated P vs.  $\lambda$  curves on the finite intervals of nonsaturation. The nonsaturated curves depart and rejoin the backbone curve at  $\lambda_{uni-A}^*$  and  $\lambda_{uni-B}^*$ . It is noted however that there is an intermediate value of  $\lambda$  at which each nonsaturated curve crosses the backbone saturation curve. The nonsaturated response is first above the saturated response and then below the saturated response. It follows from (3.26) that the crossing value of  $\lambda$  is a root to  $(1-\xi)/\lambda^2 + \xi((J_*+J)/\lambda^3 - 1) = 0$ . This crossing value of  $\lambda$  depends on  $J_*$  and we find that it occurs before the value of  $\lambda$  that gives  $J_{max}$  for saturated response.

Here it is useful to note that the ordinary derivative of  $\bar{E}_{hard}(\lambda, \bar{J}_{sat}(\lambda))$  with respect to  $\lambda$  gives, after use of the chain rule and application of both results from (3.25), that

$$P = \frac{d}{d\lambda} \bar{E}_{hard}(\lambda, \bar{J}_{sat}(\lambda)), \qquad \text{(saturated)}. \tag{3.27}$$

The corresponding result for the nonsaturated force-stretch response at any fixed value  $J_*$  is given by

$$P = \frac{d}{d\lambda} \bar{E}_{hard}(\lambda, J_*), \qquad \text{(not saturated)}. \tag{3.28}$$

Combining (3.27) and (3.28) gives a generalization of (3.26) in the form

$$P_{non} - P_{sat} = \frac{d}{d\lambda} \Big( \bar{E}_{hard}(\lambda, J_*) - \bar{E}_{hard}(\lambda, \bar{J}_{sat}(\lambda)) \Big). \tag{3.29}$$

We may use (3.29) to show that the crossing exhibited in Figure 3.10(b) is not tied to the particular constitutive forms (2.5) and (2.13). Consider any H(J) and  $\Phi(I_1, I_2, J)$  such that the saturated uniaxial response gives a local maximum in the relation between J and  $\lambda$ . In such a case, if  $J_*$  as given in (2.10) is somewhat less than the maximum value of J, then there will be an interval of nonsaturation which will again be denoted by  $\lambda_{uni-A}^* \leq \lambda \leq \lambda_{uni-B}^*$ . In particular,  $\bar{J}_{sat}(\lambda_{uni-A}^*) = \bar{J}_{sat}(\lambda_{uni-B}^*) = J_*$ . Integration of (3.29) now gives

$$\int_{uni-A}^{\lambda_{uni-B}^*} (P_{non} - P_{sat}) d\lambda = \left( \bar{E}_{hard}(\lambda, J_*) - \bar{E}_{hard}(\lambda, \bar{J}_{sat}(\lambda)) \right) \Big|_{\lambda_{uni-A}^*}^{\lambda_{uni-B}^*} = 0 - 0 = 0.$$
(3.30)

It thus follows that there is zero net area between the saturated force curve and each nonsaturated force curve on the finite interval of nonsaturation. Thus crossing of the saturated and nonsaturated force-stretch response curves must occur within the finite interval of nonsaturation.

#### 3.6 Summary

In this chapter, we discuss homogeneous deformation of swollen elastomeric gels based on the hyperelastic constitutive theory described in Chapter 2. To do this, we distinguish between the liquid saturation and the situation of loss of liquid saturation. Equibiaxial loading, uniaxial loading, and equitriaxial loading problems are then considered in turn.

- For equibiaxial loading, it is found that for M = 100µ and χ = 0.425 that the both σ and J is monotone in λ for all 0 ≤ ξ ≤ 1. Thus increasing stretch leads to both increasing stress and fluid absorption as long as the gel is saturated. When a transition from saturation to loss of saturation occurs, the gel's overall volume is then fixed (J = J\*). Further increasing stress could continue monotonically increase the equibiaxial stretch but resulting in a stiffer response than in the saturated case. It is also found by analytical derivations that for the possibility of squeezing all of the fluid out of the gel (J = 1), the equibiaxial stretch λ has to approach 0 and the corresponding stress much be negative infinite.
- For uniaxial loading, it is found that  $\sigma$  is monotonically increasing with  $\lambda$  when  $M=100\mu$  and  $\chi=0.425$  for all  $0\leq\xi\leq1$ . The volume also increases monotonically with axial stretch for  $\xi=0$ . However for the cases with  $0<\xi\leq1$  we find that the volume change ratio J exhibits a local maximum at a finite value of uniaxial stretch. Corresponding experimental results are also compared and qualitative consistence is obtained with the theoretical prediction in this work. The non-monotone behavior could result in a phenomenon of the nonsaturation bifurcation where the nonsaturated response curve first branches off of the saturated curve and later rejoins it. Analytical derivatives again shows that for all cases  $\sigma\to-\infty$  and  $\lambda\to0$  as  $J\to1$ .
- For equitriaxial loading  $(J=\lambda^3)$ , the stress is found to be monotonically increasing if  $\xi > \xi_{crit}$ , and exhibits a stress maximum if  $\xi < \xi_{crit}$ . This critical value varies with both material parameters  $\bar{M}$  and  $\chi$ . The bifurcation of stress stretch curves is also discussed but it is trivial since no further equitriaxial stretch is possible as the gel's overall volume is fixed  $(J=\lambda^3=J_*)$ .
- The attempt of explaining the load induced loss-of-saturation followed later by a load induced regain-of-saturation in the case of uniaxial loading from the

energetic viewpoint is made. The energy-stretch relation is consistent with the stress-stretch relation previously obtained.

## Chapter 4

## Eversion of a Swollen Cylindrical Tube

The eversion problem of a hyperelastic tube was first presented by Rivlin [75] for what is now known as the Mooney-Rivlin constitutive law. It was found that, in general, zero-traction boundary conditions could not be achieved pointwise at the two ends, for the assumed cylindrical deformation. This motivated Rivlin to employ zero end resultant load conditions instead. Varga [76] gave experimental examples for the eversion of different cylinders. Results showed that the the everted tube is approximately cylindrical in the region away from the two ends.

Haughton and Orr studied the eversion of both incompressible [77] and compressible [78–80] hyperelastic cylinders. The existence and uniqueness of the solutions to such problems were discussed for the materials with a class of free-energy functions proposed by Ogden [52]. In [78], an exact solution that satisfied zero-traction pointwise boundary conditions both at the lateral surfaces and the two ends was obtained for a particular compressible hyperelastic material. The specified strain-energy function led to a 1-D second order ordinary differential equation that could be solved analytically. The analytical solution also shows an interesting result that the ratio of the inner and outer deformed radii is equal to the ratio of the undeformed radii. Several other material models including the class of 'Varga' materials were considered for this eversion problem in which case only numerical solutions could be obtained.

For the more general material models associated with the so-called semi-linear strain-energy function there exists an analytical solution to the equilibrium equation of cylindrical deformation. Specially, a new way of producing the analytical solutions to this eversion problem was presented in [79]. This is involved replacing a number in the equilibrium equation of the deformation r(R) by a constant parameter in order to generalize the equation involving r(R). Then by working backwards, a class of energy functions that would generate analytical solutions was obtained.

Furthermore, Chen and Haughton [80] studied the eversion problem for compressible cylinders with the following boundary conditions: free traction at the two ends and outer surface; either a zero traction (cavity remains open) or displacement (closed cavity) boundary condition is specified at inner surface. They proved mathematically in [80] that exact solutions to the equilibrium equation with cylindrical eversion deformation exist if two conditions are satisfied, namely: (1) the cavity remains open during the eversion; (2) the strain-energy function of the hyperelastic material can be written as the sum of three minor functions each of which depends only on one of the three principal stretches.

# 4.1 The Inhomogeneous Deformation of an Everted Tube under Axial Load

In this Chapter, we consider the inhomogeneous deformation of an everted tube under axial load based on the hyperelastic continuum theory described in Chapter 2. For inhomogeneous deformation, the spatially varying stress field must satisfy the equations of equilibrium (2.17). For the constitutive forms (2.5) and (2.13) the Cauchy stress tensor is given by either (2.23) or (2.24) depending on whether the material is saturated or not saturated. The only difference between these two formulae is due to the presence of p in the nonsaturated Cauchy stress (2.24). Recalling that this p does not vary with location, it follows that  $\operatorname{div}(-p\mathbf{I}) = -\nabla p = 0$ . Thus the equilibrium

equations div  $\sigma=0$  are the same whether the gel is saturated or not saturated. The distinction in mechanical response is due to the requirement (2.20) which causes the gel to obey the constraint  $V=V_{poly}+V_{liq}$  (viz. (2.18), (2.19)) when it is no longer saturated. In the formal mathematical procedure, this constraint is met by the presence of p in the boundary conditions. These issues will be demonstrated for the inhomogeneous deformation of an everted tube subject to axial load. We shall continue to use the Flory-Huggins constitutive form (2.5) for H and the Mooney-Rivlin constitutive form (2.13) for  $\Phi$ .

#### 4.1.1 Formulation of the Everted Tube Problem

Consider a hollow circular cylinder using polar coordinates in the reference configuration  $\Omega_{\mathbf{X}}$  with

$$R_i \le R \le R_o, \quad 0 \le \Theta < 2\pi, \quad 0 \le Z \le L, \qquad (R_o > R_i > 0).$$
 (4.1)

Let it then be immersed in the fluid. In the absence of external tractions the gel undergoes free swelling. Provided that sufficient liquid is available for saturation, the deformation of the freely swollen gel cylinder is described in polar coordinates  $(\hat{r}, \hat{\theta}, \hat{z})$  as

$$\hat{r} = \zeta R, \qquad \hat{\theta} = \Theta, \qquad \hat{z} = \zeta Z.$$
 (4.2)

Here  $\zeta$  is again the free swelling stretch ratio as defined in (2.15).

Next, the swollen cylinder is everted (turned inside-out). The resulting deformation is described with respect to polar coordinates  $(r, \theta, z)$  obeying  $r_i \leq r \leq r_o$ ,  $0 \leq \theta < 2\pi$  by

$$r = f(\hat{r}), \qquad \theta = \hat{\theta}, \qquad z = -\hat{\lambda}_z \hat{z}, \qquad (\hat{\lambda}_z > 0).$$
 (4.3)

The value  $\hat{\lambda}_z$  is the mechanical stretch ratio in the axial direction, and will be called

mechanical stretch for short.

Combining (4.2) and (4.3) gives the transformation from the unswellen state  $(R, \Theta, Z)$  to the swellen everted state  $(r, \theta, z)$ :

$$r = f(\zeta R) = r(R), \qquad \theta = \hat{\theta} = \Theta, \qquad z = -\lambda_z Z,$$
 (4.4)

with

$$r_i \le r \le r_0, \quad 0 \le \theta < 2\pi, \quad -l \le z \le 0, \tag{4.5}$$

where  $\lambda_z = \hat{\lambda}_z \zeta > 0$  and  $l = \lambda_z L$ . The presence of the minus sign in the expression for z in (4.3) gives rise to the eversion, and we seek solutions such that f' < 0 so that r' < 0. In particular, it follows that

$$r(R_i) = r_o, r(R_o) = r_i.$$
 (4.6)

For now,  $\lambda_z$  is regarded as a free parameter. It will ultimately be associated with the axial load on the ends z = -l and z = 0.

The deformation gradient tensor associated with the mapping (4.4) is  $\mathbf{F} = r'\mathbf{e}_r \otimes \mathbf{e}_R + (r/R)\mathbf{e}_\theta \otimes \mathbf{e}_\Theta - \lambda_z \mathbf{e}_z \otimes \mathbf{e}_Z$  where  $\mathbf{e}_r, \mathbf{e}_\theta, \mathbf{e}_z$  and  $\mathbf{e}_R, \mathbf{e}_\Theta, \mathbf{e}_Z$  are respectively the cylindrical polar unit basis vectors in the deformed and reference configurations, and r' = dr/dR. It then follows that

$$I_{1} = r'^{2} + \left(\frac{r}{R}\right)^{2} + \lambda_{z}^{2}, \qquad I_{2} = \left(\frac{r'r}{R}\right)^{2} + \left(r'\lambda_{z}\right)^{2} + \left(\frac{r}{R}\lambda_{z}\right)^{2}, \qquad J = -\frac{r'r}{R}\lambda_{z}.$$

$$(4.7)$$

For the constitutive relations (2.13) and (2.5) it follows from (2.23) that, for saturated response, there are no shear stresses and that the normal stresses are given by

$$\sigma_{rr} = -\frac{\mu R r'}{\lambda_z r} \left[ (1 - \xi) + \xi \left( \frac{r}{R} \right)^2 + \xi \lambda_z^2 \right] + M \left[ \frac{-R}{\lambda_z r r'} + \chi \left( \frac{R}{\lambda_z r r'} \right)^2 + \ln \left( 1 + \frac{R}{\lambda_z r r'} \right) \right], \tag{4.8}$$

$$\sigma_{\theta\theta} = -\frac{\mu r}{\lambda_z R r'} \left[ (1 - \xi) + \xi \lambda_z^2 + \xi r'^2 \right] + M \left[ \frac{-R}{\lambda_z r r'} + \chi \left( \frac{R}{\lambda_z r r'} \right)^2 + \ln \left( 1 + \frac{R}{\lambda_z r r'} \right) \right], \tag{4.9}$$

$$\sigma_{zz} = -\frac{\mu R \lambda_z}{rr'} \left[ (1 - \xi) + \xi r'^2 + \xi \left( \frac{r}{R} \right)^2 \right] + M \left[ \frac{-R}{\lambda_z rr'} + \chi \left( \frac{R}{\lambda_z rr'} \right)^2 + \ln \left( 1 + \frac{R}{\lambda_z rr'} \right) \right]. \tag{4.10}$$

For nonsaturated response a common constant p is to be subtracted from these normal stress expressions.

With the above stresses, the equilibrium equations associated with the  $\theta$  and z directions are satisfied identically. The equilibrium equation associated with the r direction is

$$\frac{d}{dr} \left\{ -\mu \frac{Rr'}{\lambda_z r} \left[ (1-\xi) + \xi \left( \frac{r}{R} \right)^2 + \xi \lambda_z^2 \right] + M \left[ \frac{-R}{rr'\lambda_z} + \chi \left( \frac{R}{rr'\lambda_z} \right)^2 + \ln \left( 1 + \frac{R}{rr'\lambda_z} \right) \right] \right\} - \frac{\mu R}{\lambda_z r^2 r'} \left[ (1-\xi) + \xi \lambda_z^2 \right] \left[ r'^2 - \left( \frac{r}{R} \right)^2 \right] = 0.$$
(4.11)

The lateral surfaces of the everted tube are taken to be free of external tractions so that

$$\sigma_{rr}(r_i) = 0, \qquad \sigma_{rr}(r_o) = 0.$$
 (4.12)

Rearrangement of (4.11) yields a second order ODE for r(R) in the form

$$r'' = -\frac{2\xi \frac{rr'^{2}}{R^{3}} (r'R - r) + \left[ (1 - \xi) + \xi \lambda_{z}^{2} \right] \left[ \frac{r'^{3}}{r} - \frac{rr'}{R^{2}} \right] + \lambda_{z} \left( \frac{r'^{2}}{R} - \frac{rr'}{R^{2}} \right) F(R, r, r', \lambda_{z})}{2r' \left[ (1 - \xi) + \xi \left( \frac{r^{2}}{R^{2}} + \lambda_{z}^{2} \right) \right] + \frac{\lambda_{z}r}{R} F(R, r, r', \lambda_{z})}$$
(4.13)

where the function  $F(R, r, r', \lambda_z)$  is defined by

$$F(R, r, r', \lambda_z) = \frac{r'^2 \left[ (1 - \xi) + \xi \left( \frac{r^2}{R^2} + \lambda_z^2 \right) \right]}{J} - \frac{M}{\mu} \left( \frac{1}{J(J - 1)} - \frac{2\chi}{J^2} \right)$$
(4.14)

and J is given by  $(4.7)_3$ . Thus (4.13) with (4.12) provides an apparently well posed problem for r(R). The solution describes an everted cylinder of saturated material so long as the condition (2.20) is met. The solution is dependent upon constitutive parameters:  $\mu$ , M,  $\chi$ ,  $\xi$ , and upon the stretch parameter  $\lambda_z$ .

The solution to this problem will generally give a radially varying  $\sigma_{zz}$ . In particular, a condition of  $\sigma_{zz}$  being identically zero is not anticipated for any combination of parameters. This is connected to the observed behavior in eversion type deformations on rubbery materials mentioned at the beginning of this chapter. Namely, some flaring out of the top and bottom of an everted cylinder are observed in the absence of any tractions on the top and bottom surfaces. Thus the observed traction free deformations are not in accord with the simple eversion deformation (4.3). This suggests that tractions on the top and bottom surface caps would be necessary to sustain the simple eversion deformation. The deformation constructed on the basis of (4.13) with (4.12) is consistent with these expectations.

The normal stress  $\sigma_{zz}$  generates an overall axial force on the everted cylinder. Normalizing this axial force by the original surface area of the caps gives

$$P_{cap} \equiv \frac{2\pi}{\pi (R_o^2 - R_i^2)} \int_{r_i}^{r_o} r \sigma_{zz} dr. \tag{4.15}$$

It is to be noted that  $r_i$  and  $r_o$  defined in (4.6) are unknown before the solution is obtained. For fixed material parameters,  $P_{cap}$  will depend upon  $\lambda_z$ . The force-stretch relation  $P_{cap}$  vs.  $\lambda_z$  is analogous to the homogeneous deformation relation in uniaxial stress between P and  $\lambda$  discussed in Chapter 3. Recall that this is given in general by

(3.27), where the specialization to the Mooney-Rivlin constitutive form uses (3.21). In particular, one may then compare the relation between P and  $\lambda$  obtained from (3.27) with (3.21), to the relation between  $P_{cap}$  and  $\lambda_z$  obtained on the basis of (4.15) after the solution of (4.12) and (4.13). The former gives the force-stretch relation for the cylinder before it is everted so long as it remains saturated. The latter gives the force-stretch relation for the cylinder after it is everted so long as it too remains saturated.

### 4.2 Numerical Results for a Saturated System

We have integrated the differential equation (4.13) after suitable nondimensionalization by means of a fourth order Runge-Kutta method using the same material parameters:  $\chi = 0.425$ ,  $\bar{M} = M/\mu = 100$  that were employed in the homogeneous deformation study. A shooting procedure was used to meet the two point boundary conditions. The unswellen configuration was taken to involve  $R_0/R_i = 2$ . Calculations were performed for different values of  $\xi$  and hence different values of the free swelling stretch  $\zeta$ . For each such  $\xi$ , the problem was solved numerically for a sequence of  $\hat{\lambda}_z$ , which it is recalled is the mechanical portion of the mechanical stretch ratio that appears in (4.3).

Radial deformation of the everted cylinder is shown in Figure 4.1 (a) and (c) for the respective cases  $\xi=0$  and  $\xi=1$ . Here the horizontal axis represents dimensionless radial coordinates  $\bar{R}\equiv R/R_i$  in the reference configuration while the vertical axis gives the dimensionless radial coordinates  $\bar{r}\equiv r/(\zeta R_i)$  in the deformed configuration. As  $\hat{\lambda}_z$  increases, it is found that both the deformed inner and outer radii decrease, which is consistent with the expectation of a transverse contraction under axial extension. Figure 4.1 (b) and (d) shows the radial variation of J (normalized by  $\zeta^3$ ) which gives the gel's local volume change and hence the amount of fluid ab-

sorbed into the cylinder. It is to be noticed in panels (b) and (d) that the horizontal axis represents the deformed radial coordinate  $\bar{r}$  and so the curves start and end at different locations on the horizontal axis. For each value of mechanical stretch  $\hat{\lambda}_z$ , the volume change is relatively greater near the outer periphery, indicating that the volume fraction of liquid increases with radius in the everted cylinder.

Graphs of the normal stresses are displayed in Figure 4.2 for both  $\xi=0$  and  $\xi=1$  at a variety of mechanical stretches  $\hat{\lambda}_z$ . Note that  $\sigma_{rr}<0$  in the interior of the everted cylinder. The hoop stress  $\sigma_{\theta\theta}$  is found to be compressive in the inner portion of the cylinder and tensile in the outer portion (which is broadly consistent with the notion that the liquid is "squeezed" toward the outer portion). The axial stress  $\sigma_{zz}$  also exhibits radial variation and correlates with stretch  $\hat{\lambda}_z$  in the anticipated fashion. The qualitative form for all of the curves is shown to be quite sensitive to the value of  $\xi$ .

The relation between  $\hat{\lambda}_z$  and  $P_{cap}$  as defined in (4.15) is shown by the solid curves in Figure 4.3(a) and Figure 4.3(c) for  $\xi=0$  and  $\xi=1$ , respectively. These are compared with the uniaxial loading (without eversion) as represented by the dashed curves in the same panels. For the neo-Hookean type gel ( $\xi=0$ ), the everted cylinder undergoes greater elongation at a given load than does the uneverted cylinder. However, the opposite occurs for  $\xi=1$ . Panels (b) and (d) of Figure 4.3 show how the total cylinder volume varies with mechanical stretch, again for the respective cases  $\xi=0$  and  $\xi=1$ . Specifically, the total volume as given by (2.19) is normalized by the free swelling volume (solid curve), and compared to the normalized volume of the uneverted cylinder (dashed curve). The total volume of the uneverted cylinder is determined by the value of J in the homogeneous deformation for uniaxial stress. This value of J was previously displayed (vs. overall stretch) in Figure 3.3(b) using the now standard constitutive parameters  $\bar{M}=100$  and  $\chi=0.425$ . Recall for uniaxial stress that the relation between J and stretch was not monotonic for  $\xi>0$ . Thus

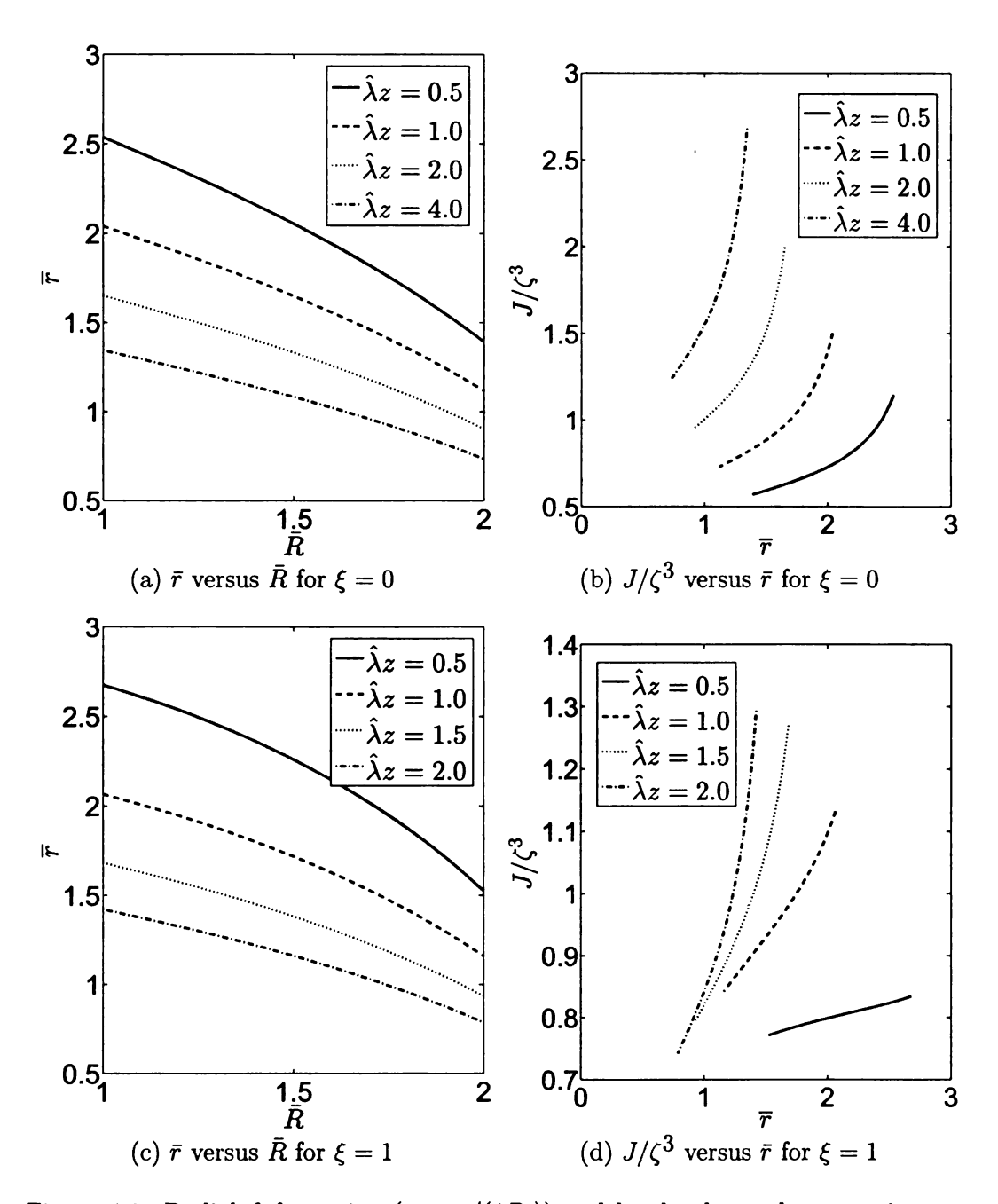
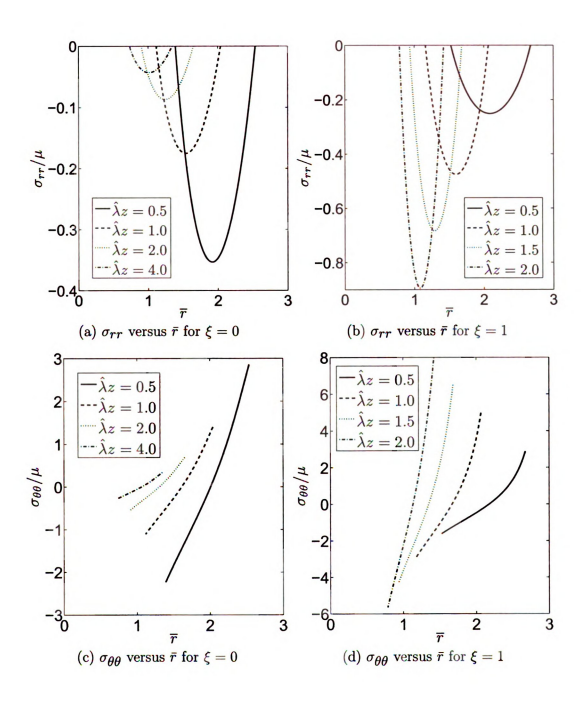


Figure 4.1: Radial deformation  $(\bar{r}=r/(\zeta R_i))$  and local volume change ratio as a function of radial position. As in previous figures,  $\bar{M}=100$  and  $\chi=0.425$ . The cylinder geometry is such that  $R_o=2R_i$ .



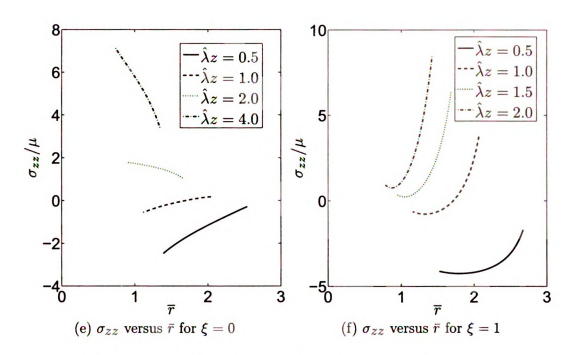


Figure 4.2: Radial distribution of normal stresses for the everted cylinder with  $R_0 = 2R_i$  using the same material parameters as in Figure 4.1.

the dashed curve in Figure 4.3(d) is not monotonic. It is to be observed from panel (b) of Figure 4.3 that the everted cylinder for  $\xi=0$  preserves the monotonic relation between volume and stretch that was found in the uneverted cylinder. Similarly, panel (d) of Figure 4.3 shows that the everted cylinder for  $\xi=1$  gives a relation between volume and stretch that is not monotonic as was the case for the uneverted cylinder with  $\xi=1$ . It is also interesting to note for both  $\xi=0$  and  $\xi=1$  that the total volume of the everted cylinder is less than that of an uneverted cylinder at the same value of stretch. Thus for both  $\xi=0$  and  $\xi=1$  the everted cylinder holds less fluid than the corresponding uneverted cylinder.

The form of the volume vs. stretch curves in panels (b) and (d) of Figure 4.3 have immediate consequences as regards the possibility of loss of saturation. The results mirror the corresponding results for the uneverted cylinder, since the everted and uneverted curves in each panel display the same qualitative form. In general, the

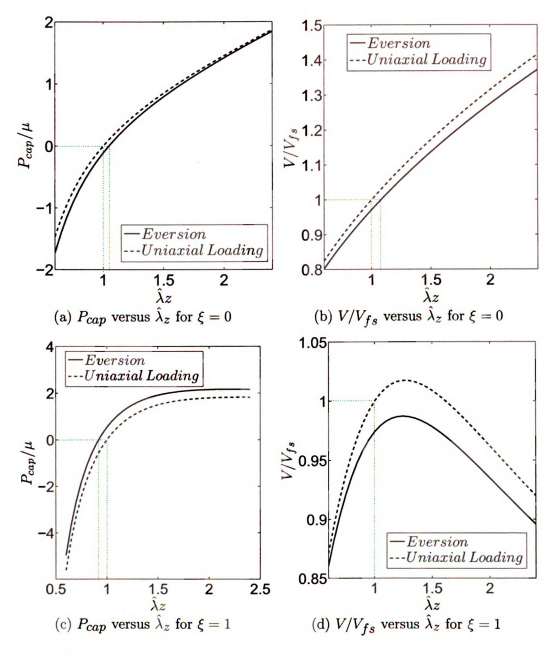


Figure 4.3: Resultant axial force as a function of mechanical stretch and total volume as a function of mechanical stretch for both the everted cylinder and the uneverted cylinder using the same material parameters as in Figure 4.1. For the everted cylinder, the reference geometry is again such that  $R_O=2R_i$ .

saturated solution holds provided that

$$\pi \lambda_z L(r_o^2 - r_i^2) \le \pi L(R_o^2 - R_i^2) + V_{liq}, \tag{4.16}$$

where it is recalled that  $\lambda_z = \hat{\lambda}_z \zeta$ . We now consider differences that occur for the respective cases  $\xi = 0$  and  $\xi = 1$  which stem from the different qualitative forms of the curves in panels (b) and (d) of Figure 4.3.

Consider first the material with  $\xi=0$ . The monotone curve for the everted cylinder in Figure 4.3b then indicates that an everted cylinder of the  $\xi=0$  material will be saturated if  $\hat{\lambda}_z$  is less than a critical value. Conversely, the everted cylinder will not be saturated if  $\hat{\lambda}_z$  exceeds the critical value. The critical value of mechanical stretch is dependent upon the amount of available fluid, and can be directly determined with the aid of Figure 4.3(b). It is to be noted from this figure that, for a given amount of fluid, the transition value of mechanical stretch for the everted cylinder exceeds the transition mechanical stretch value for the uneverted cylinder.

Consider now the material with  $\xi=1$ . Then the graphs of volume vs. stretch for both the everted cylinder and the uneverted cylinder each have a local maximum. Consequences for the uneverted cylinder were discussed in Section <sup>1</sup> and similar considerations apply to the everted cylinder. Thus the everted cylinder will be saturated for all values of stretch if the amount of available fluid exceeds that associated with the value of the local maximum. If less than this amount of fluid is available, then there will be an interval of stretch for which the everted cylinder is not saturated. It is to be noted from Figure 4.3(d) that the value of the local maximum for the uneverted cylinder gives  $V > V_{fs}$  where  $V_{fs}$  is the free swelling volume of the cylinder before eversion. Conversely, the value of the local maximum for the everted cylinder gives  $V < V_{fs}$ . Consider therefore two identical cylinders, each of which is removed from its liquid bath after free swelling so that the amount of fluid is fixed at the free

<sup>&</sup>lt;sup>1</sup>See the paragraph between equations (3.16) and (3.17).

swelling value. Let one of the two cylinders now suffer an eversion. This everted cylinder will remain saturated for any value of axial stretch. In comparison, the uneverted cylinder will immediately lose saturation if it is stretched a small amount. However, if the stretch of the uneverted cylinder becomes sufficiently large, then it too will regain saturation.

The above interpretation for a  $\xi=1$  gel is a consequence of the inequality  $V < V_{fs}$  holding for all values of stretch in the everted cylinder. More generally, for  $\xi>0$  we find that the graph of stretch vs. overall volume continues to exhibit a local maximum. However, as shown in Figure 4.4(a), the value of V at the local maximum is found to be greater than the free swelling volume provided that this positive  $\xi$  is sufficiently small. For these materials it follows that a quantity of liquid just sufficient for free swelling gives rise to an everted cylinder that loses saturation on a finite interval of stretch. The relation between force and mechanical stretch for a saturated everted cylinder using the same values of  $\xi$  as in panel (a) of Fig. 4.4 is shown in panel (b) of this same figure. These serve as backbone curves for any nonsaturated response. In order to display force vs. stretch curves associated with loss of saturation it is necessary to solve the boundary value problem for an everted cylinder that is not saturated. We consider this issue in the next section.

### 4.3 The Everted Cylinder that is Not Saturated

We now consider the consequences of a limited fluid supply for the eversion deformation. Specifically, if the total volume of a saturated, everted cylinder is calculated to be greater than  $V_{poly} + V_{liq}$  then there is insufficient fluid for the cylinder to be saturated. The resulting nonsaturated solution obeys

$$\lambda_z(r_o^2 - r_i^2) = (R_o^2 - R_i^2) + \frac{V_{liq}}{\pi L},\tag{4.17}$$

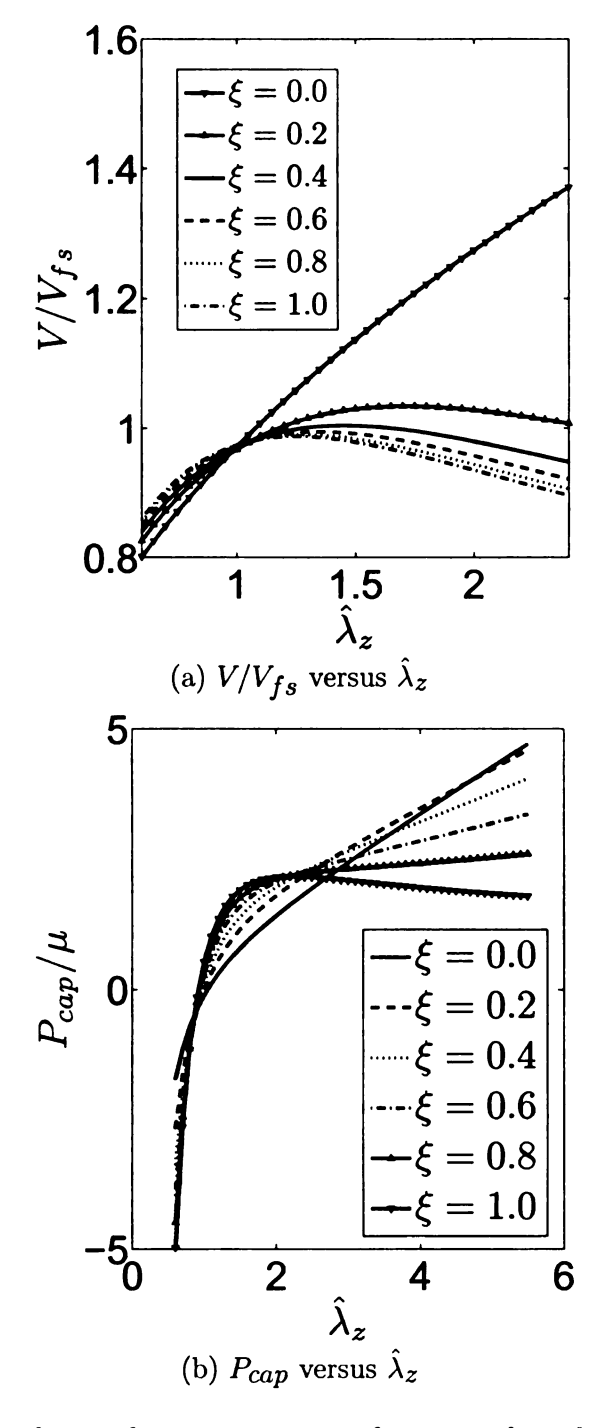


Figure 4.4: Total volume after eversion as a function of mechanical stretch, and resultant force as a function of mechanical stretch, for various values of  $\xi$ , again using  $\bar{M}=100,\,\chi=0.425$  and  $R_o=2R_i$ .

where it is recalled  $\lambda_z = \hat{\lambda}_z \zeta$ . As discussed previously, the stress equations of equilibrium are unchanged from that for a saturated system. Thus the displacement field r(R) is still subject to (4.13) where F is given by (4.14). The normal stresses are modified by subtracting the common constant p from the saturated stress relations as previously given in (4.8)-(4.10). Eliminating this constant between the two conditions in (4.12) now gives

$$-\frac{R_{i}r_{i}'}{\lambda_{z}r_{i}}\left[(1-\xi)+\xi\left(\frac{r_{i}}{R_{i}}\right)^{2}+\xi\lambda_{z}^{2}\right]+\bar{M}\left[\frac{-R_{i}}{\lambda_{z}r_{i}r_{i}'}+\chi\left(\frac{R_{i}}{\lambda_{z}r_{i}r_{i}'}\right)^{2}+\ln\left(1+\frac{R_{i}}{\lambda_{z}r_{i}r_{i}'}\right)\right]=\\-\frac{R_{o}r_{o}'}{\lambda_{z}r_{o}}\left[(1-\xi)+\xi\left(\frac{r_{o}}{R_{o}}\right)^{2}+\xi\lambda_{z}^{2}\right]+\bar{M}\left[\frac{-R_{o}}{\lambda_{z}r_{o}r_{o}'}+\chi\left(\frac{R_{o}}{\lambda_{z}r_{o}r_{o}'}\right)^{2}+\ln\left(1+\frac{R_{o}}{\lambda_{z}r_{o}r_{o}'}\right)\right],$$
(4.18)

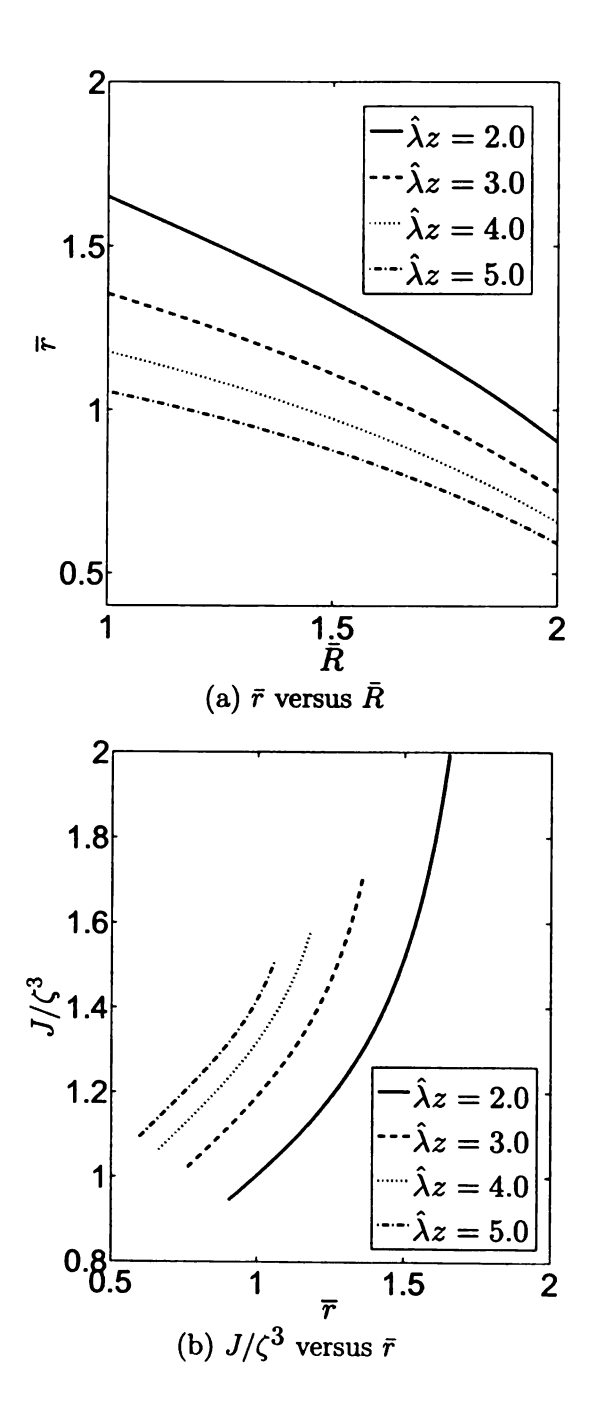
where  $r_i' = r'(R_i)$  and  $r_o' = r'(R_o)$ . The second order ODE (4.13) is to be solved subject to (4.17) and (4.18), after which p is obtained from (4.12).

For values  $V_{liq}$  that cause the saturated solution condition (4.16) to be violated, we have solved (4.13) using a double shooting method so as to meet both (4.17) and (4.18). The solutions are dependent upon the mechanical stretch  $\hat{\lambda}_z$  and the value of  $V_{liq}/\pi L$  appearing in (4.17). Each such  $V_{liq}/\pi L$  determines the range of  $\hat{\lambda}_z$  for which there is loss of saturation. As discussed in the previous section, the range of nonsaturated  $\hat{\lambda}_z$  can be unbounded (as in the  $\xi=0$  example of Figure 4.3) or can be confined to a finite interval (as in the  $\xi=1$  example of Figure 4.3).

Consider the material parameters associated with the  $\xi=0$  saturated solution fields that were previously displayed in Figure 4.1 and Figure 4.2. The relation between total volume and mechanical stretch for this material was displayed in panel (b) of Figure 4.3. Since this relation is monotonically increasing, it follows that loss of saturation could occur for any value of stretch. Following previous convention, this transition value of stretch will be denoted  $\hat{\lambda}_z^*$  and the nonsaturated solution therefore applies for  $\hat{\lambda}_z \geq \hat{\lambda}_z^*$ . Figure 4.5 displays the nonsaturated solution fields associated

with this same material for the particular value of  $V_{liq}$  that gives  $\hat{\lambda}_z^* = 2.0$ . Thus for this  $V_{liq}$  the curves in Figure 4.1 and Figure 4.2 corresponding to  $\hat{\lambda}_z \leq \hat{\lambda}_z^* = 2.0$ would continue to apply. However there would now be insufficient fluid to saturate the everted cylinder when  $\hat{\lambda}_z > 2.0$  and so the  $\hat{\lambda}_z = 4.0$  curves in Figure 4.1 and Figure 4.2 would no longer apply. Instead, the solution fields for  $\hat{\lambda}_z=4.0$  are as depicted in Figure 4.5. The solution fields for the nonsaturated everted cylinder for other values of mechanical stretch  $\hat{\lambda}_z > \hat{\lambda}_z^*$  are also shown in Figure 4.5. The nonsaturated solution is identical to the saturated solution at the transition stretch  $\hat{\lambda}_z^*$  as is verified by comparison of the curves for  $\hat{\lambda}_z = 2.0$  in Figures 4.1, 4.2 and 4.5. As the mechanical stretch increases, comparison of Figure 4.2 and Figure 4.5 reveals similar qualitative trends in the nature of the stress fields after loss of saturation. In contrast, comparison of Figure 4.1 and Figure 4.5 shows qualitative differences in the J field after loss of saturation. Specifically, the saturated solution gives values of J that increase at each point in the everted cylinder. Hence all locations absorb additional fluid as  $\hat{\lambda}_z$  increases so long as the gel is saturated. However, upon loss of saturation, it is found that the value of J now decreases on the outer portion of the cylinder (while continuing to increase in the inner portion of the cylinder). This is shown in detail in the first panel of Figure 4.6. Thus, after loss of saturation, the fixed amount of fluid within the cylinder exhibits a quasi-static migration from the outer portion of the everted cylinder to the inner portion of the everted cylinder under increasing mechanical stretch  $\hat{\lambda}_z$ .

In a similar fashion Figure 4.7 exhibits nonsaturated solution fields for the  $\xi=1$  material whose saturated solution fields were previously exhibited in Figure 4.1 and Figure 4.2. The relation between overall volume and mechanical stretch for this material is displayed in panel (d) of Figure 4.3. Since this relation exhibits a local maximum it follows that loss of saturation occurs on a finite interval of stretch. Again, following previous convention, we denote the endpoints of this interval by  $\hat{\lambda}_{z-A}^*$  and



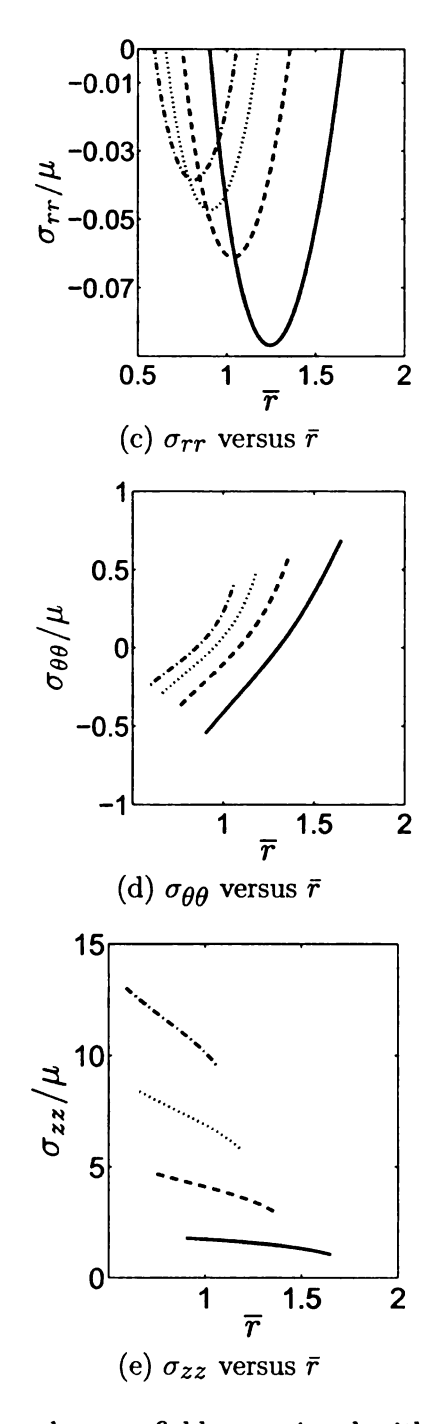


Figure 4.5: Deformation and stress fields associated with loss of saturation for an everted cylinder with  $R_o = 2R_i$ . The material parameters are  $\bar{M} = 100$ ,  $\chi = 0.425$ , and  $\xi = 0$ . Loss of saturation is taken to occur at  $\hat{\lambda}_z^* = 2.0$ . Thus the curves for  $\hat{\lambda}_z = 2.0$  are the same as the corresponding curves for  $\xi = 0$  that were displayed in Figures 4.1 and 4.2. For  $\hat{\lambda}_z > 2.0$  the curves in this figure differ from corresponding curves for a saturated gel.

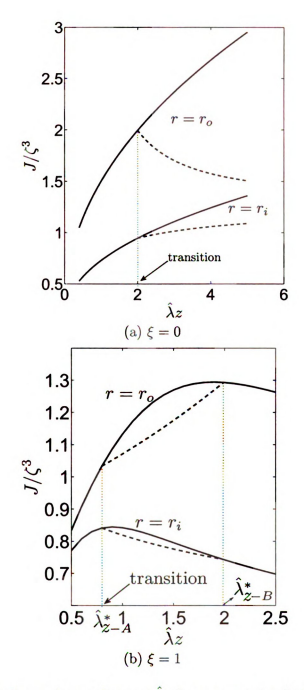
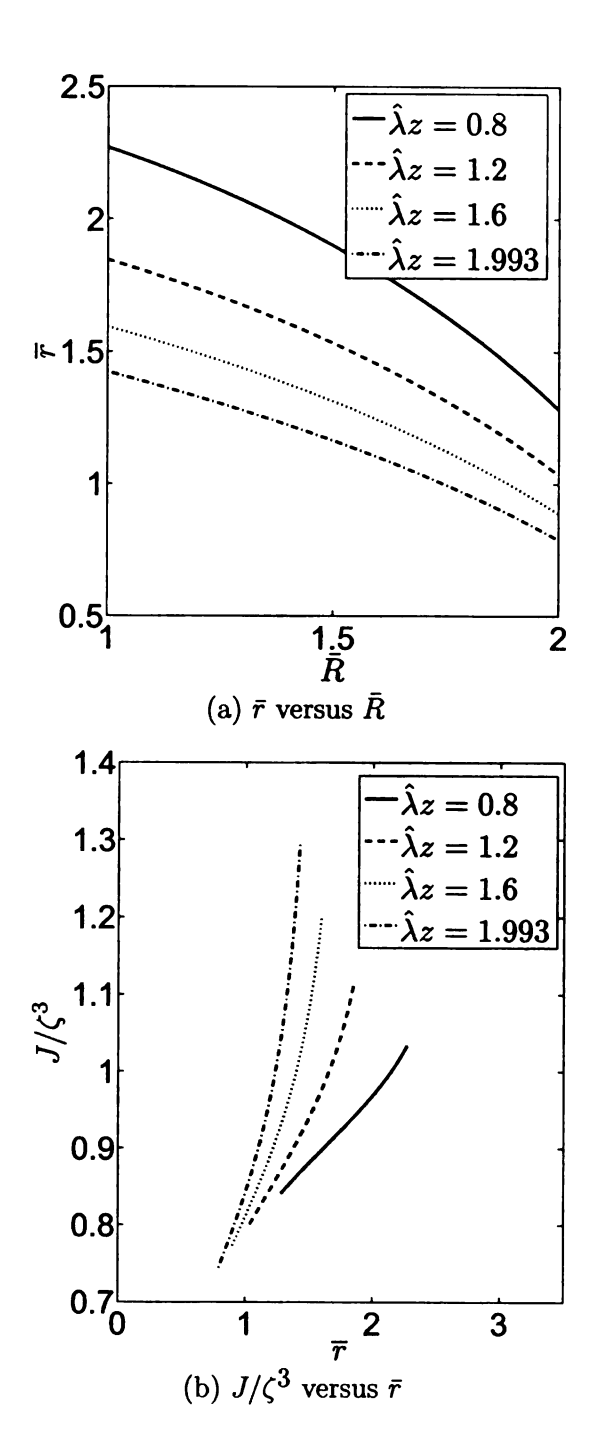


Figure 4.6: Local volume change J versus  $\hat{\lambda}_z$  for an everted cylinder with  $R_o = 2R_i$  and material parameters  $\tilde{M} = 100$ ,  $\chi = 0.425$  and either  $\xi = 0$  or  $\xi = 1$ . On the left,  $\xi = 0$  and the loss of saturation corresponds to that depicted in Figure 4.5. After loss of saturation, increasing stretch redistributes the finite amount of fluid from the outer region to the inner region. On the right,  $\xi = 1$  and the loss of saturation corresponds to that depicted in Figure 4.7. For the nonsaturated cylinder, increasing stretch now redistributes the finite amount of fluid from the inner region to the outer region.

 $\hat{\lambda}_{z-B}^*$ . For the purposes of Figure 4.7, we take  $\hat{\lambda}_{z-A}^* = 0.8$  which in turn makes  $\hat{\lambda}_{z-B}^* = 1.993$ . Once again, the fixed amount of fluid redistributes itself in a quasistatic fashion as  $\hat{\lambda}_z$  varies in the interval  $\hat{\lambda}_{z-A}^* \leq \hat{\lambda}_z \leq \hat{\lambda}_{z-B}^*$ . In particular, as  $\hat{\lambda}_z$  increases through this interval we find that fluid migrates from the inner portion of the everted cylinder to the outer portion. This is shown in detail in the second panel of Figure 4.6. For this material, after a return to saturation at  $\hat{\lambda}_{z-B}^*$ , any further increase in mechanical stretch gives a loss in overall volume, indicating that increasing mechanical stretch now expels fluid from the everted cylinder.

Recall for the fluid saturated everted cylinder that the relation between axial force and axial stretch was given previously in Figure 4.3 for both the  $\xi=0$  material (panel a) and the  $\xi=1$  material (panel c). Loss of saturation causes the response to depart away from this backbone response. The question therefore arises as to whether this departure takes place in a manner that is similar to that which occurs in the homogeneous deformation of uniaxial stress. Recall for the homogeneous deformation of uniaxial stress that the departure of the nonsaturated axial force response from the saturated backbone response was displayed in Figure 3.10(b) for the  $\xi=1$  material. The conspicuous feature of Figure 3.10(b) was that the nonsaturated axial load response for the  $\xi=1$  material was first above, and then below, the saturated axial load response. We find that similar qualitative behavior occurs for the  $\xi=1$  material as the everted cylinder is mechanically stretched. This is shown in Figure 4.8 where the difference between satuated and nonsaturated response is shown not only for the case in which  $\hat{\lambda}_{z-A}^*=0.8$ , but also for two other cases corresponding to  $\hat{\lambda}_{z-A}^*=0.9$  and  $\hat{\lambda}_{z-A}^*=1.0$ .



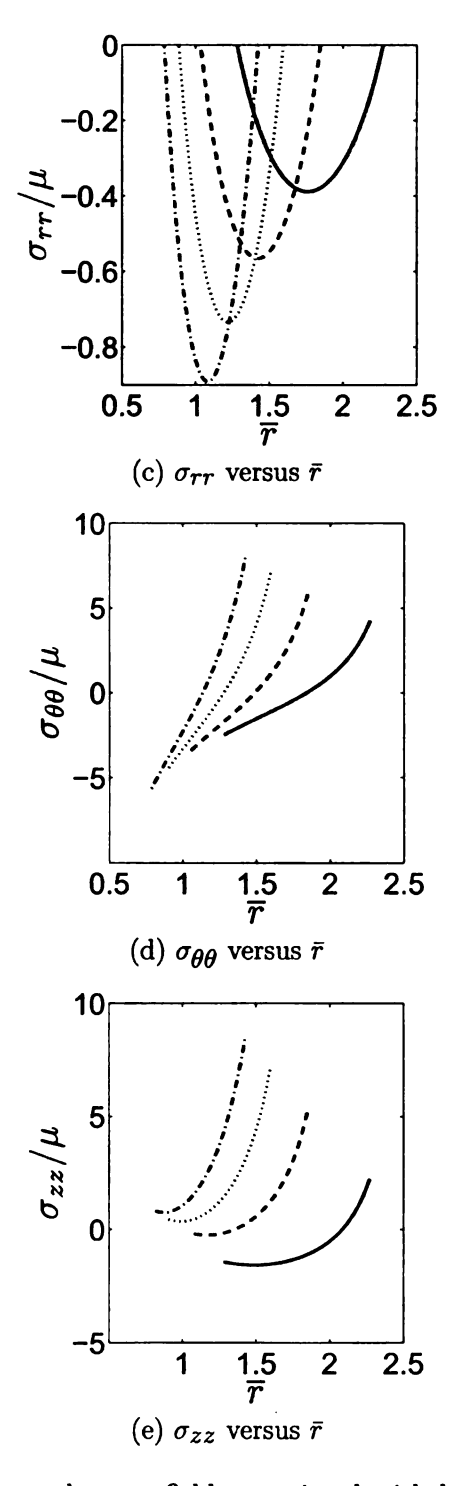


Figure 4.7: Deformation and stress fields associated with loss of saturation for an everted cylinder with  $R_o=2R_i$ . The material parameters are  $\bar{M}=100,~\chi=0.425,$  and  $\xi=1$ . The value of  $V_{liq}$  is such that loss of saturation occurs on the interval  $0.8 \leq \hat{\lambda}_z \leq 1.993$ .

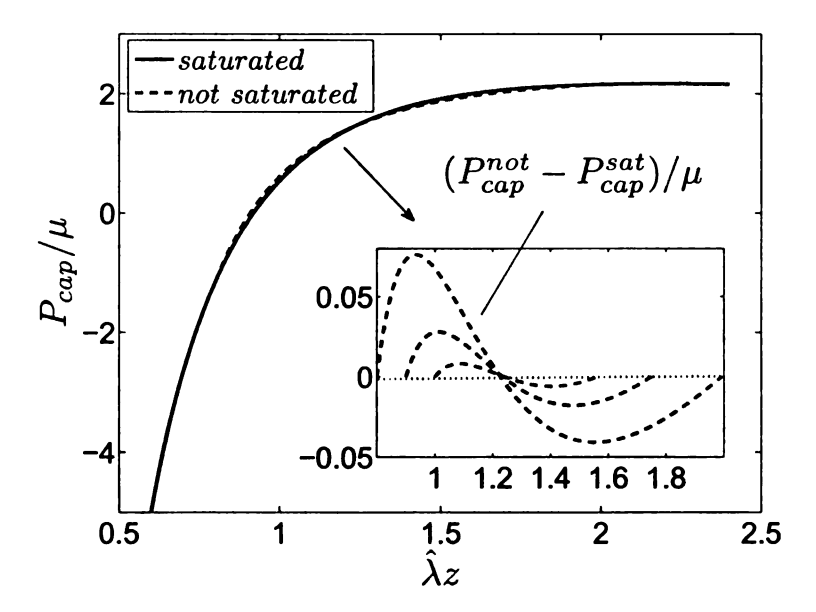


Figure 4.8: Resultant axial force as a function of mechanical stretch for the everted cylinder with  $R_o=2R_i$ . Material parameters correspond to those in Figure 4.3(c), namely:  $\bar{M}=100$ ,  $\chi=0.425$ , and  $\xi=1$ . Three different values of  $V_{liq}$  are considered, corresponding to  $\hat{\lambda}_z^*=0.8,0.9$ , and 1.0. The nonsaturated response curve is first above, and then below, the saturated response curve, and so mirrors the case of this material under homogeneous deformation (Figure 3.10(b)).

### 4.4 Summary

The problem of everting a swollen tube subject to axial loading is studied in this chapter. The inhomogeneous deformation response of the axial loaded everted tube is compared to the homogeneous deformation response of the axially loaded tube when it is not everted. Both systems can transition from saturation to nonsaturation.

- As  $\hat{\lambda}_z$  increases, it is found that both the deformed inner and outer radii decrease, which is consistent with the expectation of a transverse contraction under axial extension. For each value of  $\hat{\lambda}_z$ , the volume change is relatively greater near the outer region, indicating that the volume fraction of liquid increases with radius in the everted cylinder.
- The overall volume is calculated for the everted tube, and compared with those for an uneverted tube. It is observed that the everted cylinder for ξ = 0 preserves the monotonic relation between volume and stretch that was found in the uneverted cylinder, and similarly the everted cylinder for ξ = 1 gives a relation between volume and stretch that is not monotonic as was the case for the uneverted cylinder with ξ = 1. More generally, we found that the graph of overall volume vs. stretch exhibits a local maximum as long as ξ > 0.
- The transition to loss of saturation is also considered for the axial loaded everted tube. For  $\xi=0$  it is found that after loss of saturation the fixed amount of fluid within the cylinder exhibits a quasi-static migration from the outer portion of the everted cylinder to the inner portion as the axial stretch increases. For  $\xi=1$ , since the volume-stretch relation exhibits a local maximum it follows that loss of saturation occurs on a finite interval of stretch. As  $\hat{\lambda}_z$  increses through this interval we find that fluid migrates from the inner portion of the everted cylinder to the outer portion.

## Chapter 5

# Twisting of a Cylindrical Tube

In this chapter we discuss the absorption and redistribution of fluid in hyperelastic gels due to twisting; and in particular distinguish between saturated and unsaturated gel systems. To this end we consider a boundary value problem of radial displacement combined with azimuthal shear for an annular cylinder consisting of a fluid infused hyperelastic media. The effect of either boundary displacements or boundary tractions is considered so as to study how this alters the uniform fluid distribution when the hollow cylinder is in contact with a fluid bath at both inner and outer radii. Certain aspects of this problem were previously considered by Rajagopal and Wineman [48] for the case in which the overall volume is held fixed. Here we consider certain generalizations in which the lateral surfaces may undergo both prescribed radial displacement and prescribed relative twist. In particular these generalization permit volume change so as to allow for the consideration of both saturated states and unsaturated states.

In order to compare with the numerical results in [48] it is convenient that the elastic energy  $\Phi$  is chosen to have the same form as in [48]:

$$\Phi(I_1, I_2) = \frac{\mu_{\alpha}}{2} \left[ I_1 - 3 + \alpha (I_2 - 3) \right], \tag{5.1}$$

where  $\mu_{\alpha} > 0$  and  $\alpha \ge 0$  are material parameters. The case associated with  $\alpha = 0$  corresponds to  $\xi = 0$  and  $\mu = 2\mu_{\alpha}$  in (2.13), whereas the case associated with  $\alpha = 1$  in (5.1) can be retrieved by setting  $\xi = 1/2$  and  $\mu = 2\mu_{\alpha}$  in (2.13).

### 5.1 Twisting of a Saturated Tube

Consider a hollow circular cylinder of the gel described in the previous section. Employ polar coordinates  $(R, \Theta, Z)$  in the reference configuration such that  $R_i \leq R \leq R_0, 0 \leq \Theta < 2\pi, 0 \leq Z \leq L$  with  $R_i > 0$ . This cylinder is immersed in a liquid bath and, following Rajagopal and Wineman [48], let the coordinates  $(\hat{r}, \hat{\theta}, \hat{z})$  describe the mapping associated with this free swelling:

$$\hat{r} = \zeta R, \qquad \hat{\theta} = \Theta, \qquad \hat{z} = \zeta Z,$$
 (5.2)

where  $\zeta = J_{fs}^{1/3}$  is the free swelling stretch ratio. For H given in (2.5) and  $\Phi$  in (5.1), the free swelling volume change  $J_{fs}$  is determined by (2.4). Wineman and Rajagopal [48] using (5.1) for various  $\alpha$  take

$$M = 2.379E7 \, dyne/cm^2, \ \mu_{\alpha} = 2.375E6 \, dyne/cm^2, \ \chi = 0.425$$
 (5.3)

for a vulcanized rubber-toluene mixture. Figure 5.1 shows the the free swelling volume change  $J_{fs}$  and the free swelling stretch  $\zeta$  as a function of  $\alpha$  for the parameter values in (5.3).

In what follows it is assumed that there is always sufficient liquid available to support free swelling. In view of the conditions (2.18) - (2.20), this is a requirement that

$$V_{liq} > (J_{fs} - 1)V_{poly} = (\zeta^3 - 1)\pi(R_o^2 - R_i^2)L,$$

and the volume of the freely swollen cylinder is  $V_{fs} = J_{fs}V_{poly} = \zeta^3\pi(R_o^2 - R_i^2)L$ .

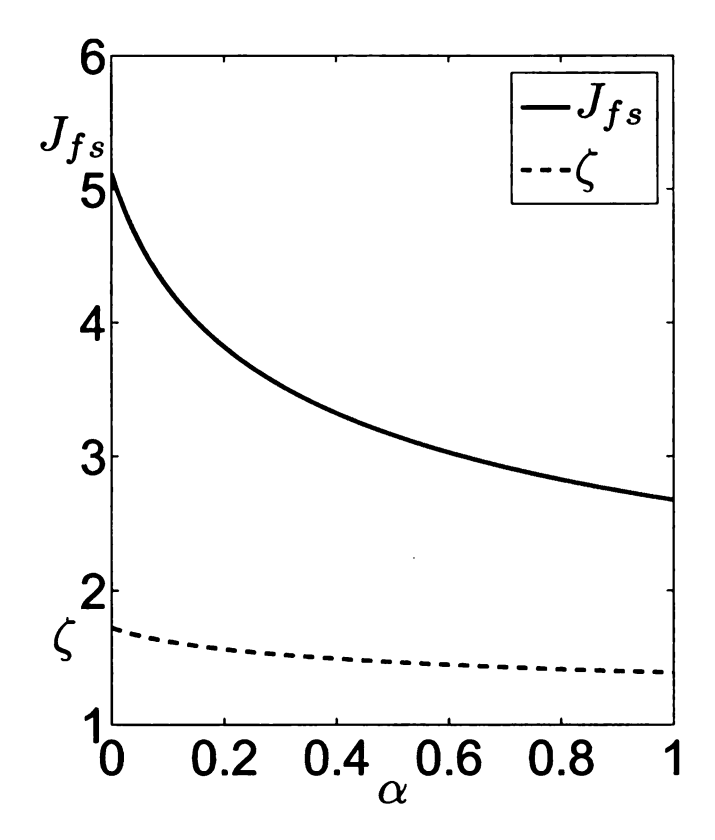


Figure 5.1: Free swelling volume change  $J_{fs}$  and stretch  $\zeta$  for different  $\alpha$  on the basis of (2.3) and (5.1) using (5.3).

Now consider loading of the swollen cylinder. Following Wineman and Rajagopal [48] attention is restricted to axially symmetric deformations that are described in polar coordinates  $(r, \theta, z)$  obeying  $r \ge 0$ ,  $0 \le \theta < 2\pi$  by

$$r = f(\hat{r}), \qquad \theta = \hat{\theta} + s(\hat{r}), \qquad z = \hat{\lambda}_z \hat{z}.$$
 (5.4)

Combining (5.2) and (5.4) gives the deformation from the unswellen state with coordinates  $(R, \Theta, Z)$  to the swellen loaded state with coordinates  $(r, \theta, z)$  as follows:

$$r = f(\zeta R) = r(R), \qquad \theta = \hat{\theta} + s(\zeta R) = \Theta + g(R), \qquad z = \lambda_z Z,$$
 (5.5)

with  $\lambda_z = \hat{\lambda}_z \zeta$ .

The deformation gradient tensor for (5.5) is given by  $\mathbf{F} = r' \mathbf{e}_r \otimes \mathbf{e}_R + (rg') \mathbf{e}_{\theta} \otimes \mathbf{e}_R + (r/R) \mathbf{e}_{\theta} \otimes \mathbf{e}_{\Theta} + \lambda_z \mathbf{e}_z \otimes \mathbf{e}_Z$  where  $\mathbf{e}_r, \mathbf{e}_{\theta}, \mathbf{e}_z$  and  $\mathbf{e}_R, \mathbf{e}_{\Theta}, \mathbf{e}_Z$  are the cylindrical polar unit basis vectors in the deformed and reference configurations, and r' = dr/dR, g' = dg/dR. It then follows that

$$I_{1} = r'^{2} + (rg')^{2} + (\frac{r}{R})^{2} + \lambda_{z}^{2}, \quad I_{2} = (\frac{r'r}{R})^{2} + (r'\lambda_{z})^{2} + (\frac{r}{R}\lambda_{z})^{2} + (rg'\lambda_{z})^{2}, \quad J = \frac{r'r}{R}\lambda_{z}.$$
(5.6)

These expressions for  $I_1$ ,  $I_2$  and  $I_3$  match those given in (23) of [48] once allowance is made for the slightly different notations used here.

For the remainder of this section it is assumed, unless stated to the contrary, that the cylinder is saturated. It follows from (2.21) that the shear stresses  $\sigma_{rz}$  and  $\sigma_{\theta z}$  vanish. For constitutive functions given by (2.3) and (5.1) the other stresses are given by

$$\sigma_{rr} = \mu_{\alpha} \frac{Rr'}{\lambda_{z}r} \left[ 1 + \alpha \left( \frac{r}{R} \right)^{2} + \alpha \lambda_{z}^{2} \right] + M \left[ \frac{R\lambda_{z}}{rr'} + \chi \left( \frac{R\lambda_{z}}{rr'} \right)^{2} + \ln \left( 1 - \frac{R\lambda_{z}}{rr'} \right) \right], \tag{5.7}$$

$$\sigma_{\theta\theta} = \mu_{\alpha} \frac{R}{\lambda_{z} r r'} \left\{ \left( 1 + \alpha \lambda_{z}^{2} \right) \left[ \left( r g' \right)^{2} + \left( \frac{r}{R} \right)^{2} \right] + \alpha \left( \frac{r r'}{R} \right)^{2} \right\} + M \left[ \frac{R \lambda_{z}}{r r'} + \chi \left( \frac{R \lambda_{z}}{r r'} \right)^{2} + \ln \left( 1 - \frac{R \lambda_{z}}{r r'} \right) \right],$$

$$(5.8)$$

$$\sigma_{zz} = \mu_{\alpha} \frac{R\lambda_{z}}{rr'} \left[ 1 + \alpha r'^{2} + \alpha \left( rg' \right)^{2} + \alpha \left( \frac{r}{R} \right)^{2} \right] + M \left[ \frac{R\lambda_{z}}{rr'} + \chi \left( \frac{R\lambda_{z}}{rr'} \right)^{2} + \ln \left( 1 - \frac{R\lambda_{z}}{rr'} \right) \right],$$
(5.9)

$$\sigma_{r\theta} = \mu_{\alpha} \frac{Rg'}{\lambda_z} \left( 1 + \alpha \lambda_z^2 \right). \tag{5.10}$$

With the above stresses, the equilibrium equation  $(2.17)_2$  in the z direction is satisfied automatically, while the equilibrium equations in the r and  $\theta$  directions give

$$\frac{d}{dr} \left\{ \mu_{\alpha} \frac{Rr'}{\lambda_{z}r} \left[ 1 + \alpha \left( \frac{r}{R} \right)^{2} + \alpha \lambda_{z}^{2} \right] + M \left[ \frac{R\lambda_{z}}{rr'} + \chi \left( \frac{R\lambda_{z}}{rr'} \right)^{2} + \ln \left( 1 - \frac{R\lambda_{z}}{rr'} \right) \right] \right\} + \frac{\mu_{\alpha}R}{\lambda_{z}r^{2}r'} \left( 1 + \alpha \lambda_{z}^{2} \right) \left[ r'^{2} - \left( rg' \right)^{2} - \left( \frac{r}{R} \right)^{2} \right] = 0,$$
(5.11)

and

$$g'' = -\left(\frac{1}{R} + \frac{2r'}{r}\right)g', (5.12)$$

where  $g'' = d^2g/dR^2$ . It is to be remarked that one could obtain equations identical to (5.11) and (5.12) using the framework in [48]. Namely, substitution from (25) -

(29) of [48] into (30) and (31) of [48] can be shown to result in (5.11) and (5.12) as given above once allowance is made for the different notation.

We comment that, in contrast to [48], the methodology used here does not invoke the mixture theory framework which, among other things, introduces separate mass densities for the intermingled fluid and solid components as well as an interactive body force when there is relative motion between these components. We do not require use of this more general framework because the equilibrium problems under consideration here always involve a stationary fluid component so that there is no relative motion between the liquid and polymer components within the gel. If we further consider time varying boundary conditions in this context, then the solutions that we obtain describe a family of equilibrium solutions. In this case the fluid redistributes itself in a quasi-static manner. This is the sense in which the term redistribution is used in [48] and is also the sense in which the term is used here. As discussed recently by Baek and Srinivasa in [71], the slow diffusion of a fluid through a swelling (and saturated) solid is also amenable to such a treatment. In fact a specific form of the governing equation is given in (42) of [71] as

$$\operatorname{div}\left(\frac{\partial \tilde{\psi}}{\partial \mathbf{F}} \mathbf{F}^T + \tilde{\psi} \mathbf{I}\right) = \mathbf{0},\tag{5.13}$$

where  $ilde{\psi}$  is the specific Helmholtz free energy and is akin to

$$E = W + \mu_{lig}(J - 1) + \mu_{poly} \tag{5.14}$$

in the present treatment. Here W is again given by (2.11) and  $\mu_{liq}$  and  $\mu_{poly}$  are positive materials constants that correspond to the chemical potential of fluid and polymer components, respectively. However the free energy  $\tilde{\psi}$  in [71] is defined per

unit current volume so that the connection to our E is that

$$\tilde{\psi} = I\!\!E/J \tag{5.15}$$

whereupon

$$\frac{\partial \tilde{\psi}}{\partial \mathbf{F}} = \frac{1}{J} \frac{\partial \mathbf{E}}{\partial \mathbf{F}} - \frac{1}{J} \mathbf{E} \mathbf{F}^{-T}$$

by virtue of  $\partial J/\partial \mathbf{F} = J\mathbf{F}^{-T}$ . Hence it follows that

$$\frac{\partial \tilde{\psi}}{\partial \mathbf{F}} \mathbf{F}^T + \tilde{\psi} \mathbf{I} = \frac{1}{J} \frac{\partial \mathbf{E}}{\partial \mathbf{F}} \mathbf{F}^T = \boldsymbol{\sigma} + \mu_{liq} \mathbf{I}$$

whereupon (5.13) is identical with  $(2.17)_2$  since  $\mu_{liq}$  is constant.

### 5.2 Twist at Constant Overall Volume

We first consider the type of boundary value problem studied by Wineman and Rajagopal in [48], which is stated as follows: the hollow tube after free swelling is held fixed at its inner radius, i.e.  $r(R_i) = \zeta R_i$  and  $g(R_i) = 0$ , while the outer radius is then rotated through a twist angle  $\psi = g(R_o)$  while maintaining the same radius  $r(R_o) = \zeta R_o$ . The governing equations are given by (5.11) and (5.12). Note that the latter of these is, in its original stress formulation,

$$\frac{d\sigma_{r\theta}}{dr} + \frac{2\sigma_{r\theta}}{r} = 0, (5.16)$$

which in turn can be immediately integrated to

$$\sigma_{r\theta} = \frac{T}{2\pi r^2},\tag{5.17}$$

where T is the constant of integration. Since  $2\pi R_i^2 \sigma_{r\theta}|_{R_i} = 2\pi R_o^2 \sigma_{r\theta}|_{R_o} = T$  it follows that T is the associated twisting moment, or torque, on the lateral surfaces. A useful nondimensionalized torque  $T^*$  is defined by the relation

$$T^* = \frac{T}{2\pi\mu_{\Omega}\lambda_z^2 R_i^2}. (5.18)$$

The boundary conditions are now taken to match those in equations (34) and (35) of [48] meaning: (A) there is no additional radial displacement of the lateral surfaces, i. e.

$$r(R_i) = \zeta R_i, \qquad r(R_o) = \zeta R_o; \tag{5.19}$$

(B) that the inner surface is rigidly clamped, i. e.  $g(R_i) = 0$ ; and (C) that the outer surface is twisted by an an amount  $\psi$ , i.e.  $g(R_o) = \psi$ . In fact, as regards the boundary conditions on g(R), it is only the relative twist that matters, i.e.

$$g(R_o) - g(R_i) = \psi, \tag{5.20}$$

since the addition of an arbitrary constant to the function g(R) merely represents a rigid body rotation about the z-axis. An alternative to specifying  $\psi$  is to specify the twisting moment T. In either case, the torque-twist relation  $(T \text{ vs. } \psi)$  is then a characteristic feature of the macroscopic response.

Finally, in keeping with [48], we specify that the height of the cylinder is kept fixed at the free swelling value  $\hat{l} = \zeta L$ . Thus the axial stretch  $\lambda_z$  is the same as the free swelling stretch  $\zeta$  so that  $\hat{\lambda}_z = 1$  in (5.4). This will in general require a resultant axial force at the caps z = 0 and  $z = \hat{l}$  given by

$$P = 2\pi \int_{r_i}^{r_o} \sigma_{zz}(r) r dr. \tag{5.21}$$

It is to be remarked that an alternative problem is to find  $\hat{\lambda}_z$ , the value of the mechanical stretch ratio, so as to give a zero resultant force at the two caps. We, however, do not consider this possibility here.

With the inner and outer radius fixed at their free swelling values and the height of the cylinder unchanged, the overall volume of the gel remains the same as that of the free swelling state. This therefore results in no net intake or exit of fluid. Rajagopal and Wineman observe this in their remarks regarding impermeable barriers at  $r_i$  and  $r_o$  before equation (18) of [48].

With the material parameters (5.3), in a cylinder with  $R_0 = 2R_i$ , we used a shooting method to obtain r(R) and g(R) obeying field equations (5.11) and (5.12) and boundary conditions (5.19) and (5.20). The numerical results for the fluid redistribution, interpreted in terms of the gel's local volume change J-1, were found to exactly match those given by Wineman and Rajagopal in [48]. Among the main features obtained by Rajagopal and Wineman [48], and confirmed here, are those shown in Figure 5.2 where we have introduced the dimensionless radial position  $\bar{R} = R/R_i$ . Figure 5.2a and Figure 5.2c show the radial variation of  $J/J_{fs}$  for  $\alpha = 0$  and  $\alpha = 1$ respectively. This ratio decreases near the inner radius and increases near the outer radius, which means that fluid redistributes itself from the inner region to the outer region of the cylinder. The rotation of the cylinder is shown in Figure 5.2b and Figure 5.2d taking  $g(R_i) = 0$ . The angle of rotation increases rapidly near the inner radius and gradually near the outer radius. The other figures in [48] can be similarly reproduced including Figure 3 and Figure 7 of [48] which give the ratio of the current liquid density in the gel to the free swelling liquid density. This ratio is denoted by  $\rho^f/\rho_{sat}^f$  in [48], and the formal connection to our notation follows with the aid of equation (24) in [48] as

$$\underbrace{\rho^f/\rho_{sat}^f}_{\text{(density ratio from [48])}} = (1 - J^{-1})/(1 - J_{fs}^{-1}).$$
(5.22)

The normal stress distribution  $\sigma_{rr}(r)$  is not displayed in [48] and so, in particular, the boundary tractions  $\sigma_{rr}(r_i)$  and  $\sigma_{rr}(r_o)$  needed to sustain this deformation were not given there. In Figure 5.3 we show the  $\sigma_{rr}$  stress distribution. For a non-zero twist angle  $\psi$  we find that  $\sigma_{rr}$  is monotonically increasing such that  $\sigma_{rr}(r_i) < 0$  and  $\sigma_{rr}(r_o) > 0$ . Thus the trend in  $\sigma_{rr}$  is similar to the trend in  $\sigma_{rr}(r_i)$  are shown in Figure 5.4.

### 5.3 Twist Induced Fluid Desorption

It follows from Figure 5.3 that if  $r_i$  is held fixed and a twist angle  $\psi$  is imposed at  $r = r_0$  then, for  $r_0$  to be kept at its free swelling value, it is necessary to supply a tensile normal stress  $\sigma_{rr}$  at  $r = r_0$ . If such a normal traction is not present, then one would anticipate a lesser value of  $r_0$  on the basis of a tensile traction having been released. This motivates the consideration of a modified boundary value problem in which the inner radius is fixed and twist is again applied at the outer radius, but the outer radius is now taken to be free of normal traction. Thus boundary conditions (5.19) are replaced by

$$r(R_i) = \zeta R_i, \qquad \sigma_{rr}(r_o) = 0. \tag{5.23}$$

Quantities associated with the solution of this problem are shown in Figure 5.3 where (a)-(h) graph the same quantities that were previously shown in Figures 1-8 of [48] respectively so as to show the effect of the outer surface being free of normal traction. In particular (b) and (f) of Figure 5.3 confirm that  $r(R_o) < \zeta R_o$  indicating that the overall volume has indeed decreased from its free swelling value. It is to be remarked

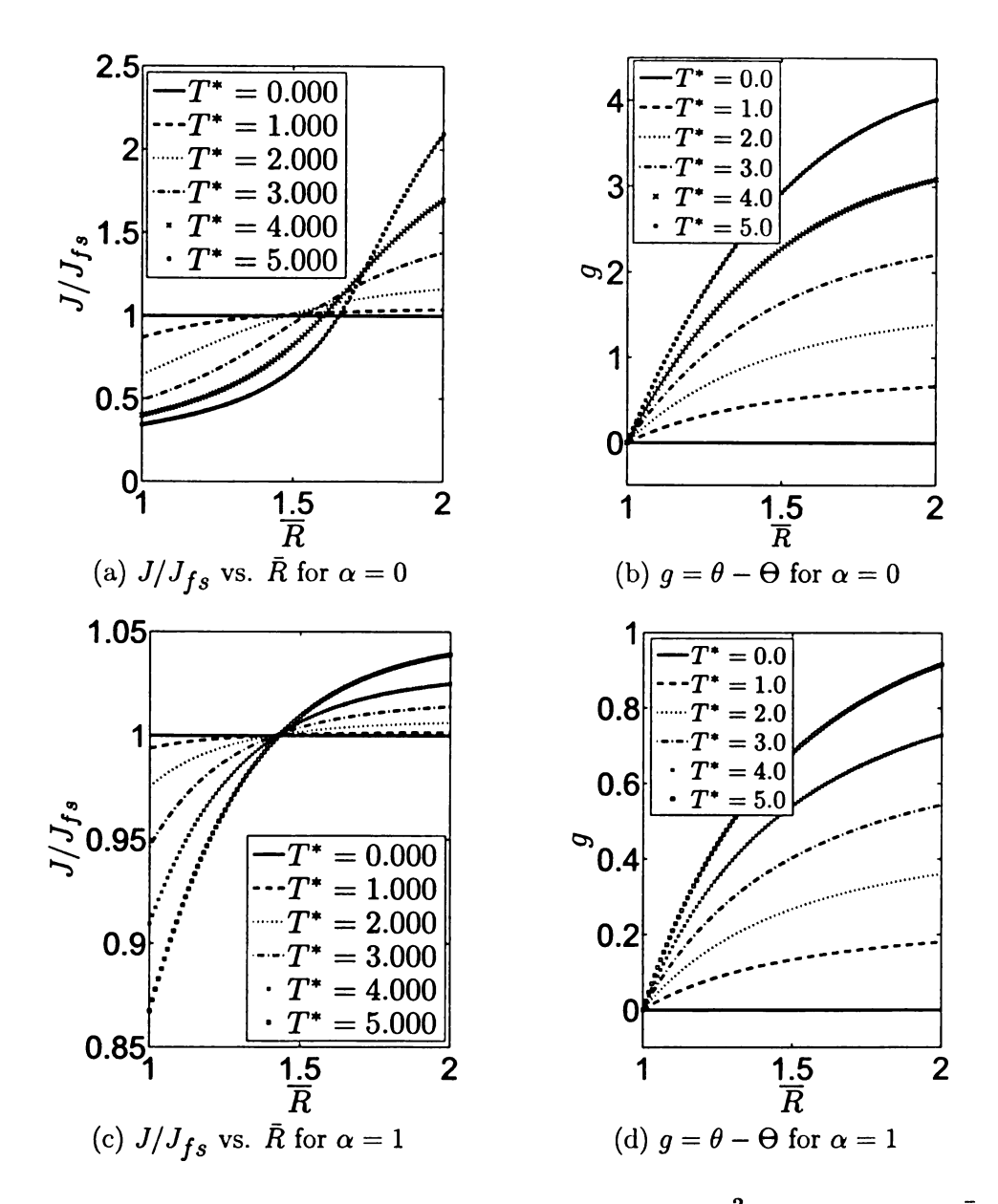


Figure 5.2: J normalized by the free swelling value  $J_{fs} = \zeta^3$  as a function of  $\bar{R} = R/R_i$  (panels (a) and (c)); and the twist  $g = \theta - \Theta$  as a function of  $\bar{R}$  (panels (b) and (d)), for boundary conditions given by (5.19) and (5.20) with  $R_o/R_i = 2$ . The problem is equivalent to that presented in [48] and panels (a), (b), (c) correspond respectively to Figures 1, 4, 5 in [48].

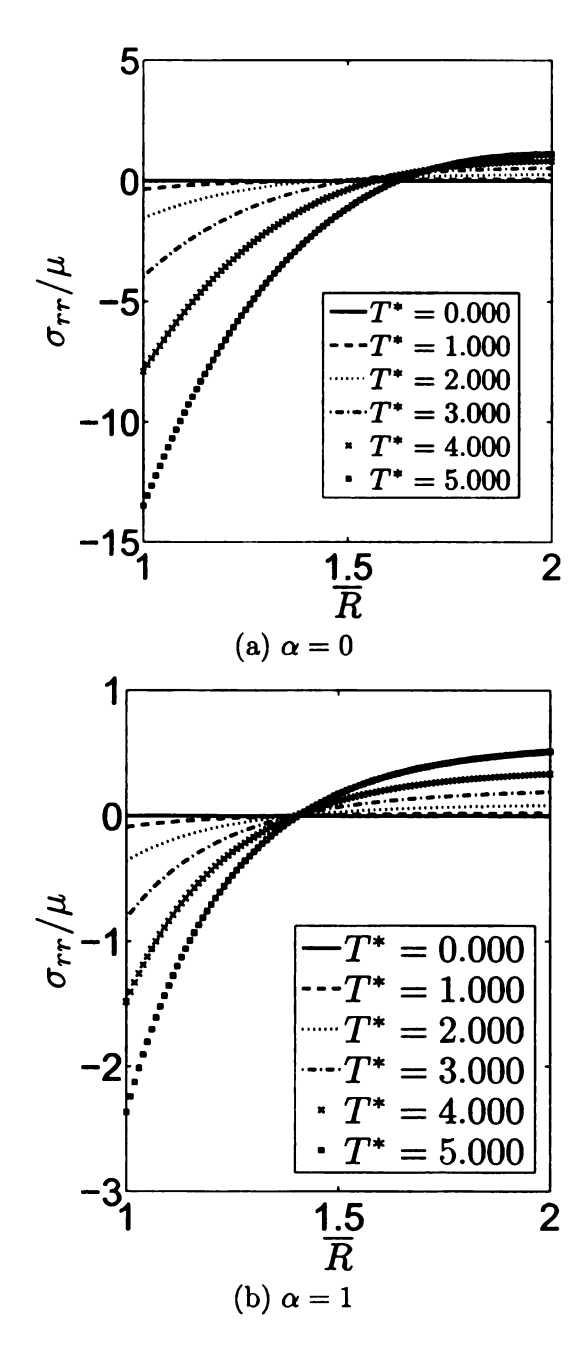
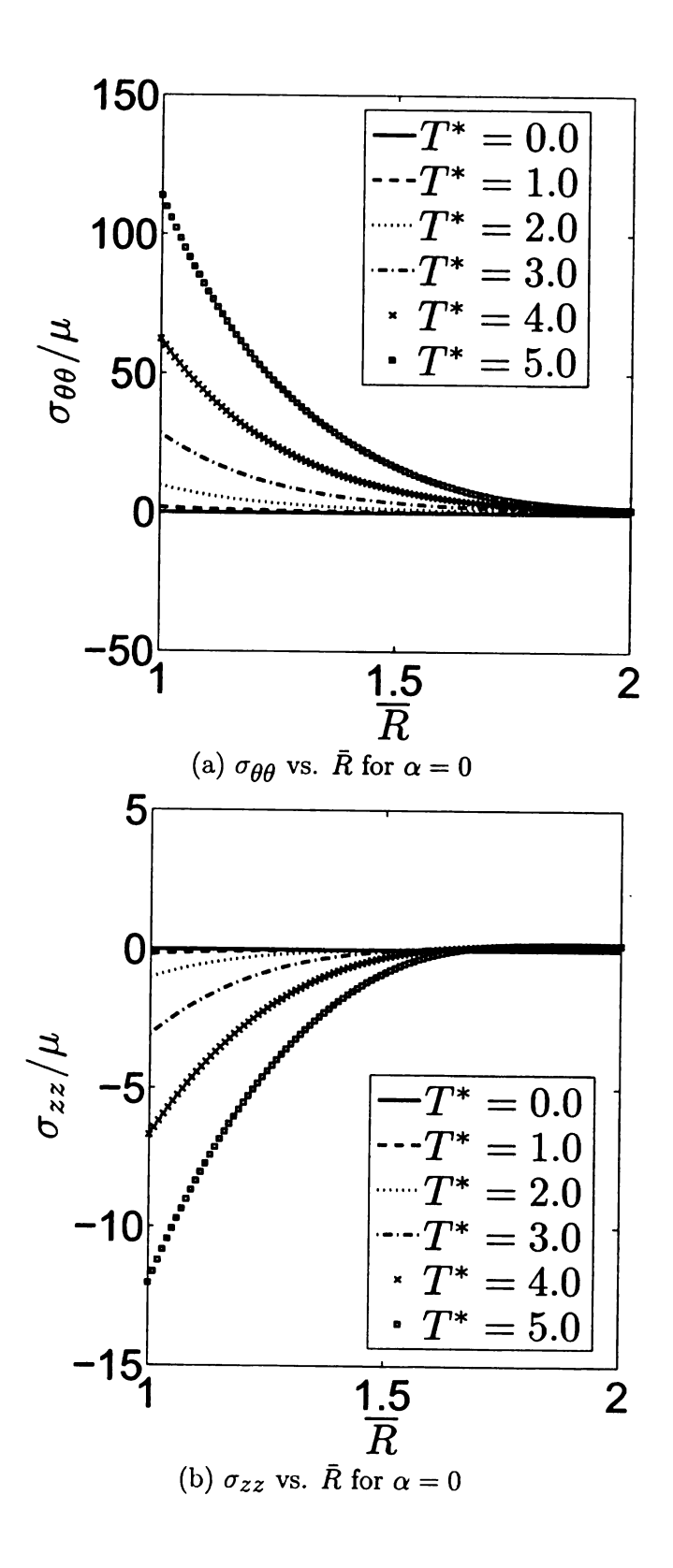


Figure 5.3: Normal stress  $\sigma_{rr}$  for the same problem as described in Figure 5.2.



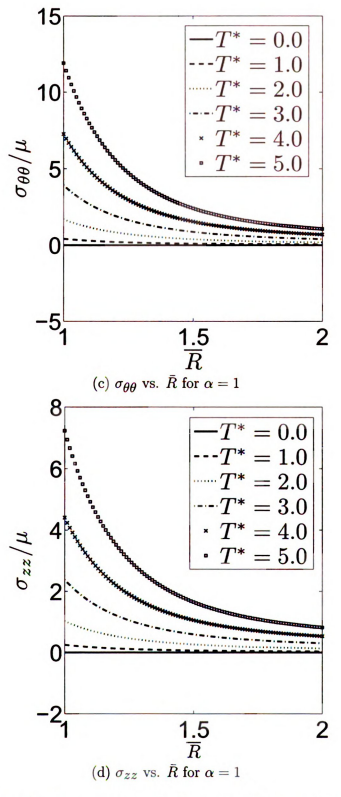


Figure 5.4: Normal stresses  $\sigma_{\theta\theta}$  and  $\sigma_{zz}$  for the same problem as described in Figure 5.2.

that an overall volume decrease was also found to be the case in the torsion problems discussed in [49] and [45].

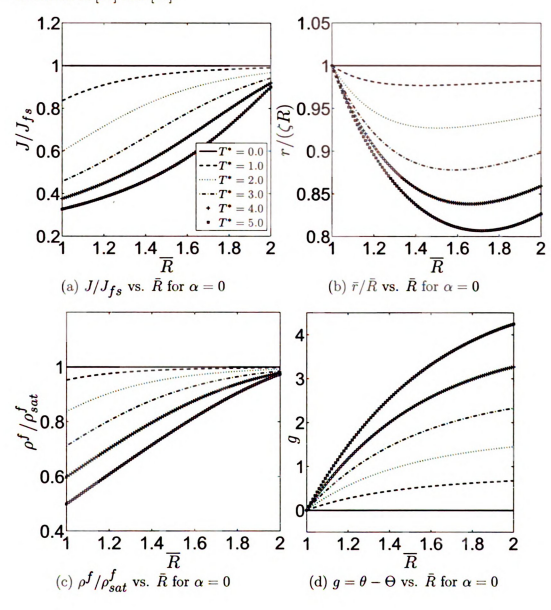


Figure 5.6(a) and Figure 5.6(c) show the decrease in  $V/V_{fs}$  as  $\psi$  increases for the two cases  $\alpha=0$  and  $\alpha=1$ . The dashed horizontal line in these figures corresponds to the volume of the unswellen polymer. It is to be noted that this horizontal line is consistent with it being the asymptotic limit of the upper curve in the event that all of the fluid is expelled as  $\psi\to\infty$ . Figure 5.6(b) and 5.6(d) give the corresponding

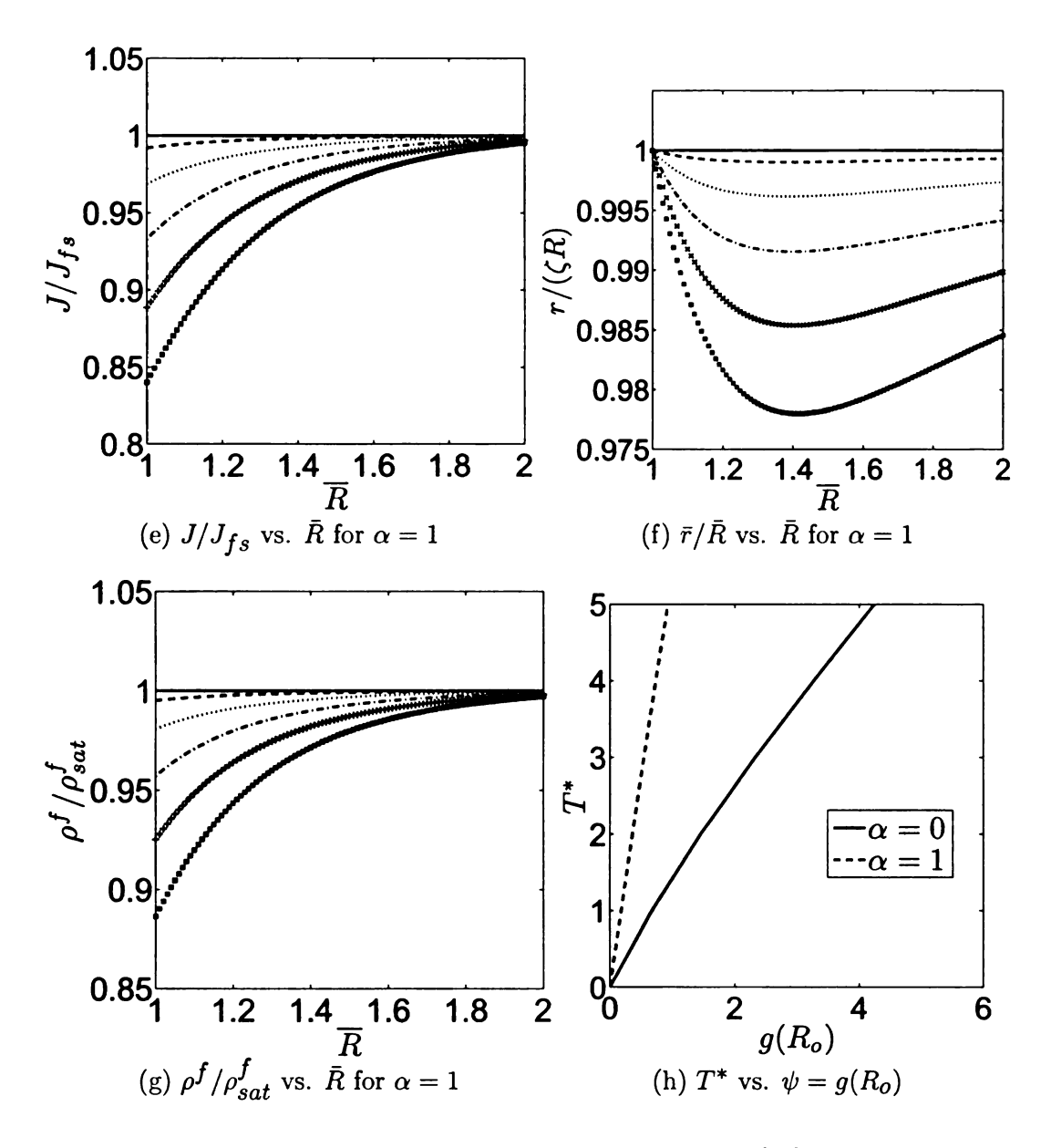


Figure 5.5: Panels (a) - (h) correspond to figures 1 - 8 of [48] provided that the boundary condition  $r_o = \zeta R_o$  is replaced by the boundary condition  $\sigma_{rr}(r_o) = 0$ . This is the problem considered in Section 5.3. Here the effect of increasing the nondimensionalized moment  $T^*$  is to drive out the previously imbibed fluid. The ratio  $\rho/\rho_{sat}^f$  is a formal calculation based on (5.22).

### 5.4 Twist Induced Fluid Absorption

We now consider what can be viewed as the converse to the problem considered in the previous section. That is  $r_0$  is now held at the free swelling value and the twist applied at  $r = r_i$  such that the *inner* surface is free of normal traction. Thus boundary conditions (5.19) are to be replaced by

$$\sigma_{rr}(r_i) = 0, \quad r(R_o) = \zeta R_o. \tag{5.24}$$

Results associated with the solution to this problem are shown in Figure 5.4. In particular, panels (a) - (g) of Figure 5.4 show the effect of the modified boundary conditions (5.24) as they compare both to the case with boundary conditions (5.19) as shown in Figures 1-7 of [48], and to the case with boundary conditions (5.23) as shown in panels (a)-(g) of Figure 5.3.

Under boundary conditions (5.24) one finds that increasing  $\psi$  tends to cause additional fluid uptake as shown by the decrease in  $r_i = r(R_i)$  in Panels (b) and (f) of Figure 5.4. As in the previous cases, twist also causes fluid to redistribute from the inner to the outer portion of the tube. The reader may have observed that we do not yet give the torque vs. twist relation, i.e. the equivalent of Figure 8 of [48], and hence the equivalent of panel (h) of Figure 5.3. A detailed discussion of the torque vs. twist relation will be given shortly.

Figure 5.8(a) and 5.8(c) show the increase in  $V/V_{fs}$  as  $\psi$  increases. Also Figures 5.8(b) and 5.8(d) give the  $\sigma_{rr}$  stress distribution. It is to be noted that  $\sigma_{rr}$  is no longer monotonic in R for sufficiently large  $T^*$ . In Figure 5.4 and Figure 5.8, for the case  $\alpha=1$ , we use the same values  $T^*=1,2,3,4$  as in Figure 5.3, but we do not use  $T^*=5$ . For  $\alpha=0$  we must employ the very much lower values  $T^*=0.2,0.4,0.6,0.8$ .

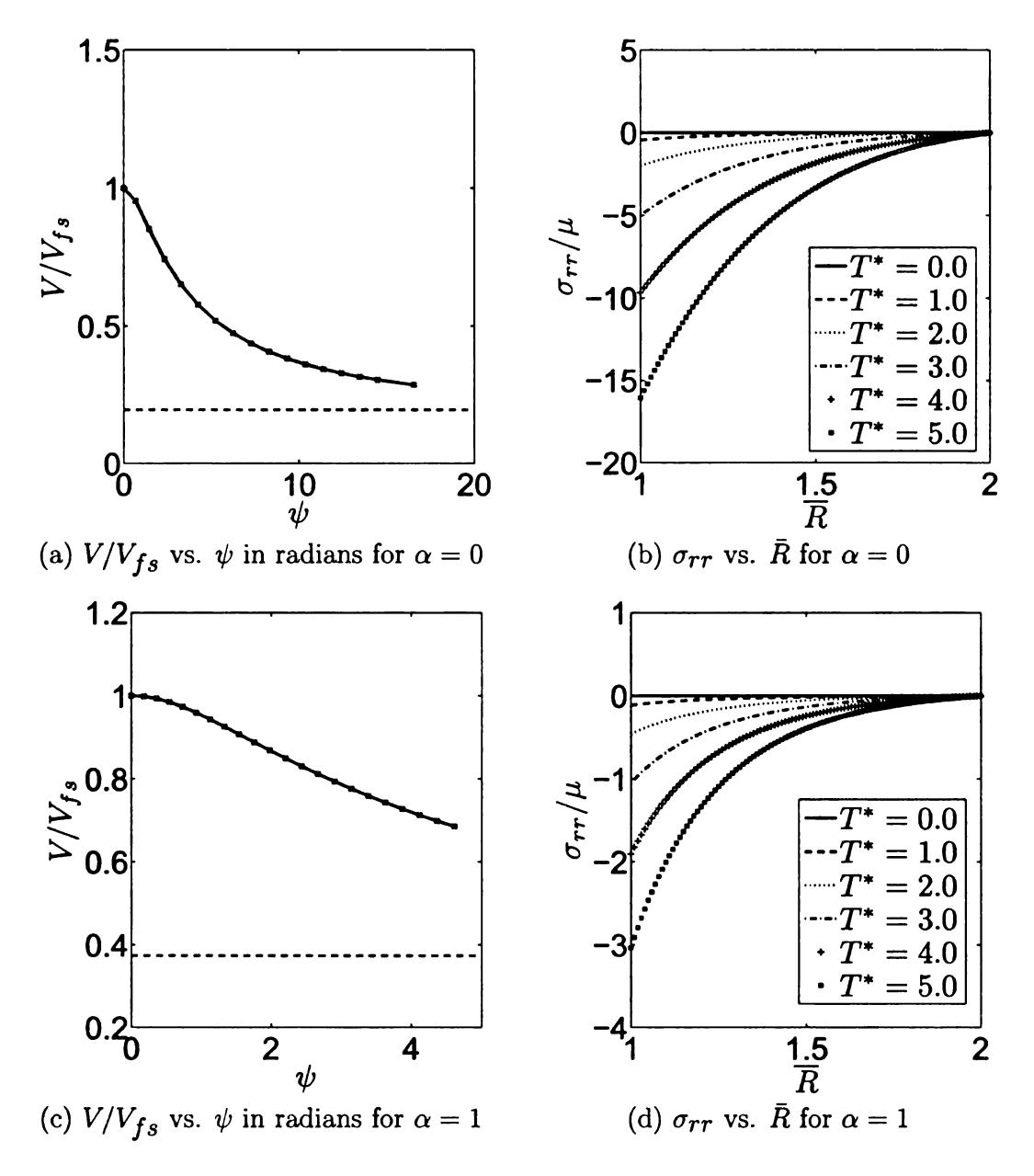
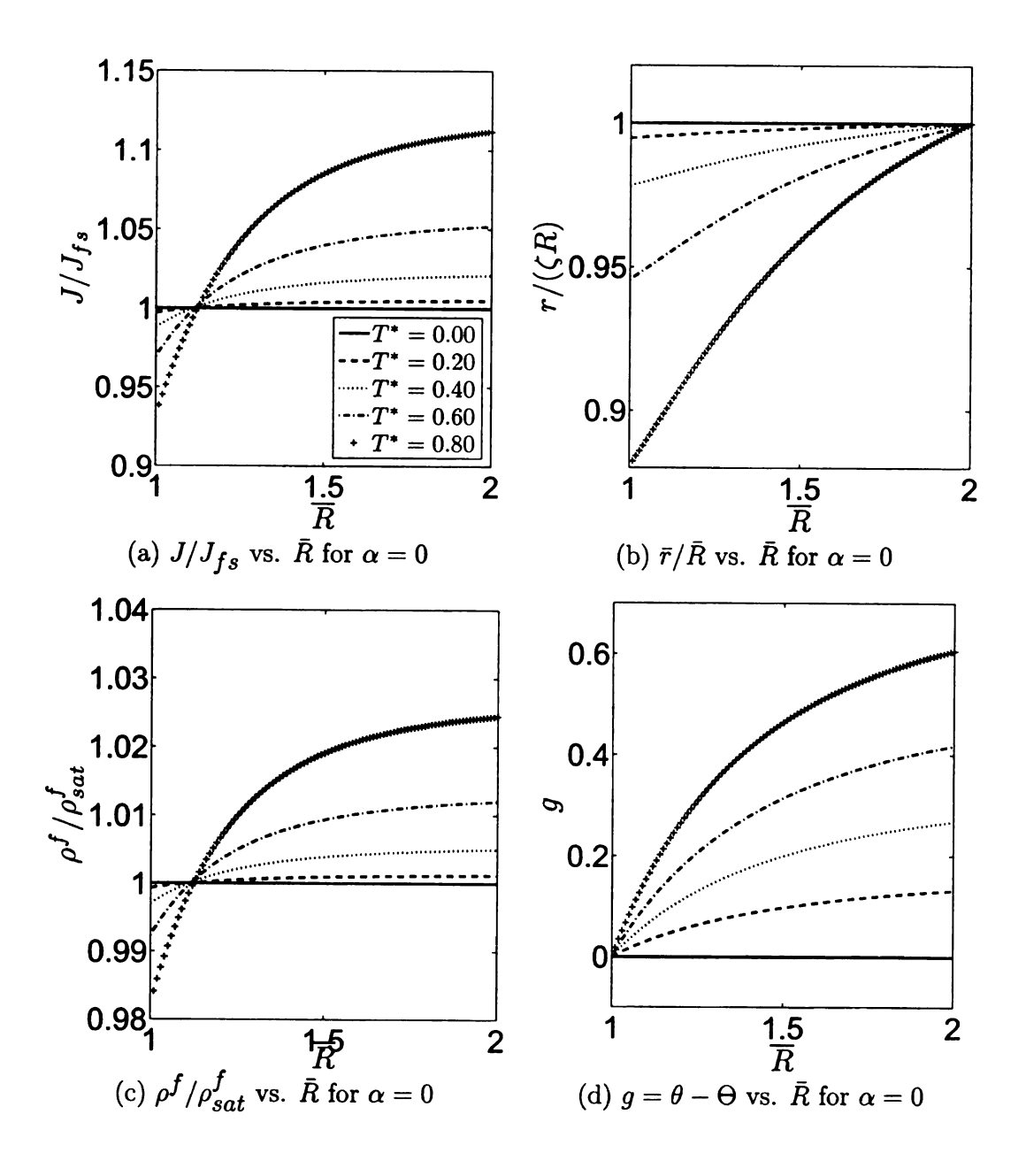


Figure 5.6: Additional graphs for the boundary value problem described in Figure 5.3. The dashed lines in panels (a) and (c) give the baseline associated with a pure polymer (no liquid) by showing the volume ratio  $V_{poly}/V_{fs} = J_{fs}^{-1}$ .



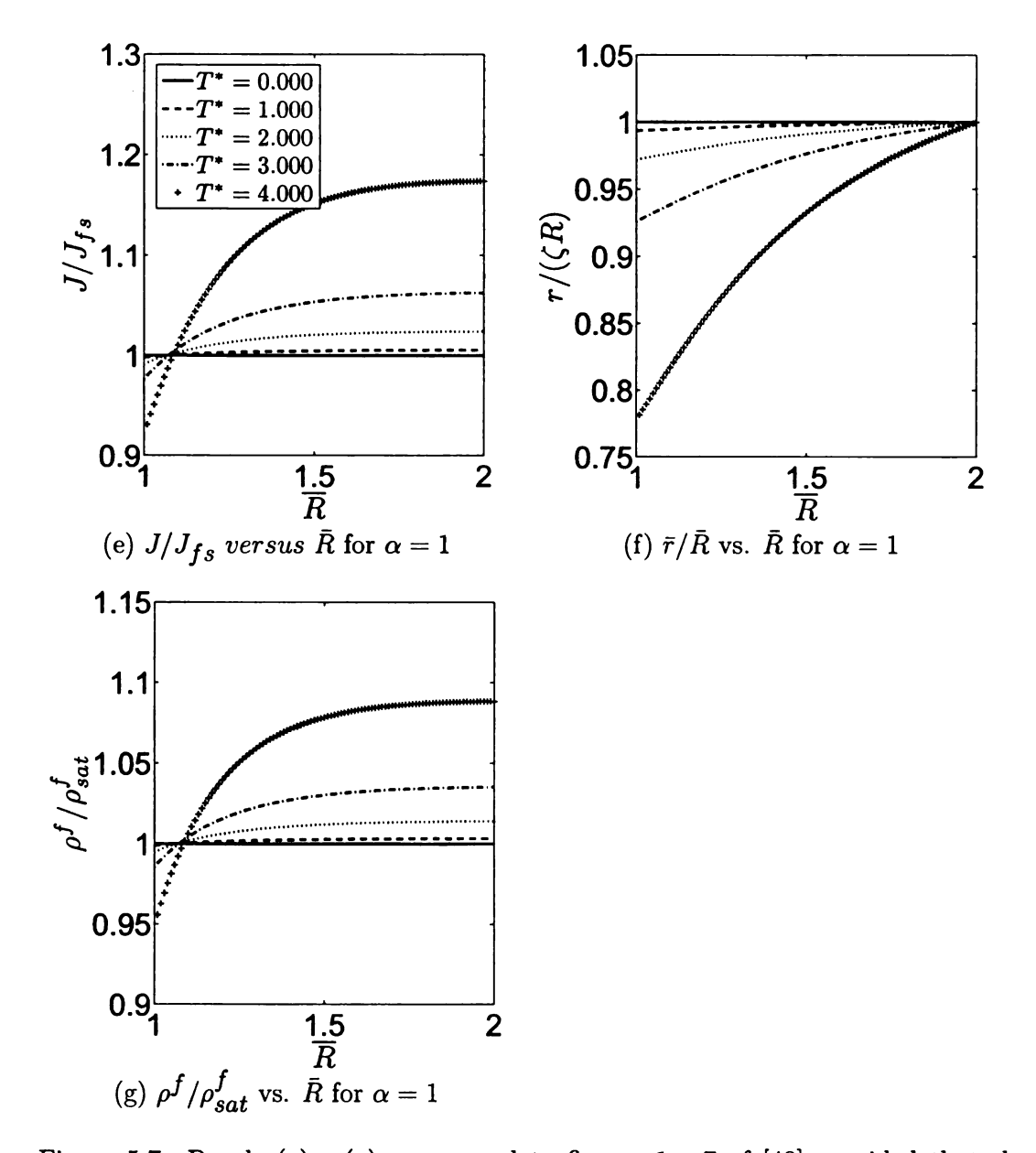


Figure 5.7: Panels (a) - (g) correspond to figures 1 - 7 of [48] provided that the boundary condition  $r_i = \zeta R_i$  is replaced by the boundary condition  $\sigma_{rr}(r_i) = 0$ . This is the problem considered in Section 5.4. The effect of increasing  $T^*$  is now to cause more liquid to enter into the system. The ratio  $\rho^f/\rho_{sat}^f$  is a formal calculation based on (5.22).

The reason for this will be discussed shortly. In addition, since fluid must pass from the exterior liquid into the gel mixture, there is the possibility that the mixture could become nonsaturated if there is insufficient fluid in the bath to provide for the swelling volume increase.

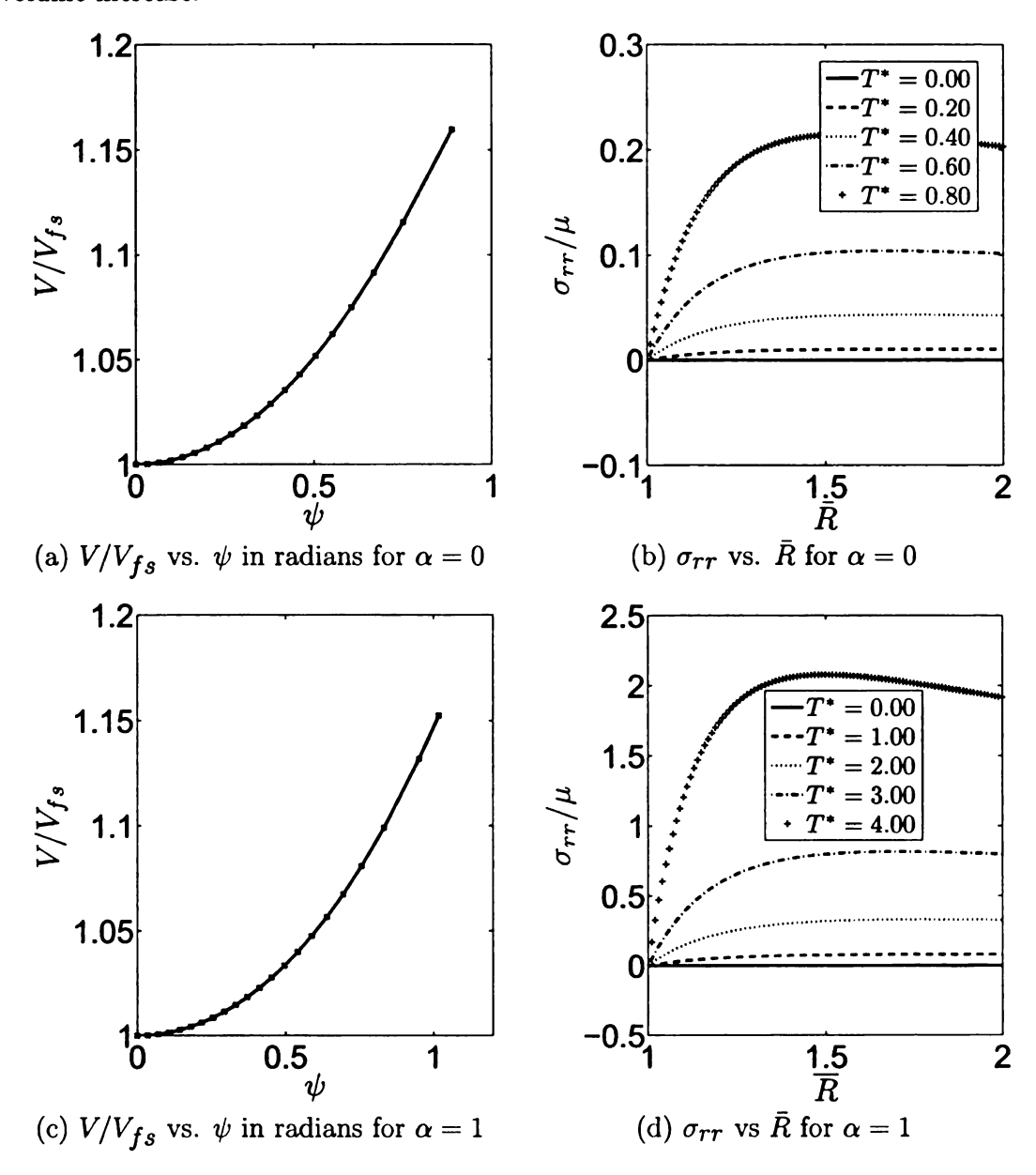


Figure 5.8: Additional graphs for the boundary value problem described in Figure 5.4.

#### 5.4.1 A Prescribed Inward Displacement of the Inner Radius

Before considering the possibility of a loss of saturation, we return to the issue of why the maximum value of  $T^*$  considered in Figure 5.8(b) is  $T^* = 0.8$  for  $\alpha = 0$  and, similarly, why the maximum value of  $T^*$  in Figure 5.8(d) is  $T^* = 4.0$  for  $\alpha = 1$ . Let us first consider the case  $\alpha = 0$ . In this case our numerical method is unable to obtain solutions if the twisting moment  $T^*$  is too large. To explore this phenomenon consider yet another boundary value problem where the boundary condition  $\sigma_{rr}(r_i) = 0$  is replaced by a condition of prescribed displacement at the inner radius. Thus boundary condition (5.19) is now replaced by

$$r(R_i) = \delta \zeta R_i, \quad r(R_0) = \zeta R_0, \tag{5.25}$$

where  $\delta = r_i/(\zeta R_i)$  is prescribed. Thus boundary condition (5.19) is the special case for which  $\delta = 1$ . Our interest is in the case  $0 < \delta < 1$  so that the inner radius displaces inward meaning that fluid is drawn into the cylinder.

It is also convenient to specify the torque  $T^*$  in place of the twisting angle  $\psi$ . Figure 5.9(a) shows graphs of  $\sigma_{rr}(r_i)$  vs.  $\delta$  at various fixed values of torque  $T^*$ . For  $\delta=1$  we recover the result that  $T^*\neq 0$  implies  $\sigma_{rr}(r_i)<0$ . It is found that the value of  $\sigma_{rr}$  at the inner radius is increasing as  $\delta$  decreases from  $\delta=1$ . A solution for the problem characterized by the previous boundary condition (5.24) corresponds to the locations where the curve in Figure 5.9(a) crosses the line  $\sigma_{rr}(r_i)=0$ . We find that such a crossing takes place only if  $T^*$  is sufficiently small, namely if  $T^*<0.937$ . However it is found that if  $T^*>0.937$  then such a crossing does not occur because the curve of  $\sigma_{rr}(r_i)$  vs.  $\delta$  is first increasing and then decreasing (as  $\delta$  decreases from one) in a way that keeps the maximum value of  $\sigma_{rr}(r_i)<0$ . This is shown in Figure 5.9(a) where the  $T^*=1$  curve remains below the  $\sigma_{rr}(r_i)=0$  axis. Thus  $T^*=0.937$  is a critical value of twisting moment beyond which we do not satisfy the condition

 $\sigma_{rr}(r_i)=0$  for any  $\delta$  and hence do not obtain solutions for the previous boundary conditions (5.24). Note from Figure 5.9(c) that if  $T^*=0.937$  then the graph of  $\sigma_{rr}(r_i)$  vs.  $\delta$  will have a single tangential intersection with the line  $\sigma_{rr}(r_i)=0$ . Furthermore the graphs in Figure 5.9(c) show that if  $T^*$  is slightly less than the critical value 0.937 then the curves in Figure 5.9 intersect the  $\sigma_{rr}(r_i)=0$  axis in two locations, indicating the existence of two solutions to the problem with the previous boundary condition (5.24). Here we remark that the graphs displayed in Figure 5.4 for  $T^*=0.2, 0.4, 0.6, 0.8$  are associated with the intersection that is closest to  $\delta=1$ . For example, the  $T^*=0.8$  graphs in Figure 5.4 (a) - (d) are associated with point A on Fig 5.9(c). We shall refer to these as standard solutions for boundary conditions (5.24).

A similar situation obtains when  $\alpha > 0$  in that there is still a critical value of the twisting moment at which the graph of  $\sigma_{rr}(r_i)$  vs.  $\delta$  has a single tangential intersection the horizontal line  $\sigma_{rr}(r_i) = 0$ . The critical twisting moment  $T^*$  varies with  $\alpha$ . For  $\alpha = 1$  the critical twisting moment is  $T^* = 4.041$ , which is why we cannot take  $T^* = 5$  in Figure 5.4 when  $\alpha = 1$ .

# 5.4.2 Further Consideration of the Problem with Boundary Condition (5.24)

It follows that, in general, solutions to the problem with boundary conditions (5.24) do not exist if  $T^*$  exceeds its critical value. Conversely, if  $T^*$  is less than its critical value, then more than one solution may exist for the given  $T^*$ . In addition, for any solution to the problem with boundary conditions (5.24), one may calculate  $\delta = r_i/(\zeta R_i)$  and so identify the solution with a solution that employs boundary conditions (5.25). In this way we have identified the standard solutions discussed in Section 3.3.1 with special values of  $\delta$ . Namely, these are the values of  $\delta$  for which the intersection of the line  $\sigma_{rr}(r_i) = 0$  with a graph from Figure 5.9 occurs closer to

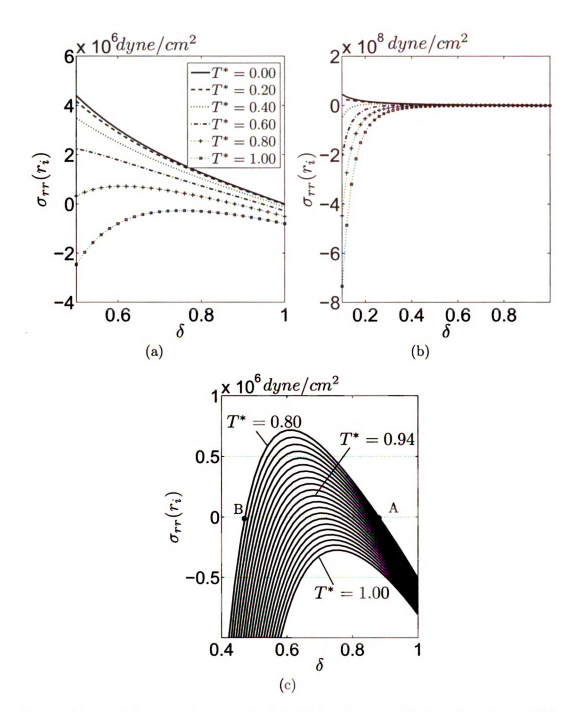


Figure 5.9:  $\sigma_{TT}(r_i)$  versus  $\delta$  for  $\alpha=0$ . Panel (a) is the magnified portion of panel (b) near  $\delta=1$ . Panel (c) provides additional curves near  $\delta=1$  with the top curve for  $T^*=0.8$ ; bottom curve for  $T^*=1.0$ , and with additional curves for  $T^*$  increments of 0.01 in between.

 $\delta = 1$  than any other intersection.

We now turn our attention to the other values of  $\delta$  at which  $\sigma_{rr}(r_i) = 0$  when there are multiple such intersections. For example, location B in panel (c) of Figure 5.9 corresponds to this solution for the case  $T^* = 0.8$  when  $\alpha = 0$ . This also provides a solution to the boundary value problem with boundary conditions (5.24) and corresponds to a smaller value of  $\delta$  and a larger value of  $\psi$  then that of the standard solution. We shall call these post-maximum solutions for reasons that will soon be apparent. These post-maximum solutions are increasingly difficult to calculate numerically as we encounter certain numerical instabilities as  $\delta$  gets small.

For  $\alpha=0$  it is found that the post-maximum solutions can be calculated relatively easily for  $\delta>0.3$ . However for  $\delta<0.3$  they are highly sensitive to the initial guess used in the iteration procedure. Furthermore for  $\delta$  less than about 0.15 we cannot easily find an initial guess providing a converging solution. Indeed the minimum value of  $\delta$  for which we can find a converging solution is also dependent on the value of  $T^*$ . The curve of  $T^*$  vs.  $\psi$  is shown in Figure 5.10(a). The absence of solutions for  $T^*$  greater than the critical value causes the graph of  $T^*$  vs.  $\psi$  to exhibit a local maximum at the critical value of  $T^*$ . The end of the curve in Figure 5.10(a) at  $\psi=1.7$  represents the limit of computable solutions by our numerical method. The ratio  $V/V_{fs}$  is displayed in Figure 5.10(b) with the same range of  $\psi$  as in Figure 5.10(a).

A similar maximum twisting moment condition has been implicated in boundary value problems in nonlinear elasticity for azimuthal shearing deformations of a form similar to (5.5), but without a notion of swelling, when subject to boundary conditions of fixed radial displacement in place of the boundary conditions considered here. In [81] a phase plane analysis of the governing ordinary differential equations for such a boundary value problem, using a compressible hyperelastic Blatz-Ko material model, is found to generate a limiting moment condition for the construction of certain

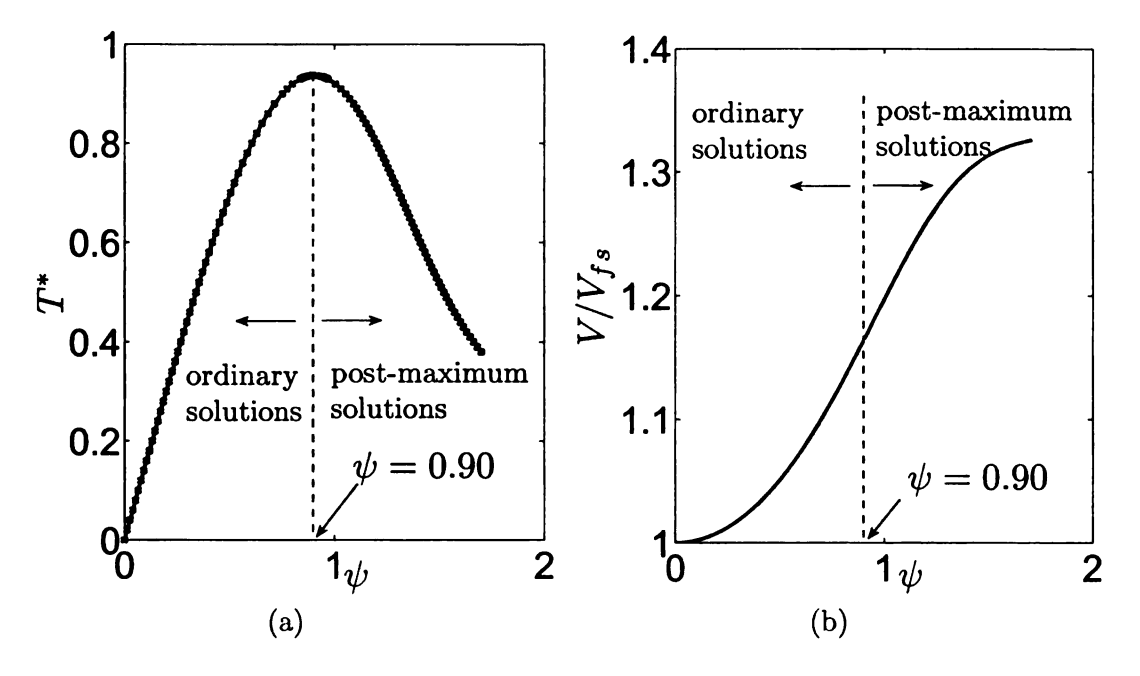


Figure 5.10: (a) Torque vs. twist relation with  $\alpha=0$  for the boundary conditions (5.24). Here  $T^*=0.937$ ,  $\psi=0.90$  corresponds to the local maximum. Also  $T^*=0.377$ ,  $\psi=1.70$  is the effective limit of our numerical calculation and corresponds to  $\delta=0.15$ . (b) Volume ratio  $V/V_{fs}$  versus twist angle  $\psi$  for the same problem.

smooth deformation solutions. In [82] the numerical treatment of such a boundary value problem for a broader class of Blatz-Ko models gives rise to numerical difficulties if the applied twisting moment becomes too large, which is also suggestive of an underlying maximum moment condition.

Figure 5.11 shows the numerical results corresponding to these post-maximum solutions. The behavior of the curves in Figure 5.11 is similar to those shown in panels (a)-(d) of Figure 5.4. Thus, at least with respect to these graphs, the post-maximum solutions are not strongly distinguished from the standard solutions. Fluid redistributes from the inner portion of the tube to the outer portion of the tube as  $T^*$  decreases. This, however, still corresponds to increasing  $\psi$ . In view of the decreasing graph of torque vs. twist for the post-maximum solutions, one would also expect basic

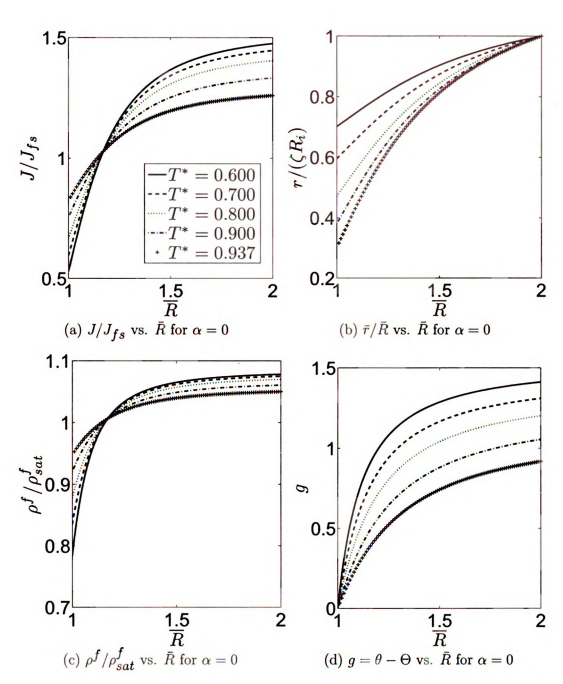


Figure 5.11: The post-maximum solutions for  $\alpha=0$ . These correspond to a continuation of panels (a) - (d) of Figure 5.4. Now  $T^*$  decreases with increasing  $\psi$  as is evident from panel (d).

differences with respect to any consideration of energetic stability (viz., eg., [83]).

### 5.5 Fluid Uptake Leading to Loss of Saturation

In the boundary value problem with condition (5.24) we have found that the overall volume increases with increasing  $\psi$ . All such volume increase is associated with uptake of liquid, and it has so far been assumed that there is always enough liquid available to support this volume increase. In other words, the analysis of Section 3.3 is predicated on the assumption that there is sufficient liquid to keep the system in a saturated state. We now consider the situation in which the amount of liquid is limited, and in particular assume that all the liquid is imbibed at some point in the loading process. The instant at which this occurs corresponds to a transition from a saturated state to a nonsaturated state. Under further increase in  $\psi$  the system remains nonsaturated and the overall cylinder volume remains fixed at the value  $V = V_{poly} + V_{liq}$ .

Since  $V=\pi\zeta L(r_o^2-r_i^2)$  and  $V_{poly}=\pi L(R_o^2-R_i^2)$ , the constraint (2.20) can be written

$$\pi \zeta L(r_o^2 - r_i^2) = \pi L(R_o^2 - R_i^2) + V_{liq}.$$
 (5.26)

In addition, (5.24) gives  $r_o = \zeta R_o$  whereupon it follows that the constraint is equivalent to a requirement that

$$r_{i} = \sqrt{\zeta^{2} R_{o}^{2} - \frac{1}{\zeta} (R_{o}^{2} - R_{i}^{2}) - \frac{V_{liq}}{\pi \zeta L}} \equiv r_{i}^{(nonsat)}.$$
 (5.27)

There will then also be a loss-of-saturation value of twist  $\psi^{(LoS)}$  and a loss-of-saturation value of moment  $T^{*(LoS)}$ .

In view of the additional specification of  $r_i$  in (5.27) the boundary conditions

(5.24) are, after loss of saturation, replaced by

$$\sigma_{rr}(r_i) = 0, \quad r(R_i) = r_i^{(nonsat)}, \quad r(R_o) = \zeta R_o.$$
 (5.28)

In contrast to the boundary conditions for the saturated cylinder, in which (5.24) specified exactly one condition at both the inner and outer radii, now two conditions are specified at the inner radius while one condition remains at the outer radius. It is however possible to meet all of the conditions (5.28) because the uniform pressure p in (2.22) is now added to all the normal stresses in (5.7) - (5.9). Note that this constant term is differentiated out of the equilibrium equations and so (5.11) and (5.12) remain as governing equations. These governing equations can now be solved subject to (5.20) and to the second two conditions in (5.28). This would seem to be a well posed problem, at least in terms of the number of boundary conditions that are employed. Indeed it is similar to the problem associated with boundary conditions (5.19) and to the problem associated with boundary conditions (5.25). After such a solution is obtained, the value of p may then be selected so as to satisfy the remaining condition  $\sigma_{rr}(r_i) = 0$  in (5.28).

As an example take  $\alpha=0$  and suppose that the transition from a saturated condition to a nonsaturated condition takes place when  $T^*=0.6$ . There is both a standard saturated solution and a post-maximum saturated solution associated with  $T^*=0.6$ . The former is with  $\psi=0.418$  and  $\delta=0.946$ ; the latter is with  $\psi=1.412$  and  $\delta=0.302$ . These correspond to different amounts of available liquid. Specifically, loss of saturation occurs for the regular solution at  $T^*=0.6$  if  $V_{liq}=40.469LR_i^3$ . Loss of saturation occurs for the post-maximum solution at  $T^*=0.6$  if  $V_{liq}=53.371LR_i^3$ . Alternatively stated, let us consider  $R_0=2R_i$  and  $\alpha=0$  for the two cases  $V_{liq}=40.469LR_i^3$  and  $V_{liq}=53.371LR_i^3$ . Then the boundary value problem with boundary conditions (5.20) and (5.24) causes complete fluid absorption under increasing  $\psi$  for

the case  $V_{liq}=40.469LR_i^3$  when  $\psi=0.418$ , in which case  $r_i^{(nonsat)}=0.946\zeta R_i$ ; and causes complete fluid absorption for the case  $V_{liq}=53.371LR_i^3$  when  $\psi=1.412$ , in which case  $r_i^{(nonsat)}=0.302\zeta R_i$ . The two values of  $V_{liq}$  are here specially chosen to give the same value  $T^*=T^{*(LoS)}=0.6$ . Thus the two cases correspond respectively to a standard saturated solution transitioning to a nonsaturated solution and to a post-maximum saturated solution transitioning to a nonsaturated solution, both for the same value  $T^*$ .

The boundary value problem for each of the two cases with  $T^{*(LoS)} = 0.6$  is solved numerically by the methodology outlined above. Since the boundary condition  $\sigma_{rr}(r_i) = 0$  is met by the freedom to choose p, the solution method is the same as that in which the radial displacement is specified at both  $R_i$  and  $R_o$ .

Figure 5.12 shows the mechanical behavior of the nonsaturated states associated with the transition taking place at the standard solution discussed above, i.e.  $V_{liq} = 40.469LR_i^3$ ,  $T^* = 0.6$ ,  $\psi = 0.418$ . Panels (a) - (d) of Figure 5.12 should be compared with panels (a) - (d) of Figure 5.4 since Figure 5.4 shows the mechanical behavior for the same system prior to the loss of saturation. In particular the graphs for the transition value  $T^* = 0.6$  are the same for both figures. In the context of this example, the  $T^* = 0.6$  curve in Figure 5.4 should now be disregarded since there is now insufficient fluid for a saturated solution when  $T^* = 0.6$ . In a similar fashion, panel (e) of Figure 5.12, which gives  $\sigma_{TT}(r)$ , should be compared to panel (b) of Figure 5.8. As  $T^*$  increases one again finds that fluid redistributes from the inner portion to the outer portion (panels (a) and (c)). Unlike the saturated solutions prior to transition, now both  $r_i$  and  $r_0$  remain fixed as  $T^*$  increases (panel (b)). Also, the twist angle  $\psi$  continues to increase with  $T^*$  (panel (d)).

Figure 5.13 show the mechanical behavior of the nonsaturated states associated with the transition taking place at the post-maximum solution discussed above, i.e.  $V_{liq} = 53.371 LR_i^3$ ,  $T^* = 0.6$ ,  $\psi = 1.412$ ,  $\delta = 0.302$ . Hence the  $T^* = 0.6$  curves in

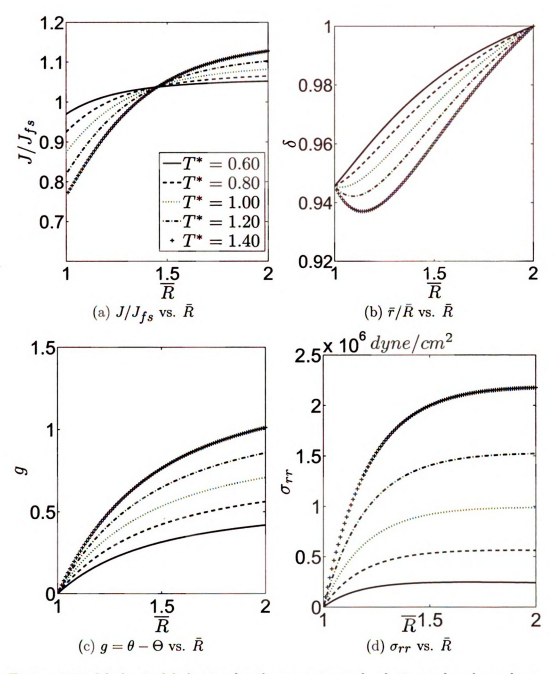


Figure 5.12: Mechanical behavior for the nonsaturated solutions when loss of saturation takes place at a standard solution with  $T^*=0.6$ . Here  $\alpha=0$  and  $V_{Iig}=40.469LR_2^3$ . The solid curve in each panel corresponds to the instant of transition while the other curves correspond to increasing  $T^*$ . The values of  $\psi$  associated with  $T^*=0.60,\,0.80,\,1.00,\,1.20,\,1.40$  are  $\psi=0.418,\,0.562,\,0.708,\,0.858,\,1.011$  respectively.

panels (a) - (d) are identical to those displayed in panels (a) - (d) of Figure 5.11. The curves in Figure 5.11 give the behavior prior to the loss of saturation. The overall behavior displayed by the curves in Figure 5.13 are similar to those in Figure 5.12. In particular  $\psi$  increases with  $T^*$  after loss of saturation. Thus the negative slope of the torque-twist graph for the post-maximum solutions prior to loss of saturation immediately changes to a positive slope torque-twist response after loss of saturation.

Figure 5.14 shows the nonsaturated torque-twist response curve corresponding to each of the two transitions for  $T^* = 0.6$ . These curves are connected to the previously displayed response curve of Figure 5.10. In each case, loss of saturation is associated with an abrupt stiffening of this macroscopic response. In particular, when loss of saturation occurs at the post-maximum solution, the torque - twist response is once again monotonically increasing.

As an additional comparison consider again the same standard solution transition state as that in Figure 5.12, namely the case with  $V_{liq}=40.469LR_i^3$ , so that transition occurs at  $T^*=0.6$ ,  $\psi=0.418$  with  $\delta=0.946$ . Specially, for this  $V_{liq}=40.469LR_i^3$  consider the three twist values  $\psi=0.220$ , 0.418, 0.620. Figure 5.15 compares the associated sequence of mechanical response curves for the saturated, transition and nonsaturated states that correspond respectively to  $\psi=0.22$ ,  $\psi=0.418$ ,  $\psi=0.62$ . In addition, this figure also shows the saturated response when  $\psi=0.62$  (which can only occur for a larger value of  $V_{liq}$ ). A comparison of the saturated and nonsaturated response for  $\psi=0.62$  makes evident the continuous volume increase and inner diameter reduction for the saturated case. In contrast, once the system is nonsaturated the value of  $r_i$  remains fixed (panel (b)) and the overall volume is unchanged. In particular, the curves in panel (a) for  $\psi=0.418$  and for  $\psi=0.62$  after loss of saturation cross over each other so as to permit J to integrate up to the same value. Also, for  $r>r_i$ , the stress  $\sigma_{rr}$  is everywhere greater for the nonsaturated case with  $\psi=0.62$  than it is for the saturated case with this same  $\psi$ .

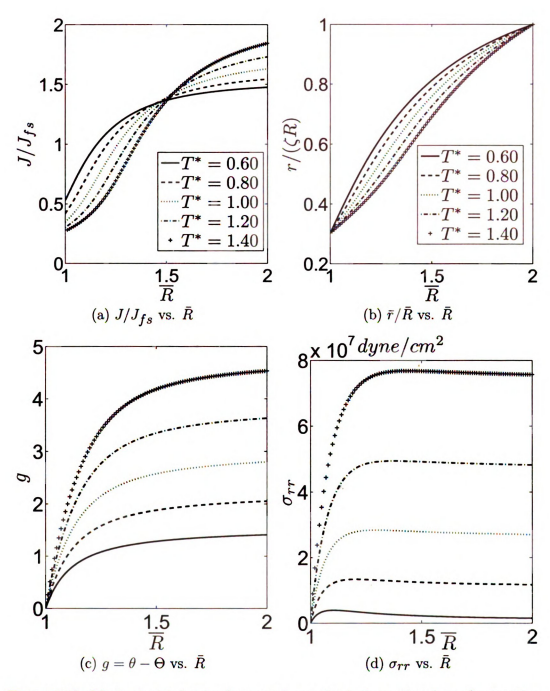


Figure 5.13: Mechanical behavior for nonsaturated solutions when loss of saturation takes place at the post-maximum solution with  $T^*=0.6$ . Here  $\alpha=0$  and  $V_{liq}=53.371LR_4^3$ . The solid curve in each panel correspond to the instant of transition while the other curves correspond to increasing  $T^*$ . The values of  $\psi$  associated with  $T^*=0.66,0.80,1.00,1.20,1.40$  are  $\psi=1.412,2.053,2.800,3.632,4.533$  respectively.

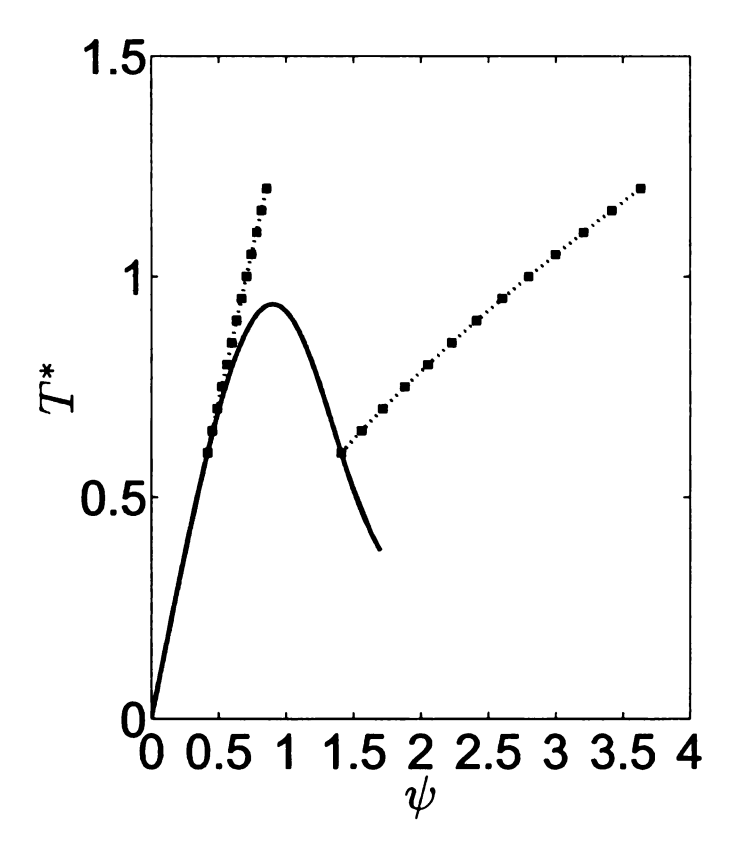


Figure 5.14: Saturated and nonsaturated torque-twist response for  $\alpha=0$ . Two examples are shown, each corresponding to  $T^*=0.6$ . The square markers on the nonsaturated curves represent computational points and the intervening dots are to guide the eye. The transition on the left occurs at a standard solution (corresponding to the solutions displayed in Figure 5.12). The transition on the right occurs at a post-maximum solution (corresponding to the solutions displayed in Figure 5.13).

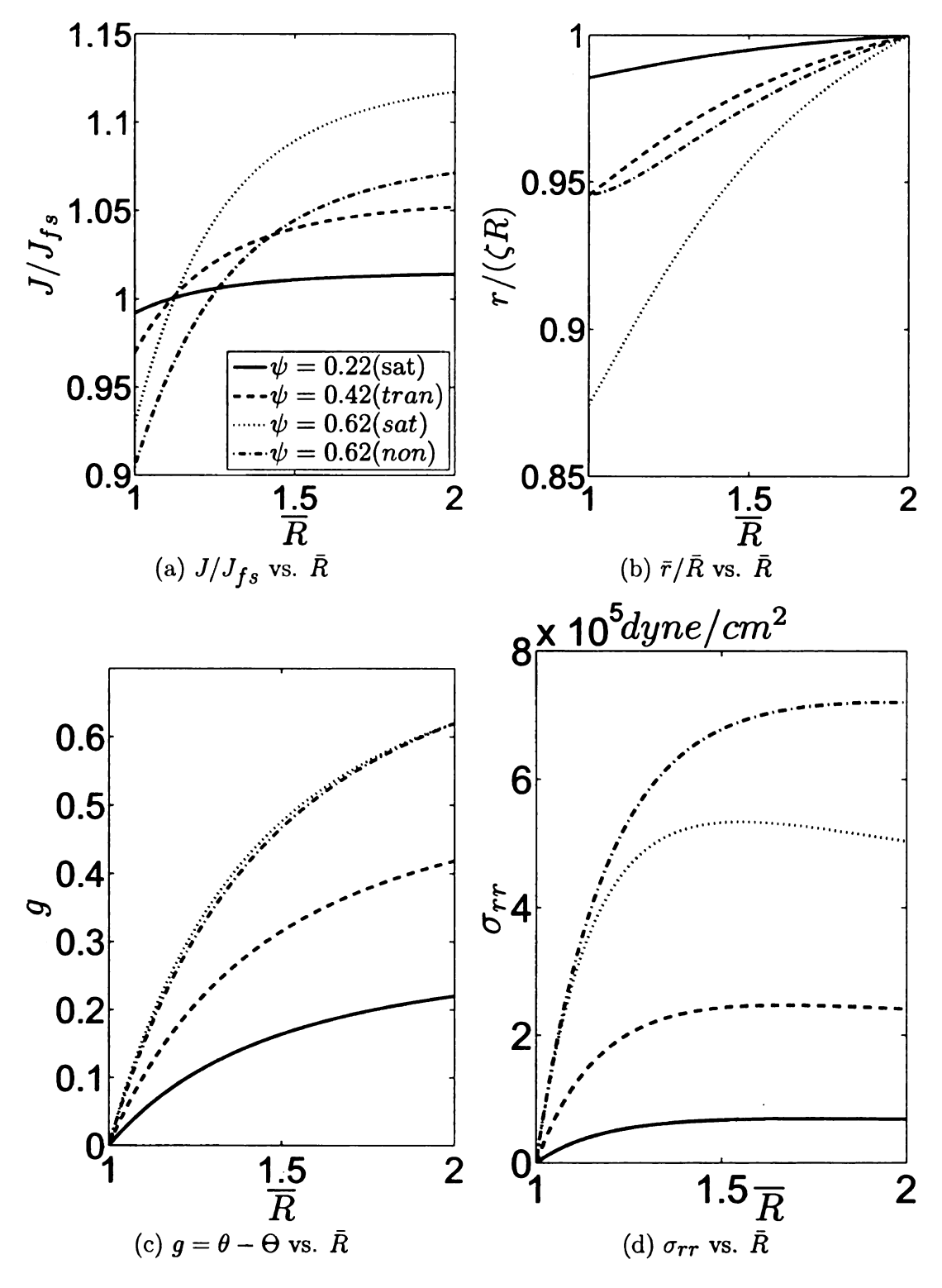


Figure 5.15: Saturated, transition and nonsaturated states associated with loss of saturation taking place from a standard solution when  $\psi=0.42$ . Thus  $\psi=0.62$  corresponds to a nonsaturated state. For comparison, the response for a hypothetical  $\psi=0.62$  saturated state is also shown.

In a similar fashion, Figure 5.16 provides the same type of comparison as in Figure 5.15 for the case in which loss of saturation occurs at a post-maximum saturated state. Here it is to be noted for  $\psi = 1.6$  that the saturated case is more depleted of fluid near  $r = r_i$  than is the nonsaturated case. In addition the  $\sigma_{rr}$  profile for the  $\psi = 1.6$  nonsaturated case is no longer everywhere above the  $\psi = 1.6$  profile for the saturated case. The exceptional regions where this ordering in  $\sigma_{rr}$  ceases to hold is again confined to a zone near  $r = r_i$ .

### 5.6 Summary

In this chapter, the problem of twisting a swollen tube is formulated based on the theoretical model described in Chapter 2. We started by replicating Wineman and Rajagopal's work [48] where they consider the problem of a volume preserved swollen cylinder under twisting in a saturated state. We obtained the exact same graphs as in [48]. Then more generally we consider different boundary conditions that do not necessarily conserve the total amount of liquid in the cylinder, we discover additional interesting effects when there is relative twist  $\psi \neq 0$  between the inner and outer radii. Replacing the condition that the outer radius maintains its free swelling value by a condition of zero normal traction causes this outer radius to displace inward, thus decreasing the overall volume. This requires fluid to exit the system. Conversely, replacing the condition that the inner radius maintains its free swelling value by a condition of zero normal traction causes this inner radius to displace inward, thus increasing the overall volume. This requires fluid to enter the system. In all cases we find for  $\psi \neq 0$  that the fluid concertration in the cylinder is an increasing function of the radius. As was the case in [48], the amount of redistribution increases with  $|\psi|$  for the broader class of problems considered here. In addition, for the problem characterized by the zero normal traction condition at the inner radius,

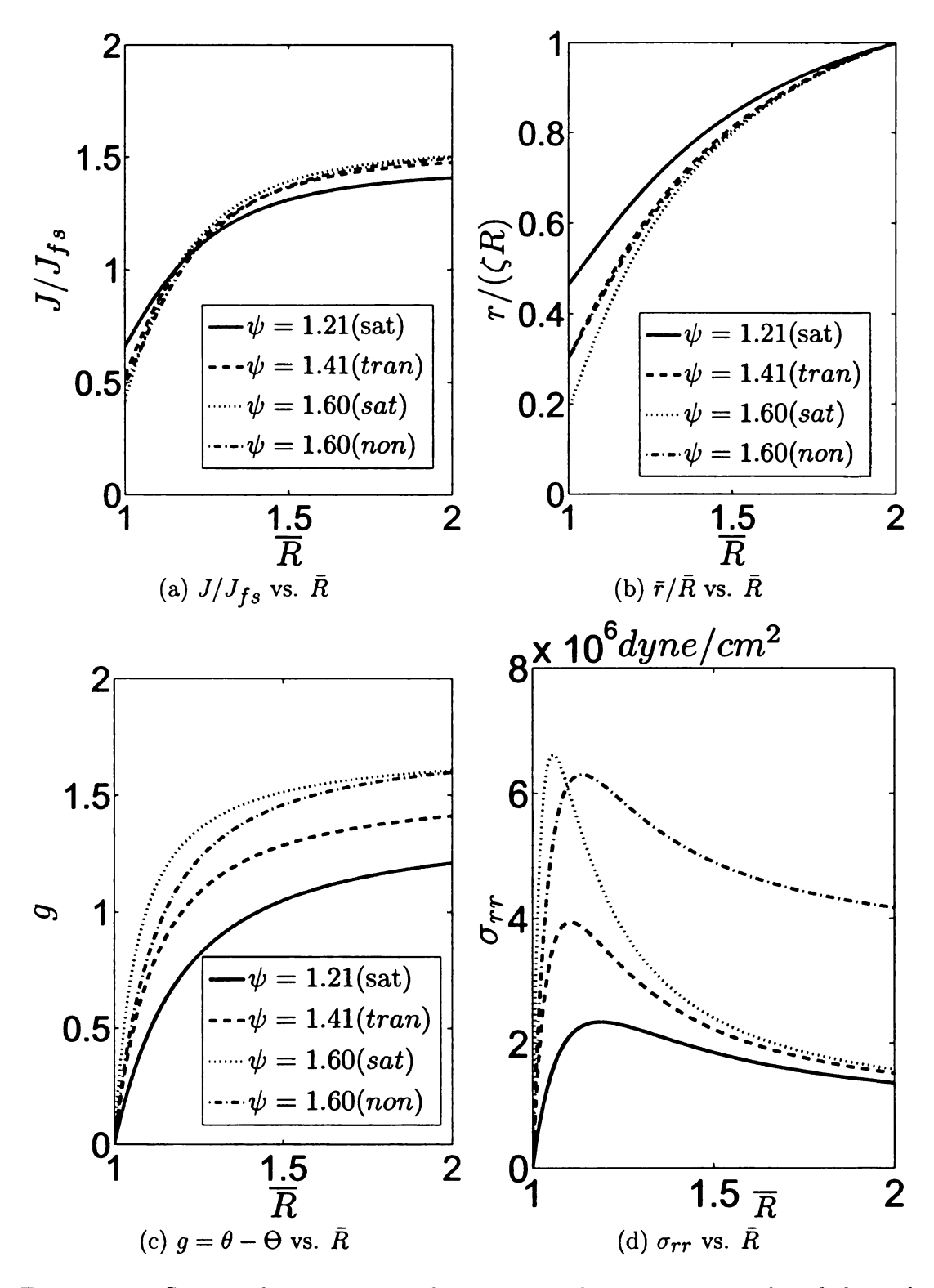


Figure 5.16: Saturated, transition and nonsaturated states associated with loss of saturation taking place from a post-maximum solution when  $\psi = 1.41$ . Thus  $\psi = 1.60$  corresponds to a nonsaturated state. For comparison, the response for a hypothetical  $\psi = 1.60$  saturated state is also shown.

we find that the relation between the twist angle  $\psi$  and the twisting moment T may lose monotonicity so that there is a maximum twisting moment that can be sustained under such circumstances.

Furthermore, for those situations that give rise to fluid uptake, we consider the consequences if, at some point in the process, all of the fluid is drawn into the system so that no additional uptake is possible. Then the transition from the saturated state to nonsaturated state occurs. The overall volume of the cylinder cannot change once the system loses saturation. The result shows that the now fixed amount of fluid continues to redistribute as  $\psi$  changes. It is also found that the relation between the twist angle  $\psi$  and the twisting moment T abruptly stiffens after loss of saturation.

## Chapter 6

## Seepage Through a Fiber Reinforced Hyperelastic Layer

The effect of a fluid solvent on the swelling of a rubbery polymer is of longstanding interest [44]. In particular, extensive experiments have been performed on the pressure-induced diffusion of fluid through polymer networks [20–23,84,85]. One of the heavily referred set of pressure-induced diffusion experiments was conducted by Paul and Ebra-Lima [24]. They recorded the nonlinear relation between the fluid flux and the pressure difference driving the solvent through a highly swollen polymer membrane layer. They also presented a combined thermodynamic and diffusion theory for this pressure-induced transport. In addition, uniaxial stretch experiments were made on the gum rubber material immersed in twelve different organic solvents that were tested in the diffusion experiments. The elastic and thermodynamic constitutive parameters were determined from these tests by using the Flory-Huggins theory. These parameters were then used widely in later works that seek to model such pressure-induced diffusive transport [46–49]. It is to be remarked that although we use the term "diffusion transport" here, other intellectual traditions may prefer the term "seepage". Here we use there terms interchangeably.

A broader continuum mechanical framework can be invoked to deal with separate mechanical balance principles for both solid and fluid component. This broader framework is known by a number of names, including: large deformation mixture theory, the theory of interacting continua, and the large deformation biphasic theory. Examples of mixture theory type treatments applied to problems involving these systems include [47,71,86], where a major focus is on time dependent swelling as liquid diffuses within the elastomeric matrix.

In this chapter we consider similar seepage problems for both isotropic and anisotropic (fiber reinforced) gels. In particular we shall use a framework recently considered by Pence [87] that provides for consistency with equilibrium problems involving solvent redistribution such as considered earlier in this thesis and also by other researchers.

### 6.1 A Biphasic Mixture Theory

#### 6.1.1 Kinematics and Notation

Following Shi et al. [46], we let  $\mathbf{X}^f$  and  $\mathbf{X}^s$  denote reference positions for fluid and particles respectively in the reference state prior to mixing. Positions of these particles at time t are determined by the respective functions  $\chi^f(\mathbf{X}^f,t)$  and  $\chi^s(\mathbf{X}^s,t)$  (Figure 6.1). We then let  $\mathbf{x}$  denote a location in the current configuration at time t, it is assumed that each such spatial location is occupied by both fluid and solid particles.

The fluid and solid velocity field are then given by

$$\mathbf{v}^{f} = \frac{\partial \chi^{f}}{\partial t} \Big|_{\mathbf{X}^{f}}, \qquad \mathbf{v}^{s} = \frac{\partial \chi^{s}}{\partial t} \Big|_{\mathbf{X}^{s}}. \tag{6.1}$$

The deformation gradient tensor associated with the motion of the solid constituent is given by

$$\mathbf{F} = \frac{\partial \boldsymbol{\chi}^{\boldsymbol{s}}}{\partial \mathbf{X}^{\boldsymbol{s}}}.\tag{6.2}$$

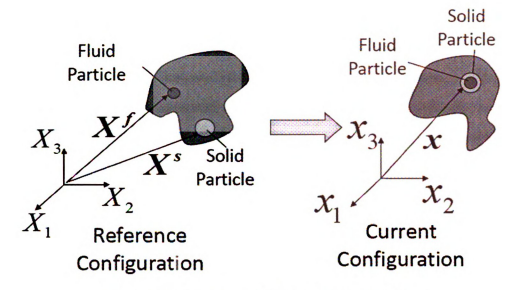


Figure 6.1: Mapping of fluid and solid particles

Let

$$J = \text{det} \mathbf{F}$$
, (6.3)

then J is the ratio of the current volume occupied by a collection of solid particles to the volume that these same particles occupy in the reference configuration. Let  $\rho^f$  denote the fluid density in the overall mixture, i.e., the mass of the fluid constituent per unit mixture volume in the current configuration. Conversely, let  $\rho^f_0$  denote the fluid density in the reference state. This  $\rho^f_0$  is a constant, whereas  $\rho^f$  is a function of  $\mathbf{x}$  and t. The fluid density is then subject to the mass conservation equation:

$$\frac{\partial \rho^f}{\partial t} + \nabla \cdot \left( \rho^f \mathbf{v}^f \right) = 0.$$
 (6.4)

The solid densities  $\rho^{g}$  in the current configuration and  $\rho_{0}^{g}$  in the reference configuration are defined in a similar fashion. Then the mass conservation of the solid phase is expressed as

$$\rho^s = \frac{1}{J}\rho_0^s. \tag{6.5}$$

The assumption that the volume of the mixture is the sum of volume of fluid

and solid constituents prior to mixing gives

$$\frac{\rho^s}{\rho_0^s} + \frac{\rho^f}{\rho_0^f} = 1. ag{6.6}$$

By substituting from (6.5) into (6.6) one obtains

$$\rho^f = \left(1 - \frac{1}{J}\right)\rho_0^f. \tag{6.7}$$

Since the total mass is the sum of the fluid and solid mass, the overall density  $\rho$  is given by

$$\rho = \rho^f + \rho^s = \frac{1}{J}\rho_0^s + \left(1 - \frac{1}{J}\right)\rho_0^f. \tag{6.8}$$

The seepage velocity w is the velocity of the fluid with respect to the solid, i.e.,

$$\mathbf{w} = \mathbf{v}^f - \mathbf{v}^s. \tag{6.9}$$

The final kinematic quantities to be introduced are the velocity gradient tensors associated with the respective motion of the fluid and solid constituents, namely,

$$\mathbf{L}^f = \nabla \otimes \mathbf{v}^f, \qquad \mathbf{L}^s = \nabla \otimes \mathbf{v}^s. \tag{6.10}$$

# 6.1.2 Fluid and Solid Partial Stresses Under Volume Constraint

In the absence of external body forces, and neglecting inertial effects, the equilibrium equations of the solid and fluid phase are given by

$$\nabla \cdot \boldsymbol{\sigma}^{s} + \mathbf{b} = \mathbf{0}, \qquad \nabla \cdot \boldsymbol{\sigma}^{f} - \mathbf{b} = \mathbf{0}, \tag{6.11}$$

where  $\sigma^s$ ,  $\sigma^f$  and **b** are, respectively, the solid partial stress, the fluid partial stress and the possible dissipative interactive force between the solid and fluid phase. The total stress  $\sigma^{tot} = \sigma^s + \sigma^f$  therefore obeys

$$\nabla \cdot \boldsymbol{\sigma}^{tot} = \mathbf{0}.\tag{6.12}$$

Let  $\Psi_{cur} = \Psi_{cur}(\mathbf{F})$  be the Helmholtz free energy of the mixture per unit mass in the current configuration. Based on a mixture theory treatment involving the first and second thermodynamic laws (details can be found in [87]), the fluid and solid partial stresses and the interactive force with the constraint of volume preservation (6.6) are given by

$$\mathbf{b} = \rho^f \frac{\partial \Psi_{cur}}{\partial \mathbf{F}} : \nabla \mathbf{F} - \frac{p_1}{\rho_0^f} \nabla \rho^f + \hat{\mathbf{b}}$$
 (6.13)

$$\boldsymbol{\sigma}^{s} = \rho \frac{\partial \Psi_{cur}}{\partial \mathbf{F}} \mathbf{F}^{T} - \frac{p_{1}}{J} \mathbf{I} + \hat{\boldsymbol{\sigma}}^{s}, \qquad \boldsymbol{\sigma}^{f} = -\frac{\rho^{f}}{\rho_{0}^{f}} p_{1} \mathbf{I} + \hat{\boldsymbol{\sigma}}^{f}.$$
(6.14)

Equation (6.11) are standard in the theory of interacting continua [48] whereas equations (6.13) and (6.14) generalize the isotropic theory equations (9), (10) and (11) of [48]. Here  $p_1$  is a Lagrange multiplier which arises due to the volume constraint (6.6). The tensors  $\hat{\sigma}^s$  and  $\hat{\sigma}^f$  are possible dissipative stresses and  $\hat{\mathbf{b}}$  is a possible dissipative interactive force. These are required to obey

$$\hat{\boldsymbol{\sigma}}^s : \mathbf{L}^s \ge 0, \quad \hat{\boldsymbol{\sigma}}^f : \mathbf{L}^f \ge 0, \quad \hat{\mathbf{b}} \cdot \mathbf{w} \ge 0.$$
 (6.15)

It follows from  $(6.11)_2$ , (6.13) and  $(6.14)_2$  that

$$\nabla p_1 = -\rho_0^f \nabla \Psi_{cur} + \frac{\rho_0^f}{\rho^f} \left( \nabla \cdot \hat{\boldsymbol{\sigma}}^f + \hat{\mathbf{b}} \right). \tag{6.16}$$

Eliminating  $p_1$  in (6.13) and (6.14) with the use of (6.7) and (6.11) gives

$$(J-1)\nabla \cdot \left(\boldsymbol{\sigma}^{mix} + \hat{\boldsymbol{\sigma}}^{s}\right) = \nabla \cdot \hat{\boldsymbol{\sigma}}^{f} - J\hat{\mathbf{b}}, \tag{6.17}$$

where  $\sigma^{mix}$  is defined by

$$\boldsymbol{\sigma}^{mix} = \rho \frac{\partial \Psi_{cur}}{\partial \mathbf{F}} \mathbf{F}^T + \rho_0^f \Psi_{cur} \mathbf{I}. \tag{6.18}$$

Exactly the same as in (2.11), let W be the Helmholtz free energy of the mixture per unit volume of the solid in its reference state. Therefore W is related to  $\Psi_{cur}$ , the Helmholtz energy per unit mixture mass in the current configuration, by

$$W = \rho J \Psi_{cur} = \rho \frac{\rho_0^s}{\rho^s} \Psi_{cur} \qquad \Leftrightarrow \qquad \Psi_{cur} = \frac{1}{\rho J} W = \frac{1}{\rho} \frac{\rho^s}{\rho_0^s} W = \frac{W}{\rho_0^s + (J-1)\rho_0^f}. \tag{6.19}$$

It then follows that (6.18) is alternatively expressed as

$$\sigma^{mix} = \frac{1}{J} \frac{\partial W}{\partial \mathbf{F}} \mathbf{F}^{T}. \tag{6.20}$$

If  $\hat{\sigma}^s$ ,  $\hat{\sigma}^f$  and  $\hat{\mathbf{b}}$  all vanish, we then obtain from (6.17) the equilibrium equation

$$\nabla \cdot \boldsymbol{\sigma}^{mix} = \mathbf{0}. \tag{6.21}$$

To also account for the dissipative affects we will use (6.17) with  $\hat{\sigma}^f = \hat{\sigma}^s = \mathbf{0}$  but  $\hat{\mathbf{b}} \neq 0$  as the governing equation for the fluid seepage problems that will be introduced in the next section.

### 6.1.3 Boundary Conditions

The boundary of the mixture can admit a variety of situations including: (a) contact with the pure fluid phase, (b) contact with a rigid support structure that

strictly isolates the mixture from any pure fluid phase, and (c) contact with a porous rigid support that permits interaction with a pure fluid phase on the other side of the support. To specify appropriate boundary conditions, let  $\bf n$  be the directional normal vector to the mixture external surface, let  $P_f$  be the pressure of any pure fluid phase that is adjacent to the mixture and let  $\bf t$  be the traction provided by any solid support structure. In particular, the traction  $\bf t$  may or may not permit interaction with the pure fluid. Certainly one boundary condition is

$$\sigma^{tot}\mathbf{n} = \mathbf{t}^{tot}, \quad \text{where } \mathbf{t}^{tot} = \mathbf{t} - P_f\mathbf{n}.$$
 (6.22)

Note that  $\mathbf{t} = \mathbf{0}$  for situation (a) given above, whereas  $P_f = 0$  for situation (b) given above. For situation (c) given above both  $\mathbf{t}$  and  $P_f$  would typically be nonzero. In general (6.22) does not provide enough boundary conditions to solve all boundary value problems of interest. Thus more boundary conditions are usually required. There is some controversy as to what these additional boundary conditions should be [88]. Here we briefly discuss two proposals for the additional boundary conditions, one is called the traction splitting boundary conditions, the other is based on an argument involving chemical potentials. After this brief discussion we will adopt the chemical potential boundary condition in what follows.

The first proposal is the traction splitting condition. As originally stated in [89] (see page 36-37), the traction splitting treatment states that the partial surface tractions associated with the solid and fluid, respectively, are proportional to their local volume fractions. In our notation this would be expressed as

$$\boldsymbol{\sigma}^{f}\mathbf{n} = \frac{\delta V^{f}}{\delta V}\mathbf{t}^{tot} = \frac{\rho^{f}}{\rho_{0}^{f}}\mathbf{t}^{tot} = \left(1 - \frac{1}{J}\right)\mathbf{t}^{tot}, \qquad \boldsymbol{\sigma}^{s}\mathbf{n} = \frac{\delta V^{s}}{\delta V}\mathbf{t}^{tot} = \frac{\rho^{s}}{\rho_{0}^{s}}\mathbf{t}^{tot} = \frac{1}{J}\mathbf{t}^{tot},$$
(6.23)

where n is again the unit normal vector. However later (see page 42 of [89]) it is

argued that the porous solid support structure has "little effect on the flow of the fluid constituent" and this is used in [89] to restrict the splitting in  $(6.23)_1$  to only the fluid pressure. Letting  $P_f$  be the fluid pressure this gives an addition boundary condition in the form  $\sigma^f = -\left(1 - \frac{1}{J}\right) P_f$ .

The second, and alternative, proposal for boundary conditions appropriate to a mixture of the type considered here consisting of an incompressible solid and incompressible fluid is often called the chemical potential continuity boundary condition. This type of treatment can be found in [71] and [90] where the chemical potential continuity boundary conditions are obtained through a variational approach of extremizing the overall free energy of the system. In the present notation, this boundary condition is stated in the following equations (see (39), (40) and (22) in [71])

$$\left[\frac{\partial \tilde{\psi}}{\partial \mathbf{F}} \mathbf{F}^T + \left(\tilde{\psi} - \rho_0^f K\right) \mathbf{I}\right] \mathbf{n} = \mathbf{t} - P_f \mathbf{n}, \quad \text{and} \quad K = K_f, \quad (6.24)$$

where

$$K_f \equiv \frac{1}{\rho_0^f} \left( P_f + \mu_{liq} \right). \tag{6.25}$$

Here  $\tilde{\psi}$  is the system Helmholtz free energy per unit current volume,  $K=K(\mathbf{x})$  is the chemical potential of the mixture,  $P_f$  is the fluid pressure at the boundary as given earlier in connection with (6.22),  $K_f$  is the chemical potential of the fluid, and  $\mu_{liq}$  is a constant that gives the Helmholtz free energy per unit current volume of the pure fluid phase. It is to be clarified that  $\tilde{\psi}$  is defined as Helmholtz free energy per unit current volume of the system, while  $\Psi_{cur}$  in (6.13) and (6.14) is defined as the free energy per unit current mass of the mixture, which does not take into account the free energy of each phase  $\mu_{poly}$  and  $\mu_{liq}$ . By this we mean

$$\tilde{\psi} = \rho \Psi_{cur} + \left(1 - \frac{1}{J}\right) \mu_{liq} + \frac{1}{J} \mu_{poly}. \tag{6.26}$$

Comparing the system free energy  $\tilde{\psi}$  with the system free energy E per unit reference volume as defined in (5.14) it follows that

$$\tilde{\psi} = \frac{1}{J} E = \frac{1}{J} W + \left(1 - \frac{1}{J}\right) \mu_{liq} + \frac{1}{J} \mu_{poly}.$$
 (6.27)

It then follows from (6.24) with the use of (6.27) that

$$\left(\frac{1}{J}\frac{\partial W}{\partial \mathbf{F}}\mathbf{F}^T + \mu_{liq}\right)\mathbf{n} = \mathbf{t} + \mu_{liq}\mathbf{n},\tag{6.28}$$

which immediately leads to

$$\sigma^{mix}\mathbf{n} = \mathbf{t} \tag{6.29}$$

by the definition of  $\sigma^{mix}$  in (6.20).

For our purposes in what follows we note that (6.17) with  $\hat{\sigma}^f = \hat{\sigma}^s = 0$  gives

$$\nabla \cdot \boldsymbol{\sigma}^{mix} + \frac{J}{J-1}\hat{\mathbf{b}} = \mathbf{0}. \tag{6.30}$$

In addition, following Parasad and Rajagopal [88] the dissipative interactive force  $\hat{\mathbf{b}}$  will eventually be taken to be proportional to the seepage velocity  $\mathbf{w}$  by virtue of the following form

$$\hat{\mathbf{b}} = \frac{\alpha}{J} \left( \frac{1}{J-1} \right)^{n-1} \mathbf{w},\tag{6.31}$$

where  $\alpha > 0$  is a material diffusive constant, and n > 0.

## 6.2 Free Swelling of a Fiber Reinforced Hyperelastic Layer

We consider a fiber reinforced gel consisting of an anisotropic hyperelastic solid that is immersed in solvent. Prior to immersion the solid is taken to be in the form

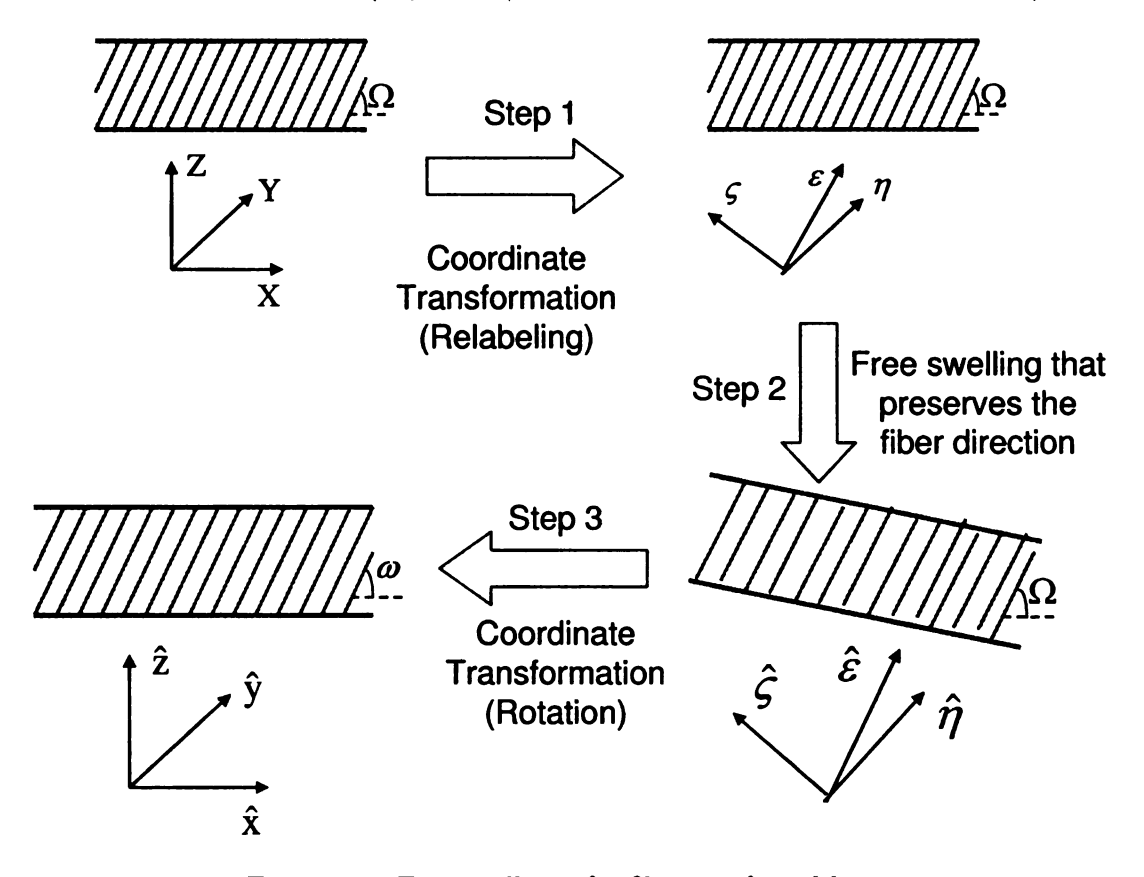


Figure 6.2: Free swelling of a fiber reinforced layer

Z) denote the position of particles in the reference configuration. Let M denote the unit vector of the fiber reinforcing direction in the reference configuration and assume that the fibers in the reference configuration lie in the (X, Z)-plane. Thus we take

$$\mathbf{M} = \cos\Omega \,\mathbf{e}_X + \sin\Omega \,\mathbf{e}_Z. \tag{6.32}$$

We assume that the fibers are at their natural length in this reference configuration. Now let the reinforced layer be immersed in a fluid environment and swell freely to an equilibrated state with  $(\hat{x}, \hat{y}, \hat{z})$  describing position in the swollen configuration. We wish to describe the resulting free swelling in a manner such that the (X, Y)- plane has the same orientation as the  $(\hat{x}, \hat{y})$ -plane. To describe this homogeneous deformation it is convenient to decompose the free swelling into three steps (Figure 6.2). The first step is a coordinate relabeling transformation that transforms the (X, Y, Z) coordinates to  $(\varepsilon, \eta, \varsigma)$  by a rotation through angle  $\Omega$  about the Y axis. This aligns the  $\varepsilon$  axis with the fiber direction. The mapping function and its gradient are given by

$$\left\{
\begin{aligned}
\varepsilon &= X \cos \Omega + Z \sin \Omega \\
\eta &= Y \\
\varsigma &= -X \sin \Omega + Z \cos \Omega
\end{aligned}
\right\}, \qquad \mathbf{F}_{1} = \begin{bmatrix}
\cos \Omega & 0 & \sin \Omega \\
0 & 1 & 0 \\
-\sin \Omega & 0 & \cos \Omega
\end{bmatrix}, \quad \text{(step 1)}.$$

The second step is a free swelling that preserves the coordinate directions ( $\varepsilon$ ,  $\eta$ ,  $\varsigma$ ). Let  $\lambda_1$  be the stretch ratio along the direction of the fibers while the stretches in all the transverse directions are the same and so denoted by  $\lambda_2$ . This gives

$$\begin{cases}
\hat{\varepsilon} = \lambda_1 \varepsilon \\
\hat{\eta} = \lambda_2 \eta \\
\hat{\varsigma} = \lambda_2 \varsigma
\end{cases}, \qquad \mathbf{F}_2 = \begin{bmatrix} \lambda_1 & 0 & 0 \\ 0 & \lambda_2 & 0 \\ 0 & 0 & \lambda_2 \end{bmatrix}, \quad (\text{step 2}). \tag{6.34}$$

The third step is a coordinate rotation transformation that rotates the coordinates  $(\hat{\varepsilon}, \hat{\eta}, \hat{\varsigma})$  to  $(\hat{x}, \hat{y}, \hat{z})$  by an as yet unspecified angle  $-\omega$  about the  $\hat{\eta}$  axis

$$\begin{cases}
\hat{x} = \hat{\varepsilon} \cos \omega - \hat{\zeta} \sin \omega \\
\hat{y} = \hat{\eta} \\
\hat{z} = \hat{\varepsilon} \sin \omega + \hat{\zeta} \cos \omega
\end{cases}, \qquad \mathbf{F}_{3} = \begin{bmatrix}
\cos \omega & 0 & -\sin \omega \\
0 & 1 & 0 \\
\sin \omega & 0 & \cos \omega
\end{bmatrix}, \quad (\text{step 3}).$$
(6.35)

Therefore the deformation gradient  $\mathbf{F}$  associated with the mapping from the reference configuration (X, Y, Z) to the free swelling configuration  $(\hat{x}, \hat{y}, \hat{z})$  is given by

$$\mathbf{F} = \mathbf{F_3}\mathbf{F_2}\mathbf{F_1} = \begin{vmatrix} \lambda_1 \cos \Omega \cos \omega + \lambda_2 \sin \Omega \sin \omega & 0 & \lambda_1 \sin \Omega \cos \omega - \lambda_2 \cos \Omega \sin \omega \\ 0 & \lambda_2 & 0 \\ \lambda_1 \cos \Omega \sin \omega - \lambda_2 \sin \Omega \cos \omega & 0 & \lambda_1 \sin \Omega \sin \omega + \lambda_2 \cos \Omega \cos \omega \end{vmatrix},$$
(6.36)

and so

$$\hat{x} = (\lambda_1 \cos \Omega \cos \omega + \lambda_2 \sin \Omega \sin \omega) X + (\lambda_1 \sin \Omega \cos \omega - \lambda_2 \cos \Omega \sin \omega) Z,$$

$$\hat{y} = \lambda_2 Y,$$
(6.37)

$$\hat{z} = (\lambda_1 \cos \Omega \sin \omega - \lambda_2 \sin \Omega \cos \omega) X + (\lambda_1 \sin \Omega \sin \omega + \lambda_2 \cos \Omega \cos \omega) Z.$$

The left and right Cauchy-Green deformation tensor that follows from (6.36) is given as

$$\mathbf{B} = \mathbf{F}\mathbf{F}^{T} = \begin{bmatrix} \lambda_{1}^{2}\cos^{2}\omega + \lambda_{2}^{2}\sin^{2}\omega & 0 & \left(\lambda_{1}^{2} - \lambda_{2}^{2}\right)\sin\omega\cos\omega \\ 0 & \lambda_{2}^{2} & 0 \\ \left(\lambda_{1}^{2} - \lambda_{2}^{2}\right)\sin\omega\cos\omega & 0 & \lambda_{1}^{2}\sin^{2}\omega + \lambda_{2}^{2}\cos^{2}\omega \end{bmatrix}$$
(6.38)

and

$$\mathbf{C} = \mathbf{F}^{T} \mathbf{F} = \begin{bmatrix} \lambda_{1}^{2} \cos^{2} \Omega + \lambda_{2}^{2} \sin^{2} \Omega & 0 & \left(\lambda_{1}^{2} - \lambda_{2}^{2}\right) \sin \Omega \cos \Omega \\ 0 & \lambda_{2}^{2} & 0 \\ \left(\lambda_{1}^{2} - \lambda_{2}^{2}\right) \sin \Omega \cos \Omega & 0 & \lambda_{1}^{2} \sin^{2} \Omega + \lambda_{2}^{2} \cos^{2} \Omega \end{bmatrix}.$$
(6.39)

Thus 
$$I_1 = \text{tr}(\mathbf{B}) = \lambda_1^2 + 2\lambda_2^2$$
,  $I_2 = \frac{1}{2} \left[ \text{tr}(\mathbf{B})^2 - \text{tr}(\mathbf{B}^2) \right] = 2\lambda_1^2\lambda_2^2 + \lambda_2^4$  and  $J = \sqrt{I_3} = \text{det}\mathbf{F} = \lambda_1\lambda_2^2$ .

The angle  $\omega$  is now chosen so as to satisfy

$$\lambda_1 \cos \Omega \sin \omega - \lambda_2 \sin \Omega \cos \omega = 0 \quad \Rightarrow \quad \omega = \arctan \left(\frac{\lambda_2}{\lambda_1} \tan \Omega\right).$$
 (6.40)

With this choice of  $\omega$  the planes Z = constant remain at their original orientation after free swelling. It then follows from (6.37) that

$$\hat{x} = \left(\frac{\lambda_1 \cos \Omega}{\sqrt{1 + \frac{\lambda_2^2}{\lambda_1^2} \tan^2 \Omega}} + \frac{\lambda_2 \sin \Omega}{\sqrt{1 + \frac{\lambda_1^2}{\lambda_2^2} \cot^2 \Omega}}\right) X$$

$$+ \left(\frac{\lambda_1 \sin \Omega}{\sqrt{1 + \frac{\lambda_2^2}{\lambda_1^2} \tan^2 \Omega}} - \frac{\lambda_2 \cos \Omega}{\sqrt{1 + \frac{\lambda_1^2}{\lambda_2^2} \cot^2 \Omega}}\right) Z,$$

$$\hat{y} = \lambda_2 Y,$$

$$\hat{z} = \left(\frac{\lambda_1 \sin \Omega}{\sqrt{1 + \frac{\lambda_1^2}{\lambda_2^2} \cot^2 \Omega}} + \frac{\lambda_2 \cos \Omega}{\sqrt{1 + \frac{\lambda_2^2}{\lambda_2^2} \tan^2 \Omega}}\right) Z.$$

$$(6.41)$$

The requirement (6.40) is simply one specification of the rigid body rotation associated with a free swelling homogeneous deformation. For our purpose it is the particular rigid body rotation that corresponds to the boundary value problem of interest in this study. This is because it preserves the orientation of the planes Z=0 which will be a fixed boundary in what follows. Note also for the special case  $\lambda_1=\lambda_2=\lambda$  that (6.41) simplifies as expected to the equi-axial free swelling  $\hat{x}=\lambda X$ ,  $\hat{y}=\lambda Y$ ,  $\hat{z}=\lambda Z$ .

# 6.3 Constitutive Theory

The free energy function W will be taken as the sum of the three terms. These are: an isotropic elastic energy  $\Phi(I_1, I_2)$  due to the deformation of the matrix in which the fibers are embedded, the mixing energy H(J) due to the mixing entropy and mixing enthalpy, and an extra term  $\gamma \Phi_{fib}(I_4)$  due to the stretching of the fiber

reinforcement. This gives

$$W = \Phi(I_1, I_2) + H(J) + \gamma \Phi_{fib}(I_4). \tag{6.42}$$

We take the Mooney-Rivlin model (2.13) for the elastic energy term  $\Phi$  and the Flory-Huggins form (2.5) for the mixing energy term H. For the last term of (6.42),  $\gamma > 0$  is a material modulus and  $I_4 = \mathbf{FM} \cdot \mathbf{FM}$  is the square of the fiber stretch as discussed in [91]. On the basis of models in [91] and [92], the fiber energy  $\Phi_{fib}(I_4)$  in (6.42) will be taken as

$$\Phi_{fib}(I_4) = \frac{1}{2} (I_4 - 1)^2. \tag{6.43}$$

We first consider the homogeneous deformation for free swelling with  $\mathbf{F}$  given by (6.36). Then (6.21) is automatically satisfied and it follows from (6.29) with  $\mathbf{t} = \mathbf{0}$  for all possible orientations  $\mathbf{n}$  that  $\boldsymbol{\sigma}^{mix}$  must vanish identically. It thus follows from (6.20) and (6.42) that

$$-\frac{2}{J}\frac{\partial\Phi}{\partial I_{2}}\mathbf{B}^{2} + \frac{2}{J}\left(\frac{\partial\Phi}{\partial I_{1}} + I_{1}\frac{\partial\Phi}{\partial I_{2}}\right)\mathbf{B} + \frac{dH}{dJ}\mathbf{I} + 2\frac{\gamma}{J}\frac{d\Phi_{fib}}{dI_{4}}\mathbf{F}\mathbf{M} \otimes \mathbf{F}\mathbf{M} = \mathbf{0}.$$
 (6.44)

Expanding the above equations gives

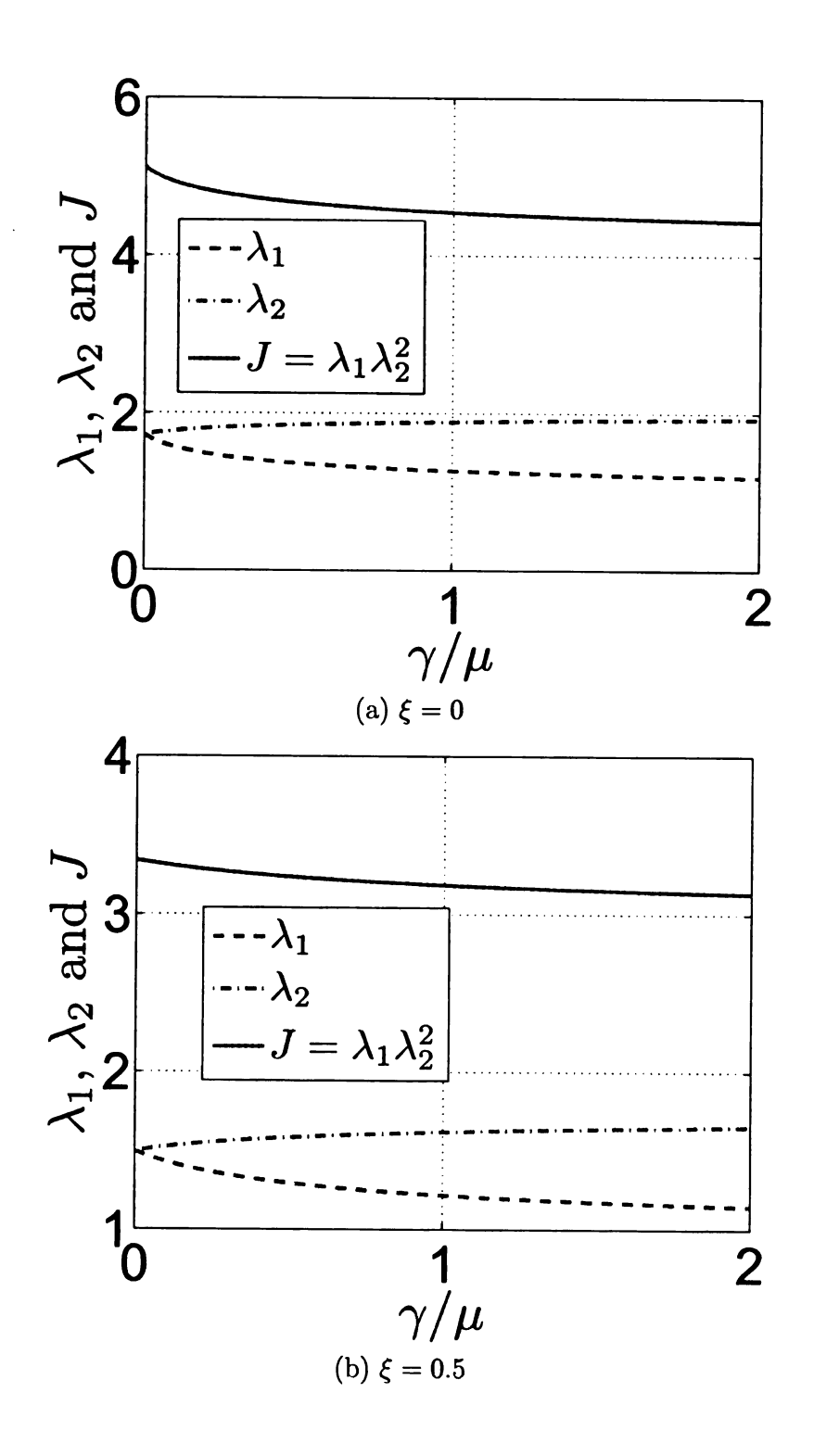
$$\begin{split} \mu \left( 1 - \xi \right) \left( \lambda_{1}^{2} \cos^{2} \omega + \lambda_{2}^{2} \sin^{2} \omega \right) \\ + \mu \xi \left[ \lambda_{2}^{4} \sin^{2} \omega + \lambda_{1}^{2} \lambda_{2}^{2} \left( \sin^{2} \omega + 2 \cos^{2} \omega \right) \right] + Jh(J) + 2\gamma \left( \lambda_{1}^{2} - 1 \right) \lambda_{1}^{2} \cos^{2} \omega = 0, \\ \mu \left( 1 - \xi + \xi \lambda_{2}^{2} \right) \left( \lambda_{1}^{2} - \lambda_{2}^{2} \right) + 2\gamma \left( \lambda_{1}^{2} - 1 \right) \lambda_{1}^{2} = 0, \\ \mu \left[ 1 - \xi + \xi \left( \lambda_{1}^{2} + \lambda_{2}^{2} \right) \right] \lambda_{2}^{2} + Jh(J) = 0, \\ \mu \left( 1 - \xi \right) \left( \lambda_{1}^{2} \sin^{2} \omega + \lambda_{2}^{2} \cos^{2} \omega \right) \\ + \mu \xi \left[ \lambda_{2}^{4} \cos^{2} \omega + \lambda_{1}^{2} \lambda_{2}^{2} \left( \cos^{2} \omega + 2 \sin^{2} \omega \right) \right] + Jh(J) + 2\gamma \left( \lambda_{1}^{2} - 1 \right) \lambda_{1}^{2} \sin^{2} \omega = 0. \end{split}$$

It can be shown that if  $(6.45)_2$  and  $(6.45)_3$  hold, then  $(6.45)_1$  and  $(6.45)_4$  are automatically satisfied. The free swelling principal stretches  $\lambda_1$  and  $\lambda_2$  are now determined from  $(6.45)_2$  and  $(6.45)_3$ . Note that  $(6.45)_2$  and  $(6.45)_3$  are independent of  $\omega$ . This is as expected since one may verify that  $(6.45)_2$  and  $(6.45)_3$  follow from a principal frame analysis of (6.44) by taking  $\mathbf{F} = \lambda_2 \mathbf{I} + (\lambda_1 - \lambda_2) \mathbf{M} \otimes \mathbf{M}$ .

The stretches  $\lambda_1$ ,  $\lambda_2$  and the corresponding values of J are plotted in Figure 6.3 for various values of  $\gamma$ . The special free swelling case for which  $\gamma=0$  means that there is no fiber effect so that  $\lambda_1=\lambda_2$  and  $J=\lambda_1^3$ . Note if  $\gamma>0$  then  $\lambda_2>\lambda_1$  since the additional resistance of the fibers causes less extension in the fiber direction under free swelling. Note that the orientation of the fibers  $\omega$  after the free swelling as given by (6.38) is dependent upon the reinforcement coefficient  $\gamma$  since  $\gamma$  determines the difference between the fiber stretch  $\lambda_1$  and the stretch  $\lambda_2$  that is orthogonal to the fibers. In particular, since  $\lambda_2>\lambda_1$ , it follows from (6.40) that  $\omega\geq\Omega$  ( $\omega>\Omega$  if  $0<\Omega<\pi/2$ ) and also that the difference between  $\omega$  and  $\Omega$  increases with  $\gamma$  (see Figure 6.4).

# 6.4 Steady State Diffusion through a Fiber Reinforced Layer

Now we consider pressure-driven diffusion of fluid through such a swollen fiber reinforced layer. The bottom of the layer is taken to be fixed to a rigid porous plate that is attached to the gel after free swelling (Figure 6.5). Let (x, y, z) denote coordinates in the deformed configuration. The pressure driven diffusion is anticipated to cause either a compaction or an expansion in the layer, and the presence of the fibers is anticipated to cause a further shearing deformation. Based on (6.41) the overall deformation from the original reference state to the deformed state is therefore taken



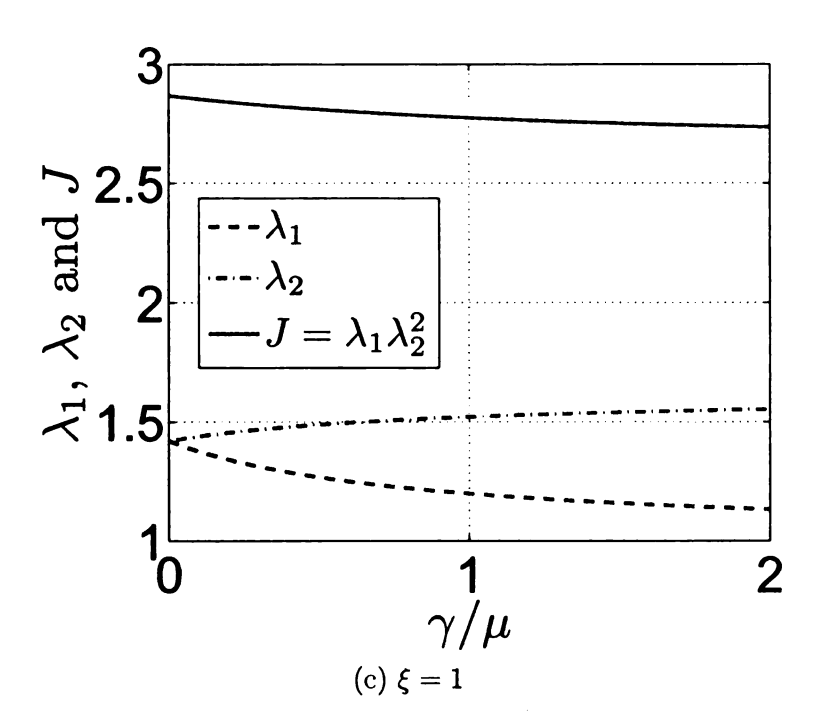


Figure 6.3: Stretch ratios of free swelling with fibers versus  $\gamma$  for  $\xi=0,\,\xi=0.5$  and  $\xi=1$  ( $M/\mu=100,\,\chi=0.425$ )

to be

$$x = \hat{x} + s(\hat{z}) = \Lambda_1 X + f(Z),$$
 (6.46)

$$y = \hat{y} = \lambda_2 Y,\tag{6.47}$$

$$z = u(\hat{z}) = g(Z),\tag{6.48}$$

where

$$\Lambda_1 = \lambda_1 \cos \Omega \cos \omega + \lambda_2 \sin \Omega \sin \omega. \tag{6.49}$$

Here the two expressions that multiply Z in  $(6.41)_1$  and  $(6.41)_3$  have been absorbed into the functions f(Z) and g(Z) respectively. Note that  $\Omega$  is the original fiber orientation and so known at the outset while  $\lambda_1$  and  $\lambda_2$  are regarded as known from the free swelling analysis (e.g. from Figure 6.3). Thus  $\omega$  is known in terms of this parameter from (6.40) after which  $\Lambda_1$  follows from (6.49). Note also that certain

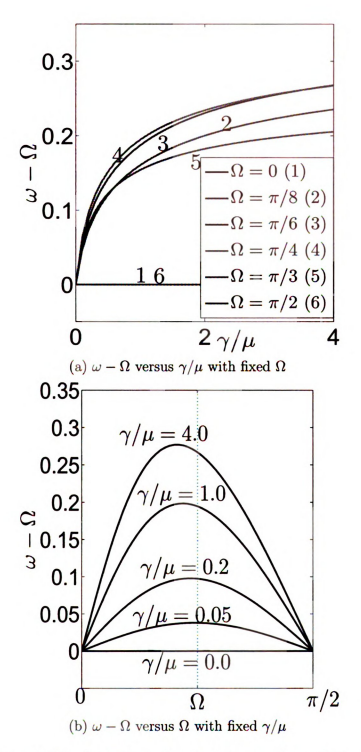
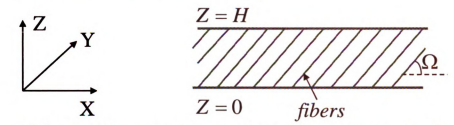
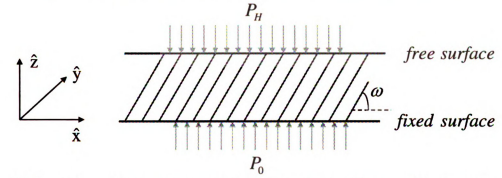


Figure 6.4: The variation of the change in orientation angle  $\omega-\Omega$  (in radians) with  $\xi=0$  and  $M/\mu=100,~\chi=0.425.$ 

care must be taken with (6.46) since (6.37) shows that  $f(Z) \neq s(\hat{z})$  since, instead,  $f(Z) = (\lambda_1 \sin \Omega \cos \omega - \lambda_2 \cos \Omega \sin \omega) Z + s(\hat{z}).$ 



(a) Original reference configuration (prior to immersion in solvent)



(b) Depiction of the pressure part of the boundary conditions with respect to the free swelling configuration

Figure 6.5: Representation of a pressure differential that will cause diffusional fluid seepage through a fiber reinforced layer

We first consider a steady-state diffusion in which case the solid particles are not in motion ( $\mathbf{v}^s = \mathbf{0}$ ). The fluid motion is assumed to be confined in the z direction, meaning

$$v^f = v^f(z)e_z$$
. (6.50)

Therefore the seepage velocity  $\mathbf{w} = \mathbf{v}^f$ .

The deformation gradient tensor F and left Cauchy-Green deformation tensor B associated with the mapping (6.46)-(6.48) from the reference configuration (X, Y, Z) to the swollen configuration (x, y, z) associated with the steady state diffusion are

then given by

$$\mathbf{F} = \begin{bmatrix} \Lambda_1 & 0 & f' \\ 0 & \lambda_2 & 0 \\ 0 & 0 & g' \end{bmatrix}, \qquad \mathbf{B} = \begin{bmatrix} \Lambda_1^2 + f'^2 & 0 & f'g' \\ 0 & \lambda_2^2 & 0 \\ f'g' & 0 & g'^2 \end{bmatrix}, \qquad (6.51)$$

where f' = df/dZ, g' = dg/dZ. Thus  $I_1 = \Lambda_1^2 + \lambda_2^2 + f'^2 + g'^2$ ,  $I_2 = \Lambda_1^2 \lambda_2^2 + \lambda_2^2 f'^2 + (\Lambda_1^2 + \lambda_2^2) g'^2$  and  $J = \Lambda_1 \lambda_2 g'$ .

It follows from (6.44) with (2.13), (2.5) and (6.43) that the hyperelastic stresses are

$$\begin{split} \sigma_{xx}^{mix} &= \frac{\mu}{J} \left\{ \left[ 1 + \xi \left( \lambda_{2}^{2} - 1 \right) \right] \left( f'^{2} + \Lambda_{1}^{2} \right) + \xi \Lambda_{1}^{2} g'^{2} \right\} + h(J) \\ &\quad + \frac{2\gamma}{J} \Phi'_{fib} \left( I_{4} \right) \left( \Lambda_{1}^{2} \cos^{2} \Omega + f'^{2} \sin^{2} \Omega + \Lambda_{1} f' \sin 2\Omega \right), \\ \sigma_{yy}^{mix} &= \frac{\mu}{J} \lambda_{2}^{2} \left[ 1 + \xi \left( \Lambda_{1}^{2} - 1 + f'^{2} + g'^{2} \right) \right] + h(J), \\ \sigma_{zz}^{mix} &= \frac{\mu}{J} \left[ 1 + \xi \left( \Lambda_{1}^{2} + \lambda_{2}^{2} - 1 \right) \right] g'^{2} + h(J) + \frac{2\gamma}{J} \Phi'_{fib} \left( I_{4} \right) g'^{2} \sin^{2} \Omega, \\ \sigma_{xz}^{mix} &= \sigma_{zx}^{mix} = \frac{\mu}{J} \left[ 1 + \xi \left( \lambda_{2}^{2} - 1 \right) \right] f'g' + \frac{2\gamma}{J} \Phi'_{fib} \left( I_{4} \right) g' \sin \Omega \left( \Lambda_{1} \cos \Omega + f' \sin \Omega \right), \\ \sigma_{xy}^{mix} &= \sigma_{yz}^{mix} = 0, \end{split}$$
(6.52)

where 
$$h(J) = dH(J)/dJ$$
 and  $\Phi'_{fib}(I_4) = d\Phi_{fib}(I_4)/dI_4 = I_4 - 1$ .

It is to be remarked here that the assumption upon the fluid diffusion direction in (6.50) can now be verified by the use of (6.16) with  $\hat{\sigma}^f = 0$  by making use of the fact that  $p_1$  and  $\Psi_{cur}$  are independent of planar coordinates x and y. Namely, since  $p_1$  and  $\Psi_{cur}$  in (6.16) vary only in the z-direction, it may then be concluded that the vector  $\hat{\mathbf{b}}$  must be in the z-direction. Therefore it must then follow from (6.31) that  $\mathbf{w}$  is similarly aligned in the z-direction.

In view of (6.52) the governing equation (6.30) is automatically satisfied in the

y direction, whereas the governing equations in the x and z directions give

$$\frac{d}{dz}\sigma_{xz}^{mix} = 0, (6.53)$$

and

$$\frac{d}{dz}\sigma_{zz}^{mix} + \frac{\alpha v^f}{(J-1)^n} = 0. ag{6.54}$$

It is remarked here that the derivatives d/dz in the Eulerian system are eventually transformed into derivatives in Lagrangian system d/dZ through the connection  $d/dZ = d/dz \cdot dz/dZ = g' \cdot d/dz$ .

The fluid velocity is now determined by the mass conservation equation (6.4). For steady-state flow, the integral form of (6.4) in the z direction immediately gives

$$v^f = \frac{q}{\rho^f} = \frac{q/\rho_0^f}{1 - 1/J},\tag{6.55}$$

where q is an as yet unknown constant which can in turn be related to the fluid mass flux.

We now turn to consider the boundary conditions. At the bottom (Z=0), the solid deformation is constrained, leading to

$$f(0) = 0, (6.56)$$

$$g(0) = 0. (6.57)$$

Based on (6.29), the boundary conditions for this steady-state flow problem are

$$\sigma_{zz}^{mix}(0) = T_0, \qquad \sigma_{zz}^{mix}(H) = 0,$$
 (6.58)

where  $T_0$  is the traction reaction due to the support provided by the rigid porous

plate. It follows from the equilibrium equation (6.12) and the boundary condition (6.22) that

$$T_0 = P_H - P_0. (6.59)$$

At the top there is no support structure so that  $\mathbf{t} = \mathbf{0}$ , hence requiring in addition to  $(6.58)_2$  that  $\sigma_{zy}^{mix}(H) = 0$  and  $\sigma_{zx}^{mix}(H) = 0$ . The first of these,  $\sigma_{zy}^{mix}(H) = 0$ , is automatic by (6.52). It is also to be remarked that (6.59) shows that the boundary conditions (6.58) are only dependent on the pressure difference  $P_H - P_0$ . Thus the fluid flow is only affected by the pressure difference  $P_H - P_0$  rather than the specific values of fluid pressure  $P_H$  on the upstream side or  $P_0$  on the downstream side.

In order to study the problem in more detail we shall temporarily imagine a broader class of boundary conditions at Z = H than that given by the above condition  $\sigma_{zx}^{mix}(H) = 0$ . Namely we consider either specifying the shear displacement  $f_h$  with associated boundary condition

$$f(H) = f_h \tag{6.60}$$

or else we may specify the shear traction  $\tau^s$  with associated boundary condition

$$\sigma_{zx}^{mix}(H) = \tau^s. (6.61)$$

In particular, (6.61) with  $\tau^s=0$  recovers the boundary condition of physical interest for a free surface

$$\sigma_{zx}^{mix}(H) = 0. ag{6.62}$$

In principle, (6.53) with (6.52) provides an ordinary differential equation involving f'(Z), g'(Z), f''(Z) and g''(Z). Substituting from (6.55) into (6.54) and again using (6.52) provides another such second-order ordinary differential equation for f(Z) and g(Z). This second ordinary differential equation also contains the as yet unknown constant q from (6.55). Thus for a well-posed problem we anticipate the

need for five boundary conditions. There are indeed 5 boundary conditions, namely four from (6.56)-(6.58) and one from either (6.60) or (6.61). Therefore this seems to be a well-posed boundary value problem at least from a mathematical point of view. Hence it should be possible to set up a numerical routine to solve this problem.

An interesting aspect to this problem is that in the absence of fiber reinforcing  $(\gamma = 0)$  the solution will involve f = 0. This can be seen by solving (6.53) with boundary condition (6.56). This f = 0 solution also corresponds to the type of situation considered by previous researchers in [46] and [71].

#### 6.4.1 Numerical Analysis

We take the following nondimensional forms

$$\bar{Z} = \frac{Z}{H}, \quad \bar{f} = \frac{f}{H}, \quad \bar{g} = \frac{g}{H}, \quad \bar{\gamma} = \frac{\gamma}{\mu}, \quad \bar{M} = \frac{M}{\mu},$$
 (6.63)

and

$$f' = \frac{df}{dZ} = \frac{d\bar{f}}{d\bar{Z}} = \bar{f}', \quad g' = \frac{dg}{dZ} = \frac{d\bar{g}}{d\bar{Z}} = \bar{g}',$$

$$f'' = \frac{df'}{dZ} = \frac{d\bar{f}'}{Hd\bar{Z}} = \frac{1}{H}\bar{f}'', \quad g'' = \frac{dg'}{dZ} = \frac{d\bar{g}'}{Hd\bar{Z}} = \frac{1}{H}\bar{g}''.$$
(6.64)

With the use of  $(6.52)_3$ ,  $(6.52)_4$  and (6.55), the governing equations (6.53) and (6.54) become two nondimensional second order ordinary differential equations, which are too long to be displayed here and so given in Appendix A.

A 4-th order Runge-Kutta Scheme and a shooting method are adopted to solve these two nondimensional governing equations. In particular it is most efficient to assign the constant q and to calculate  $P_H - P_0$ . Some of the material parameters are obtained from Paul and Ebra-Lima [24]:  $\mu = 2.375 \times 10^6 \ dyne/cm^2$ ,  $\chi = 0.425$ ,  $M = 100\mu$ ,  $\rho_0^f = 0.869 \ g/cm^3$ . The initial thickness of the slab is taken to be the same as that of the experiments described in [24], namely  $H = 0.0265 \ cm$ .

First we consider the case where there are no fibers  $(\gamma = 0)$  and hence no shear

displacement  $(f(Z) \equiv 0)$ . This case corresponds to the experiments conducted in [24]. Since f is formally eliminated in this case, the three relevant boundary conditions are then given by

$$g(0) = 0, \quad \sigma_{zz}^{mix}(0) = P_H - P_0, \quad \sigma_{zz}^{mix}(H) = 0.$$
 (6.65)

Numerical solutions associated with the above boundary conditions are shown in Figure 6.6a and compared with the experimental data in [24]. Thus the shooting involves matching to the value  $\sigma_{zz}^{mix}(H) = 0$ . In this case, since f' = 0 and  $\gamma = 0$  in  $(6.52)_4$ , it follows that  $\sigma_{zx}^{mix} = 0$  everywhere for this solution.

The values  $\xi=0$ , n=5,  $\alpha=1.556\times 10^{19}~gm/cc\cdot day$  give a good fit to the experimental data from [24] (solid curve in Figure 6.6(a)). For the sake of comparison these values of n and  $\alpha$  are then used to obtain the the flux-pressure curve associated with  $\xi=1$  (dashed line in Figure 6.6(a)). This comparison shows that the  $\xi=1$  model predicts far less mass flux at any fixed pressure difference than does the  $\xi=0$  neo-Hookean model for the same n and  $\alpha$ . The variation of the nondimensional normal displacement  $(z-\hat{z})/H$  along the plate thickness is also shown in Figure 6.7(a) for  $\xi=0$  at the pressure difference  $P_H-P_0=200psi$ .

Conversely for  $\xi=1$  we find that the values of n=16,  $\alpha=3.014\times 10^{20}~gm/cc\cdot day$  give a good fit to the same set of experimental data (solid curve in Figure 6.6(b)). These values of n and  $\alpha$  are then used to obtain the flux-pressure curve associated with  $\xi=0$  (dashed curve in Figure 6.6(b)). This shows that the  $\xi=0$  model predicts much greater mass flux at any fixed pressure difference than the model of  $\xi=1$ . The nondimensional normal displacement  $(z-\hat{z})/H$  along the thickness direction is depicted in Figure 6.7(b) for the case where  $\xi=1$  and  $P_H-P_0=200psi$ .

Figure 6.7 for both  $\xi = 0$  and  $\xi = 1$  shows that the isotropic layer is contracted in the thickness direction from its free swelling value. The maximum normal displace-

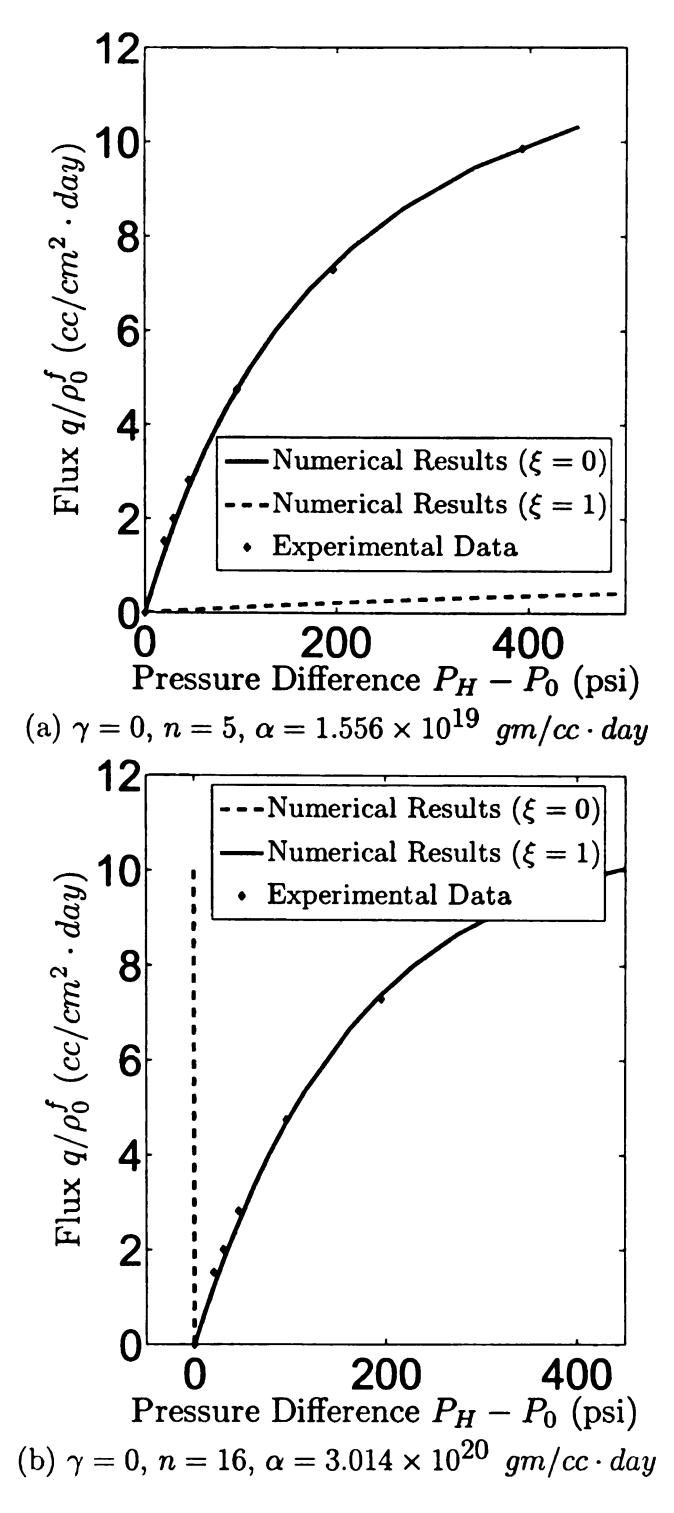


Figure 6.6: Comparison of the numerical results with the experimental data [24]

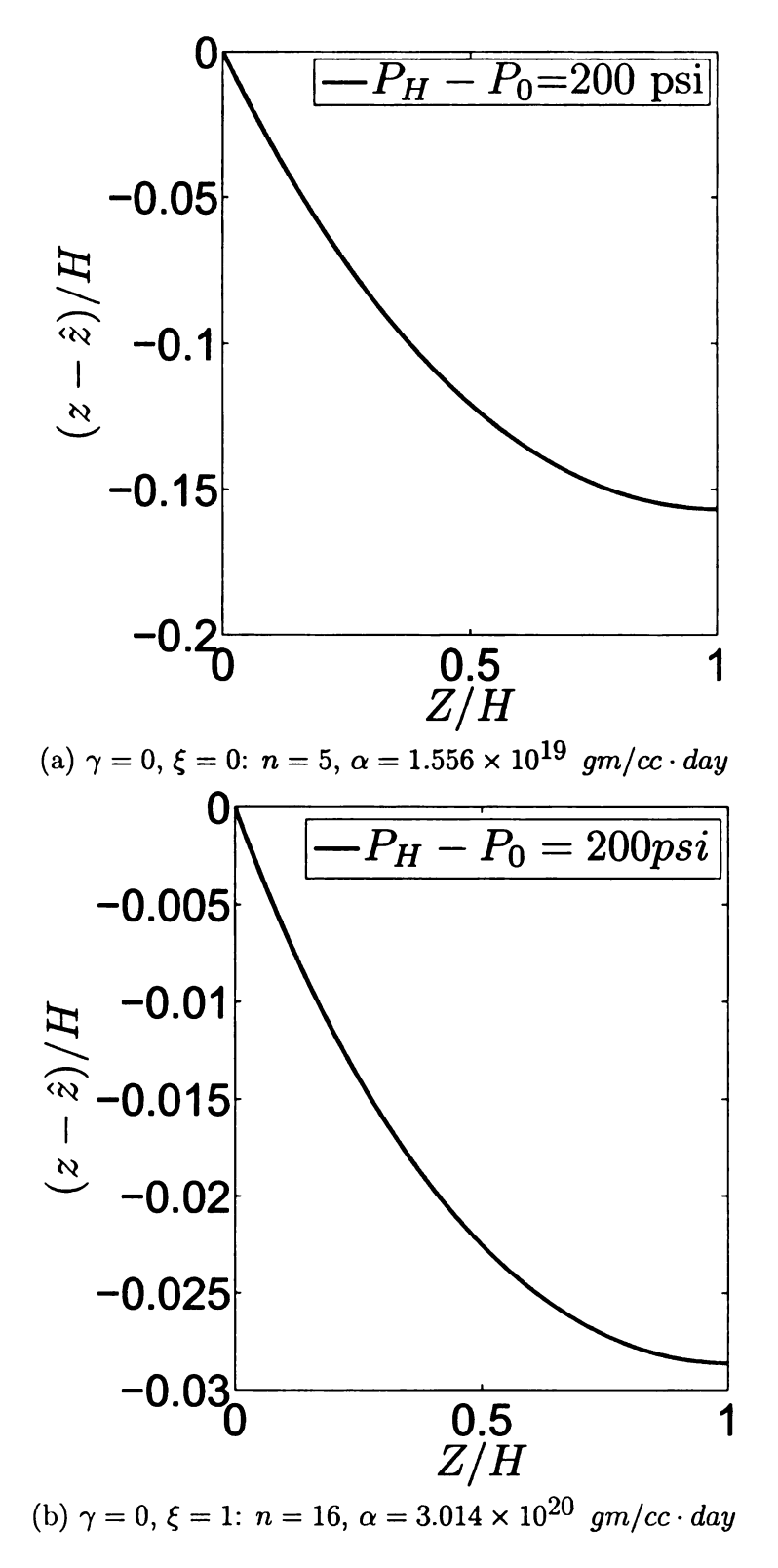


Figure 6.7: The variation of nondimensional displacement in the thickness direction after free swelling at  $P_H - P_0 = 200 psi$  with  $\gamma = 0$  for  $\xi = 0$  and  $\xi = 1$ .

ment associated with the fluid diffusion (which occurs at the upstream boundary Z=H) with various pressure difference  $P_H-P_0$  is shown in Figure 6.8 for both  $\xi=0$  (with n=5,  $\alpha=1.556\times 10^{19}~gm/cc\cdot day$ ) and for  $\xi=1$  (with n=16,  $\alpha=3.014\times 10^{20}~gm/cc\cdot day$ ).

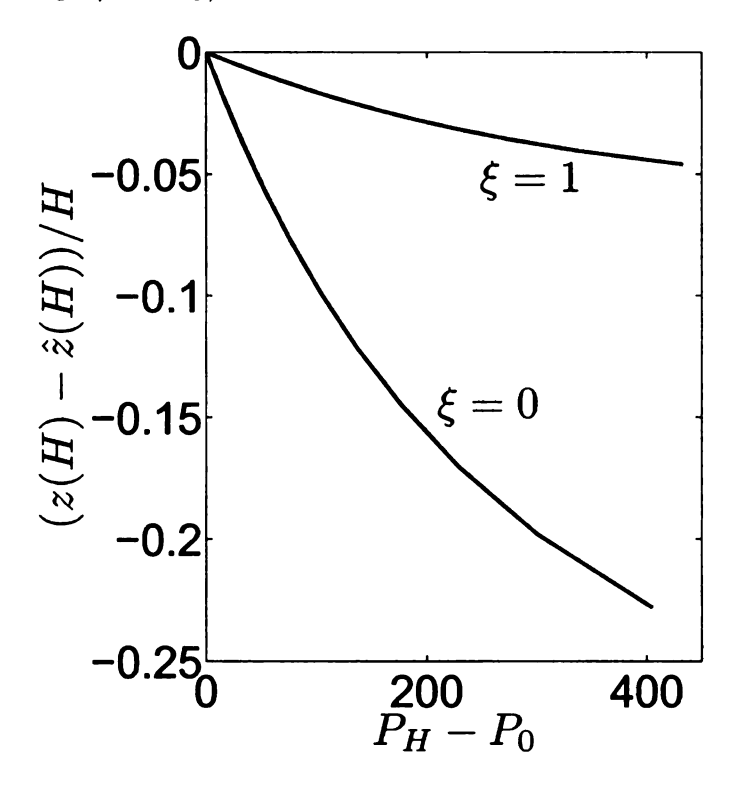


Figure 6.8: The normal displacement of the free surface vs. pressure difference for the material parameters in Figure 6.7(a) with  $\xi = 0$  and Figure 6.7(b) with  $\xi = 1$ 

# 6.4.2 Boundary Value Problems

Now we begin to study the effect of fiber reinforcement. This in turn requires the consideration of the shear displacement f(Z) in the x-direction. The constitutive model requires specification of  $\Omega$  and  $\gamma$ . In what follows we take  $\Omega = \pi/4$  and consider the effects of various  $\gamma$ . In the numerical analysis that follows, the material parameter  $\xi$  is taken to be 0. Accordingly we will choose the corresponding values of n=5,  $\alpha=1.556\times 10^{19}~gm/cc\cdot day$ .

#### Lateral constraint boundary condition at Z = H

First we discuss the cases in which there is a fiber effect  $(\gamma \neq 0)$  but with the surface Z = H held fixed in the lateral direction after free swelling. Define

$$\Gamma(Z) = \left[ \lambda_1 \sin \Omega \left( 1 + \frac{\lambda_2^2}{\lambda_1^2} \tan^2 \Omega \right)^{-1/2} - \lambda_2 \cos \Omega \left( 1 + \frac{\lambda_1^2}{\lambda_2^2} \cot^2 \Omega \right)^{-1/2} \right] Z$$
(6.66)

so that it follows from (6.41) that  $\Gamma(Z)$  is the pure free swelling shear displacement that is associated with the fiber reinforcement. The boundary conditions that we first wish to consider are given by

$$f(0) = 0, \quad g(0) = 0, \quad \sigma_{zz}^{mix}(0) = P_H - P_0,$$
  
 $f(H) - \Gamma(H) = 0, \quad \sigma_{zz}^{mix}(H) = 0.$  (6.67)

The fourth order Runge-Kutta scheme with the shooting method is again employed to solve this boundary value problem. The flux-pressure difference relation obtained from this procedure is depicted in Figure 6.9(a). It shows that if the fiber reinforcing parameter  $\bar{\gamma}$  is increased then a larger pressure difference is required to sustain the same amount of fluid flux. The shear stress  $\sigma_{zx}^{mix}$  at the top surface Z = H that is necessary to maintain this deformation is then plotted in Figure 6.9(b).

We now turn to consider the fiber deformation, and begin by recalling that the fibers remains straight lines after free swelling since free swelling is a homogeneous deformation. However, with the pressure difference and fluid flow, the deformation is no longer homogeneous and so the fibers now become curved (see Figure 6.10). Their deformed geometry and slope are shown in Figure 6.11.

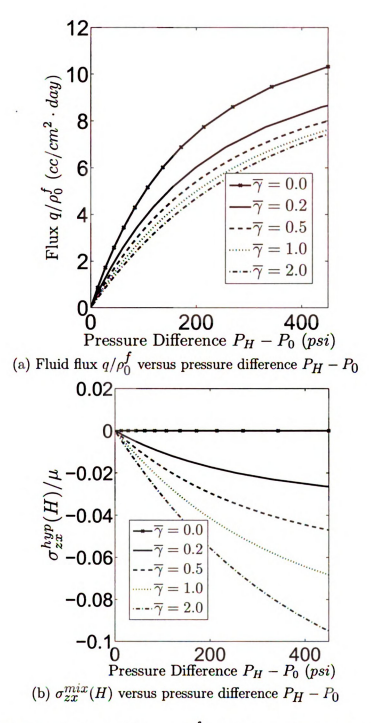


Figure 6.9: Variation of the fluid flux  $q/p_0^f$  and the required reactive shear stress  $\sigma_{xx}^{mix}(H)$  with pressure difference  $P_H - P_0$  for various fiber reinforcement coefficients  $\overline{\gamma}$  with  $\xi = 0$ , n = 5,  $\alpha = 1.556 \times 10^{19}$   $gm/cc \cdot day$  when the boundary conditions are given by (6.67).

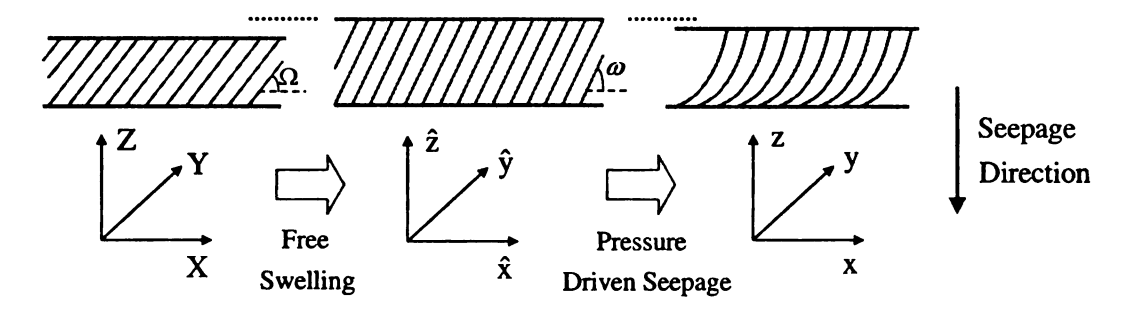


Figure 6.10: The fibers become curved in the inhomogeneous deformation associated with pressure driven fluid seepage as depicted in panel (c). This is a schematic representation.

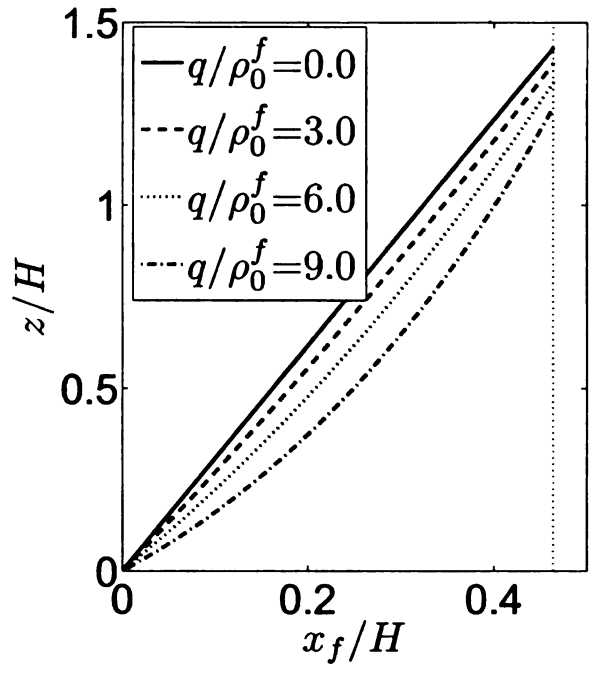
#### No shear traction boundary condition at Z = H

In the second case, we consider a free surface boundary condition at the top of the layer Z = H. Then the corresponding boundary conditions are

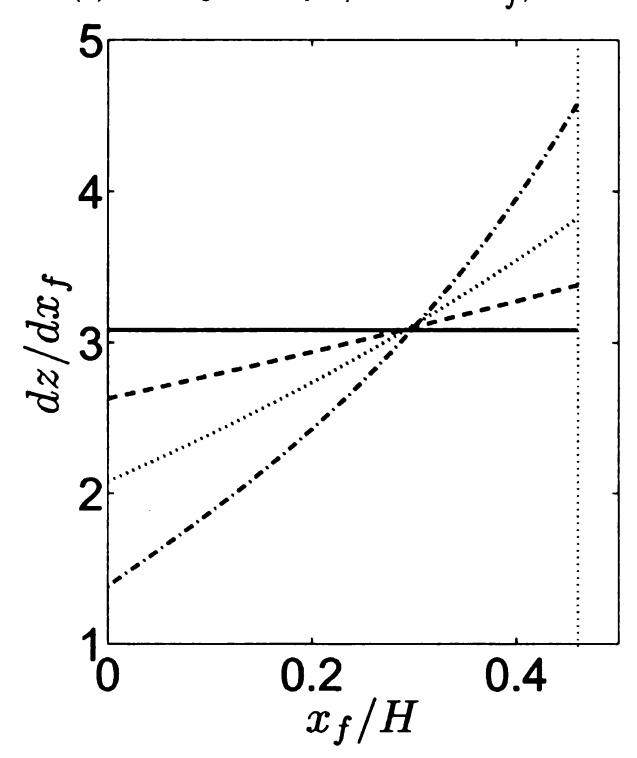
$$f(0) = 0, \quad g(0) = 0, \quad \sigma_{zz}^{mix}(0) = P_H - P_0,$$
  
 $\sigma_{zx}^{mix}(H) = 0, \quad \sigma_{zz}^{mix}(H) = 0.$  (6.68)

The relation between the flux and the pressure difference as determined from numerical solution of this boundary value problem is depicted in Figure 6.12(a). Again, the numerical results show that stiffer fibers tend to decrease the fluid flux for the same pressure difference. The additional lateral displacement at the top surface Z = H after free swelling  $f(H) - \Gamma(H)$  is also plotted in Figure 6.12(b).

This then motivates us to study the effect of the initial fiber orientation on the shear displacement of the free surface. To consider this effect, we first keep the fiber reinforcing coefficient at  $\bar{\gamma}=2.0$  and vary the pressure differences  $P_H-P_0$  (Figure 6.13(a)). The results show that the maximum shearing displacement of the free surface occurs at fiber orientation angle  $\Omega > \pi/4$ . If  $P_H-P_0$  is small then the angle  $\Omega$  associated with this maximum is very near  $\pi/4$ . As  $P_H-P_0$  increases the angle  $\Omega$  that locates the maximum also increases. In the other way, we could instead keep



(a) Fiber geometry z/H versus  $x_f/H$ 



(b) The slope of the fibers  $dz/dx_f$  versus  $x_f/H$ 

Figure 6.11: The fiber geometry at various seepage rates with  $\bar{\gamma}=2.0,\,\xi=0,\,n=5$  and  $\alpha=1.556\times 10^{19}\,$  gm/cc·day when the boundary conditions are given by (6.67). ( $x_f$  denotes the projected distance onto x-axis between an arbitrary point on the fiber and the tip (z=0) of the same fiber.)

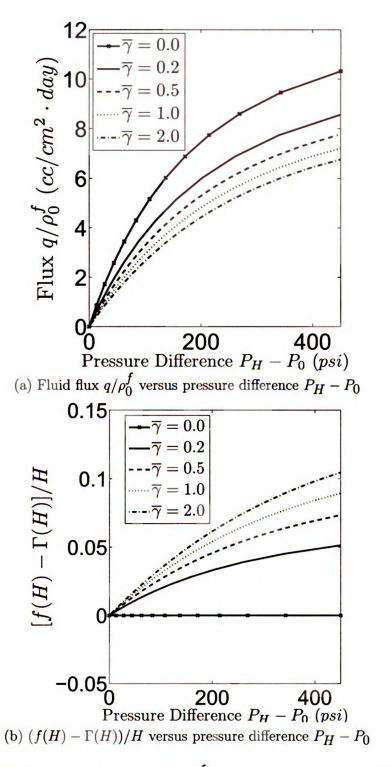


Figure 6.12: Variation of the fluid flux  $q/\rho_0^f$  and shear displacement  $f(H) - \Gamma(H)$  with pressure difference  $P_H - P_0$  for various fiber reinforcement coefficients  $\overline{\gamma}$  with  $\xi = 0$ , n = 5,  $\alpha = 1.556 \times 10^{19} \ gm/cc \cdot day$  when the boundary conditions are given by (6.68).

 $P_H - P_0$  fixed (at 200psi in Figure 6.13(b)) and vary the fiber reinforcing coefficient  $\bar{\gamma}$ . It is again found that the maximum shear occurs at an angle  $\Omega$  greater than  $\pi/4$ . However it is now found that this angle is close to  $\pi/4$  when  $\bar{\gamma}$  is large. The angle increases further beyond  $\pi/4$  as  $\bar{\gamma}$  decreases.

Define

$$\Upsilon(Z) = \left[\lambda_1 \left(1 + \frac{\lambda_1^2}{\lambda_2^2} \cot^2 \Omega\right)^{-1/2} \sin \Omega + \lambda_2 \left(1 + \frac{\lambda_2^2}{\lambda_1^2} \tan^2 \Omega\right)^{-1/2} \cos \Omega\right] Z,$$
(6.69)

where  $\Upsilon(Z)$  is the normal displacement caused by the free swelling deformation (6.41). Then the dependence of the normal displacement on original fiber orientation for different pressure difference is shown in Figure 6.14(a) and for different  $\bar{\gamma}$  is shown in Figure 6.14(b).

Again in this case, the fibers become curved and their deformed geometry is shown in Figure 6.15. In particular, comparing Figure 6.11(a) to Figure 6.15(a) shows that the traction free boundary condition gives rise to more overall shortening of the layer in the z-direction for the same amount of fluid seepage. A corresponding conclusion holds if the pressure difference is kept fixed.

# 6.5 General Formulation for Non Steady State Diffusion

In this section, we discuss the time dependent fluid seepage problem in which case the fluid velocity changes with time. The various field variables are now functions of (z,t). In particular we consider the following initial-boundary value problem. We start with a steady state flow problem as described in Section 6.4 with an initial upstream pressure  $P_H^I$ , an initial downstream pressure  $P_0^I$ , and hence an initial fluid pressure difference  $P_H^I - P_0^I$ . We then suddenly change the upstream and downstream

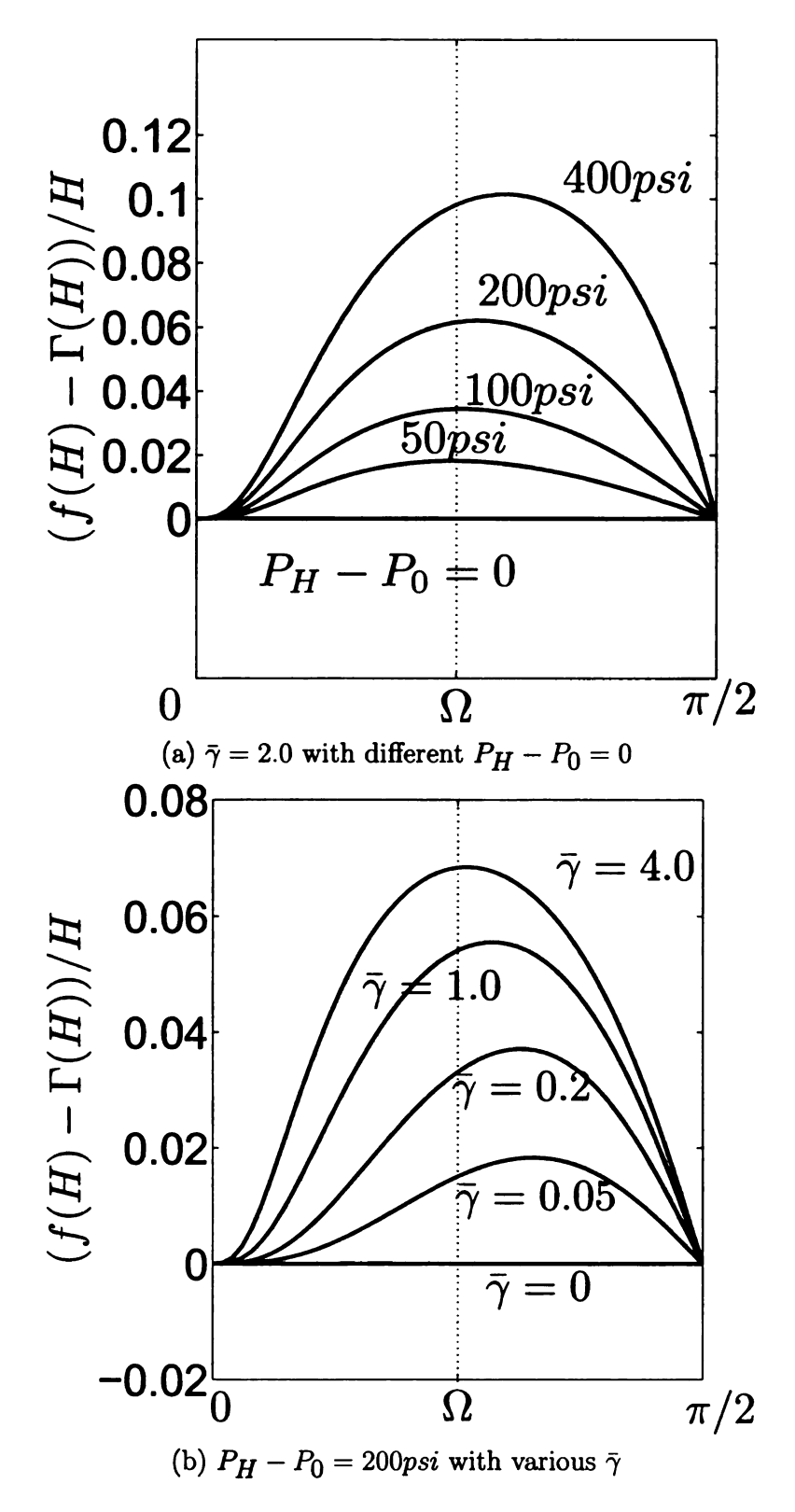


Figure 6.13: The shear displacements as a function of the initial fiber orientation under a free surface traction boundary condition at Z = H.

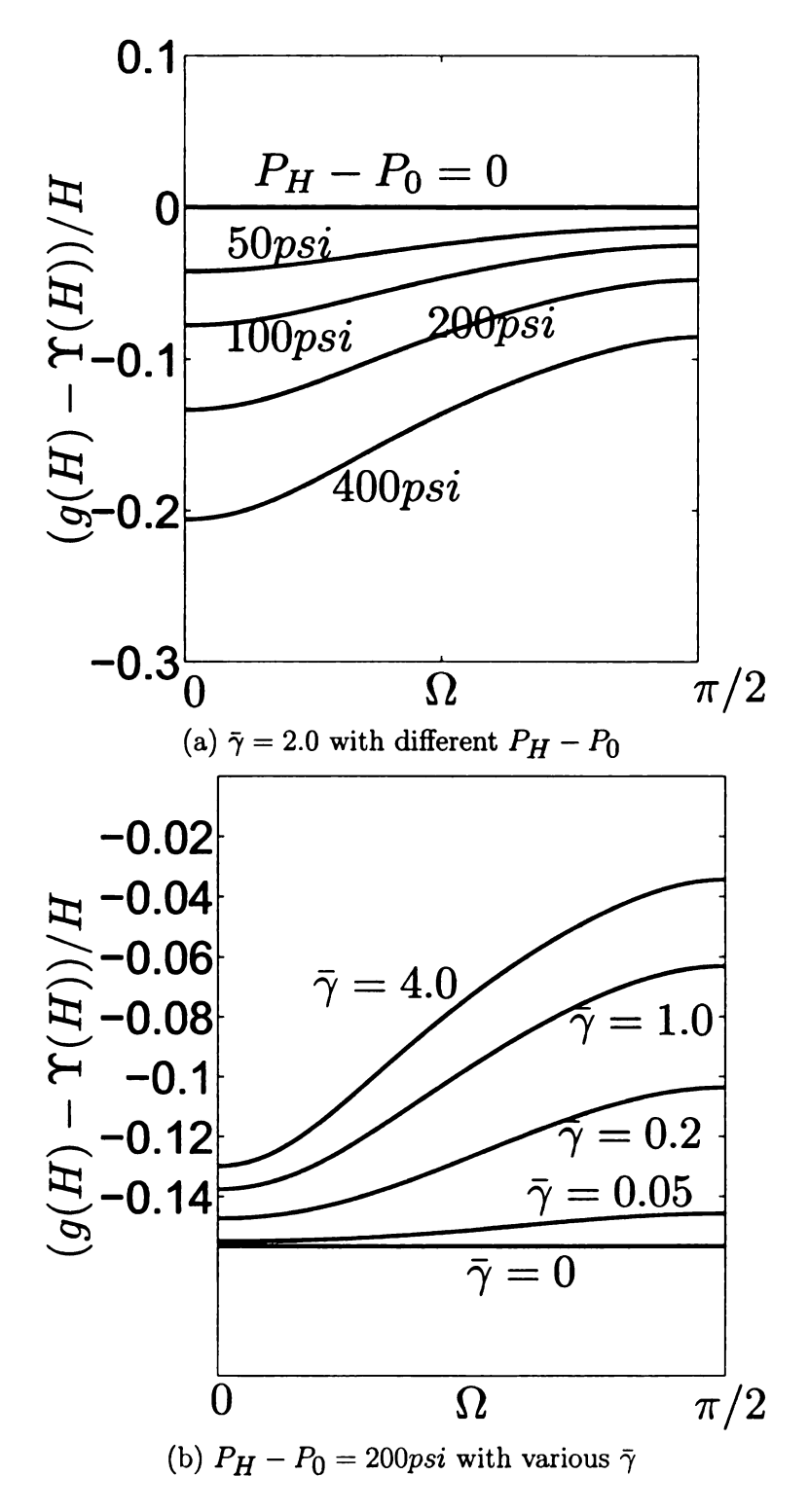
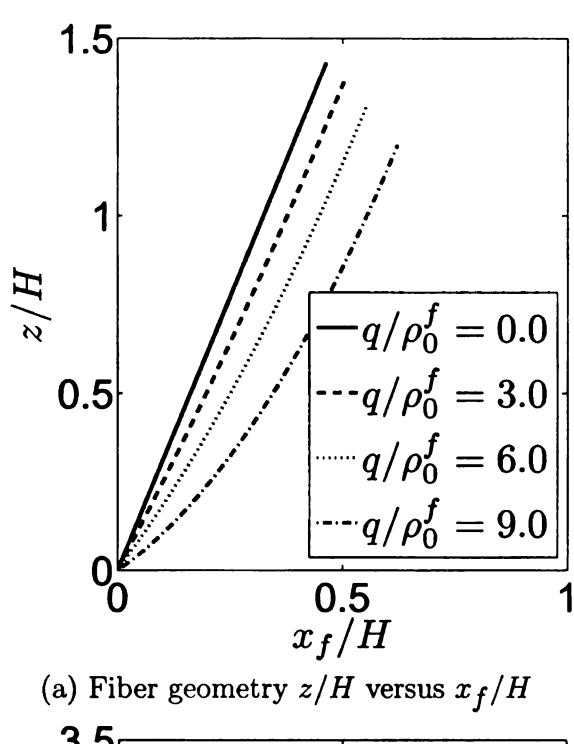
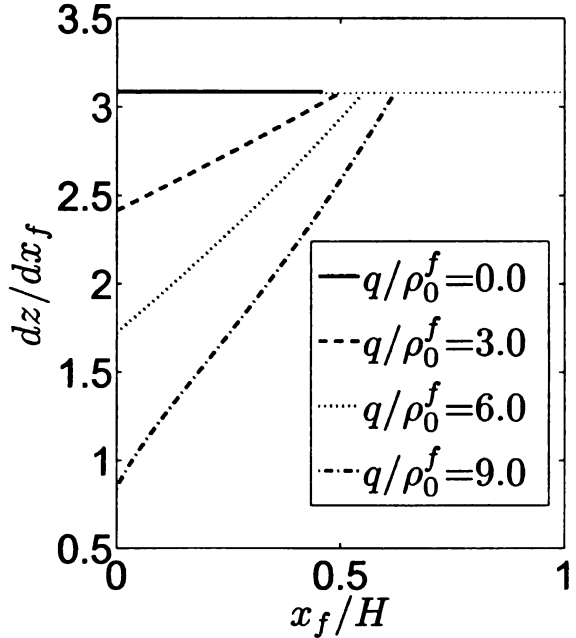


Figure 6.14: The normal displacements as a function of initial fiber orientations with a free surface traction boundary condition at Z = H.





(b) The slope of the fibers  $dz/dx_f$  versus  $x_f/H$ 

Figure 6.15: The fiber geometry at various seepage rates with  $\bar{\gamma}=2.0,\,\xi=0,\,n=5$  and  $\alpha=1.556\times 10^{19}~gm/cc\cdot day$  when the boundary conditions are given by (6.68). The common slope value at Z=H in (b) is a direct consequence of the boundary conditions (6.68)<sub>4</sub> and (6.68)<sub>5</sub>.

pressures to  $P_H^F$  and  $P_0^F$  so that the pressure difference abruptly becomes  $P_H^F - P_0^F$ . The evolution of the solid deformation as well as the fluid flux is of interest. As  $t \to \infty$  one would anticipate that the solution to this problem would approach the steady state diffusion associated with  $P_H^F - P_0^F$ .

The boundary condition for t > 0 follow again from (6.58) and (6.59) as

$$\sigma_{zz}^{mix}(0,t) = P_H^F - P_0^F, \qquad \sigma_{zz}^{mix}(H,t) = 0.$$
 (6.70)

Note that it makes no difference whether the pressure change  $\Delta P = (P_H^F - P_0^F) - (P_H^I - P_0^I)$  occurs all on the upstream side (Z = H), all on the downstream side (Z = 0), or in some combination.

Now the solid velocity  $\mathbf{v}^s$  is no longer zero but  $\mathbf{v}^s = v_x^s \hat{\mathbf{e}}_x + v_z^s \hat{\mathbf{e}}_z$  instead. Similarly the fluid velocity  $\mathbf{v}^f = v_x^f \hat{\mathbf{e}}_x + v_z^f \hat{\mathbf{e}}_z$  We now recall that the dissipative interactive force  $\hat{\mathbf{b}}$  as well as seepage velocity  $\mathbf{w}$  only has the component in the z direction (see the discussion after (6.52)). Since  $\mathbf{w} = \mathbf{v}^f - \mathbf{v}^s = (v_x^f - \dot{f})\hat{\mathbf{e}}_x + (v_z^f - \dot{g})\hat{\mathbf{e}}_z$  it follows that  $v_x^f - \dot{f} = 0$ . Here we denote

$$\dot{f} = v_x^s = \frac{\partial f(Z, t)}{\partial t} \Big|_{Z}, \quad \dot{g} = v_z^s = \frac{\partial g(Z, t)}{\partial t} \Big|_{Z}.$$
 (6.71)

The mass balance equation (6.4) no longer gives the steady state condition (6.55) but instead now gives

$$\frac{\partial}{\partial t} \left( 1 - \frac{1}{J} \right) + \frac{\partial}{\partial z} \left[ \left( 1 - \frac{1}{J} \right) v_z^f \right] = 0. \tag{6.72}$$

The stress equilibrium equations now become

$$\frac{\partial}{\partial z}\sigma_{xz}^{mix} = 0, (6.73)$$

and

$$\frac{\partial}{\partial z}\sigma_{zz}^{mix} + \frac{\alpha(v_z^f - \dot{g})}{(J-1)^n} = 0. \tag{6.74}$$

For the convenience of the numerical scheme it is necessary to transform the Eulerian partial derivatives into Lagrangian partial derivatives in the following analysis. For an arbitrary variable  $\varphi = \varphi(z,t) = \varphi[z(Z,t),t]$ , its Lagrangian partial derivatives could be determined from their Eulerian forms with the use of chain rule:

$$\frac{\partial \varphi}{\partial Z}\Big|_{t} = \frac{\partial \varphi}{\partial z}\Big|_{t} \frac{\partial z}{\partial Z}\Big|_{t} = \frac{\partial \varphi}{\partial z}\Big|_{t} g'(Z, t), \qquad (g'(Z, t) = \frac{\partial z(Z, t)}{\partial Z}\Big|_{t})$$

$$\frac{\partial \varphi}{\partial t}\Big|_{Z} = \frac{\partial \varphi}{\partial t}\Big|_{z} + \frac{\partial \varphi}{\partial z}\Big|_{t} \frac{\partial z}{\partial t}\Big|_{Z} = \frac{\partial \varphi}{\partial t}\Big|_{z} + \frac{\partial \varphi}{\partial z}\Big|_{t} \dot{g}(Z,t), \qquad (\dot{g}(Z,t) = \frac{\partial z(Z,t)}{\partial t}\Big|_{Z}).$$

Therefore it follows that

$$\frac{\partial \varphi}{\partial z}\Big|_{t} = \frac{\partial \varphi}{\partial Z}\Big|_{t} \frac{1}{g'(Z, t)} \tag{6.75}$$

and

$$\frac{\partial \varphi}{\partial t}\Big|_{z} = \frac{\partial \varphi}{\partial t}\Big|_{Z} - \frac{\partial \varphi}{\partial z}\Big|_{t} \dot{g}(Z, t) = \frac{\partial \varphi}{\partial t}\Big|_{Z} - \frac{\partial \varphi}{\partial Z}\Big|_{t} \frac{\dot{g}(Z, t)}{g'(Z, t)}, \tag{6.76}$$

where the second equality of (6.76) has made use of (6.75).

#### 6.5.1 Isotropic Layer

In this section, we consider the transient diffusion problem described in Section 6.5 for the special case in which the layer is isotropic ( $\gamma = 0$ ). Thus  $\lambda_1 = \lambda_2 = \lambda_1$  and there is again no shear displacement, i.e.,  $f(Z) \equiv 0$ . Thus the stress equilibrium equation (6.73) in the x-direction is trivial. Making use of (6.75) to evaluate  $\partial \sigma_{zz}^{mix}/\partial z$  it is found that the governing equation (6.74) in the z-direction

gives

$$\left[1 + \xi(2\lambda^2 - 1) + \frac{\lambda^4}{\mu}h'(\lambda^2 g')\right]g'' + \frac{\alpha\lambda^2}{\mu}\left(\frac{1}{\lambda^2 g' - 1}\right)^n(v_z^f - \dot{g})g' = 0, \quad (6.77)$$

where h'(J) = dh/dJ.

Using (6.75) and (6.76) to express (6.72) in terms of Lagrangian partial derivatives, and then eliminating  $v_z^f$  between that result and (6.72) gives a partial differential equation for g(Z,t) that is third order in space and first order in time. This equation is of the form

$$\dot{g}' = \frac{1}{C} F_1(g') g''' + \frac{1}{C} F_2(g') g''^2, \tag{6.78}$$

where  $F_1(g')$  and  $F_2(g')$  are both unit free functions of the single field variable g', and  $C = \alpha \lambda^4/\mu$ . Note that C has units of  $\sec/cm^2$ . These functions are given in Appendix B The most obvious boundary condition is given by the fixed displacement boundary condition  $g(0,t) \equiv 0$  at the downstream location Z = 0. It is also possible to obtain boundary values for g'(0,t) and g'(H,t). These are found by solving equation (6.70) using (6.52) with  $\gamma = 0$  and  $J = \lambda^2 g'$ . This is done numerically and does not present any special difficulty. It is also necessary to assign an initial condition for g(Z,0) for 0 < Z < H. This is given by the steady state solution associated with the pressure difference  $P_H^I - P_0^I$ . With respect to the (z,t) domain there is now a discontinuity in g'(Z,t) at the corner (Z,t) = (0,0) because  $\lim_{t \to 0} g'(0,t)$  comes from the boundary condition while  $\lim_{Z \to 0} g'(Z,0)$  comes from the initial condition. Note also that no such discontinuity in g'(Z,t) occurs at the corner (Z,t) = (H,0).

We partition the space domain by using a mesh  $Z_0,...,Z_I$  and time domain using a mesh  $t_0,....,t_N$ . In particular, at each time step there are I-1 internal nodes (i=1,2,...,I-1) since i=0 and i=I are boundary nodes. We assume a uniform partition both in space and in time, so the difference between two consecutive space

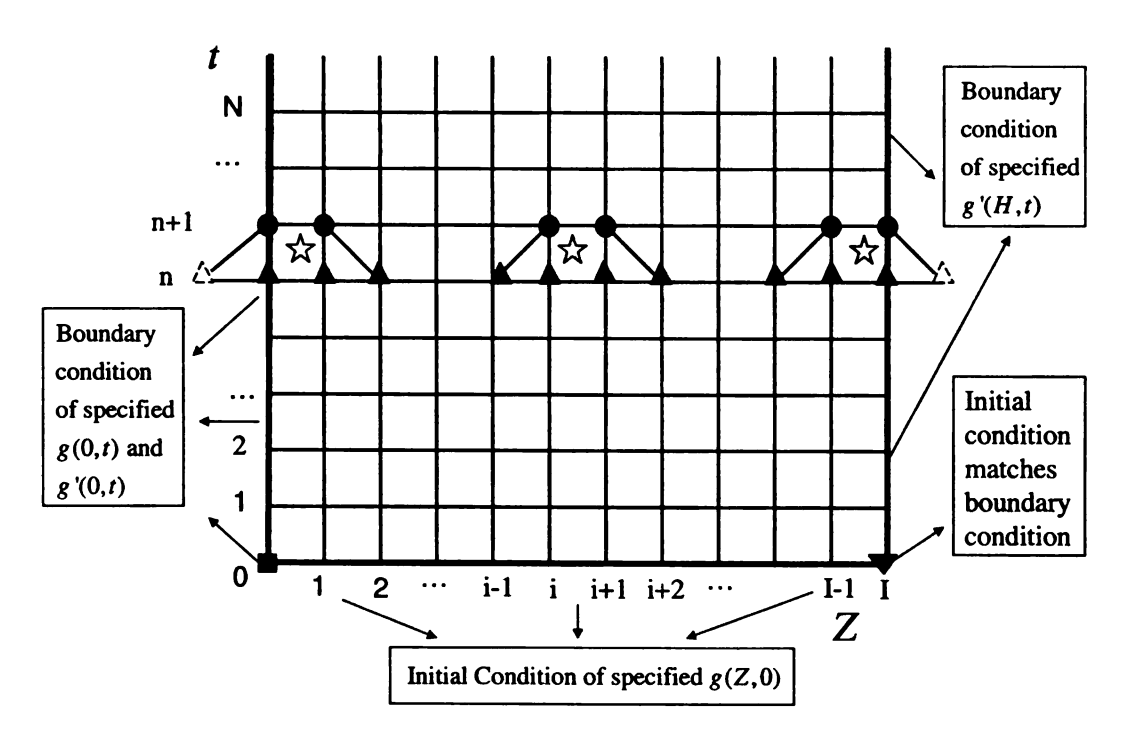


Figure 6.16: An explicit forward time-stepping scheme

points will be  $\Delta Z$  and between two consecutive time points will be  $\Delta t$ . The points

$$g(Z_i, t_n) = g_i^n$$
  $(i = 0, 1, 2, ..., I, n = 0, 1, 2, ...N)$ 

will represent the numerical approximation of g(Z,t). Using the initial and boundary condition the numerical solution may proceed by an explicit forward time-stepping scheme using a 6 node stencil to discretize (6.78) as shown in Figure 6.16. In particular suppose the stencil involves two nodes (i, n + 1), (i + 1, n + 1) on the time step n + 1 and four nodes (i - 1, n), (i, n), (i + 1, n), (i + 2, n) on the time step n. These six nodes comprises a stencil, whose "center" is at  $(i + \frac{1}{2}, n + \frac{1}{2})$  as represented by the stars in Figure 6.16. The discrete form of (6.78) on the basis of this stencil is now written as

$$\Xi_{i+\frac{1}{2},n+\frac{1}{2}}^{left} = \Xi_{i+\frac{1}{2},n+\frac{1}{2}}^{right}$$
(6.79)

with

$$\Xi_{i+\frac{1}{2},n+\frac{1}{2}}^{left} = \frac{\frac{1}{\Delta t}(g_{i+1}^{n+1} - g_{i+1}^n) - \frac{1}{\Delta t}(g_i^{n+1} - g_i^n)}{\Delta Z} 
\Xi_{i+\frac{1}{2},n+\frac{1}{2}}^{right} = F_1\left(\frac{g_{i+1}^n - g_i^n}{\Delta Z}\right) \frac{g_{i+2}^n - 3g_{i+1}^n + 3g_i^n - g_{i-1}^n}{C(\Delta Z)^3} 
+ \frac{1}{C}F_2\left(\frac{g_{i+1}^n - g_i^n}{\Delta Z}\right) \left[\frac{1}{2(\Delta Z)^2}(g_{i+2}^n - g_{i+1}^n - g_i^n + g_{i-1}^n)\right]^2.$$
(6.80)

Assume that numerical values have been obtained for g(Z,t) at time step n and observe that  $g_0^{n+1}$  is known from the boundary condition. It is then desired to obtain numerical values for g(Z,t) at time step n+1 by using the explicit scheme (6.79) for i=0, 1, 2, ..., I-1. It is to be noted that the use of (6.79) for both i=0 and i=I-1 requires the consideration of a virtual node as shown by the dashed triangles in Figure 6.16. The values  $g_{-1}^n$  and  $g_{I+1}^n$  of these two virtual nodes are determined from the known boundary values g'(0,t) and g'(H,t) through

$$g'(0,t) = \frac{1}{2\Delta Z}(g_1^n - g_{-1}^n), \text{ and } g'(H,t) = \frac{1}{2\Delta Z}(g_{I+1}^n - g_{I-1}^n).$$
 (6.81)

Numerical solution of the partial differential equation (6.78) is then obtained through the forward time stepping scheme (6.79). In particular, at the end of time step n the values of  $g_i^n$  are known for i=0,1,2,...,I. The values  $g_{-1}^n$  and  $g_{I+1}^n$  then follow from (6.81). The value  $g_0^{n+1}$  is also known from the boundary condition. Then (6.79) for i=0,1,2,...,I-1 gives I equations for the I unknowns  $g_i^{n+1}$  (i=1,2,...,I). These equations are easily solved in a sequential manner since the only unknown in (6.79) for i=0 is  $g_1^{n+1}$ , the only new unknown in (6.79) for i=1 is then  $g_2^{n+1}$ , etc.

Figure 6.17 shows the results of such a numerical calculation. The initial pressure difference in this example is  $P_H^I - P_0^I = 50 psi$ . The pressure difference is then suddenly changed to  $P_H^F - P_0^F = 200 psi$ . The approach to the steady state solution

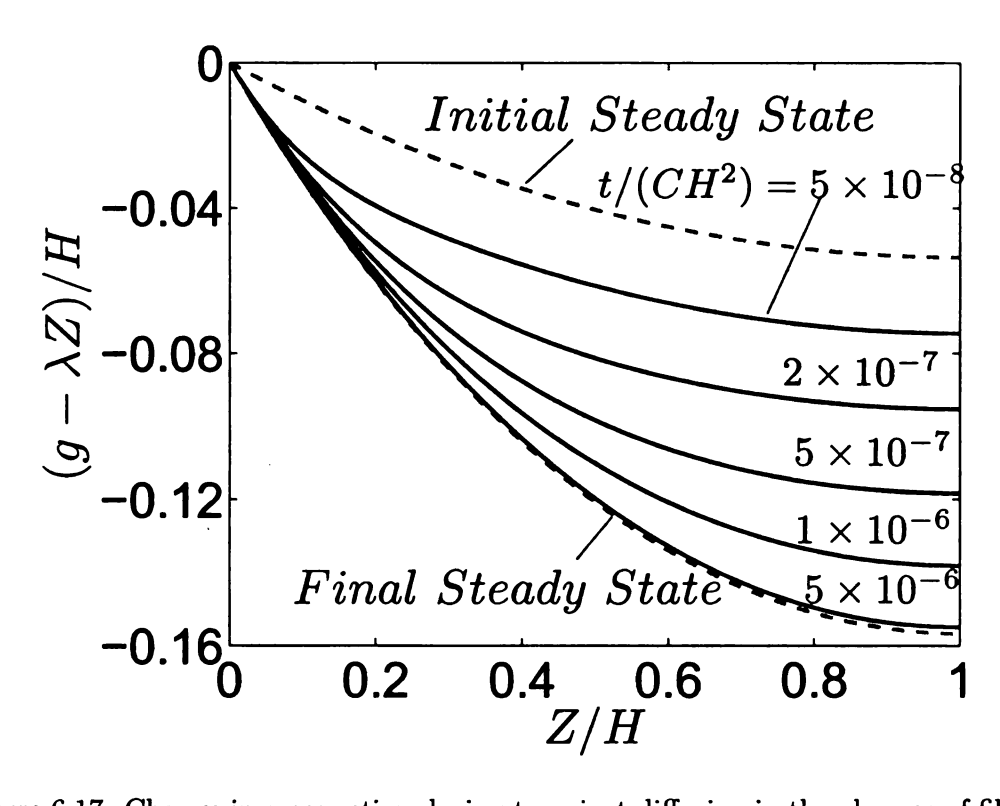


Figure 6.17: Change in compaction during transient diffusion in the absence of fibers  $(\bar{\gamma}=0)$  for a material with  $\xi=0,\ M/\mu=100$ . In this simulation the steady state seepage with  $P_H-P_0=50psi$  is abruptly altered to  $P_H-P_0=200psi$ .

is evident.

Base on the results in Figure 6.17, the profile of fluid density ratio  $\rho^f$  could be determined as in Figure 6.18. In this case  $\rho^f = (1 - J^{-1}) \rho_0^f = (1 - \lambda^{-2} g'^{-1}) \rho_0^f$ .

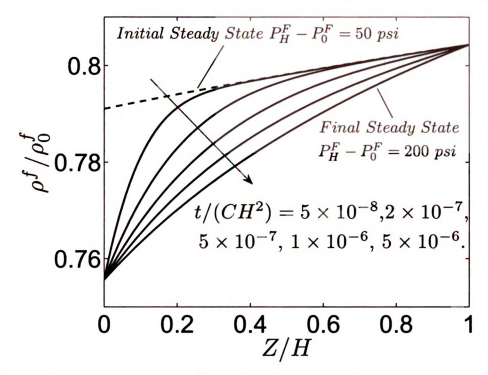


Figure 6.18: The variation of  $\rho^f/\rho_0^f$  along the thickness for the simulation considered in Figure 6.17.

The variation of normal stresses  $\sigma_{xx}^{mix}$  and  $\sigma_{zx}^{mix}$  along the thickness direction is shown in (Figure 6.19). Note here the symmetry gives  $\sigma_{yy}^{mix} = \sigma_{xx}^{mix}$ .

The total mass of fluid per unit current cross-section area within the layer  $\Sigma$  can also be obtained by  $\Sigma = \int_0^h \rho^f dz = \int_0^H \rho^f g' dZ = \int_0^1 \rho^f g' H d\bar{Z}$  (Figure 6.20). The numerical routine shows good convergence of the function g to its large time steady state value.

The example connected to Figure 6.17 - Figure 6.20 concerns the transition from one steady state flow to another steady state flow. Alternatively, one can begin with an initial state that involves free swelling and hence no flow by virtue of  $P_H - P_0 = 0$ . Then by abruptly raising the value of  $P_H - P_0$  one obtains a transient flow condition

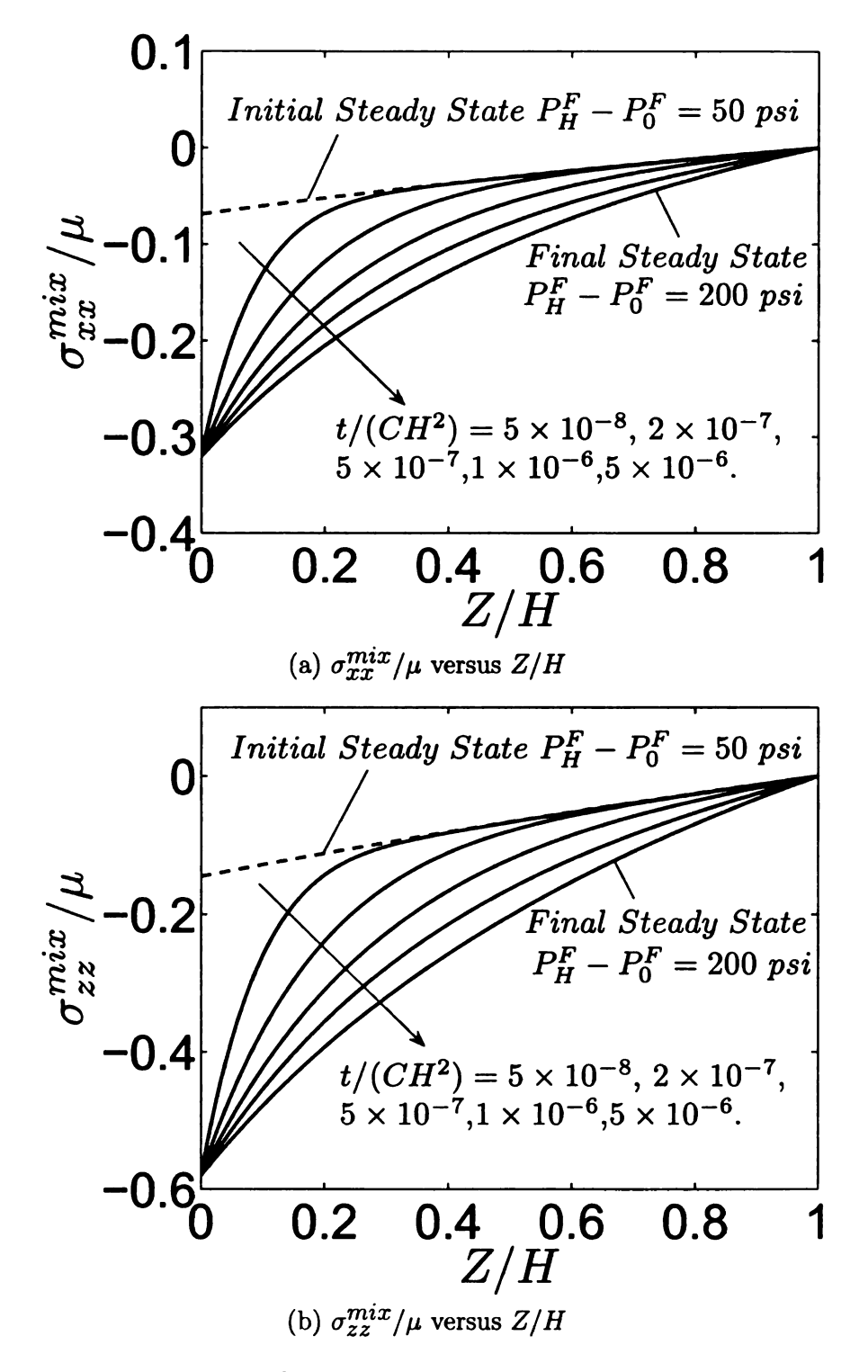


Figure 6.19: The variation of normal stresses along the thickness direction for the simulation considered in Figure 6.17.

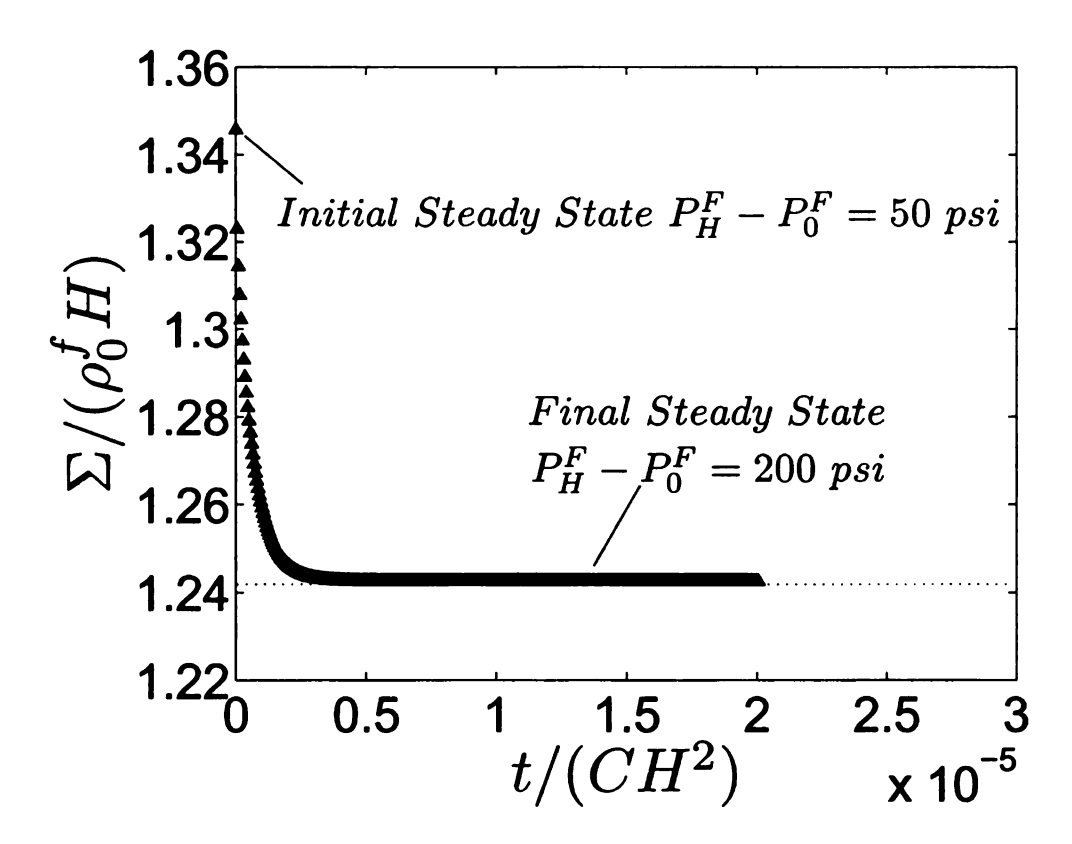


Figure 6.20: The amount of fluid in the layer changes with time: from its initial steady state value (where  $P_H - P_0 = 50 psi$ ), and finally approaching the final steady state value (where  $P_H - P_0 = 200 psi$ ).

that will approach a steady state for large time. Figure 6.21 shows this phenomena in a manner similar to Figure 6.20 for a variety of  $P_H^F - P_0^F$  values.

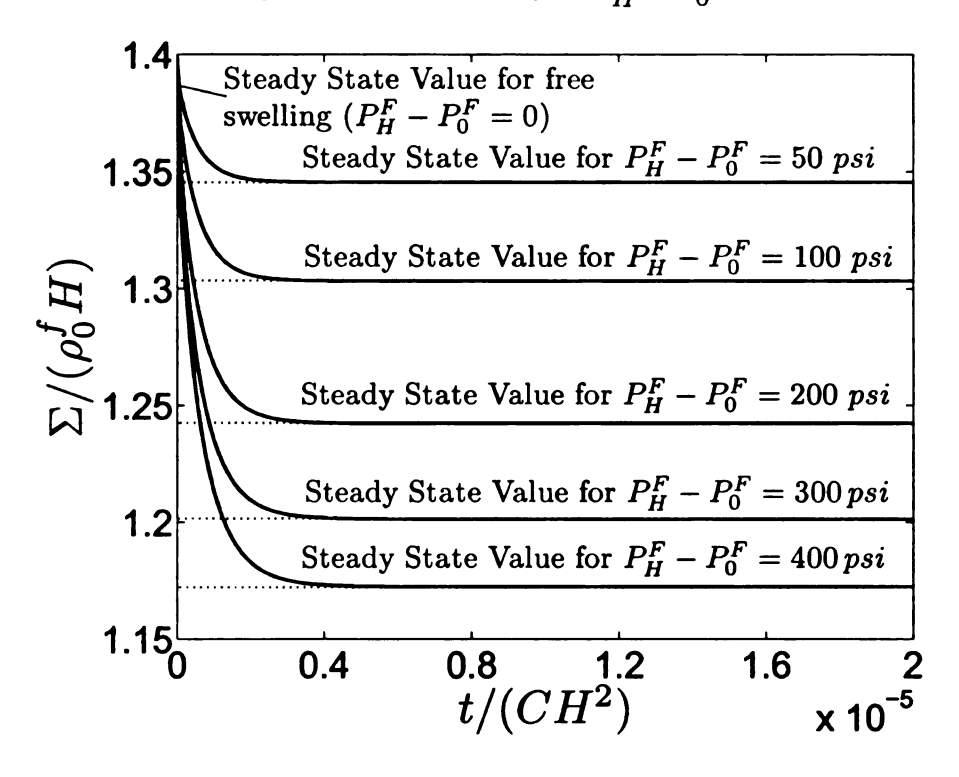


Figure 6.21: The change of interstitial fluid amount with time for various pressure difference. Free swelling state  $(P_H - P_0 = 0)$  is abruptly altered when  $P_H - P_0$  is suddenly changed to 50psi, 100psi, 200psi, 300psi, and 400psi, respectively.

# 6.5.2 Fiber Reinforced Layer

Now we consider the transient diffusion problem for a fiber reinforced layer. As in the previous section, we suddenly increase the pressure difference from  $P_H^I - P_0^I$  to  $P_H^F - P_0^F$  and analyze the evolution of the solid deformation and the fluid flux.

The stress equilibrium equations are the same as in (6.73) and (6.74). The fluid mass balance equation is again given by (6.72). By substituting from (6.74) into (6.72), the evolution equation regarding the time derivative of g(Z,t) is obtained as follows:

$$\dot{g}' = \frac{1}{C'} F_3(f', f'', f''', g', g'', g'''), \tag{6.82}$$

where  $C' = \alpha \Lambda_1^2 \lambda_2^2 / \mu$ , and  $F_3$  is a complicated function of f', f'', f''', g', g'' and g''' that is too cumbersome to display here. It is given in Appendix C. This equation is the generalization of the previous equation (6.78) to the case of fiber reinforcement.

It is immediate that one set of boundary conditions is

$$f(0,t) = 0$$
, and  $g(0,t) = 0$ . (6.83)

The remaining traction boundary conditions are as follows. First condition (6.70) continues to hold, namely

$$\sigma_{zz}^{mix}(0,t) = P_H^F - P_0^F, \quad \sigma_{zz}^{mix}(H,t) = 0.$$
 (6.84)

The remaining traction boundary conditions follow from the requirement that  $\sigma_{xz}(H, t) = 0$  which, in conjunction with (6.53), gives

$$\sigma_{xz}^{mix}(0,t) = 0, \quad \sigma_{xz}^{mix}(H,t) = 0.$$
 (6.85)

In fact (6.53) gives the immediate first integral

$$\sigma_{TZ}(Z,t) = 0. \tag{6.86}$$

Note also that by using (6.52) it follows that  $(6.84)_1$  and  $(6.85)_1$  provide two equations for f'(0,t) and g'(0,t). Similarly  $(6.84)_2$  and  $(6.85)_2$  provide two equations for f'(H,t) and g'(H,t). These equations can be solved numerically for constant values f'(0,t), g'(0,t), f'(H,t) and g'(H,t) prior to the consideration of the time-stepping numerical routine.

For 0 < Z < H, initial values of f(Z,t) and g(Z,t) are given by the steady state solution to the problem with fiber reinforcement. With these boundary and initial

conditions, we may proceed with the numerical iteration by using the same forward time stepping scheme as in Figure 6.16. Observe that the only time derivatives that appear in the formulation are  $\dot{g}$  and  $\dot{g}'$ , and these time derivatives only appear in equation (6.82). Therefore, we obtain nodal values  $g_i^{n+1}$  for i=1,2,...,I-1,I when we move from time step n to time step n+1. It is then necessary to use (6.86) to solve for  $f_i^{n+1}$  for i=1,2,...,I-1,I from these  $g_i^{n+1}$ . Similar virtual nodes for i=-1 and i=I+1 are then created in the time-stepping stencil scheme. Namely, the values of  $f_{-1}^{n+1}$ ,  $g_{-1}^{n+1}$ ,  $f_{I+1}^{n+1}$  and  $g_{I+1}^{n+1}$  will be introduced to complete the scheme with the use of the boundary values of f'(0,t), f'(H,t), g'(0,t) and g'(H,t) as in (6.81).

Numerical approximation of the profiles of f(Z,t) and g(Z,t) is shown in Figure 6.22. The parameters are chosen as follows:  $\xi = 0$ , the fiber reinforcement coefficient  $\bar{\gamma} = 1.0$  and the original orientation angle of the fibers  $\Omega = \pi/4$ . Recalling the definitions in (6.66) and (6.69), the function  $\Gamma(Z)$  and  $\Upsilon(Z)$  represent, respectively, the pure shear and normal deformation caused by the fiber-reinforced free swelling. Figure 6.22(a) and Figure 6.22(b) then depict the evolution of  $f(Z) - \Gamma(Z)$  (shear displacement due to pure pressure difference) and  $g(Z) - \Upsilon(Z)$  (contraction due to pure pressure difference), respectively.

Comparison of Figure 6.22 with Figure 6.17 indicates that the presence of fibers causes the time for the system to achieve its final steady state to increase by nearly two orders of magnitude over that of the isotropic case. The shear displacement and the normal contraction for the fiber-reinforced transient diffusion process with an increased fiber coefficient  $\bar{\gamma}=10$  is shown in Figure 6.23. The overall way in which the transient deformation approaches the steady state deformation is found to be relatively insensitive to the the initial fiber orientation  $\Omega$  as seen in Figures 6.24 and 6.25.

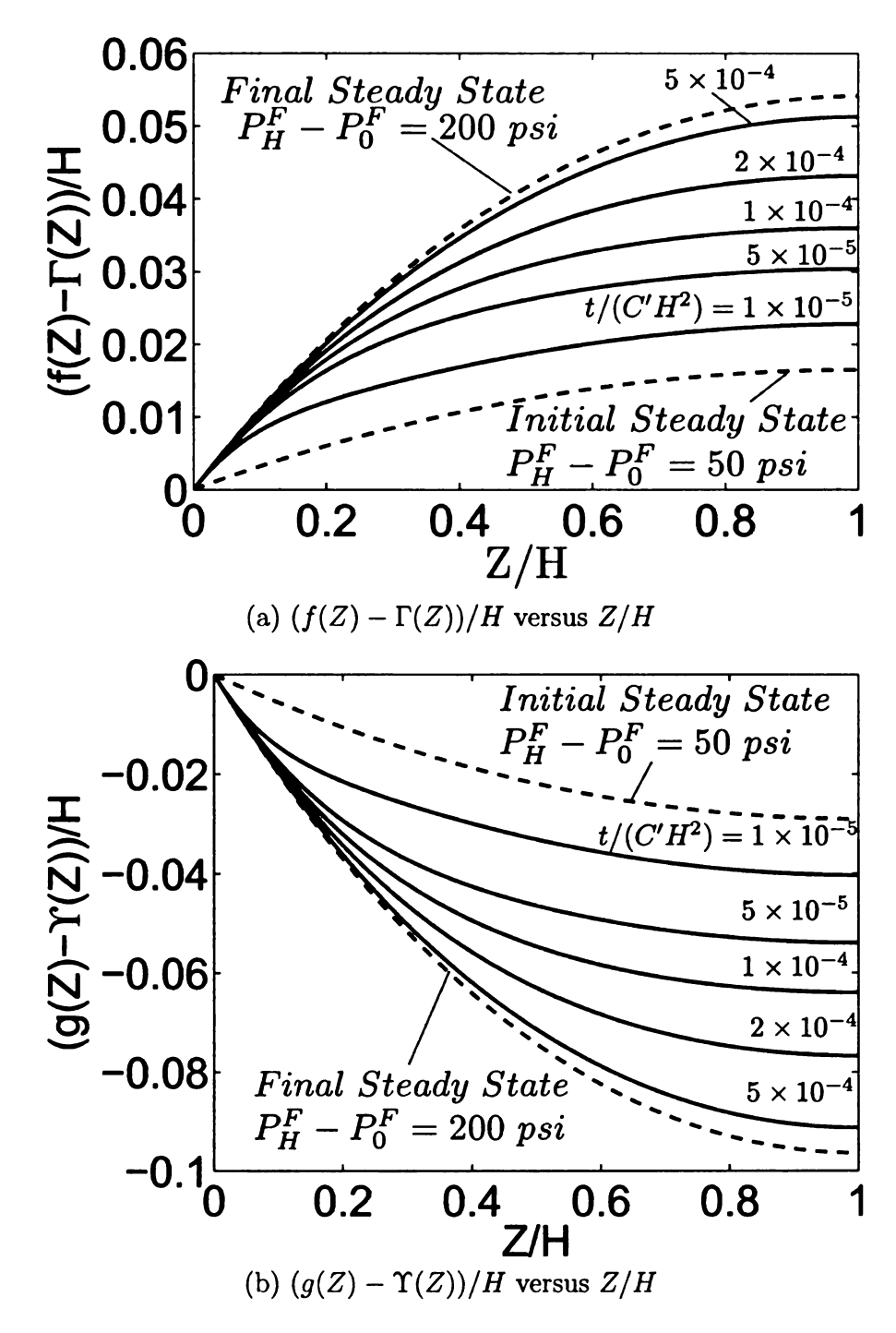


Figure 6.22: The shear and normal contraction associated with fiber reinforced transient diffusion where  $\bar{\gamma} = 1.0$ ,  $\Omega = 45^{\circ}$ , and  $\xi = 0$ .

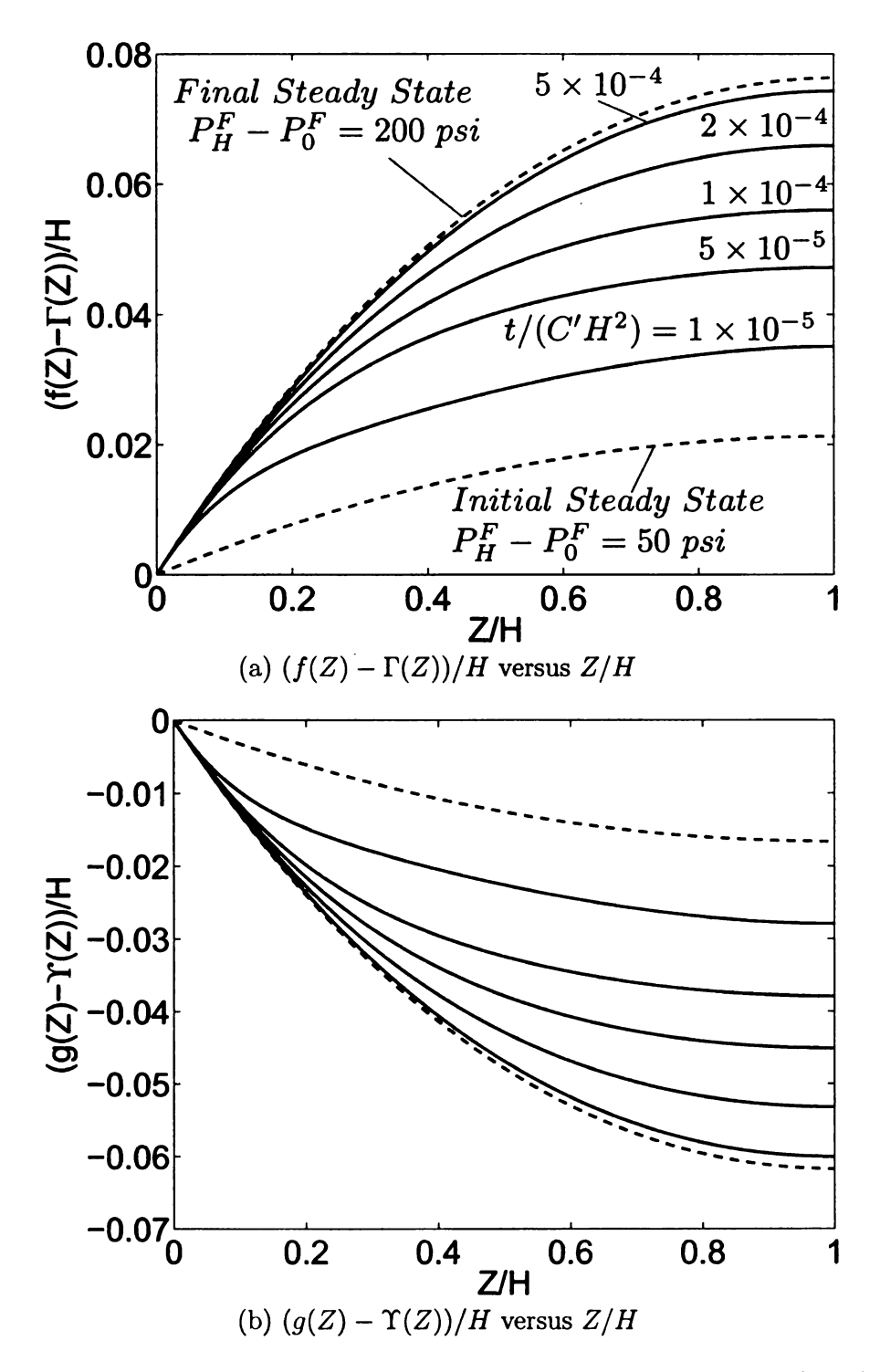
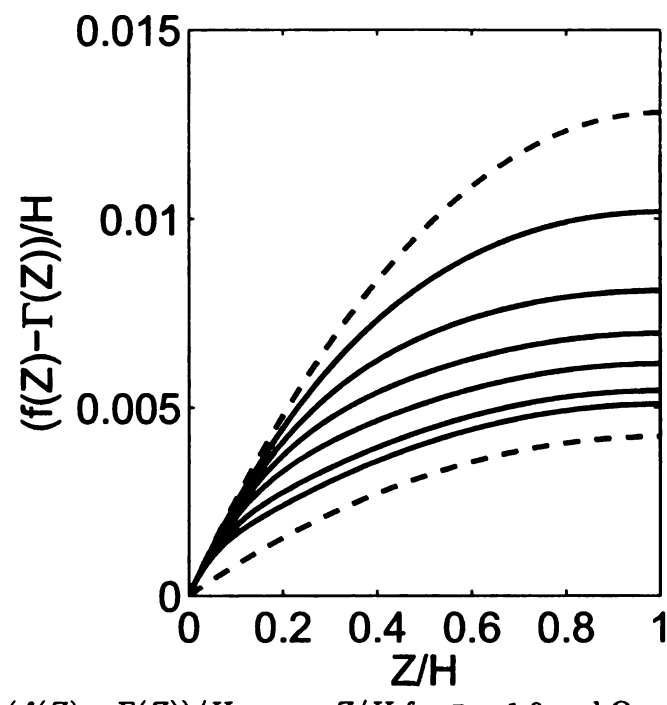
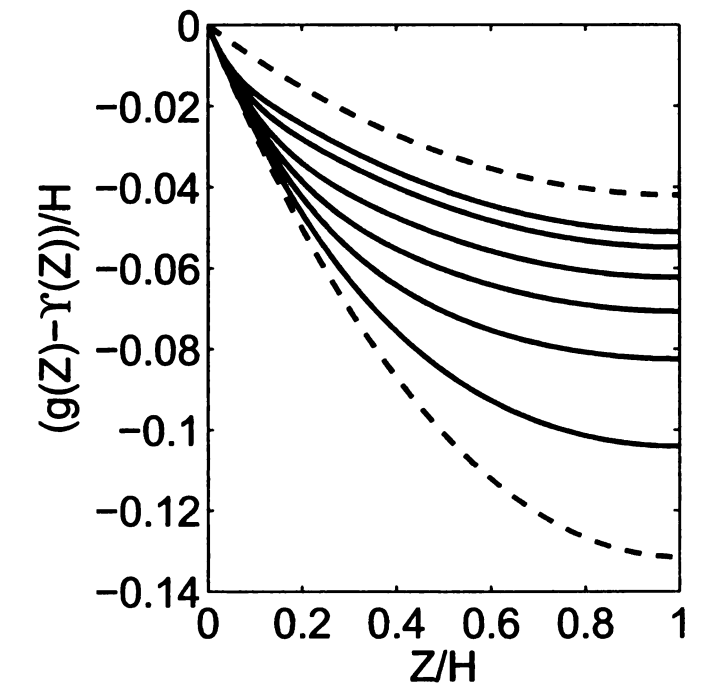


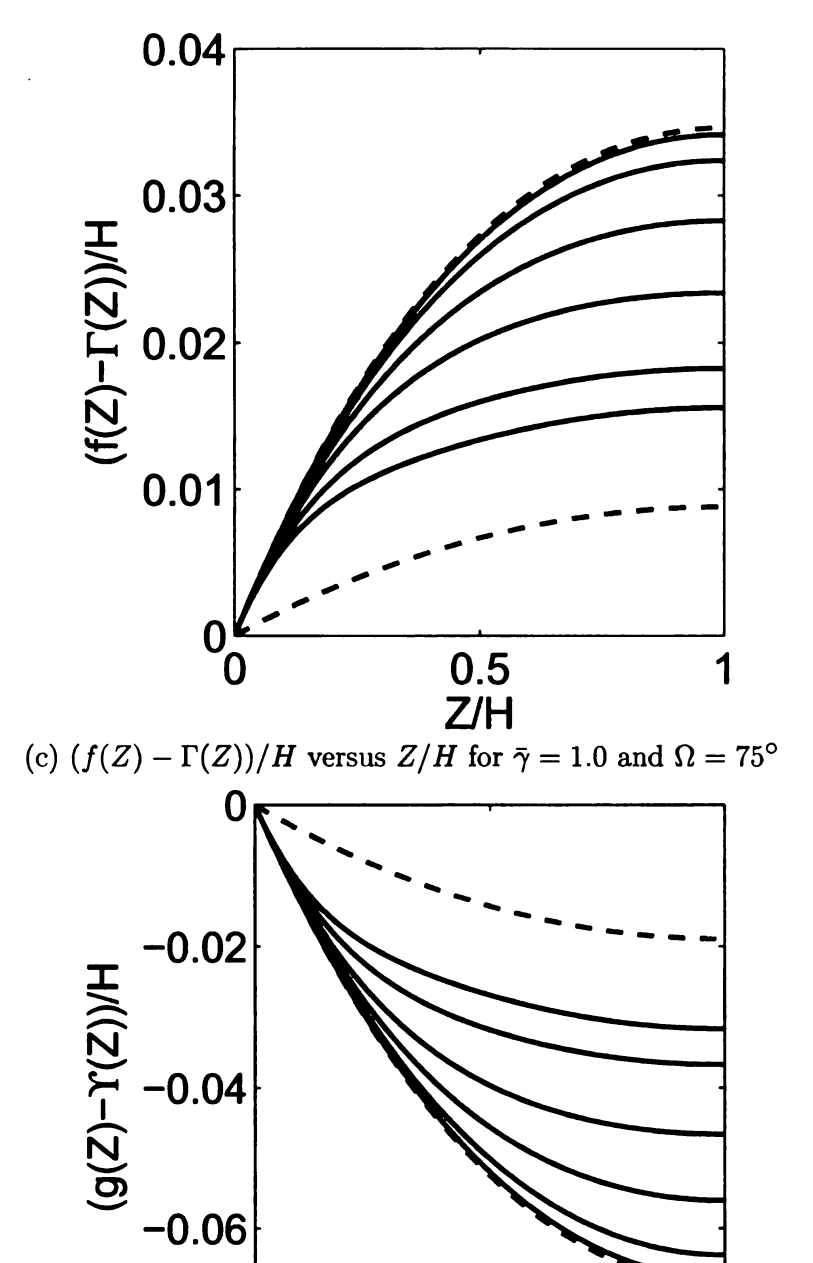
Figure 6.23: The shear and normal contraction associated with fiber reinforced transient diffusion where  $\bar{\gamma} = 10.0$ ,  $\Omega = 45^{\circ}$ , and  $\xi = 0$ .



(a)  $(f(Z) - \Gamma(Z))/H$  versus Z/H for  $\bar{\gamma} = 1.0$  and  $\Omega = 15^\circ$ 



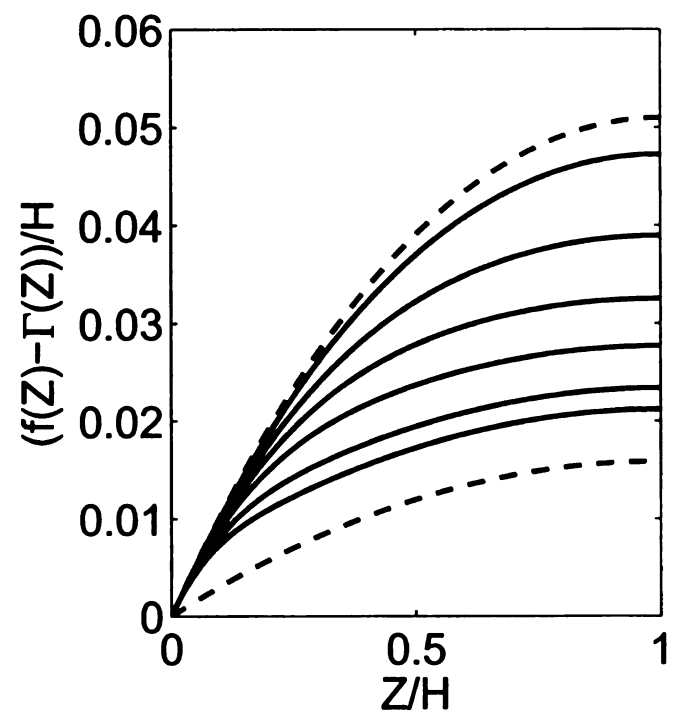
(b)  $(g(Z) - \Upsilon(Z))/H$  versus Z/H for  $\bar{\gamma} = 1.0$  and  $\Omega = 15^\circ$ 



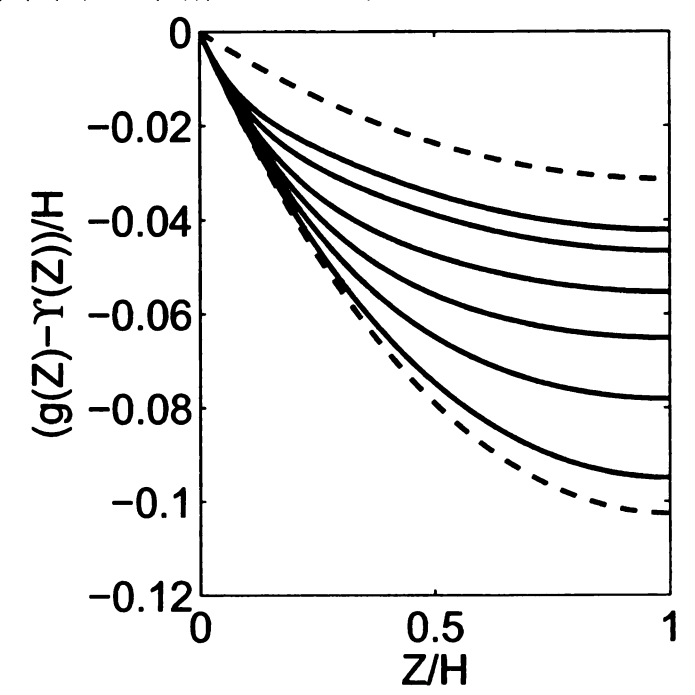
0.5 Z/H (d)  $(g(Z) - \Upsilon(Z))/H$  versus Z/H for  $\bar{\gamma} = 1.0$  and  $\Omega = 75^{\circ}$ 

-0.08<sup>L</sup><sub>0</sub>

Figure 6.24: The shear and normal contraction associated with fiber reinforced transient diffusion where  $\bar{\gamma}=1.0,~\Omega=15^{\circ}$  and  $\Omega=75^{\circ}$ 



(a)  $(f(Z) - \Gamma(Z))/H$  versus Z/H for  $\bar{\gamma} = 1.0$  and  $\Omega = 40^\circ$ 



(b)  $(g(Z) - \Upsilon(Z))/H$  versus Z/H for  $\bar{\gamma} = 1.0$  and  $\Omega = 40^\circ$ 

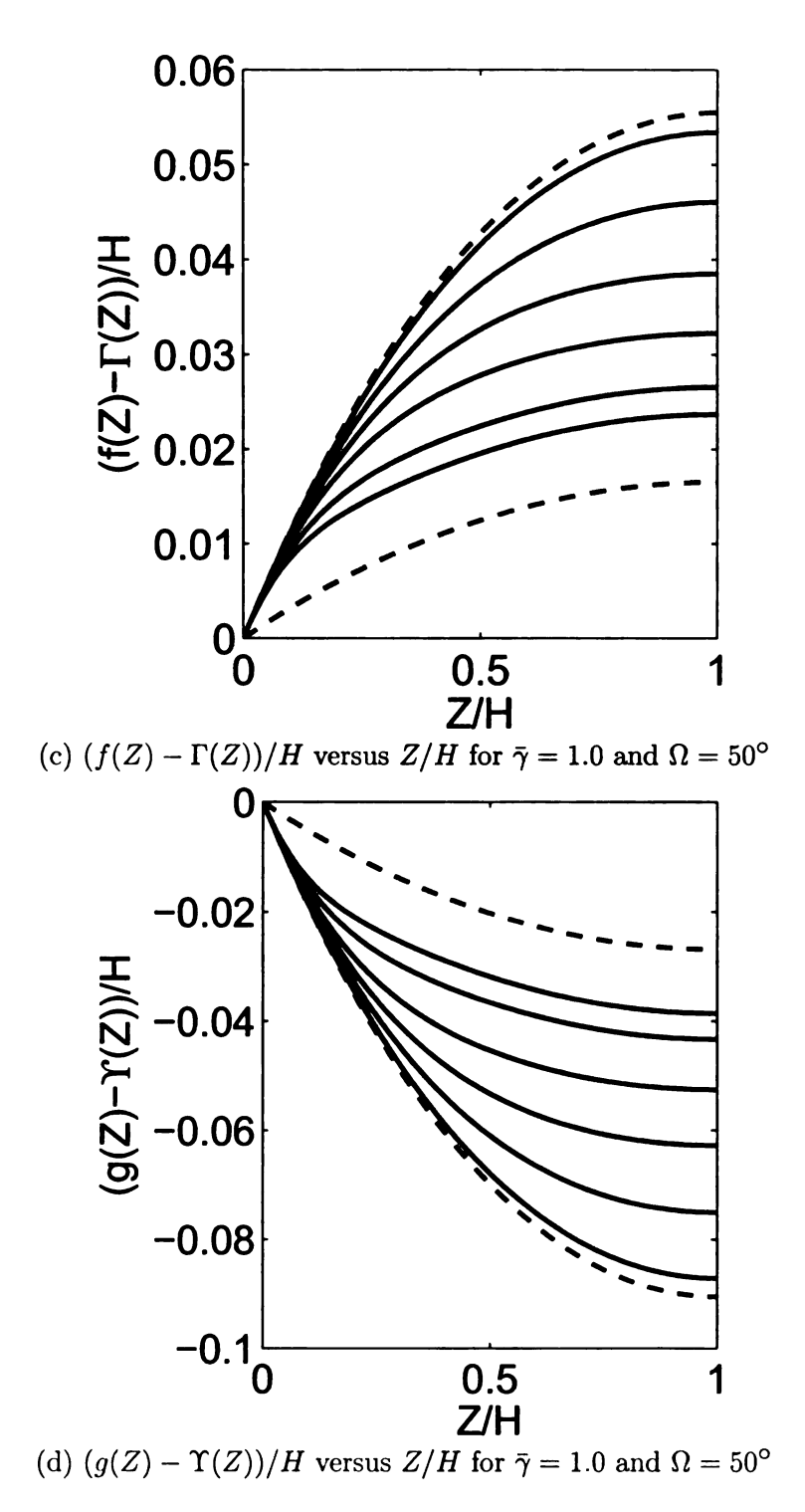


Figure 6.25: The shear and normal contraction associated with fiber reinforced transient diffusion where  $\bar{\gamma}=1.0,\,\Omega=40^{\circ}$  and  $\Omega=50^{\circ}$ 

#### 6.6 Summary

In this chapter, We study the pressure driven fluid diffusion through a hyperelastic porous layer. Both steady state and transient diffusion cases are considered with particular interests in the effects of fiber reinforcement on the diffusion process.

- It is found that the original fiber orientation angle  $\Omega$  is changed to  $\omega$  during the homogeneous deformation of free swelling. This angle change  $\omega \Omega$  is monotonic with the fiber reinforcing coefficient  $\bar{\gamma}$  for a certain angle  $\Omega$  (0 <  $\Omega$  <  $\pi$ /2). For a fixed fiber reinforcing coefficient  $\bar{\gamma}$ , the angle change exhibits a maximum value (greater than  $\pi$ /4 if  $\bar{\gamma} > 0$ ) for different values of  $\Omega$ .
- For steady state pressure driven fluid seepage in the absence of fiber reinforcing it is found that the model (6.52) with  $\xi = 0$  provides a good match to experimental curve in [24] by taking n = 5 and  $\alpha = 1.556 \times 10^{19} gm/cc \cdot day$ . These values are then used in the fiber reinforced model ( $\bar{\gamma} \neq 0$ ).
- For steady state pressure driven fluid seepage in the fiber reinforced material, the resulting nonhomogeneous deformation causes the fibers to be curved. Both lateral constraint boundary condition and no shear traction boundary condition at the surface Z = H are considered. In the first case, it is found as predicted that a) both flux and the shearing stress at Z = H increases monotonically with the pressure difference; b) the fiber reinforcement causes more fluid flux and greater shearing stress at Z = H with a given pressure difference; c) the fibers get further curved as γ̄ increases. In the second case, it is again found that a) both flux and the shearing displacement at Z = H increases monotonically with the pressure difference; b) the fiber reinforcement causes more fluid flux and greater shearing displacement at Z = H with a certain pressure difference; c) the fibers get further curved as γ̄ increases but with a common slope at Z = H. The effects of both pressure difference P<sub>H</sub> P<sub>0</sub> and γ̄ on the shearing

displacement at Z = H are studied.

• Transient diffusion process is studied in the problem where a abrupt pressure difference change is applied. Numerical solutions are obtained by using an explicit forward time-stepping scheme. It has shown that the presence of fibers causes the time for the system to achieve its final steady state to increase by nearly two orders of magnitude over that of the isotropic case.

### Chapter 7

### Conclusion

In this dissertation, we focused on theoretical modeling and numerical simulation on the mechanical response of swollen elastomeric gels. To do this, we first introduce a hyperelastic constitutive theory involving the generalized Flory-Huggins framework. We then consider the static equilibrium response including homogeneous and inhomogeneous deformation induced by different mechanical loading conditions. In particular we consider the equilibrium states in which these mechanical loadings can lead to both fluid loss (swelling reduction) and fluid gain (swelling increase). For loadings that give fluid gain, we consider the transition from the state of liquid saturation to that of nonsaturation at a particular point on the quasi-static load path. Numerical simulations are introduced to solve the stress equilibrium equations. In what follows list the major numerical results.

• In Chapter 3, the homogeneous deformation is first discussed. It is found that both the stress and the overall volume of the gel are monotone with the stretch for equibiaxial loading, while the volume change exhibits a local maximum at a certain uniaxial stretch for the case  $\xi = 1$ . For equitriaxial loading, the stress is found to be monotonically increasing if  $\xi$  is greater than a critical value  $\xi_{crit}$ , and exhibits a stress maximum if  $\xi < \xi_{crit}$ . In all cases, nonsaturated

bifurcation always leads to a stiffer response.

- In Chapter 4, the inhomogeneous deformation of everting a swollen tube subject to axial loading is studies. Numerical results show that the deformed inner and outer radii decrease as the axial stretch increases. The overall volume of the tube is monotone in the axial stretch if ξ = 0 but exhibits a local maximum as long as ξ > 0. The transition to a nonsaturated state preserves the overall gel volume but alters the distribution of the fluid content within the gel. For the cases ξ = 0 and ξ = 1 this results in opposite directions of the fluid quasi-static migration in the everted cylinder.
- In Chapter 5, the problem of twisting a swollen tube is considered. Two sorts of boundary value problems leading to the change in the overall gel volume are solved. Either the inner or outer surface is fixed radially while let the other lateral surface be free of normal traction. The case where the inner surface is free of normal traction gives rise to fluid uptake, which makes the transition to a nonsaturated state possible. The result show that relation between the twist angle and the twist moment abruptly stiffers after loss of saturation.

As the second part of this work, the pressure driven fluid diffusion through a fiber reinforced hyperelastic media is investigated in Chapter 6. To study the relative motion between the fluid and polymer matrix, we invoke a large deformation biphasic mixture theory that specially deals with separate mechanical balance principles for each. Both steady-state and non-steady-state diffusion processes are considered. Numerical analysis involving a forward time-stepping scheme is utilized in order to obtain time dependent swelling behavior of elastomeric matrix as well as the redistribution of the fluid concentration during diffusion. Numerical simulation shows: a) the fiber orientation angle is changed during the homogeneous of free swelling; b) steady state seepage causes the original straight fibers to be curved; c) fiber reinforcement

causes more flux and greater deformation of the polymer network; d) the study of transient diffusion process shows that the presence of fibers causes the convergence time to increase greatly over that of the isotropic case.

There are several potential directions to expand this work. Firstly, the current numerical simulations take the values of the material parameters  $\bar{M}$ ,  $\chi$ , and  $\mu$  directly from the experimental data in [24] for the specific combination of toluene and vulcanized rubber. In order to compare with other experimental data on different gels, adjustment might be made according to the corresponding materials. Furthermore, this work takes Mooney-Rivlin elastic energy function for the elastic deformation of the polymer network, and Flory-Huggins' theory to interpret the mixing entropic and enthalpic effects between the elastomer and the liquid. However, we are also able to embed more general material models into the current framework.

Another possible improvement is to consider more complicate geometries, and also other constitutive models involving viscoelastic behaviors, which many sorts of polymers bear. To do this, finite element methods might be adopted to solve the more complicate time and loading rate dependent equations.

## **APPENDIX**

## Appendix A

## Nondimensional Form of Governing Equations of Steady State Diffusion Problem

By introducing the nondimentionized process in (6.63) and (6.64), the stress equilibrium equations (6.53) and (6.53) then become

$$\mathcal{F}_1(\bar{f}', \bar{g}')\bar{f}'' + \mathcal{F}_2(\bar{f}', \bar{g}')\bar{g}'' = 0$$
 (A.1)

and

$$\mathcal{F}_{3}(\bar{f}', \bar{g}')\bar{g}'' + \mathcal{F}_{4}(\bar{f}', \bar{g}')\bar{f}'' + \frac{\alpha q H}{\mu \rho_{0}^{f}} \frac{\Lambda_{1}^{2} \lambda_{2}^{2} \bar{g}'^{2}}{(\Lambda_{1} \lambda_{2} \bar{g}' - 1)^{n+1}} = 0, \tag{A.2}$$

where 
$$\mathcal{F}_1(\bar{f}',\bar{g}') = 1 + \xi \left(\lambda_2^2 - 1\right)$$
  
  $+ 2\bar{\gamma} \left[\sin^4\Omega(3\bar{f}'^2 + \bar{g}'^2) + 3\Lambda_1^2\sin^2\Omega\sin2\Omega\bar{f}' + \sin^2\Omega\left(3\Lambda_1^2\cos^2\Omega - 1\right)\right],$   
 $\mathcal{F}_2(\bar{f}',\bar{g}') = 2\bar{\gamma} \left(\Lambda_1^2\sin2\Omega + 2\sin^2\Omega\bar{f}'\right)\sin^2\Omega\bar{g}',$   
 $\mathcal{F}_3(\bar{f}',\bar{g}') = 1 + \xi \left(\Lambda_1^2 + \lambda_2^2 - 1\right) + \Lambda_1^2\lambda_2^2h'(\Lambda_1\lambda_2\bar{g}')/\mu$   
 $+ 2\bar{\gamma} \left[\sin^4\Omega(\bar{f}'^2 + 3\bar{g}'^2) + \Lambda_1^2\sin2\Omega\sin^2\Omega\bar{f}' + \sin^2\Omega\left(\Lambda_1^2\cos^2\Omega - 1\right)\right],$   
 $\mathcal{F}_4(\bar{f}',\bar{g}') = 2\bar{\gamma} \left(\Lambda_1^2\sin2\Omega + 2\sin^2\Omega\bar{f}'\right)\sin^2\Omega\bar{g}',$  and  $h'(J) = dh(J)/dJ.$ 

## Appendix B

# Functions $F_1(g')$ and $F_2(g')$

$$F_1(g') = \frac{[A + Bh'(\lambda^2 g')](\lambda^2 g' - 1)^{n+1}}{g'^2},$$
(B.1)

$$F_{2}(g') = \frac{Bh''(\lambda^{2}g')\lambda^{2}(\lambda^{2}g'-1)^{(n+1)} + (n+1)[A+Bh'(\lambda^{2}g')](\lambda^{2}g'-1)^{n}\lambda^{2}}{g'^{2}} - 2\frac{[A+Bh'(\lambda^{2}g')](\lambda^{2}g'-1)^{n+1}}{g'^{3}},$$
(B.2)

where  $A = 1 + \xi(2\lambda^2 - 1)$  and  $B = \lambda^4/\mu$ .

## Appendix C

# Function $F_3(f', f'', f''', g', g'', g''')$

$$F_{3}(f', f'', f''', g'', g''') = 2\bar{\gamma}(AA + BB) + CC * DD * g'' + \frac{(J-1)^{n+1}}{g'^{2}}(DD'g'' + DDg'''),$$
(C.1)

where

$$AA = \frac{(n+1)(J-1)^{n}\Lambda_{1}\lambda_{2}g''g' - (J-1)^{n+1}g''}{g'^{2}} (2\sin^{2}\Omega f' + \Lambda_{1}\sin 2\Omega)\sin^{2}\Omega f'',$$

$$BB = \frac{(J-1)^{n+1}}{g'}\sin^{2}\Omega \left[2\sin^{2}\Omega f''^{2} + (2\sin^{2}\Omega f' + \Lambda_{1}\sin 2\Omega)f'''\right],$$

$$CC = \frac{(n+1)(J-1)^{n}\Lambda_{1}\lambda_{2}g''g' - 2(J-1)^{n+1}g''}{g'^{3}},$$

$$DD = 1 + \xi(\Lambda_{1}^{2} + \lambda_{2}^{2} - 1) + \Lambda_{1}^{2}\lambda_{2}^{2}h'(J) + 2\bar{\gamma}\sin^{2}\Omega \left[\sin^{2}\Omega(f'^{2} + 3g'^{2}) + \Lambda_{1}^{2}\cos^{2}\Omega - 1 + \Lambda_{1}\sin 2\Omega f'\right],$$

$$DD' = \Lambda_{1}^{3}\lambda_{2}^{3}h''(J)g'' + 4\bar{\gamma}\left[\sin^{4}\Omega(f'f'' + 3g'g'') + \Lambda_{1}\sin 2\Omega\sin^{2}\Omega f''\right],$$

$$J = \Lambda_{1}\lambda_{2}g' \text{ and } h''(J) = d^{2}h(J)/dJ^{2}.$$

# **BIBLIOGRAPHY**

#### **Bibliography**

- [1] B. Baroli, "Hydrogels for tissue engineering and delievery of tissue-inducing substances," J. Pharm. Sci., vol. 96, no. 9, pp. 2197–2223, 2007.
- [2] Y. Qiu and K. Park, "Environment-sensitive hydrogels for drug delivery," Adv. Drug Deliv. Rev., vol. 53, no. 321-339, 2001.
- [3] J. C. Wheeler, J. A. Woods, and M. J. Cox et al., "Evolution of hydrogel polymers as contact lenses, surface coatings, dressings, and drug delivery systems," *J. Long Term Eff. Med. Implants*, vol. 6, no. 3-4, pp. 207-217, 1996.
- [4] T. Noguchi, T. Yamamuro, M. Oka, P. Kumar, Y. Kotoura, S. H. Hyon, and Y. Ikada, "Poly(vinyl alcohol) hydrogel as an artificial articular-cartilage-evaluation of biocompatibility," *J. Appl. Biomater.*, vol. 2, no. 2, pp. 101–107, 1991.
- [5] D. J. Beebe, J. Moore, J. M. Bauer, Q. Yu, R. H. Liu, C. Devadoss, and B. H. Jo, "Functional hydrogel structures for autonomous flow control inside micro-fluidic channels," *Nature*, vol. 404, 2000.
- [6] L. Bromberg and E. Ron, "Temperature-responsive gels and thermogelling polymer matrices for protein and peptide delivery," Adv. Drug Deliv. Rev., vol. 31, pp. 197–221, 1998.
- [7] D. Schmaljohann, "Thermo- and ph-responsive polymers in drug delivery," Adv. Drug Deliv. Rev., vol. 58, pp. 1655-1670, 2006.
- [8] E. S. Gil and S. M. Hudson, "Stimuli-responsive polymers and their bioconjugates," *Prog. Polym. Sci.*, vol. 29, pp. 1173–1222, 2004.
- [9] G. Gerlach, M. Guenther, J. Sorber, G. Suchaneck, K. F. Arndt, and A. Richter, "Chemical and ph sensors based on the swelling behavior of hydrogels," *Sens. Actuators B Chem.*, vol. 111, pp. 555–561, Nov. 2005.
- [10] A. Mamada, T. Tanaka, D. Kungwatchakun, and M. Irie, "Photoinduced phase transition of gels," *Macromolecules*, vol. 23, pp. 1517–1519, 1990.
- [11] A. Suzuki, T. Ishii, and Y. Maruyama, "Optical switching in polymer gels," J. Appl. Phys., vol. 80, pp. 131–136, 1996.

- [12] S. K. De, N. R. Aluru, B. Johnson, W. C. Crone, D. J. Beebe, and J. Moore, "Equilibrium swelling and kinetics of ph-responsive hydrogel: models, experiments, and simulations," *J. Microelectromech. Syst.*, vol. 11, pp. 544–555, October 2002.
- [13] L. R. G. Treloar, The physics of rubber elasticity. Oxford Univ. Press, 1975.
- [14] G. Gee, "The interaction between rubber and liquids.9. the elastic behavior of dry and swollen rubbers," *Trans. Faraday Soc.*, vol. 42, no. 8, pp. 585–598, 1946.
- [15] S. M. Gumbrell, L. Mullins, and R. S. Rivlin, "Departures of the elastic behavior of rubbers in simple extension from the kinetic theory," *Trans. Faraday Soc.*, vol. 49, no. 12, pp. 1495–1505, 1953.
- [16] L. Mullins, "Determination of degree of crosslinking in natural subber vulcanizates: Part iv. stress-strain behavior at large extensions," J. Appl. Polym. Sci., vol. 2, no. 6, pp. 257-263, 1959.
- [17] G. B. Mckenna, K. M. Ffynn, and Y. Chen, "Experiments on the elasticity of dry and swollen networks: implications for the frenkel-flory-rehner hypothesis," *Macromolecules*, vol. 22, no. 4507-4512, 1989.
- [18] R. A. Paxton and A. M. Al-Jumaily, "Swelling of polyelectrolyte hydrogels using a finite element model," *Polymer*, vol. 47, pp. 5997–6003, 2006.
- [19] O. C. Zienkiewicz, A. H. C. Chan, M. Pastor, D. K. Paul, and T. Shiomi, "Static and dynamic behaviour of soils: a rational approach to quantitative solutions. i. fully saturated problems," Proceedings of the Royal Society of London. Series A, Mathematical and Physical Sciences, vol. 429, no. 1877, pp. 285-309, 1990.
- [20] S. Prager, "Diffusion of hydrocarbons in polyisobutylene," J. Am. Chem. Soc., vol. 73, pp. 4072–4075, 1951.
- [21] R. E. Pattle, "Diffusion of 1-benzeneazo-2-naphthol in swollen rubber," Trans. Faraday Soc., vol. 62, pp. 1776–1784, 1966.
- [22] N. A. Pepper and C. T. Reinhart, "Solute diffusion in swollen membranes 1. a new theory," J. Membr. Sci., vol. 15, no. 3, pp. 275-287, 1983.
- [23] C. J. Guo, D. D. Kee, and B. Harrison, "Diffusion of organic solvents in rubber membranes measured via a new permeation cell," J. Appl. Polym. Sci., vol. 56, no. 7, pp. 823–829, 2003.
- [24] D. R. Paul and O. M. Ebra-Lima, "Pressure-induced diffusion of organic liquids through highly swollen polymer membranes," J. Appl. Polym. Sci., vol. 14, no. 2201-2224, 1970.
- [25] M. Mooney, "A theory of large elastic deformation," J. Appl. Phys., vol. 11, no. 9, pp. 582-592, 1940.

- [26] R. S. Rivlin, "Large elastic deformations of isotropic materials.1. fundamental concepts," *Phil. Trans. R. Soc. Lond. A-Math. Phys. Sci.*, vol. 240, no. 822, pp. 459-508, 1948.
- [27] P. J. Flory, "Theory of elasticity of polymer networks-effect of local constraints on junctions," J. Chem. Phys., vol. 66, no. 12, pp. 5720-5729, 1977.
- [28] P. J. Flory and B. Erman, "Theory of elasticity of polymer networks. 3.," *Macro-molecules*, vol. 15, no. 3, pp. 800-806, 1982.
- [29] R. J. Gaylord and J. F. Douglas, "Rubber elasticity-a scaling approach," *Polym. Bullet.*, vol. 18, no. 4, pp. 347-354, 1987.
- [30] R. J. Gaylord and J. F. Douglas, "The localization model of rubbber elasticity .2.," *Polym. Bullet.*, vol. 23, no. 5, pp. 529-533, 1990.
- [31] E. A. Dimarzio, "Contribution to a liquid-like theory of rubber elasticity," J. Chem. Phys., vol. 36, no. 6, pp. 1562–1570, 1962.
- [32] E. A. Dimarzio, "Contribution to a liquid-like theory of rubber elasticity .2. existence of a  $(\lambda_x \lambda_y + \lambda_y \lambda_z + \lambda_z \lambda_x)$  term," *Polymer*, vol. 35, no. 9, pp. 1819–1826, 1994.
- [33] E. M. Arruda and M. C. Boyce, "A 3-dimensional constitutive model for the large stretch behavior of rubber elastic materials," *J. Mech. Phys. Solid*, vol. 41, no. 2, pp. 389-412, 1993.
- [34] W. H. Han, F. Horkay, and G. B. Mckenna, "Mechanical and swelling behaviors of rubber: a comparion of some molecular models with experiment," *Math. Mech. Solids*, vol. 4, pp. 139–167, 1999.
- [35] R. S. Rivlin and D. W. Saunders, "Large elastic deformations of isotropic materials. 7. experiments on the deformation of rubber," *Phil. Trans. R. Soc. Lond. A-Math. Phys. Sci.*, vol. 243, no. 865, pp. 251-288, 1951.
- [36] H. Pak and P. J. Flory, "Relationship of stress to uniaxial strain in crosslinked poly(dimethylsiloxane) over the full range from large compression to high elongations," J. Polym. Sci. B-Polym. Sci., vol. 17, no. 11, pp. 1845–1854, 1979.
- [37] G. Allen, M. J. Kirkham, J. Padget, and C. Price, "Thermodynamics of rubber elasticity at constant volume," *Trans. Faraday Soc.*, vol. 67, no. 581, pp. 1278–1292, 1971.
- [38] P. J. Flory and Y. I. Tatara, "Elastic free-energy and elastic equation of state-elongation and swelling of polydimethylsiloxane networks," J. Polym. Sci. B-Polym. Phys., vol. 13, no. 4, pp. 683-702, 1975.
- [39] M. C. Boyce and E. M. Arruda, "Swelling and mechanical stretching of elastomeric materials," *Math. Mech. Solids*, vol. 6, pp. 641-659, 2001.

- [40] G. Gee and L. R. G. Treloar, "The interaction between rubber and liquids. 1. a thermodynimic study of the system rubber-benzene.," *Trans. Faraday Soc.*, vol. 38, no. 147-165, 1942.
- [41] P. J. Flory, "Thermodynamics of high polymer solutions," J. Chem. Phys., vol. 10, pp. 51-61, 1942.
- [42] M. L. Huggins, "Some properties of solutions of long-chain compounds," J. Phys. Chem., vol. 46, pp. 151–158, 1942.
- [43] M. L. Huggins, "Theory of solutions of high polymers," J. Am. Chem. Soc., vol. 64, pp. 1712-1719, 1942.
- [44] L. R. G. Treloar, "The equilibrium swelling of cross-linked amorphous polymers," *Proceedings of the Royal Society of London*, vol. A200, pp. 176–183, 1950.
- [45] L. R. G. Treloar, "Swelling of a rubber cylinder in torsion: part 1. theory.," *Polymer*, vol. 13, pp. 195-202, 1972.
- [46] J. J. Shi, K. R. Rajagopal, and A. S. Wineman, "Applications of the theory of interacting continua to the diffusion of a fluid through a non-linear elastic media," *Int. J. Eng. Sci.*, vol. 19, no. 6, pp. 871-889, 1981.
- [47] M. V. Gandhi, K. R. Rajagopal, and A. S. Wineman, "Some nonlinear diffusion problems within the context of the theory of interacting continua," *Int. J. Eng. Sci.*, vol. 25, no. 11-12, pp. 1441-1457, 1987.
- [48] A. S. Wineman and K. R. Rajagopal, "Shear induced redistribution of fluid within a uniformly swollen nonlinear elastic cylinder," *Int. J. Eng. Sci.*, vol. 30, no. 11, pp. 1583–1595, 1992.
- [49] M. V. Gandhi, M. Usman, A. S. Wineman, and K. R. Rajagopal, "Combined extension and torsion of a swollen cylinder within the context of mixture theory," *Acta Mech.*, vol. 79, pp. 81–95, 1989.
- [50] S. P. Marra, K. T. Ramesh, and D. A. S., "Characterization and modeling of compliant active materials," J. Mech. Phys. Solids, vol. 51, pp. 1723-1743, 2003.
- [51] S. P. Marra, K. T. Ramesh, and D. A. S., "The actuation of a biometic poly(vinyl alcohol)-poly(acrylic acid) gel," *Phil. Trans. R. Soc. A*, vol. 360, pp. 175–198, 2002.
- [52] R. W. Ogden, "Large deformation isotropic elasticity: On the correlation of theory and experiment for incompressible rubberlike solids," *Phil. Trans. R. Soc.* A, vol. 326, pp. 565-584, 1972.
- [53] J. Dolbow, E. Fried, and H. Ji, "A numerical strategy for inverstigating the kinetic response of stimulus-responsive hydrogels," Comput. Methods Appl. Mech. Eng., vol. 194, no. 4447-4480, 2005.

- [54] J. Dolbow, E. Fried, and H. Ji, "Chemical induced swelling of hydrogels," J. Mech. Phys. Solids, vol. 52, no. 51-84, 2004.
- [55] J. Dolbow, E. Fried, and H. Ji, "Kinetics of thermally induced swelling of hydrogels," *Int. J. Solids Struct.*, vol. 43, no. 1878-1907, 2006.
- [56] S. Ramtani, "Steady diffusion of an ideal fluid through a pre-stressed and reinforced hollow conduit subjected to combined finite deformations," *Int. J. Solids .Struct.*, vol. 44, no. 14-15, pp. 4819-4829, 2007.
- [57] K. Garikipati, E. M. Arruda, and K. Grosh, "A continuum treatment of growth in biological tissue: the coupling of mass transport and mechanics," J. Mech. Phys. Solids, vol. 52, pp. 1595-1625, JULY 2004.
- [58] R. M. Bowen, "Theory of mixtures," Cont. Phys., vol. III, pp. 1-127, 1976.
- [59] B. Markert, "A biphasic continuum approach for viscoelastic high-porosity foams: Comprehensive theory, numerics, and application," Arch. Comput. Method Eng., vol. 15, pp. 371-446, DEC 2008.
- [60] M. Landervik and R. Larsson, "Modeling of large inelastic deformations of foams with respect to the point of compaction," Eur. J. Mech. A-Solids, vol. 27, no. 2, pp. 234-246, 2008.
- [61] P. H. af Segerstada, R. Larssona, and S. Toll, "A constitutive equation for opencell cellular solids, including viscoplasticity, damage and deformation induced anisotropy," *Int. J. Plast.*, vol. 24, no. 5, pp. 896-914, 2008.
- [62] J. Korsawe and G. Starke, "A least-squares mixed finite element method for biots consolidation problem in porous media," SIAM J. Numer. Anal., vol. 43, no. 1, pp. 318-339, 2005.
- [63] J. Korsawe, G. Starke, and W. Wang, "Finite element analysis of poro-elastic consolidation in porous media: Standard and mixed approaches," Comput. Methods Appl. Mech. Eng., vol. 195, no. 9-12, pp. 1096-1115, 2006.
- [64] B. Markert, "A constitutive approach to 3-d nonlinear fluid flow through finite deformable porous continua with application to a high-porosity polyurethane foam," *Transport Porous Med.*, vol. 70, no. 3, pp. 427-450, 2007.
- [65] W. Ehlers, "Constitutive equations for granular materials in geomechanical context," Cont. Mech. Environ. Sci. Geophys., vol. 337, pp. 313-402, 1993.
- [66] W. Ehlers and G. Eippers, "Finite elastic deformations in liquid-saturated and empty porous solids," *Transport Porous Med.*, vol. 34, pp. 179–191, 1999.
- [67] A. P. del Palomar and M. Doblare, "On the numerical simulation of the mechanical behaviour of articular cartilage," Int. J. Numer. Meth. Eng., vol. 67, no. 9, pp. 1244–1271, 2006.

- [68] S. Diebels, "A macroscopic description of the quasi-static behavior of granular materials based on the theory of porous media," *Granul. Matter*, vol. 2, pp. 143– 152, JUN 2000.
- [69] R. Larsson, M. Wysocki, and S. Toll, "Process-modeling of composites using two-phase porous media theory," Euro. J. Mech. A-Solids, vol. 23, pp. 15–36, JAN-FEB 2004.
- [70] B. Markert, B. Monastyrskyy, and W. Ehlers, "Fluid penetration effects in porous media contact," *Contin. Mech. Therm.*, vol. 20, pp. 303-315, OCT 2008.
- [71] S. Baek and A. R. Srinivasa, "Diffusion of a fluid through an elastic solid undergoing large deformation," Int. J. Non-Linear Mech., vol. 39, pp. 201-218, 2004.
- [72] W. Hong, X. Zhao, J. Zhou, and Z. Suo, "A theory of coupled diffusion and large deformation in polymeric gels," J. Mech. Phys. Solids, vol. 56, pp. 1779–1793, 2008.
- [73] W. Hong, Z. Liu, and Z. Suo, "Inhomogeneous swelling of a gel in equilibrium with a solvent and mechanical load," *Int. J. Solids Struct.*, vol. 46, pp. 3282–3289, 2009.
- [74] R. J. Monroe, "Measuring the mechanical response of swollen hydrogels," Master's thesis, Michigan State University, 2008.
- [75] R. S. Rivlin, "Large elastic deformation of isotropic materials. vi. further results in the theory of torsion, shear and flexure," *Phil. Trans. R. Soc. Lond. A*, vol. 242, no. 845, pp. 173–195, 1949.
- [76] O. H. Varga, "Stress-strain behavior of elastic materials," Interscience, 1966.
- [77] D. M. Haughton and A. Orr, "On the eversion of incompressible elastic cylinders," Int. J. Non-Linear Mech., vol. 30, pp. 81-95, 1995.
- [78] D. M. Haughton and A. Orr, "On the eversion of compressible elastic cylinders," Int. J. Solids Struct., vol. 34, pp. 1893–1914, 1997.
- [79] D. M. Haughton and A. Orr, "Further results for the eversion of highly compressible elastic cylinders," *Math. Mech. Solids*, vol. 1, pp. 355-367, 1996.
- [80] Y.-C. Chen and D. M. Haughton, "Existence of exact solutions for the eversion of elastic cylinders," J. Elast., vol. 49, pp. 79–88, 1997.
- [81] J. G. Simmonds and P. Warne, "Azimuthal shear of compressible or incompressible, non-linearly elastic polar orthotropic tubes of infinite extent," *Int. J. Non-Linear Mech.*, vol. 27, pp. 447-464, 1992.

- [82] A. S. Wineman and W. K. Waldron Jr., "Normal stress effects induced during circular shear of a compressible non-linear elastic cylinder," Int. J. Non-Linear Mech., vol. 30, pp. 323-339, 1995.
- [83] N. Kikuchi and N. Triantafyllidis, "On a certain class of elastic materials with non-elliptic energy densities," Q. Appl. Math., vol. 40, pp. 241-248, 1982.
- [84] E. S. Tarleton, J. P. Robinson, and M. Salman, "Solvent-induced swelling of membranes - measurements and influence in nanofiltration," J. Membr. Sci., vol. 280, pp. 442-450, Sept. 2006.
- [85] E. S. Tarleton, J. P. Robinson, S. J. Smith, and J. J. W. Na, "New experimental measurements of solvent induced swelling in nanofiltration membranes," J. Membr. Sci., vol. 261, pp. 129-135, SEP 2005.
- [86] K. R. Rajagopal, A. S. Wineman, and M. Gandhi, "On boundary conditions for a certain class of problems in mixture theory," *Int. J. Eng. Sci.*, vol. 24, no. 8, pp. 1453-1463, 1986.
- [87] T. J. Pence, "Comments on the continuum theory of finitely deformed solid-fluid mixtures," unpublished notes.
- [88] S. C. Parasad and K. R. Rajagopal, "On the diffusion of fluids through solids undergoing large deformations," *Math. Mech. Solids*, vol. 11, pp. 291-305, 2006.
- [89] K. R. Rajagopal and L. Tao, Mechanics of Mixtures. World Scientific, 1996.
- [90] M. Buonsanti, R. Fosdick, and G. Royer-Carfagni, "Chemomechanical equilibrium of bars," J. Elast., vol. 84, pp. 167–188, 2006.
- [91] H. Demirkoparan and T. J. Pence, "Swelling of an internally pressurized nonlinearly elastic tube with fiber reinforcing," *Int. J. Solids .Struct.*, vol. 44, no. 11-12, pp. 4009–4029, 2007.
- [92] G. Y. Qiu and T. J. Pence, "Remarks on the behavior of simple directionally reinforced incompressible nonlinearly elastic solids," *J. Elast.*, vol. 49, no. 1, pp. 1–30, 1997.

